HAL
open science

Renormalization invariance of many-body observables within pionless effective field theory

Mehdi Drissi

To cite this version:

Mehdi Drissi. Renormalization invariance of many-body observables within pionless effective field theory. Nuclear Theory [nucl-th]. Université Paris Saclay (COmUE), 2018. English. NNT : 2018SACLS414 . tel-02021304

HAL Id: tel-02021304

https://theses.hal.science/tel-02021304v1

Submitted on 15 Feb 2019

HAL is a multi-disciplinary open access archive for the deposit and dissemination of scientific research documents, whether they are published or not. The documents may come from teaching and research institutions in France or abroad, or from public or private research centers.

L'archive ouverte pluridisciplinaire **HAL**, est destinée au dépôt et à la diffusion de documents scientifiques de niveau recherche, publiés ou non, émanant des établissements d'enseignement et de recherche français ou étrangers, des laboratoires publics ou privés.

NNT : 2018SACLS414

Thèse de doctorat

Renormalization invariance of many-body observables within pionless effective field theory

Thèse de doctorat de l'Université Paris-Saclay
préparée à l'Université Paris-Sud
au sein de l'Irfu/DPhN du CEA Saclay

École doctorale n°576
Particules, Hadrons, Énergie, Noyau,
Instrumentation, Imagerie, Cosmos et Simulation
(PHENIICS)

Spécialité de doctorat : Structure et réactions nucléaires

Thèse présentée et soutenue à Saclay, le 25/10/2018, par

Mehdi DRISSI

Composition du Jury :

Christian Forssén	Professeur Chalmers University	(Rapporteur, Président)
Andreas Nogga	Chargé de recherche Julich Forschungszentrum	(Rapporteur)
Arnau Rios Huguet	Maître de conférences University of Surrey	(Examinateur)
Ubirajara van Kolck	Directeur de recherche Université Paris-Sud	(Examinateur)
Thomas Duguet	Ingénieur de recherche CEA-Saclay	(Directeur de thèse)
Vittorio Somà	Ingénieur de recherche CEA-Saclay	(Co-directeur)

Acknowledgements

Here we are, at the end of a three years journey, spent to reach the title of Doctor, the prerequisite to accomplish my childhood dream, being a researcher. Among the unexpected encountered along the path has been the omnipresence of the English language, characteristic of the stimulating international environment I had the chance to work in. I will soon switch to French but before I would like to take advantage of this opportunity to thanks all the non French native people I had the chance to meet. Whether briefly at a workshop, in depth during a summer school or more regularly at the lab, the meeting has always been a pleasure and an enriching experience to me. I would also like to thank the jury for taking the time of assessing the work produced during those three years and for coming from different parts of Europe to attend my defence. I hope in the future to keep on meeting such a diversity of mind and cultures.

De retour en français, voilà l'occasion de remercier mes deux directeurs de thèse, Thomas et Vittorio, qui m'ont introduit et guidé au sein de la théorie de la physique nucléaire. Sans la clarté et la rigueur de Thomas je n'aurais jamais pu m'approprier la langue et les subtilités qui règnent au sein de la communauté de la physique nucléaire. J'ai eu la chance de trouver chez eux une confiance et une souplesse d'esprit qui m'ont permis d'explorer assez librement les problèmes théoriques auxquels la physique nucléaire fait face. Cela m'a permis de développer une vision d'ensemble et de m'attaquer à un de ces problèmes majeurs dont la thèse fait l'étude. La gentillesse et les encouragements de Vittorio, en particulier lors des moments les plus confus, m'ont permis de surmonter le découragement et les difficultés rencontrés et je souhaite l'en remercier. Mais ce serait occulter la moitié si je n'évoquais pas l'ambiance du DPhN dans laquelle j'ai eu la chance d'évoluer. Mes compagnons d'infortune, théoriciens comme Pierre et Benjamin, ou expérimentateurs comme Loïc et Christopher, ont largement contribué à son installation. Je n'oublierai pas cette vie qui y régnait, que ce soit à travers les sessions de run extrême le long du versant moulonien, les telenovelas vidonnesque, les cafés et sorties précaires organisés par Jason et Nancy (et maintenant Zoé), les supervisions d'étudiant de master avec Aurélie et Adrien, ou par de simples discussions improvisées autour d'un café. Je souhaite pour les doctorants qui suivent, un environment aussi dynamique et divertissant.

Mais la vie ne s'arrête pas au labo et j'ai été assez chanceux de faire des rencontres tout aussi fascinantes et diverses lors de médiations scientifiques au Palais de la Découverte. Je pense au publique avec qui j'ai pû partager ce goût de la science mais surtout aux médiateurs et aux Anges, ces jeunes chercheurs plein de bonnes intentions et de bienveillance qui ont égayé nombre de mes soirées. Je les remercie eux ainsi que toutes les personnes que j'ai rencontrées (plus ou moins régulièrement) au gré de mes péripéties en région parisienne. En particulier, je souhaite remercier un événement tout à fait fortuit qui m'a permis de faire la rencontre de Déborah. Son soutien et son optimisme communicatif représentent beaucoup pour moi et je tiens pour cela à l'en remercier.

Je souhaite profiter de l'occasion pour remercier aussi mes amis bretons et ma famille qui

n'ont pas manqué une occasion de m'encourager pendant que j'avançais sur le chemin du doctorat. Enfin, je souhaite adresser un grand merci à mes parents, pour leur patience et leurs conseils qui continuent de me guider.

Contents

Introduction . . . . . **i**

1. Quantum many-body observables **1**
1.1. A-body problem 1
1.1.1. Generalities 1
1.1.2. Hamiltonian operator 2
1.1.3. Schrödinger equation 3
1.1.4. Observables 3
1.2. Green's functions 4
1.2.1. Definitions 4
1.2.2. Observables 6
1.2.3. Spectral functions 8
1.3. Perturbation theory 9
1.3.1. Hamiltonian partitioning 9
1.3.2. Unperturbed system 9
1.3.3. Perturbative expansion 12

2. Pionless Effective Field Theory **17**
2.1. Ultraviolet divergences and renormalization 17
2.1.1. Pionless Hamiltonian 17
2.1.2. Perturbation theory 20
2.1.3. Renormalization schemes 22
2.1.4. Power-counting rules 25
2.2. Renormalization in the two-body sector 29
2.2.1. Tree-level renormalization 31
2.2.2. One-loop renormalization 32
2.2.3. Exact renormalization 33

3. Equation of state of neutron matter **37**
3.1. Infinite neutron matter 38
3.1.1. Perturbation theory 38
3.1.2. Energy per particle 39
3.2. Self-consistent Green's functions 40
3.2.1. Equations of motion 41
3.2.2. Spectral function in the iterative procedure 45
3.3. Self-energy approximations 46
3.3.1. Hartree-Fock approximation 46
3.3.2. Second Born approximation 47

3.3.3. Ladder approximation . . . 48
3.3.4. Renormalization in self-consistent Green's functions . . . 49
3.4. Numerical computations . . . 51
3.4.1. Self-consistent Green's function numerical scheme . . . 51
3.4.2. Numerical approximations . . . 52
3.4.3. Numerical results . . . 54
3.4.4. Non-self consistent Hartree-Fock calculation . . . 59
3.5. Analytical calculations . . . 60
3.5.1. Analytical calculation in the ladder approximation . . . 60
3.5.2. Reduction to Hartree-Fock and second Born approximations . . . 69
3.5.3. Comparative study . . . 71

4. Ultraviolet divergences of many-body diagrams . . . 81
4.1. Ultraviolet divergences in many-body calculations . . . 81
4.1.1. General problem . . . 81
4.1.2. Analysis of medium-insertion diagrams . . . 82
4.2. Analysis of particle-hole diagrams . . . 92
4.2.1. General integrals . . . 92
4.2.2. Asymptotic theorem . . . 94
4.2.3. General procedure . . . 96
4.3. Example of applications . . . 98
4.3.1. Random phase approximation . . . 99
4.3.2. Hartree-Fock perturbation theory . . . 102
4.4. Discussion . . . 104

Conclusion . . . 107

Appendices 109

A. Feynman rules for k-body Green's functions . . . 111

B. Calculation of R functions . . . 113
B.1. R_0 . . . 113
B.1.1. $M(y;s)$ integrals . . . 113
B.1.2. v integral . . . 114
B.2. R_1 . . . 116

C. BPHZ renormalization procedure . . . 117

Synthèse en français . . . 121

Bibliography . . . 127

Introduction

Low-energy nuclear physics is undergoing a major renewal. On Earth, successive generations of radioactive beam facilities are moving their focus towards short-lived, exotic isotopes and open up new regions of the nuclear chart to experimental enquiry. In outer space, supernovae explosions and compact stars constitute unique laboratories for testing nuclear matter in extreme conditions. Altogether, this quest towards the limits of existence of nuclear systems is taking us deeper into the fundamental questions that are driving this area of physics, namely

- how basic interactions between protons and neutrons emerge from the gauge theory of interacting quarks and gluons, i.e. quantum chromodynamics (QCD) ?

- how nucleons bind inside a nucleus and what are the limits of existence of the latter with respect to the strong force in terms of its mass, neutron-proton imbalance and angular momentum ?

- how the complex phenomenology of nuclei emerges from elementary inter-nucleon interactions?

Addressing these questions poses major challenges both experimentally and theoretically. In spite of several decades of efforts, low-energy nuclear physics remains an open and difficult problem. In particular, an accurate and systematic description of low-energy nuclear systems is still out of reach.

Over the last decades, many theoretical approaches have been developed to address the nuclear A-body problem, with their originality and heterogeneity reflecting the complexity of nuclear systems. Traditionally, they are separated into two categories: (i) *ab initio* methods that rely on the idea that properties of the system as a whole can be described in terms of structureless nucleons and interactions between them and (ii) *effective* approaches, which formulate the problem in terms of interactions between more effective degrees of freedoms. While the first category of methods constitutes the "holy grail" of low-energy nuclear theory, the second category currently provides the way to access the large majority of nuclei.

In recent years, the incoming flow of data on short-lived nuclei as well as the external demand for reliable nuclear physics inputs have challenged existing theoretical approaches. Considerable focus has moved towards aspects like internal consistency, predictive power and a thorough estimation of theoretical uncertainties. On the one hand *effective* approaches, often adjusted to reproduce a particular zone of the nuclide chart or tuned in a biased way to stable nuclei, have encountered problems in delivering consistent predictions away from known data. On the other hand, *ab initio* approaches, which aim at solving the A-body Schrödinger equation in terms of elementary inter-nucleon forces, have undergone major developments and are emerging as a method of choice for light and medium-mass nuclei.

Introduction

Advances in *ab initio* techniques occurred via two main steps over the past twenty years. A first breakthrough took place in the 90s, when first supercomputers enabled the application of Monte-Carlo and configuration-interaction techniques to the nuclear many-body problem [1, 2]. Such methods aim to solve the many-body problem "exactly", i.e. by processing all possible multi-particle configurations (directly or through a Monte-Carlo sampling) in a large enough model space. The resulting calculations successfully reproduce structure as well as reaction properties of light nuclei with high accuracy. Recent examples are the unified description of the structure of ^{6}Li and deuterium-^{4}He dynamics [3] or the electromagnetic and neutral-weak response functions of ^{4}He and ^{12}C [4]. The cost of such simulations however scales at least exponentially, thus dramatically with the number of particles, which limits these techniques to nuclei with a few (of the order of ten) nucleons, even with modern computing facilities.

A second breakthrough took place over the last ten years and combined the use of chiral interactions and similarity renormalization group (SRG) methods[1] [5] with the introduction of controlled approximations for the Schrödinger equation. Here, by "controlled" one means that the uncertainty brought by such approximations is *a posteriori* bounded from above, usually via convergence tests. Such approximations rely on a truncated expansion of the solution to the A-body problem, typically expressible via a series of perturbation diagrams that are appropriately resummed. Compared to the "exact" many-body techniques applied to light nuclei, the use of such methods allowed bringing down the scaling from exponential to polynomial, while maintaining many-body uncertainties at the few per cent level. As a result, since a few years, *ab initio* calculations can access the region of medium-mass isotopes (i.e. up to few tens of nucleons).

In practice, traditional many-body calculations rely on the given of a nuclear Hamiltonian H and on the search for its exact eigenstates in all A-body sectors of interest, i.e. the goal is to solve the Schrödinger equation

$$H \left|\Psi_m^{\mathrm{A}}\right\rangle = E_m^{\mathrm{A}} \left|\Psi_m^{\mathrm{A}}\right\rangle \tag{1}$$

where m indexes the set of solution, to the best accuracy possible .

In this context, the Hamiltonian can be modeled in various ways. The current paradigm consists of building H within the framework of chiral effective field theory (χEFT) [6, 7, 8] such that it takes the form of a series

$$H_\chi \equiv H_\chi^{\mathrm{LO}} + H_\chi^{\mathrm{SL}O} = H_\chi^{\mathrm{LO}} + \sum_{p=1}^{\infty} H_\chi^{\mathrm{N}^p\mathrm{LO}} \tag{2}$$

where the leading-order (LO) and the sub-leading orders (SLOs) are organized according to a set of power-counting (PC) rules. Historically first to have been proposed, Weinberg's power counting [7, 8] happens to fit with traditional many-body calculations, i.e. independently of the order at which SLOs are truncated, Eq. (1) is meant to be solved exactly to access observables such as E_m^{A}. However, Weinberg's PC has been recently disqualified on the basis that the EFT must be (order-by-order) renormalizable and alternative PCs have been proposed [9]. In addition to modifying the order at which certain contributions enter the Hamiltonian, new PCs

[1] SRG methods are based on a unitary transformation (hence leaving A-body observables untouched) aiming at decoupling low- and high-momentum components in the interaction, thus making the solution of the A-body problem "more perturbative".

stipulate that, while LO is to be solved exactly according to traditional many-body calculations, SLOs must be computed in perturbation relatively to the LO solution. It happens that the same scheme underlines the PC at play in pionless effective field theory ($\not{\pi}$EFT) that was indeed shown to satisfy renormalizability at LO up to four-body systems [10].

In view of the above, the goal of the present thesis is to investigate the renormalization invariance of many-body observables computed within the framework of $\not{\pi}$EFT in A-body sectors with $\mathrm{A} \gg 10$. Hopefully the lessons learnt can be extended to χEFT. The program obviously departs from traditional many-body calculations given that SLOs *must* be solved in perturbation relative to the LO solution, i.e. in the spirit of the distorded wave approximation (DWA). As mentioned above, this scheme has already been shown to work successfully up to four-body systems on the basis of a LO Hamiltonian containing contact 2- and 3-body interactions. A first important issue, however, relates to the fact that, while $H_{\not{\pi}}^{\mathrm{LO}}$ can indeed be solved exactly in few-body systems, it is intrinsically impossible, i.e. numerically intractable for many decades to come, to do so when computing many-body observables for $\mathrm{A} \gg 10$. Consequently, one *must* design an additional expansion and truncation when proceeding to the first step of the program that consists of solving

$$H_{\not{\pi}}^{\mathrm{LO}} \left|\Psi_m^{\mathrm{A}}\right\rangle^{(\mathrm{LO})} = E_m^{\mathrm{A(LO)}} \left|\Psi_m^{\mathrm{A}}\right\rangle^{(\mathrm{LO})} \quad . \tag{3}$$

Typical truncations applicable to A-body systems with $\mathrm{A} \gg 10$ are nowadays implemented on the basis of non-perturbative self-consistent Green's function (SCGF) [11, 12], coupled cluster (CC) [13, 14] and in-medium similarity renormalization group [15, 16] methods or on the basis of many-body perturbation theory (MBPT) [17, 18]. In this thesis, SCGF and MBPT constitute the working tools of interest. The main goal is to investigate the implications of having to solve Eq. (3) only approximately on the renormalization invariance of A-body observables at LO. This study only constitutes a first step given that SLO contributions must eventually be investigated as well. This will, however, only be relevant once the LO has been elucidated given that SLOs must be handled relatively to it.

The manuscript is organized as follows. Chap. 1 sets up notations, defines key quantities and introduces the basics of MBPT that are used throughout the rest of the thesis. Chap. 2 introduces $\not{\pi}$EFT and discusses the need to renormalize ultraviolet divergences. In Chap. 3, the equation of state (EoS) of infinite neutron matter is computed via SCGF theory on the basis of the $\not{\pi}$EFT LO potential, previously renormalized by solving the Schrödinger equation exactly in the two-body sector in agreement with PC rules. Attempting to fulfill the PC rule in infinite neutron matter as well, "as exact as possible" SCGF calculations are performed by using the most advanced truncation scheme nowadays available denoted as the "self-consistent ladder approximation" and that happens to be exact in the two-body sector. In doing so, the (lack of) renormalizability of the results is scrutinized in details, including a thorough check of the numerical approximations at play in the calculations. The question of renormalizability is further investigated by degrading the many-body truncation to low-order in MBPT and complemented by detailed analytical derivations. Based on these results, the renormalizable character of (sets of) MBPT diagrams is studied formally in Chap. 4, paying particular attention to the requirement that such a renormalizability is independent of the A-body sector under consideration. This opens the path to formulate the renormalization of a wide range of many-body truncation schemes in the future.

Chapter 1.

Quantum many-body observables

In this introductory chapter the notations are set and key many-body quantities used throughout the manuscript are introduced. The general aspects of MBPT, whose associated Feynman diagrammatics is used extensively throughout the document, are also detailed. Contrarily, SCGF theory is left to be introduced later on in Chap. 3 where its connection to MBPT is briefly discussed as well.

1.1. A-body problem

1.1.1. Generalities

We focus on quantum systems that can be described via a finite number of interacting degrees of freedom characterized by a basis $\mathscr{B}_1 \equiv \{|\mu\rangle\}$ of the one-body Hilbert space denoted as $\mathscr{H}_1$. The one-dimensional space spanned by the non-degenerate vacuum state $|0\rangle$ is denoted as $\mathscr{H}_0$.

Elementary degrees of freedom being defined, the description of systems made out of A of them is obtained via states of the A-body Hilbert space

$$\mathscr{H}_{\mathrm{A}} = \bigotimes_{i=1}^{\mathrm{A}} \mathscr{H}_1(i) \tag{1.1}$$

constituting the so-called A-*body sector*. Eventually, general many-body states are elements of the Fock space defined as

$$\mathcal{F} \equiv \bigoplus_{\mathrm{A}=0}^{+\infty} \mathscr{H}_{\mathrm{A}} \ . \tag{1.2}$$

The present focus is on many-body systems of identical fermions. Consequently, the Hilbert space of physically allowed states is reduced to A-body states that are antisymmetric under the exchange of any pair of particles[1].

[1]Many-body boson systems can be studied in a similar fashion with the difference that many-body states are symmetric under the exchange of any pair of particles.

1.1.2. Hamiltonian operator

The second quantization formalism introduces creation and annihilation operators $(a_\mu^\dagger, a_\mu)$ associated with the one-body basis $\mathscr{B}_1$via

$$\forall \mu,\ a_\mu^\dagger \left|0\right\rangle = \left|\mu\right\rangle \ , \tag{1.3a}$$

$$a_\mu \left|0\right\rangle = 0 \ , \tag{1.3b}$$

along with the anticommutation rules

$$\{a_\mu^\dagger, a_\nu\} = \delta_{\mu\nu} \ , \tag{1.4a}$$

$$\{a_\mu^\dagger, a_\nu^\dagger\} = 0 \ , \tag{1.4b}$$

$$\{a_\mu, a_\nu\} = 0 \ , \tag{1.4c}$$

with $\{\ .\ ,\ .\ \}$ being the anticommutator bracket.

Single-particle creation and annihilation operators provide a basis to represent operators O acting on $\mathcal{F}$ such that

$$O \equiv \sum_{p,q=0}^{+\infty} \frac{1}{p!q!} \sum_{\substack{\mu_1\ldots\mu_p \\ \nu_1\ldots\nu_q}} o^{pq}_{\mu_1\ldots\mu_p\nu_1\ldots\nu_q}\ a_{\mu_1}^\dagger \ldots a_{\mu_p}^\dagger a_{\nu_q} \ldots a_{\nu_1} \ , \tag{1.5}$$

where $o^{pq}_{\mu_1\ldots\mu_p\nu_1\ldots\nu_q}$ are fully antisymmetric complex numbers i.e.

$$\forall\ P,\ o^{pq}_{\mu_1\ldots\mu_p\nu_1\ldots\nu_q} = (-1)^{\sigma(P)} o^{pq}_{P(\mu_1\ldots\mu_p|\nu_1\ldots\nu_q)} \ , \tag{1.6}$$

where $\sigma(P)$ is the signature of the permutation P. The notation $P(\ldots|\ldots)$ denotes a separation into the indices of p creation operators and of q annihilation operators such that the permutations are only considered between members of the same group. Two subcases are of particular interest. The operator O is referred to as

1. a particle-number conserving k-body operator whenever it writes as

$$O = \frac{1}{(\mathrm{k}!)^2} \sum_{\substack{\mu_1\ldots\mu_\mathrm{k} \\ \nu_1\ldots\nu_\mathrm{k}}} o^{\mathrm{kk}}_{\mu_1\ldots\mu_\mathrm{k}\nu_1\ldots\nu_\mathrm{k}}\ a_{\mu_1}^\dagger \ldots a_{\mu_\mathrm{k}}^\dagger a_{\nu_\mathrm{k}} \ldots a_{\nu_1} \ , \tag{1.7}$$

2. a particle-number changing operator whenever it writes as

$$O = \frac{1}{p!q!} \sum_{\substack{\mu_1\ldots\mu_p \\ \nu_1\ldots\nu_q}} o^{pq}_{\mu_1\ldots\mu_p\nu_1\ldots\nu_q}\ a_{\mu_1}^\dagger \ldots a_{\mu_p}^\dagger a_{\nu_q} \ldots a_{\nu_1} \ , \tag{1.8}$$

   where $k \equiv p - q$ denotes now the number of particles the operator adds[2] to the A-body state it acts on.

[2]The integer k can be negative, in which case the operator removes $-k$ particles to the states it acts on.

The nuclear Hamiltonian H is particle-number conserving and can, thus, be decomposed as a sum of k-body Hermitian operators, i.e.

$$H = T + V \ , \tag{1.9a}$$

$$T \equiv \frac{1}{(1!)^2} \sum_{\alpha\beta} t_{\alpha\beta}\, a^\dagger_\alpha a_\beta \ , \tag{1.9b}$$

$$V \equiv \frac{1}{(2!)^2} \sum_{\alpha\beta\gamma\delta} v_{\alpha\beta\gamma\delta}\, a^\dagger_\alpha a^\dagger_\beta a_\delta a_\gamma + \dots \ , \tag{1.9c}$$

with T the kinetic energy, V the interaction potential and where antisymmetrized two-body matrix elements are implied. In order to avoid un-necessary complications we restrict ourselves to the case of two-body interactions[3], i.e. higher-body operators represented by dots in (1.9c) are omitted.

1.1.3. Schrödinger equation

Traditional many-body calculations rely on the given of a nuclear Hamiltonian H and on the search for its exact eigenstates in all A-body sectors of interest, i.e. the goal is to solve the Schrödinger equation

$$H \left|\Psi^{\mathrm{A}}_m\right\rangle = E^{\mathrm{A}}_m \left|\Psi^{\mathrm{A}}_m\right\rangle \ , \tag{1.10a}$$

$$A \left|\Psi^{\mathrm{A}}_m\right\rangle = \mathrm{A} \left|\Psi^{\mathrm{A}}_m\right\rangle \ , \tag{1.10b}$$

where A denotes the particle-number operator. The ground-state of the A-body system relates to the minimal energy $E^{\mathrm{A}}_0 \equiv \min_m \left\{E^{\mathrm{A}}_m\right\}$ for the number of particles A. The ground-state energy E^{A}_0 is presently assumed to be non-degenerate.

1.1.4. Observables

One typically wishes to compute the expectation value of a particle-number-conserving k-body operator O in a given eigenstate of H

$$O^{\mathrm{A}}_m \equiv \frac{\langle\Psi^{\mathrm{A}}_m|O|\Psi^{\mathrm{A}}_m\rangle}{\langle\Psi^{\mathrm{A}}_m|\Psi^{\mathrm{A}}_m\rangle} \ . \tag{1.11}$$

In particular, the ground-state expectation value is usefully expressed in terms of the ground-state k-body density matrix

$$\rho^{(\mathrm{A},k)}_{\substack{\mu_1\dots\mu_k\\ \nu_1\dots\nu_k}} \equiv \frac{\langle\Psi^{\mathrm{A}}_0|a^\dagger_{\nu_1}\dots a^\dagger_{\nu_k} a_{\mu_k}\dots a_{\mu_1}|\Psi^{\mathrm{A}}_0\rangle}{\langle\Psi^{\mathrm{A}}_0|\Psi^{\mathrm{A}}_0\rangle} \ , \tag{1.12}$$

according to

$$O^{\mathrm{A}}_0 = \frac{1}{(\mathrm{k}!)^2} \sum_{\substack{\nu_1\dots\nu_k\\ \mu_1\dots\mu_k}} o^{\mathrm{kk}}_{\mu_1\dots\mu_{\mathrm{k}}\nu_1\dots\nu_{\mathrm{k}}}\, \rho^{(\mathrm{A},k)}_{\substack{\nu_1\dots\nu_k\\ \mu_1\dots\mu_k}} \ . \tag{1.13}$$

[3]For nuclear systems such as nuclei and nuclear matter, one should eventually consider at least three-nucleon interactions [19, 20, 21].

More generally, one wishes to compute matrix elements of a particle-number-changing operator O between eigenstates of H

$$O_{mn}^{\mathrm{AA}'} \equiv \frac{\langle \Psi_m^{\mathrm{A}} | O | \Psi_n^{\mathrm{A}'} \rangle}{\sqrt{\langle \Psi_m^{\mathrm{A}} | \Psi_m^{\mathrm{A}} \rangle} \sqrt{\langle \Psi_n^{\mathrm{A}'} | \Psi_n^{\mathrm{A}'} \rangle}} \ . \tag{1.14}$$

1.2. Green's functions

The many-body problem is presently reformulated in terms of k-body Green's functions that are eventually related to (a subset of) the many-body observables introduced above.

1.2.1. Definitions

Heisenberg picture

The time-evolution operator associated to H is defined through

$$\left| \Psi^{\mathrm{A}}(t) \right\rangle \equiv U(t,t') \left| \Psi^{\mathrm{A}}(t') \right\rangle \ , \tag{1.15}$$

where $\left| \Psi^{\mathrm{A}}(t) \right\rangle$ is in the Schrödinger picture, i.e. it satisfies time-dependent Schrödinger's equation

$$i \frac{\partial}{\partial t} \left| \Psi^{\mathrm{A}}(t) \right\rangle = H \left| \Psi^{\mathrm{A}}(t) \right\rangle \ . \tag{1.16}$$

In the case of a time-independent Hamiltonian, U depends only on $t - t'$ as

$$U(t,t') = e^{-iH(t-t')} \equiv U(t-t') \ . \tag{1.17}$$

Given an operator O in the Schrödinger picture, its representation in the Heisenberg picture is defined by

$$\bar{O}(t) \equiv e^{iHt} O \ e^{-iHt} \ . \tag{1.18}$$

In particular, creation and annihilation operators in the Heisenberg picture are given by

$$\bar{a}_\mu(t) \equiv e^{iHt} a_\mu \ e^{-iHt} \ , \tag{1.19a}$$

$$\bar{a}_\mu^\dagger(t) \equiv e^{iHt} a_\mu^\dagger \ e^{-iHt} \ . \tag{1.19b}$$

k-body Green's function

The k-body Green's function associated with the A-body ground-state is defined as

$$i^k G^{(\mathrm{A},k)}_{\substack{\mu_1 \ldots \mu_k \\ \nu_1 \ldots \nu_k}}(t_{\mu_1}, \ldots, t_{\mu_k}, t_{\nu_1}, \ldots, t_{\nu_k}) \equiv \frac{\langle \Psi_0^{\mathrm{A}} | \mathrm{T} \left[\bar{a}_{\mu_k}(t_{\mu_k}) \ldots \bar{a}_{\mu_1}(t_{\mu_1}) \bar{a}_{\nu_1}^\dagger(t_{\nu_1}) \ldots \bar{a}_{\nu_k}^\dagger(t_{\nu_k}) \right] | \Psi_0^{\mathrm{A}} \rangle}{\langle \Psi_0^{\mathrm{A}} | \Psi_0^{\mathrm{A}} \rangle} \ , \tag{1.20}$$

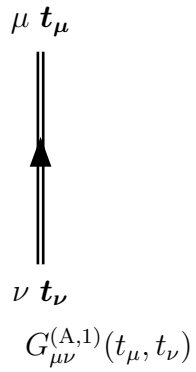

Figure 1.1. Diagrammatic representation of $G^{(\mathrm{A},1)}_{\mu\nu}(t_\mu, t_\nu)$.

where T denotes the time-ordering operator[4]. A case of particular interest is given by the one-body Green's function

$$iG^{(\mathrm{A},1)}_{\mu\nu}(t_\mu, t_\nu) \equiv \frac{\langle \Psi^{\mathrm{A}}_0 | \mathrm{T}\left[\bar{a}_\mu(t_\mu)\bar{a}^\dagger_\nu(t_\nu)\right] | \Psi^{\mathrm{A}}_0 \rangle}{\langle \Psi^{\mathrm{A}}_0 | \Psi^{\mathrm{A}}_0 \rangle} \,, \tag{1.21}$$

whose diagrammatic representation is given in Fig. 1.1.

It is convenient to work with the energy representation of Green's functions obtained by Fourier transforming the time representation introduced above. As H is time-independent, Green's functions are time-translationally invariant. This translates into the conservation of energy in the energy representation. Formally, the Fourier transformed k-body Green's function reads as

$$\begin{aligned} &2\pi\delta(\omega_{\mu_1} + \cdots + \omega_{\mu_k} - \omega_{\nu_1} - \cdots - \omega_{\nu_k}) G^{(\mathrm{A},k)}_{\substack{\mu_1\ldots\mu_k \\ \nu_1\ldots\nu_k}}(\omega_{\mu_1}, \ldots, \omega_{\mu_k}, \omega_{\nu_1}, \ldots, \omega_{\nu_k}) \\ &\equiv \int \mathrm{d}t_{\mu_1} \ldots \mathrm{d}t_{\mu_k} \mathrm{d}t_{\nu_1} \ldots \mathrm{d}t_{\nu_k} e^{i(\omega_{\mu_1} t_{\mu_1} + \cdots + \omega_{\mu_k} t_{\mu_k})} e^{-i(\omega_{\nu_1} t_{\nu_1} + \cdots + \omega_{\nu_k} t_{\nu_k})} G^{(\mathrm{A},k)}_{\substack{\mu_1\ldots\mu_k \\ \nu_1\ldots\nu_k}}(t_{\mu_1}, \ldots, t_{\mu_k}, t_{\nu_1}, \ldots, t_{\nu_k}) \,, \end{aligned} \tag{1.22}$$

which simplifies for the one-body Green's function as[5]

$$2\pi\delta(\omega_\mu - \omega_\nu) G^{(\mathrm{A},1)}_{\mu\nu}(\omega_\mu, \omega_\nu) \equiv \int \mathrm{d}t_\mu \mathrm{d}t_\nu e^{i\omega_\mu t_\mu} e^{-i\omega_\nu t_\nu} G^{(\mathrm{A},1)}_{\mu\nu}(t_\mu, t_\nu) \,. \tag{1.23}$$

Two-time k-body Green's function

We further introduce a specific two-time reduction of the ground-state k-body Green's function by setting the k annihilation (creation) operators at the same time t_μ (t_ν)

$$\begin{aligned} i^k G^{(\mathrm{A},k)}_{\substack{\mu_1\ldots\mu_k \\ \nu_1\ldots\nu_k}}(t_\mu, t_\nu) &\equiv i^k G^{(\mathrm{A},k)}_{\substack{\mu_1\ldots\mu_k \\ \nu_1\ldots\nu_k}}(t_\mu, \ldots, t_\mu, t_\nu, \ldots, t_\nu) \\ &= \frac{\langle \Psi^{\mathrm{A}}_0 | \mathrm{T}\left[\bar{a}_{\mu_k}(t_\mu) \ldots \bar{a}_{\mu_1}(t_\mu) \bar{a}^\dagger_{\nu_1}(t_\nu) \ldots \bar{a}^\dagger_{\nu_k}(t_\nu)\right] | \Psi^{\mathrm{A}}_0 \rangle}{\langle \Psi^{\mathrm{A}}_0 | \Psi^{\mathrm{A}}_0 \rangle} \end{aligned} \tag{1.24}$$

[4]The time-ordering operator orders a product of operators in decreasing order according to their time labels (i.e., larger times to the left) and multiplies the result with the signature of the permutation used to achieve the corresponding reordering.

[5]For the one-body Green's function, it is convenient to use the shorthand notation $G^{(\mathrm{A},1)}_{\mu\nu}(\omega) \equiv G^{(\mathrm{A},1)}_{\mu\nu}(\omega, \omega)$.

$$
\begin{aligned}
&= \theta(t_\mu - t_\nu) \frac{\langle \Psi_0^{\mathrm{A}} | \bar{a}_{\mu_k}(t_\mu) \dots \bar{a}_{\mu_1}(t_\mu) \bar{a}^\dagger_{\nu_1}(t_\nu) \dots \bar{a}^\dagger_{\nu_k}(t_\nu) | \Psi_0^{\mathrm{A}} \rangle}{\langle \Psi_0^{\mathrm{A}} | \Psi_0^{\mathrm{A}} \rangle} \\
&\quad + (-1)^k \theta(t_\nu - t_\mu) \frac{\langle \Psi_0^{\mathrm{A}} | \bar{a}^\dagger_{\nu_1}(t_\nu) \dots \bar{a}^\dagger_{\nu_k}(t_\nu) \bar{a}_{\mu_k}(t_\mu) \dots \bar{a}_{\mu_1}(t_\mu) | \Psi_0^{\mathrm{A}} \rangle}{\langle \Psi_0^{\mathrm{A}} | \Psi_0^{\mathrm{A}} \rangle} \\
&\equiv i^k G^{(\mathrm{A},k)+}_{\substack{\mu_1 \dots \mu_k \\ \nu_1 \dots \nu_k}}(t_\mu, t_\nu) + i^k G^{(\mathrm{A},k)-}_{\substack{\mu_1 \dots \mu_k \\ \nu_1 \dots \nu_k}}(t_\mu, t_\nu) \ , \qquad (1.25)
\end{aligned}
$$

where $G^{(\mathrm{A},k)+}$ and $G^{(\mathrm{A},k)-}$ define retarded and advanced two-time k-body Green's functions, respectively.

k-body density matrix

The ground-state k-body density matrix introduced in Eq. (1.12) is recovered from the (two-time) k-body Green's function in the equal-time limit[6]

$$
\begin{aligned}
\rho^{(\mathrm{A},k)}_{\substack{\mu_1 \dots \mu_k \\ \nu_1 \dots \nu_k}} &= (-i)^k G^{(\mathrm{A},k)}_{\substack{\mu_1 \dots \mu_k \\ \nu_1 \dots \nu_k}}(t, \dots, t, t^+, \dots, t^+) \\
&\equiv (-i)^k G^{(\mathrm{A},k)}_{\substack{\mu_1 \dots \mu_k \\ \nu_1 \dots \nu_k}}(t, t^+) \ , \qquad (1.26)
\end{aligned}
$$

where the limit is taken according to $t^+ \equiv \lim_{\epsilon \to 0}(t + \epsilon)$ with $\epsilon > 0$.

1.2.2. Observables

A-body ground-state observables

According to Eqs. (1.13) and (1.26), the ground-state expectation value of any k-body operator O can be accessed from the knowledge of equal-time k-body Green's function via

$$
O_0^{\mathrm{A}} = \frac{(-i)^k}{(\mathrm{k}!)^2} \sum_{\substack{\nu_1 \dots \nu_k \\ \mu_1 \dots \mu_k}} o^{\mathrm{kk}}_{\mu_1 \dots \mu_\mathrm{k} \nu_1 \dots \nu_\mathrm{k}} \, G^{(\mathrm{A},k)}_{\substack{\mu_1 \dots \mu_k \\ \nu_1 \dots \nu_k}}(t, t^+) \ . \qquad (1.27)
$$

In particular the ground-state energy associated with the Hamiltonian introduced in Eq. (1.9) is obtained from the equal-time 1- and 2-body Green's functions according to

$$
E_0^{\mathrm{A}} = -\frac{i}{(1!)^2} \sum_{\mu\nu} t_{\mu\nu} \, G^{(\mathrm{A},1)}_{\nu\mu}(t, t^+) - \frac{1}{(2!)^2} \sum_{\alpha\beta\gamma\delta} v_{\alpha\beta\gamma\delta} \, G^{(\mathrm{A},2)}_{\substack{\gamma\delta \\ \alpha\beta}}(t, t^+) \ . \qquad (1.28)
$$

Eigenspectrum of $(\mathrm{A} \pm k)$-body systems

Departing from the equal-time limit, the two-time A-body ground-state k-body Green's function introduced in Eq. (1.24) provides further access to the complete spectroscopy of $(\mathrm{A} \pm k)$-body systems via its pole structure over the complex plane in the energy representation[7].

[6] Given the time-independence of H, k-body Green's functions are independent of a global shift in time such that $G^{(\mathrm{A},k)}_{\substack{\mu_1 \dots \mu_k \\ \nu_1 \dots \nu_k}}(t, \dots, t, t^+, \dots, t^+) = G^{(\mathrm{A},k)}_{\substack{\mu_1 \dots \mu_k \\ \nu_1 \dots \nu_k}}(0, \dots, 0, 0^+, \dots, 0^+)$.

[7] Other two-time reductions of the A-body ground-state k-body Green's function can provide access to other observables introduced in Sec. 1.1.4, e.g. excitation energies in the A-body sector. Because these observables are not explicitly discussed later on in the present document and because introducing them would lead to unnecessary lengthy developments, we do not elaborate on them here.

This is a powerful feature of Green's functions that can be recognized via the introduction of their Lehmann representations. Making the time dependence of the two-time k-body Green's function fully explicit

$$i^k G^{(\mathrm{A},k)}_{\substack{\mu_1\ldots\mu_k\\ \nu_1\ldots\nu_k}}(t_\mu,t_\nu) = \theta(t_\mu-t_\nu)e^{iE_0^{\mathrm{A}}(t_\mu-t_\nu)}\frac{\langle\Psi_0^{\mathrm{A}}|a_{\mu_k}\ldots a_{\mu_1}e^{-iH(t_\mu-t_\nu)}a^\dagger_{\nu_1}\ldots a^\dagger_{\nu_k}|\Psi_0^{\mathrm{A}}\rangle}{\langle\Psi_0^{\mathrm{A}}|\Psi_0^{\mathrm{A}}\rangle} + (-1)^k\theta(t_\nu-t_\mu)e^{iE_0^{\mathrm{A}}(t_\nu-t_\mu)}\frac{\langle\Psi_0^{\mathrm{A}}|a^\dagger_{\nu_1}\ldots a^\dagger_{\nu_k}e^{-iH(t_\nu-t_\mu)}a_{\mu_k}\ldots a_{\mu_1}|\Psi_0^{\mathrm{A}}\rangle}{\langle\Psi_0^{\mathrm{A}}|\Psi_0^{\mathrm{A}}\rangle}\ , \tag{1.29}$$

and introducing a completeness relation in $\mathscr{H}_{\mathrm{A}+k}$ ($\mathscr{H}_{\mathrm{A}-k}$) in the retarded (advanced) part, one obtains

$$i^k G^{(\mathrm{A},k)}_{\substack{\mu_1\ldots\mu_k\\ \nu_1\ldots\nu_k}}(t_\mu,t_\nu) = \theta(t_\mu-t_\nu)\sum_{m\in\mathscr{H}_{\mathrm{A}+k}} e^{i(E_0^{\mathrm{A}}-E_m^{\mathrm{A}+k})(t_\mu-t_\nu)}\ U^{(\mathrm{A},k)m}_{\mu_1\ldots\mu_k}\ U^{(\mathrm{A},k)m*}_{\nu_1\ldots\nu_k} + (-1)^k\theta(t_\nu-t_\mu)\sum_{m\in\mathscr{H}_{\mathrm{A}-k}} e^{i(E_0^{\mathrm{A}}-E_m^{\mathrm{A}-k})(t_\nu-t_\mu)}\ V^{(\mathrm{A},k)m*}_{\nu_1\ldots\nu_k}\ V^{(\mathrm{A},k)m}_{\mu_1\ldots\mu_k}\ , \tag{1.30}$$

where k-nucleon addition and removal spectral amplitudes are respectively defined as

$$U^{(\mathrm{A},k)m}_{\mu_1\ldots\mu_k} \equiv \frac{\langle\Psi_0^{\mathrm{A}}|a_{\mu_k}\ldots a_{\mu_1}|\Psi_m^{\mathrm{A}+k}\rangle}{\sqrt{\langle\Psi_0^{\mathrm{A}}|\Psi_0^{\mathrm{A}}\rangle\langle\Psi_m^{\mathrm{A}+k}|\Psi_m^{\mathrm{A}+k}\rangle}}\ , \tag{1.31a}$$

$$V^{(\mathrm{A},k)m}_{\nu_1\ldots\nu_k} \equiv \frac{\langle\Psi_0^{\mathrm{A}}|a^\dagger_{\nu_1}\ldots a^\dagger_{\nu_k}|\Psi_m^{\mathrm{A}-k}\rangle}{\sqrt{\langle\Psi_0^{\mathrm{A}}|\Psi_0^{\mathrm{A}}\rangle\langle\Psi_m^{\mathrm{A}-k}|\Psi_m^{\mathrm{A}-k}\rangle}}\ . \tag{1.31b}$$

Eventually, Fourier transforming Eq. (1.30) with respect to $t_\mu - t_\nu$ leads to the so-called Lehmann representation of the two-time k-body Green's function

$$i^k G^{(\mathrm{A},k)}_{\substack{\mu_1\ldots\mu_k\\ \nu_1\ldots\nu_k}}(\omega) = i\left(\sum_{m\in\mathscr{H}_{\mathrm{A}+k}}\frac{U^{(\mathrm{A},k)m}_{\mu_1\ldots\mu_k}\ U^{(\mathrm{A},k)m*}_{\nu_1\ldots\nu_k}}{\omega-(E_m^{\mathrm{A}+k}-E_0^{\mathrm{A}})+i\eta} - (-1)^k\sum_{m\in\mathscr{H}_{\mathrm{A}-k}}\frac{V^{(\mathrm{A},k)m*}_{\nu_1\ldots\nu_k}\ V^{(\mathrm{A},k)m}_{\mu_1\ldots\mu_k}}{\omega-(E_0^{\mathrm{A}}-E_m^{\mathrm{A}-k})-i\eta}\right)\ . \tag{1.32}$$

As Eq. (1.32) demonstrates, the exact A-body ground-state two-time reduced k-body Green's function $G^{(\mathrm{A},k)}(\omega)$ possesses single poles associated to k-nucleon addition/removal energies to/from the ground state of the A-body system

$$E_m^{+k} \equiv E_m^{\mathrm{A}+k} - E_0^{\mathrm{A}}\ , \tag{1.33a}$$

$$E_m^{-k} \equiv E_0^{\mathrm{A}} - E_m^{\mathrm{A}-k}\ . \tag{1.33b}$$

The poles associated to $E_m^{\mathrm{A}+k}$ ($E_m^{\mathrm{A}-k}$) are shifted infinitesimally below (above) the real axis. In the case of a non-degenerate A-body ground state, the combined $E_m^{\pm k}$ spectrum displays a gap $E_0^{+k} - E_0^{-k}$ between the lowest k-nucleon additional energy and the highest k-nucleons removed energy.

In state-of-the-art many-body (i.e. $\mathrm{A} \gg 10$) calculations, this feature is typically exploited from the computation of the one-body Green's function to access the spectroscopy of $(\mathrm{A}\pm 1)$-body systems [22]. In few-body systems, and as discussed in Chap. 2, this feature is typically exploited by computing the vacuum (i.e. $\mathrm{A}=0$) two-time k-body ($k=2,3,4$) Green's function to access eigenenergies of the k-body system relative to the particle vacuum.

1.2.3. Spectral functions

From the Lehmann representation of two-time k-body Green's functions and the identity

$$\frac{1}{\omega \pm i\eta} = \mathcal{P}\frac{1}{\omega} \mp i\pi\delta(\omega) \ , \tag{1.34}$$

the k-particle spectral function is given by

$$S^{(\mathrm{A},k)+}_{\substack{\mu_1\ldots\mu_k\\ \nu_1\ldots\nu_k}}(\omega) \equiv -2\,\mathrm{Im}\, i^{k-1} G^{(\mathrm{A},k)}_{\substack{\mu_1\ldots\mu_k\\ \nu_1\ldots\nu_k}}(\omega) \tag{1.35a}$$

$$= \sum_{m\in\mathscr{H}_{\mathrm{A}+k}} U^{(\mathrm{A},k)m}_{\mu_1\ldots\mu_k}\, U^{(\mathrm{A},k)m*}_{\nu_1\ldots\nu_k}\ (2\pi)\delta(\omega - E^{+k}_m) \ , \tag{1.35b}$$

for $\omega \geq E^{+k}_0$ and by zero otherwise. Similarly, the k-hole spectral function is given by

$$S^{(\mathrm{A},k)-}_{\substack{\mu_1\ldots\mu_k\\ \nu_1\ldots\nu_k}}(\omega) \equiv +2\,\mathrm{Im}\, i^{k-1} G^{(\mathrm{A},k)}_{\substack{\mu_1\ldots\mu_k\\ \nu_1\ldots\nu_k}}(\omega) \tag{1.35c}$$

$$= \sum_{m\in\mathscr{H}_{\mathrm{A}-k}} V^{(\mathrm{A},k)m*}_{\nu_1\ldots\nu_k}\, V^{(\mathrm{A},k)m}_{\mu_1\ldots\mu_k}\ (2\pi)\delta(\omega - E^{-k}_m) \ , \tag{1.35d}$$

for $\omega \leq E^{-k}_0$ and by zero otherwise. The diagonal part of the full k-body spectral function

$$S^{(\mathrm{A},k)}_{\substack{\mu_1\ldots\mu_k\\ \nu_1\ldots\nu_k}}(\omega) \equiv S^{(\mathrm{A},k)+}_{\substack{\mu_1\ldots\mu_k\\ \nu_1\ldots\nu_k}}(\omega) - (-1)^k S^{(\mathrm{A},k)-}_{\substack{\mu_1\ldots\mu_k\\ \nu_1\ldots\nu_k}}(\omega) \tag{1.36}$$

provides the probability density to remove or add k particles with quantum numbers $\mu_1 \ldots \mu_k$ from the A-body ground state while leaving the system at the energy ω. The k-body spectral function verifies the sum rule

$$\int_{-\infty}^{+\infty} \frac{\mathrm{d}\omega}{2\pi}\ S^{(\mathrm{A},k)}_{\substack{\mu_1\ldots\mu_k\\ \nu_1\ldots\nu_k}}(\omega) = 1 \ . \tag{1.37}$$

Eventually, the two-time k-body Green's function can be re-expressed back in terms of the k-particle and k-hole spectral functions according to

$$\begin{aligned} i^k G^{(\mathrm{A},k)}_{\substack{\mu_1\ldots\mu_k\\ \nu_1\ldots\nu_k}}(\omega) &= i\left(\int \frac{\mathrm{d}\omega'}{2\pi} \frac{S^{(\mathrm{A},k)+}_{\substack{\mu_1\ldots\mu_k\\ \nu_1\ldots\nu_k}}(\omega')}{\omega - \omega' + i\eta} - (-1)^k \int \frac{\mathrm{d}\omega'}{2\pi} \frac{S^{(\mathrm{A},k)-}_{\substack{\mu_1\ldots\mu_k\\ \nu_1\ldots\nu_k}}(\omega')}{\omega - \omega' - i\eta}\right) \\ &= i^k G^{(\mathrm{A},k)+}_{\substack{\mu_1\ldots\mu_k\\ \nu_1\ldots\nu_k}}(\omega) + i^k G^{(\mathrm{A},k)-}_{\substack{\mu_1\ldots\mu_k\\ \nu_1\ldots\nu_k}}(\omega) \ , \end{aligned} \tag{1.38}$$

and the retarded and advanced two-time k-body Green's functions in terms of the k-body spectral function according to

$$i^k G^{(\mathrm{A},k)+}_{\substack{\mu_1\ldots\mu_k\\ \nu_1\ldots\nu_k}}(\omega) = +i \int \frac{\mathrm{d}\omega'}{2\pi} \frac{S^{(\mathrm{A},k)}_{\substack{\mu_1\ldots\mu_k\\ \nu_1\ldots\nu_k}}(\omega')}{\omega - \omega' + i\eta} \ , \tag{1.39a}$$

$$i^k G^{(\mathrm{A},k)-}_{\substack{\mu_1\ldots\mu_k\\ \nu_1\ldots\nu_k}}(\omega) = -(-1)^k i \int \frac{\mathrm{d}\omega'}{2\pi} \frac{S^{(\mathrm{A},k)}_{\substack{\mu_1\ldots\mu_k\\ \nu_1\ldots\nu_k}}(\omega')}{\omega - \omega' - i\eta} \ . \tag{1.39b}$$

Interestingly, for a Hamiltonian containing 1- and 2-body operators, as defined in Eq. (1.9), the ground-state energy in the A-body sector can be expressed in terms of the sole one-body Green's function (via its associated one-hole spectral function) by virtue of the Galitskii-Migdal-Koltun (GMK) sum rule [23, 24, 25]

$$E^{\mathrm{A}}_0 = \frac{1}{2}\sum_{\mu\nu} \int_{-\infty}^{+\infty} \frac{\mathrm{d}\omega}{2\pi}\ \left[t_{\mu\nu} + \omega\ \delta_{\mu\nu}\right] S^{(\mathrm{A},1)-}_{\mu\nu}(\omega) \ . \tag{1.40}$$

1.3. Perturbation theory

This section introduces the computation of Green's functions in perturbation theory.

1.3.1. Hamiltonian partitioning

The general strategy of (methods built on) MBPT relies on partitioning the Hamiltonian according to

$$H \equiv H_0 + H_1 \tag{1.41a}$$

such that Eq. (1.10) can be solved exactly for H_0. Corrections due to H_1 are then added in perturbation. The decomposition (1.41a) offers a great flexibility. We presently limit ourself to decompositions of the Hamiltonian where H_0 is a particle-number conserving diagonal one-body operator, i.e.

$$H_0 \equiv h^{11} \ , \tag{1.41b}$$

$$H_1 \equiv \breve{h}^{11} + h^{22} \ , \tag{1.41c}$$

with

$$h^{11} \equiv \sum_{\mu} h^{11}_{\mu\mu} a^\dagger_\mu a_\mu \ , \tag{1.41d}$$

$$\breve{h}^{11} \equiv \sum_{\mu\nu} \breve{h}^{11}_{\mu\nu} a^\dagger_\mu a_\nu \ , \tag{1.41e}$$

$$h^{22} \equiv \frac{1}{(2!)^2} \sum_{\alpha\beta\gamma\delta} h^{22}_{\alpha\beta\gamma\delta} a^\dagger_\alpha a^\dagger_\beta a_\delta a_\gamma \ , \tag{1.41f}$$

such that

$$h^{11}_{\mu\mu} \equiv e_\mu \ , \tag{1.41g}$$

$$\breve{h}^{11}_{\mu\nu} \equiv t_{\mu\nu} - e_\mu \delta_{\mu\nu} \ , \tag{1.41h}$$

$$h^{22}_{\alpha\beta\gamma\delta} \equiv v_{\alpha\beta\gamma\delta} \ . \tag{1.41i}$$

Diagrammatically, $\breve{h}^{11}_{\mu\nu}$ ($h^{22}_{\alpha\beta\gamma\delta}$) is represented by a dot with one (two) incoming and one (two) outgoing leg(s) as depicted in Fig. 1.2. In the following, *unperturbed quantities* refer to quantities computed for the system associated to H_0. General considerations to prefer a certain decomposition over another are usually based on conservation (or breaking) of symmetries, proximity[8] of H_0 to the full H and ease to compute unperturbed observables and their corrections. In the present case, a particular partitioning is characterized by the choice of h^{11}. In this respect, the set of single-particle energies $\{e_\mu\}$ is arbitrary, except that they are increasingly ordered by convention.

1.3.2. Unperturbed system

The unperturbed basis is made out of eigenstates of H_0 and A.

[8]Proximity means here that perturbative corrections are small for observables of interest.

Figure 1.2. Diagrammatic representation of $\breve{h}^{11}_{\mu\nu}$ and $h^{22}_{\alpha\beta\gamma\delta}$.

A-body sector

In the targeted A-body sector, the ground-state of H_0 plays the role of the reference state and is the Slater determinant obtained by occupying the single-particle states associated with the A lowest single-particle energies $e_1, \ldots, e_{\mathrm{A}}$, i.e.

$$\left|\Phi_0^{\mathrm{A}}\right\rangle \equiv \prod_{\mu=1}^{\mathrm{A}} a_\mu^\dagger \left|0\right\rangle \ . \tag{1.42}$$

Unperturbed excited states are generated via particle-hole excitations of the reference state, i.e.

$$\left|\Phi_{ij\ldots}^{ab\ldots}\right\rangle \equiv a_a^\dagger a_b^\dagger \ldots a_j a_i \left|\Phi_0^{\mathrm{A}}\right\rangle \ , \tag{1.43}$$

where the convention is that single-particle indices $i, j, \ldots$ correspond to hole states (i.e. occupied states in $\left|\Phi_0^{\mathrm{A}}\right\rangle$) while single-particle indices $a, b, \ldots$ correspond to particle states (i.e. unoccupied states in $\left|\Phi_0^{\mathrm{A}}\right\rangle$). The corresponding unperturbed A-body eigenenergies are given by

$$\epsilon_0^{\mathrm{A}} \equiv \langle \Phi_0^{\mathrm{A}} | H_0 | \Phi_0^{\mathrm{A}} \rangle = \sum_{i=1}^{A} e_i \ , \tag{1.44a}$$

$$\epsilon_{ij\ldots}^{ab\ldots} \equiv \langle \Phi_{ij\ldots}^{ab\ldots} | H_0 | \Phi_{ij\ldots}^{ab\ldots} \rangle = \epsilon_0^{\mathrm{A}} + (e_a + e_b + \cdots - e_i - e_j - \ldots) \ . \tag{1.44b}$$

(A$\pm k$)-body sector

Similarly, any $\mathscr{H}_{\mathrm{A}\pm k}$ possesses an orthonormal basis of unperturbed eigenstates of H_0 built from p-particle/q-hole excitations of $\left|\Phi_0^{\mathrm{A}}\right\rangle$

$$\left|\Phi_{i_1\cdots i_q}^{a_1\cdots a_p}\right\rangle \equiv a_{a_1}^\dagger \ldots a_{a_p}^\dagger a_{i_q} \ldots a_{i_1} \left|\Phi_0^{\mathrm{A}}\right\rangle \ , \tag{1.45}$$

where $p - q = \pm k$. The unperturbed eigenenergies are given by

$$\epsilon_{i_1\cdots i_q}^{a_1\cdots a_p} \equiv \epsilon_0^{\mathrm{A}} + (e_{a_1} + \ldots + e_{a_p}) - (e_{i_1} + \ldots + e_{i_q}) \ . \tag{1.46}$$

Interaction picture

The time evolution operator in the interaction picture is defined as

$$U_I(t,t') \equiv e^{iH_0t}U(t,t')e^{-iH_0t} = e^{iH_0t}e^{-iH(t-t')}e^{-iH_0t} \ , \tag{1.47}$$

which again depends only on $t-t'$ for time-independent H_0 and H.

More generally, an operator O is defined in the interaction picture through

$$O(t) \equiv e^{iH_0t}O\ e^{-iH_0t} \ . \tag{1.48}$$

In particular the time-dependence of creation and annihilation operators in the interaction picture is explicitly given by

$$a_\mu(t) = e^{-ie_\mu t}a_\mu \ , \tag{1.49a}$$

$$a^\dagger_\mu(t) = e^{ie_\mu t}a^\dagger_\mu \ . \tag{1.49b}$$

Unperturbed Green's functions

The unperturbed k-body Green's function associated with the unperturbed A-body ground-state reads as

$$i^k G^{(\mathrm{A},k)0}_{\substack{\mu_1\dots\mu_k\\ \nu_1\dots\nu_k}}(t_{\mu_1},\dots,t_{\mu_k},t_{\nu_1},\dots,t_{\nu_k}) \equiv \frac{\langle\Phi_0^\mathrm{A}|\mathrm{T}\left[a_{\mu_k}(t_{\mu_k})\dots a_{\mu_1}(t_{\mu_1})a^\dagger_{\nu_1}(t_{\nu_1})\dots a^\dagger_{\nu_k}(t_{\nu_k})\right]|\Phi_0^\mathrm{A}\rangle}{\langle\Phi_0^\mathrm{A}|\Phi_0^\mathrm{A}\rangle} \ , \tag{1.50}$$

where $a_\mu(t_\mu)$ and $a^\dagger_\nu(t_\nu)$ denote now annihilation and creation operators in the interaction picture (see Eq. (1.49)), respectively. Correspondingly, the unperturbed k-body density matrix reads as

$$\begin{aligned}\rho^{(\mathrm{A},k)0}_{\substack{\mu_1\dots\mu_k\\ \nu_1\dots\nu_k}} &\equiv \frac{\langle\Phi_0^\mathrm{A}|a^\dagger_{\nu_1}\dots a^\dagger_{\nu_k}a_{\mu_k}\dots a_{\mu_1}|\Phi_0^\mathrm{A}\rangle}{\langle\Phi_0^\mathrm{A}|\Phi_0^\mathrm{A}\rangle}\\ &= (-1)^k i^k G^{(\mathrm{A},k)0}_{\substack{\mu_1\dots\mu_k\\ \nu_1\dots\nu_k}}(t,\dots,t,t^+,\dots,t^+) \ ,\end{aligned} \tag{1.51}$$

and is non-zero only if the sets $(\mu_1,\dots,\mu_k)$ and $(\nu_1,\dots,\nu_k)$ are identical and correspond to k hole states.

Focusing on the unperturbed one-body Green's function, one has

$$iG^{(\mathrm{A},1)0}_{\mu\nu}(t_\mu,t_\nu) \equiv \frac{\langle\Phi_0^\mathrm{A}|\mathrm{T}\left[a_\mu(t_\mu)a^\dagger_\nu(t_\nu)\right]|\Phi_0^\mathrm{A}\rangle}{\langle\Phi_0^\mathrm{A}|\Phi_0^\mathrm{A}\rangle} \tag{1.52a}$$

$$= \theta\left(t_\mu-t_\nu\right)\sum_a \delta_{\mu a}\delta_{\nu a}e^{-ie_a(t_\mu-t_\nu)} - \theta\left(t_\nu-t_\mu\right)\sum_i \delta_{\mu i}\delta_{\nu i}e^{ie_i(t_\nu-t_\mu)} \tag{1.52b}$$

$$\equiv iG^{(\mathrm{A},1)0+}_{\mu\nu}(t_\mu,t_\nu) + iG^{(\mathrm{A},1)0-}_{\mu\nu}(t_\mu,t_\nu) \tag{1.52c}$$

where $G^{(\mathrm{A},1)0+}_{\mu\nu}$ and $G^{(\mathrm{A},1)0-}_{\mu\nu}$ denote the unperturbed retarded and advanced propagators respectively[9]. The diagrammatic representation of $G^{(\mathrm{A},1)0}_{\mu\nu}(t_\mu,t_\nu)$ is given in Fig. 1.3. Fourier

[9] They are also referred to as particle and hole propagators, respectively.

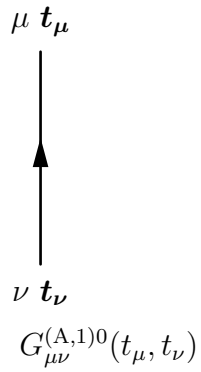

Figure 1.3. Diagrammatic representation of $G^{(\mathrm{A},1)0}_{\mu\nu}(t_\mu, t_\nu)$.

transforming (1.52b), one eventually obtains the Lehmann representation of the unperturbed one-body propagator i.e.

$$iG^{(\mathrm{A},1)0}_{\mu\nu}(\omega) = i\left(\sum_a \frac{\delta_{\mu a}}{\omega - e_a + i\eta} + \sum_i \frac{\delta_{\mu i}}{\omega - e_i - i\eta}\right)\delta_{\mu\nu} \ . \tag{1.53}$$

Similarly to Eq. (1.32), $G^{(\mathrm{A},1)0}_{\mu\nu}(\omega)$ possesses a pole structure associated to unperturbed one-nucleon addition and removal energies, which actually reduce to one-particle and one-hole energies, respectively. Again, in the case of a non-degenerate unperturbed reference state the corresponding spectrum displays a gap between the highest hole-state energy and the lowest particle-state energy.

1.3.3. Perturbative expansion

When $H_1 = 0$, the unperturbed basis discussed in section 1.3.2 constitutes the eigenstates of interest. This is no longer the case when $H_1 \neq 0$. In this case the correlated ground-state $\left|\Psi^{\mathrm{A}}_0\right\rangle$ is a linear combination of the $\left|\Phi^{\mathrm{A}}_m\right\rangle$ obtained via the time evolution of $\left|\Phi^{\mathrm{A}}_0\right\rangle$. The adiabatic transition between unperturbed basis states and eigenstates of H is obtained on the basis of Gell-Mann and Low theorem [26] which, assuming adiabacity, reads

$$\forall m, \left|\Psi^{\mathrm{A}}_m\right\rangle = U_I(0, -\infty)\left|\Phi^{\mathrm{A}}_m\right\rangle \ . \tag{1.54}$$

Exploiting this adiabatic connection, a few steps of calculations allow one to rewrite the exact k-body Green's function under the form

$$\begin{aligned} i^k G^{(\mathrm{A},k)}{}_{\substack{\mu_1\ldots\mu_k \\ \nu_1\ldots\nu_k}}(t_{\mu_1}\ldots t_{\mu_k}, t_{\nu_1}\ldots t_{\nu_k}) \\ = \frac{\langle\Phi^{\mathrm{A}}_0|\mathrm{T}\left[U_I(+\infty,-\infty)a_{\mu_k}(t_{\mu_k})\ldots a_{\mu_1}(t_{\mu_1})a^\dagger_{\nu_1}(t_{\nu_1})\ldots a^\dagger_{\nu_k}(t_{\nu_k})\right]|\Phi^{\mathrm{A}}_0\rangle}{\langle\Phi^{\mathrm{A}}_0|U_I(+\infty,-\infty)|\Phi^{\mathrm{A}}_0\rangle} \ . \end{aligned} \tag{1.55}$$

Formally, (1.47) can be written as [27]

$$U_I(t, t') = \mathrm{T}e^{-i\int_{t'}^{t}\mathrm{d}t_1 H_1(t_1)} \ , \tag{1.56}$$

and the perturbative expansion obtained by writing the Taylor series associated to Eq. (1.56)

$$U_I(t,t') = \sum_{n=0}^{+\infty} \frac{(-i)^n}{n!} \int_{t'}^{t} \mathrm{d}t_1 \ldots \int_{t'}^{t} \mathrm{d}t_n \mathrm{T}\left[H_1(t_1)\ldots H_1(t_n)\right] \ . \tag{1.57}$$

Inserting Eq. (1.57) in both the numerator and the denominator of Eq. (1.55) one obtains

$$\begin{aligned} & i^k G^{(\mathrm{A},k)}{}_{\substack{\mu_1\ldots\mu_k \\ \nu_1\ldots\nu_k}}(t_{\mu_1}\ldots t_{\mu_k}, t_{\nu_1}\ldots t_{\nu_k}) \\ & \quad = \sum_{n=0}^{+\infty} \frac{(-i)^n}{n!} \int_{-\infty}^{+\infty} \mathrm{d}t_1 \ldots \int_{-\infty}^{+\infty} \mathrm{d}t_n \\ & \qquad \langle \Phi_0^{\mathrm{A}} | \mathrm{T}\left[H_1(t_1)\ldots H_1(t_n) a_{\mu_k}(t_{\mu_k})\ldots a_{\mu_1}(t_{\mu_1}) a^\dagger_{\nu_1}(t_{\nu_1})\ldots a^\dagger_{\nu_k}(t_{\nu_k})\right] | \Phi_0^{\mathrm{A}} \rangle \\ & \quad / \sum_{n=0}^{+\infty} \frac{(-i)^n}{n!} \int_{-\infty}^{+\infty} \mathrm{d}t_1 \ldots \int_{-\infty}^{+\infty} \mathrm{d}t_n \langle \Phi_0^{\mathrm{A}} | \mathrm{T}\left[H_1(t_1)\ldots H_1(t_n)\right] | \Phi_0^{\mathrm{A}} \rangle \ . \end{aligned} \tag{1.58}$$

Using time-dependent Wick's theorem [27] with respect to $\left|\Phi_0^{\mathrm{A}}\right\rangle$, appropriate groups of terms can be associated to a Feynman diagram with k incoming and k outgoing external lines, where the lines in the diagram denote unperturbed one-body Green's functions, or propagators, $G^{(\mathrm{A},1)0}$. For detailed Feynman rules, see App. A. Further achieving the cancellation of unlinked terms, i.e. disconnected parts without external lines, between the numerator and the denominator, one obtains the master formula

$$\begin{aligned} & i^k G^{(\mathrm{A},k)}{}_{\substack{\mu_1\ldots\mu_k \\ \nu_1\ldots\nu_k}}(t_{\mu_1}\ldots t_{\mu_k}, t_{\nu_1}\ldots t_{\nu_k}) \\ & \quad = \sum_{n=0}^{+\infty} \frac{(-i)^n}{n!} \int_{-\infty}^{+\infty} \mathrm{d}t_1 \ldots \int_{-\infty}^{+\infty} \mathrm{d}t_n \\ & \qquad \langle \Phi_0^{\mathrm{A}} | \mathrm{T}\left[H_1(t_1)\ldots H_1(t_n) a_{\mu_k}(t_{\mu_k})\ldots a_{\mu_1}(t_{\mu_1}) a^\dagger_{\nu_1}(t_{\nu_1})\ldots a^\dagger_{\nu_k}(t_{\nu_k})\right] | \Phi_0^{\mathrm{A}} \rangle_L \ , \end{aligned} \tag{1.59}$$

where the subscript L is referring to the restriction to linked diagrams only. Examples of low-order linked diagrams contributing to the 1-body (2-body) Green's function are displayed in Fig. 1.4 (Fig. 1.5).

Expanding the k-body Green's function in perturbation thus allows one to express it in terms of $G^{(\mathrm{A},1)0}_{\mu\nu}(t_\mu, t_\nu)$ under the form of a series

$$i^k G^{(\mathrm{A},k)}_{\substack{\mu_1\ldots\mu_k \\ \nu_1\ldots\nu_k}}(t_{\mu_1}\ldots t_{\mu_k}, t_{\nu_1}\ldots t_{\nu_k}) = \sum_{n=0}^{+\infty} \sum_{\mathcal{G}_n^{(\mathrm{A},k)}} \mathcal{A}^{\mathcal{G}_n^{(\mathrm{A},k)}}_{\substack{\mu_1\ldots\mu_k \\ \nu_1\ldots\nu_k}}(t_{\mu_1}\ldots t_{\mu_k}, t_{\nu_1}\ldots t_{\nu_k}) \tag{1.60}$$

where n denotes the number of interaction vertices contained in the linked diagram $\mathcal{G}_n^{(\mathrm{A},k)}$ and $\mathcal{A}^{\mathcal{G}_n^{(\mathrm{A},k)}}_{\substack{\mu_1\ldots\mu_k \\ \nu_1\ldots\nu_k}}(t_{\mu_1}\ldots t_{\mu_k}, t_{\nu_1}\ldots t_{\nu_k})$ its associated amplitude. The infinite series is meant to be truncated at a given order p, i.e. all terms with $n \leq p$ are included. A typical n^{th}-order

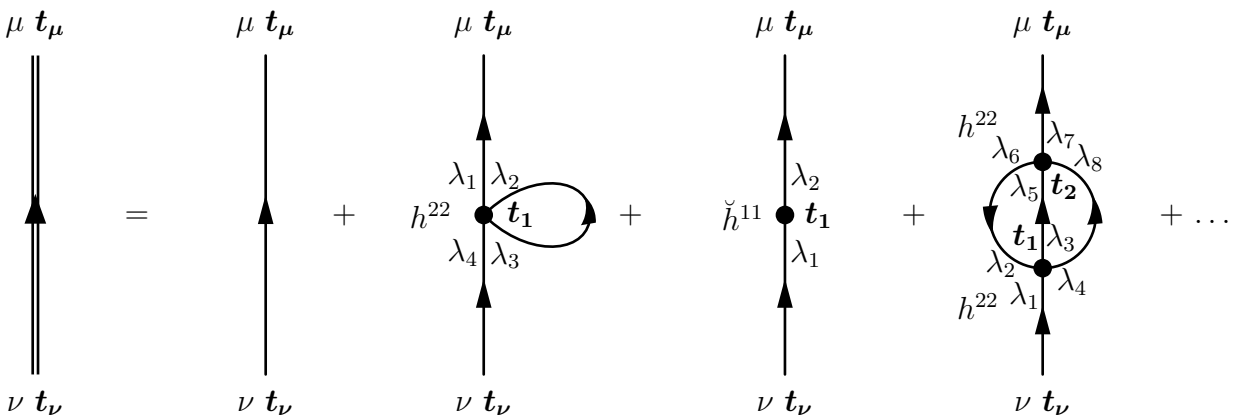

Figure 1.4. Example of labeled Feynman diagrams contributing to $G^{(\mathrm{A},1)}_{\mu\nu}(t_\mu, t_\nu)$ at zero, first and second order.

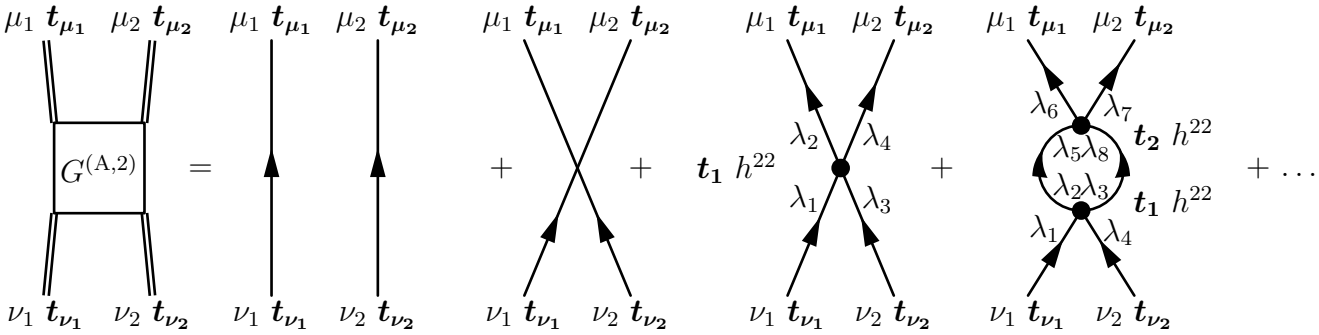

Figure 1.5. Example of labeled Feynman diagrams contributing to $G^{(\mathrm{A},2)}_{\substack{\mu_1\mu_2\\ \nu_1\nu_2}}(t_{\mu_1}t_{\mu_2}, t_{\nu_1}t_{\nu_2})$ at zero, first and second order.

amplitude takes the form

$$\begin{aligned}
&\mathcal{A}^{\mathcal{G}_n^{(\mathrm{A},k)}}_{\substack{\mu_1\dots\mu_k\\ \nu_1\dots\nu_k}}(t_{\mu_1}\dots t_{\mu_k}, t_{\nu_1}\dots t_{\nu_k}) = \\
&\quad (-1)^\sigma \frac{(-i)^n}{n!}\sum_\lambda \frac{h^{p_1q_1}_{\lambda\dots\lambda}}{p_1!q_1!}\dots\frac{h^{p_nq_n}_{\lambda\dots\lambda}}{p_n!q_n!}\int \mathrm{d}t_1\dots\mathrm{d}t_n \\
&\qquad\qquad \prod_{e\in I} iG^{(\mathrm{A},1)0}_{\lambda\lambda}(t_i,t_j)\prod_{e\in E_{in}} iG^{(\mathrm{A},1)0}_{\lambda\nu}(t_i,t_\nu)\prod_{e\in E_{out}} iG^{(\mathrm{A},1)0}_{\mu\lambda}(t_\mu,t_j)
\end{aligned} \tag{1.61}$$

where, for a diagram $\mathcal{G}_n^{(\mathrm{A},k)}$, σ is an integer, λ, μ and ν denote generic single-particle labels for internal, external outgoing and external incoming lines, respectively. Labels p_i and q_i characterize the number of creation and annihilation operators associated with the vertex i whereas t_i denotes the corresponding time label. Eventually, I is the set of internal lines, E_{in} the set of k incoming lines and E_{out} the set of k outgoing lines. Single-particle indices λ, μ and ν have been stripped of their label in the matrix elements and one-body Green's functions for the sake of concision.

In the energy representation the equivalent expression is obtained by Fourier transformation

of Eq. (1.61) as in (1.22)

$$\begin{aligned}
&\mathcal{A}^{\mathcal{G}_n^{(\mathrm{A},k)}}_{\substack{\mu_1\dots\mu_k\\ \nu_1\dots\nu_k}}(\omega_{\mu_1}\dots\omega_{\mu_k},\omega_{\nu_1}\dots\omega_{\nu_k}) = \\
&(-1)^{\sigma}\frac{(-i)^n}{n!}\sum_{\lambda}\frac{h^{p_1q_1}_{\lambda\dots\lambda}}{p_1!q_1!}\dots\frac{h^{p_nq_n}_{\lambda\dots\lambda}}{p_n!q_n!}\int\frac{\mathrm{d}\omega_\lambda}{2\pi}\dots\prod_{i=1}^{n}2\pi\delta\left(\pm\omega_\lambda\cdots-\omega_\mu\cdots+\omega_\nu\dots\right) \\
&\qquad\qquad\times\prod_{e\in I}iG^{(\mathrm{A},1)0}_{\lambda\lambda}(\omega_\lambda)\prod_{e\in E_{in}}iG^{(\mathrm{A},1)0}_{\lambda\nu}(\omega_\nu)\prod_{e\in E_{out}}iG^{(\mathrm{A},1)0}_{\mu\lambda}(\omega_\mu)
\end{aligned} \tag{1.62}$$

where the additional factor of Dirac functions ensures energy conservation at every vertex of $\mathcal{G}_n^{(\mathrm{A},k)}$.[10] This generic form of the nth-order amplitude contributing to the k-body Green's function expanded in perturbation with respect to the reference state $\left|\Phi_0^{\mathrm{A}}\right\rangle$ will play an important role later on in the document.

[10]Dirac factors originate from time-integrals of the form

$$\int \mathrm{d}t_i e^{it_i(\pm\omega_\lambda\cdots-\omega_\mu\cdots+\omega_\nu\dots)} = 2\pi\delta(\pm\omega_\lambda\cdots-\omega_\mu\cdots+\omega_\nu\dots)\ ,$$

where each exponential contribution comes from replacing time-dependent by energy-dependent Green's functions.

Chapter 2.

Pionless Effective Field Theory

While nuclear many-body observables are usually computed for a generic Hamiltonian, regardless of the renormalization procedure of the potential, this thesis aims at testing the renormalization invariance of observables computed within the frame of $\not{\pi}$EFT in A-body sectors with A $\gg$ 10. This must however be done while taking into account the fact that the PC rule stipulating that $H_{\not{\pi}}^{\mathrm{LO}}$ must be solved to all orders is intractable beyond few-body sectors. Our main goal is thus to investigate the impact of such an inherent feature on the renormalization invariance of many-body observables.

To be in position to address the above question in Chap. 3 and Chap. 4, the present chapter is dedicated to introducing the pionless Hamiltonian $H_{\not{\pi}}$ and its necessary renormalization. Following the PC rule, the LO pionless potential at play in neutron matter (i.e. a contact 2-body operator only) is then renormalized to all orders in Sec. 2.2 on the basis of the S-wave scattering length. Anticipating the discussion of Chap. 3 and Chap. 4, this procedure is also provided at tree and one-loop levels. These LO pionless potential(s) will be used as an input to SCGF and MBPT calculations in the following chapters.

2.1. Ultraviolet divergences and renormalization

In this section, the Hamiltonian $H_{\not{\pi}}$ stemming from $\not{\pi}$EFT is defined. Emphasis is then put on ultraviolet (UV) divergences emerging from perturbative calculations and on the renormalization procedure employed to deal with them. Eventually, power-counting rules and their implications for nuclear systems are discussed.

2.1.1. Pionless Hamiltonian

To define an EFT, degrees of freedom of interest need to be first specified. For (very) low-energy nuclear systems the sole explicit degrees of freedom at play are structure-less nucleons of momentum and energy $Q \ll 1$ GeV. Experimentally, nucleons are described with a spin $s = \frac{1}{2}$ and isospin $t = \frac{1}{2}$. Consequently, only one set of fermionic creation and annihilation operators $(a_\mu^\dagger, a_\mu)$ verifying Eq. (1.4) is needed. Here we recall that the μ index refers to one-body states of a nucleon, e.g. , in a position basis

$$\{\mu\} \longleftrightarrow \left\{\vec{r}, s = \frac{1}{2}, s_z, t = \frac{1}{2}, t_3\right\} \ , \tag{2.1}$$

where $\vec{r}$ is the spatial position of the nucleon, s_z the projection of its spin along the z axis and t_3 the projection of the isospin such that $t_3 = +\frac{1}{2}$ for a neutron and $t_3 = -\frac{1}{2}$ for a

proton. As a short-hand notation, creation and annihilation operators are denoted as $a^\dagger_{\vec{r}\sigma}$ and $a_{\vec{r}\sigma}$, respectively, where the couple of discrete indices $(s_z t_3)$ is denoted as σ[1]. These creation/annihilation operators are related to their momentum counterparts via a Fourier transformation

$$a_{\vec{p}\sigma} \equiv \int \frac{\mathrm{d}^3\vec{p}}{(2\pi)^3} \; e^{-i\vec{p}.\vec{r}} \; a_{\vec{r}\sigma} \; , \tag{2.2a}$$

$$a^\dagger_{\vec{p}\sigma} \equiv \int \frac{\mathrm{d}^3\vec{p}}{(2\pi)^3} \; e^{i\vec{p}.\vec{r}} \; a^\dagger_{\vec{r}\sigma} \; , \tag{2.2b}$$

with $\vec{p}$ the nucleon linear momentum.

The general principle of EFT is to *write down the most general Hamiltonian consistent with the symmetries of the problem* [6]. At energies $Q \ll 1$ GeV, nucleons can be considered to be non-relativistic so that the Hamiltonian is required to possess Galilean symmetry. A further simplification is to limit the study to spin and isospin-independent Hamiltonians, thus, adding symmetry restrictions.[2] This will simplify further calculations without changing the conclusions about renormalization of many-body calculations.

With these degrees of freedom and symmetries, the most general Hamiltonian reads[3]

$$\begin{aligned} H_{\not{\pi}} = \int \mathrm{d}^3\vec{r} \quad & \Bigg\{ N^\dagger_{\vec{r}} \left(-\frac{\overrightarrow{\nabla}^2}{2m} \right) N_{\vec{r}} + \frac{C_0}{2} (N^\dagger_{\vec{r}} N_{\vec{r}})^2 \\ & - \frac{1}{16} C_2 \left[(N_{\vec{r}} N_{\vec{r}})^\dagger \left(N_{\vec{r}} \overleftrightarrow{\nabla}^2 N_{\vec{r}} \right) + \text{h.c.} \right] \\ & - \frac{1}{8} C_2' (N_{\vec{r}} \overleftrightarrow{\nabla} N_{\vec{r}})^\dagger \cdot (N_{\vec{r}} \overleftrightarrow{\nabla} N_{\vec{r}}) + \frac{1}{6} D_0 (N^\dagger_{\vec{r}} N_{\vec{r}})^3 + \dots \Bigg\} \; , \end{aligned} \tag{2.3}$$

where m is the nucleon mass, C_0 and C_2 are S-wave contact coupling constants, C_2' is a P-wave contact coupling constant and D_0 is a three-body contact coupling constant. The four-component nucleon spinor $N_{\vec{r}}$ is defined as

$$N_{\vec{r}} \equiv \begin{pmatrix} a_{\vec{r}\,+\frac{1}{2}\,+\frac{1}{2}} \\ a_{\vec{r}\,-\frac{1}{2}\,+\frac{1}{2}} \\ a_{\vec{r}\,+\frac{1}{2}\,-\frac{1}{2}} \\ a_{\vec{r}\,-\frac{1}{2}\,-\frac{1}{2}} \end{pmatrix} \; , \tag{2.4a}$$

$$N^\dagger_{\vec{r}} \equiv \begin{pmatrix} a^\dagger_{\vec{r}\,+\frac{1}{2}\,+\frac{1}{2}} & a^\dagger_{\vec{r}\,-\frac{1}{2}\,+\frac{1}{2}} & a^\dagger_{\vec{r}\,+\frac{1}{2}\,-\frac{1}{2}} & a^\dagger_{\vec{r}\,-\frac{1}{2}\,-\frac{1}{2}} \end{pmatrix} \; . \tag{2.4b}$$

Here h.c. denotes the Hermitian conjugate and the spatial derivative operator $\overleftrightarrow{\nabla}$ is defined by

$$A \overleftrightarrow{\nabla} B \equiv A(\nabla B) - (\nabla A)\, B \; . \tag{2.5}$$

[1] Kronecker delta on σ are thus defined as $\delta_{\sigma'\sigma} \equiv \delta_{s'_z s_z} \delta_{t'_3 t_3}$.

[2] In particular, Coulomb interaction is ruled out as it breaks the isospin symmetry. Spin-isospin projectors are also trivialized to identity operators.

[3] There is no mixing between particles and their associated anti-particles as a consequence of the non-relativistic approximation. This decoupling and the general form of the Hamiltonian can be recovered by taking the non-relativistic limit of a relativistic quantum field theory. This is done either by a Foldy-Wouthuysen transformation [28] or within the heavy-baryon formalism [29, 30] using reparameterization invariance [31].

The ellipsis indicates higher derivatives, partial waves and many-body operators contributing to the Hamiltonian. As a short-hand, in the following, space/momentum integrals are denoted with a sum symbol[4] i.e.

$$\sum_{\vec{r}} \longleftrightarrow \int \mathrm{d}^3\vec{r}\,, \tag{2.6a}$$

$$\sum_{\vec{p}} \longleftrightarrow \int \frac{\mathrm{d}^3\vec{p}}{(2\pi)^3}\,. \tag{2.6b}$$

In the momentum basis, $H_{\not\pi}$ reads as[5]

$$\begin{aligned} H_{\not\pi} = &\sum_{\sigma}\sum_{\vec{p}} h^{11}_{\vec{p}\vec{p}}\, a^\dagger_{\vec{p}\sigma} a_{\vec{p}\sigma} \\ &+ \frac{1}{2!}\sum_{\sigma_1\sigma_2}\sum_{\substack{\vec{p}_1'\vec{p}_2' \\ \vec{p}_1\vec{p}_2}} h^{22}_{\vec{p}_1'\vec{p}_2'\vec{p}_1\vec{p}_2}\; a^\dagger_{\vec{p}_1'\sigma_1} a^\dagger_{\vec{p}_2'\sigma_2} a_{\vec{p}_2\sigma_2} a_{\vec{p}_1\sigma_1} \\ &+ \frac{1}{3!}\sum_{\sigma_1\sigma_2\sigma_3}\sum_{\substack{\vec{p}_1'\vec{p}_2'\vec{p}_3' \\ \vec{p}_1\vec{p}_2\vec{p}_3}} h^{33}_{\vec{p}_1'\vec{p}_2'\vec{p}_3'\vec{p}_1\vec{p}_2\vec{p}_3}\; a^\dagger_{\vec{p}_1'\sigma_1} a^\dagger_{\vec{p}_2'\sigma_2} a^\dagger_{\vec{p}_3'\sigma_3} a_{\vec{p}_3\sigma_3} a_{\vec{p}_2\sigma_2} a_{\vec{p}_1\sigma_1} \\ &+ \dots\,. \end{aligned} \tag{2.7}$$

Introducing $\vec{q}$ and $\vec{q}\,'$ ($\vec{P}$ and $\vec{P}\,'$) as the relative (total) momentum of two incoming and outgoing nucleons, respectively,

$$\vec{q} \equiv \frac{\vec{p}_1 - \vec{p}_2}{2}\,, \tag{2.8a}$$

$$\vec{q}\,' \equiv \frac{\vec{p}_1' - \vec{p}_2'}{2}\,, \tag{2.8b}$$

$$\vec{P} \equiv \frac{\vec{p}_1 + \vec{p}_2}{2}\,, \tag{2.8c}$$

$$\vec{P}\,' \equiv \frac{\vec{p}_1' + \vec{p}_2'}{2}\,, \tag{2.8d}$$

the spatial part of the direct-product matrix elements of the 1-, 2- and 3-body components of the Hamiltonian read as

$$h^{11}_{\vec{p}'\vec{p}} = (2\pi)^3\,\delta\left(\vec{p}' - \vec{p}\right)\frac{p^2}{2m}\,, \tag{2.9a}$$

$$h^{22}_{\vec{p}_1'\vec{p}_2'\vec{p}_1\vec{p}_2} = (2\pi)^3\,\delta\left(\vec{p}_1' + \vec{p}_2' - \vec{p}_1 - \vec{p}_2\right)\left(C_0 + C_2\left(\frac{q'^2 + q^2}{2}\right) + C_2'\vec{q}\,'\cdot\vec{q} + \dots\right)\,, \tag{2.9b}$$

$$h^{33}_{\vec{p}_1'\vec{p}_2'\vec{p}_3'\vec{p}_1\vec{p}_2\vec{p}_3} = (2\pi)^3\,\delta\left(\vec{p}_1' + \vec{p}_2' + \vec{p}_3' - \vec{p}_1 - \vec{p}_2 - \vec{p}_3\right)\left(D_0 + \dots\right)\,, \tag{2.9c}$$

where $\dots$ denotes contributions associated with higher powers of momenta. Two-body vertices with 0 and 2 powers of momenta, and the three-body vertex with zero power of momentum, are represented diagrammatically in Fig. 2.1.

[4] The sum symbol should not be understood as a discretization of the corresponding integral.

[5] Direct-product matrix elements (i.e. before antisymmetrization) are presently employed, hence the different pre-factors from Eq. (1.5).

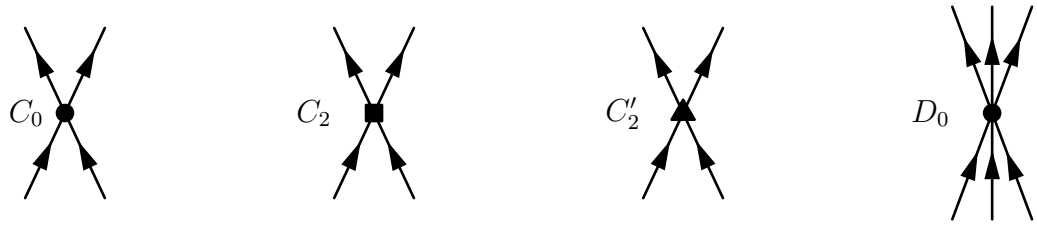

Figure 2.1. Diagrammatic representation of several vertices in $\not\pi$EFT.

A Hamiltonian of the type (2.7) is, however, insufficient to yield a well-defined theory. When computing contributions in perturbation theory, integrals of the type (1.61) turn out to be generally divergent. One could modify the Hamiltonian matrix elements for large momenta such that any order of MBPT yields a finite result [32, 33, 34]. Such a modification of the Hamiltonian is however arbitrary, leading to nuclear models that strongly rely on UV physics, which departs from the EFT approach[6]. On the contrary, Secs. 2.1.2-2.1.3 discuss *renormalization schemes* designed to deal with these divergences in a UV independent way.

2.1.2. Perturbation theory

While solving the A-body Schrödinger equation can be done formally in any particular perturbation theory[7], the renormalization of the Hamiltonian is traditionally studied in few-body systems. To this extent, a specific perturbation theory setting - introduced below - is typically employed. The UV analysis is then performed on the Feynman amplitudes associated to this perturbation theory.

Unperturbed system

Let us now specify the perturbation theory setting typically employed in few-body systems in view of the general MBPT introduction provided in Chap. 1. The pionless $H_{\not\pi}$ is trivially partitioned according to

$$H_{\not\pi} = H_0 + H_1 \ , \tag{2.10a}$$

$$H_0 = T_{\not\pi} \equiv \sum_{\vec{p}\sigma} h^{11}_{\vec{p}\vec{p}} a^\dagger_{\vec{p}\sigma} a_{\vec{p}\sigma} \ , \tag{2.10b}$$

$$H_1 = V_{\not\pi} \equiv \frac{1}{2!} \sum_{\sigma_1\sigma_2} \sum_{\substack{\vec{p}_1'\vec{p}_2' \\ \vec{p}_1\vec{p}_2}} h^{22}_{\vec{p}_1'\vec{p}_2'\vec{p}_1\vec{p}_2} \ a^\dagger_{\vec{p}_1'\sigma_1} a^\dagger_{\vec{p}_2'\sigma_2} a_{\vec{p}_2\sigma_2} a_{\vec{p}_1\sigma_1} + \dots \ , \tag{2.10c}$$

[6]In the spirit of [32, 33, 34], one could try to consider a class of UV physics models and attempt to quantify errors as the dependence on the assumed UV physics. However, the errors thus quantified depend on the arbitrary class of UV physics models which should at least be justified by physical considerations such as compatibility with higher-energy physics. Even then, only a lower-bound on the error would be reached by such considerations.

[7]Let us recall that a perturbation theory is defined for a certain partitioning of the Hamiltonian. Different partitionings lead to different perturbation expansions.

such that the unperturbed one-body part is simply given by the kinetic energy that is conveniently diagonal in the momentum basis. Correspondingly, single-particle energies associated to this partitioning are single-particle kinetic energies

$$e_{\vec{p}\sigma} \equiv h^{11}_{\vec{p}\vec{p}} = \frac{p^2}{2m} \ , \tag{2.11}$$

and are thus spin and isospin independent.

The study of a k-body system relies on computing the two-time reduction of the k-body Green's function associated to the particle vacuum $|0\rangle$ in order to look for its poles. Correspondingly, this implies that the perturbation theory is further set by using the particle vacuum as the reference state. In agreement with Sec. 1.3.2, the unperturbed basis of $\mathscr{H}_k$ is given by the set of k-particle/0-hole excitations of the particle vacuum $|0\rangle$ that presently acts as the unperturbed ground-state of H_0 in $\mathscr{H}_0$

$$\left|\Phi^{\vec{p}_1\sigma_1\ldots\vec{p}_k\sigma_k}\right\rangle = a^\dagger_{\vec{p}_1\sigma_1}\ldots a^\dagger_{\vec{p}_k\sigma_k}\,|0\rangle \ . \tag{2.12a}$$

In this particular case where A = 0, unperturbed states in the Hilbert spaces of interest thus consist only of k particle excitations. Given that the unperturbed energy of the particle vacuum is $\epsilon^0_0 = 0$, the unperturbed eigenenergies of the Slater determinants introduced above are nothing but

$$\epsilon^{\vec{p}_1\sigma_1\ldots\vec{p}_k\sigma_k} = \sum_{i=1}^{k}\frac{p_i^2}{2m} \ . \tag{2.12b}$$

From Eq. (2.11) and Eq. (1.53), the unperturbed one-body Green's function in the energy representation reads as

$$iG^{(0,1)0}_{\vec{p}\sigma\vec{p}'\sigma'}(\omega) = \frac{i}{\omega - \frac{p^2}{2m} + i\eta}\,(2\pi)^3\delta(\vec{p}-\vec{p}')\delta_{\sigma\sigma'} \ , \tag{2.13}$$

and thus only contains poles associated to one-particle additional energies. Indeed, there is no one-particle removal energies given that no single-particle state is occupied in the reference state $|0\rangle$.

Similarly, the two-time reduction of the k-body Green's function in its Lehmann representation contains only poles associated to k-particles additional states namely

$$i^k G^{(0,k)}_{\substack{\mu_1\ldots\mu_k\\ \nu_1\ldots\nu_k}}(\omega) = i\sum_{m\in\mathscr{H}_k}\frac{U^{(0,k)m}_{\mu_1\ldots\mu_k}\,U^{(0,k)m*}_{\nu_1\ldots\nu_k}}{\omega - (E^k_m - E^0_0) + i\eta} \ , \tag{2.14}$$

where, as a shorthand, $\mu_i \equiv \vec{p}_i\sigma_i$ and $\nu_i \equiv \vec{p}'_i\sigma'_i$. In terms of spectral amplitudes defined in (1.31), this corresponds to the fact that

$$V^{(0,k)m}_{\nu_1\ldots\nu_k} = 0 \ . \tag{2.15}$$

Given that $E^0_0 \equiv \langle 0|H_{\not{\pi}}|0\rangle = 0$, the poles of $G^{(0,k)}_{\substack{\mu_1\ldots\mu_k\\ \nu_1\ldots\nu_k}}(\omega)$ directly form the spectrum of $H_{\not{\pi}}$ in the k-body sector.

Ultraviolet divergences

In the perturbation theory defined above, general integrals of the form (1.62) associated to diagrams $\mathcal{G}_n^{(0,k)}$ are characterized by their *superficial degree of divergence*[8]

$$D(\mathcal{G}_n^{(0,k)}) \equiv 5L - 2I + \sum_i 2i\ V_{2i} \tag{2.16}$$

where L is the number of loops in $\mathcal{G}_n^{(0,k)}$, I its number of internal lines and V_{2i} the number of vertices containing $2i$ spatial[9] derivatives.[10] In order to analyse the UV divergences, the *power-counting theorem*, rigorously proven by Weinberg [35], Hepp [36] and Zimmerman [37] follows.

$\mathcal{A}^{\mathcal{G}_n^{(0,k)}}_{\substack{\mu_1\ldots\mu_k\\ \nu_1\ldots\nu_k}}$ *is finite if and only if* $D(\mathcal{G}_n^{(0,k)}) < 0$ *and* $D(\gamma) < 0$ *for any subgraph* γ *composed of internal lines of* $\mathcal{G}_n^{(0,k)}$.

In their papers the complete proof was actually done for relativistic free propagators but can be easily adapted for the non-relativistic propagator $G^{(0,1)0}_{\vec{p}\sigma\vec{p}'\sigma'}$ as defined in Eq. (2.13). The negativity of $D(\mathcal{G}_n^{(0,k)})$ does not *a priori* hold for any graph $\mathcal{G}_n^{(0,k)}$. Examples of UV divergent graphs are given in Tab. 2.1. Dealing with UV divergent graphs is done via a *renormalization scheme*.

2.1.3. Renormalization schemes

A renormalization scheme consists in introducing, as a first step, a regularization that makes all integrals (1.62) finite. For analytical calculations, the dimensional regularization [38] is most often used. It indeed makes calculations easier and avoids breaking symmetries of the Hamiltonian. However, such a regularization is only well-defined for finite orders in perturbative theory and can fail when used without care in a non-perturbative setting [11]. In this thesis, all computations use a cut-off regularization instead. The one reason is the non-perturbativeness of nuclear systems, which, eventually, requires the use of (infinite) resummations of perturbative contributions. Using a cut-off regularization is also convenient to benchmark numerical calculations that intrinsically rely on cut-offs. Concretely, cut-off regularization consists in modifying H_1 at high-energy, e.g. [12]

$$\begin{aligned} h^{22}_{\Lambda\ \vec{p}_1'\vec{p}_2'\vec{p}_1\vec{p}_2} &= (2\pi)^3\delta\left(\vec{p}_1' + \vec{p}_2' - \vec{p}_1 - \vec{p}_2\right) \\ &\quad \times v_\Lambda(2q')\left(C_0 + C_2\left(\frac{q'^2 + q^2}{2}\right) + C_2'\vec{q}'\cdot\vec{q} + \ldots\right) v_\Lambda(2q)\ , \end{aligned} \tag{2.17}$$

[8] Assuming the diagram does not contain lines connecting incoming and outgoing states i.e. external legs directly connected without intermediate internal lines.

[9] Any potential time derivatives appearing in the Hamiltonian can be absorbed via a field redefinition.

[10] This formula is related to asymptotic coefficients as defined in [35]. For example, the asymptotic coefficient in the $(\omega, \vec{p})$ vector space of $iG^{(0,1)0}_{\vec{p}\sigma\vec{p}\sigma}(\omega) \equiv \frac{i}{\omega - \frac{p^2}{2m} + i\eta}$ is -2 hence the $-2I$ contribution in the superficial degree of divergence.

[11] See [39] for an example and a thorough discussion around this matter.

[12] In general, the regularization function can take the form $v_\Lambda(\vec{p}_1', \vec{p}_2', \vec{p}_1, \vec{p}_2)$.

where v_Λ can be any function making integrals (1.62) finite and verifying

$$\forall q \ , \ \lim_{\Lambda \to +\infty} v_\Lambda(q) = 1 \ , \tag{2.18}$$

which ensures that the original theory is recovered in the limit $\Lambda \to +\infty$. The cut-off Λ is the characteristic scale at which integrals in (1.62) are affected by v_Λ such that they become finite. In this thesis, a separable regulator function is used to simplify calculations compared to a more general regularization. The general notation v_Λ is used as long as possible for the regulator function. For numerical evaluations, a Gaussian regulator will be employed i.e.

$$v_\Lambda(q) = e^{-\frac{q^2}{\Lambda^2}} \ . \tag{2.19}$$

The second step of a renormalization scheme consists in subtracting terms that are not dominated by a (strictly) negative power of Λ (e.g. divergent terms) for $\Lambda \to +\infty$. This is typically done explicitly by introducing counter-terms in the Hamiltonian[13]. In practice, the counter-terms are computed by introducing a Λ dependence in the coupling constants, e.g. for $\not{\pi}$EFT, Eq. (2.17) is replaced by

$$\begin{aligned} h^{22}_{\Lambda\ \vec{p}_1'\vec{p}_2'\vec{p}_1\vec{p}_2} &= (2\pi)^3 \delta\left(\vec{p}_1' + \vec{p}_2' - \vec{p}_1 - \vec{p}_2\right) \\ &\quad \times v_\Lambda(2q') \left(C_0(\Lambda) + C_2(\Lambda) \left(\frac{q'^2 + q^2}{2} \right) + C_2'(\Lambda) \vec{q}' \cdot \vec{q} + \dots \right) v_\Lambda(2q) \ . \end{aligned} \tag{2.20}$$

Note that the Λ dependence of coupling constants is computed to make the amplitude of a particular set of Feynman diagrams finite. Considering any other set (even adding a single Feynman diagram) might lead to a different Λ dependence. Once the counter-terms are computed, the additional Feynman diagrams (incorporating those counter-terms) to cancel the UV divergences are, for instance, explicitly given by the BPHZ procedure (see App. C or [37] for more details).

Eventually, coupling constants are fixed by imposing matching conditions from the computation of a set of observables used to fit the theory.[14] Following this program, the computation of any other observable should be independent of the choice of the regularization function v_Λ as any change of Λ would be compensated by a change in the Λ dependence of the coupling constants. Physically, this is interpreted as the fact that in an EFT the ultraviolet physics is effectively embedded in its coupling constants.

Through the renormalization procedure, each considered contribution $\mathcal{A}^{\mathcal{G}_n^{(0,k)}}_{\substack{\mu_1 \dots \mu_k \\ \nu_1 \dots \nu_k}}$ becomes well-defined. To compute the k-body Green's function exactly, all $\mathcal{A}^{\mathcal{G}_n^{(0,k)}}_{\substack{\mu_1 \dots \mu_k \\ \nu_1 \dots \nu_k}}$ have to be summed, which is not possible. Consequently, a truncation on the set of $\mathcal{A}^{\mathcal{G}_n^{(0,k)}}_{\substack{\mu_1 \dots \mu_k \\ \nu_1 \dots \nu_k}}$ has to be stipulated to enable the evaluation of observables. In the EFT approach, contributions at leading order (LO) and corrections at sub-leading orders are estimated *a priori* through *power-counting rules* that are discussed in the following subsection.

[13] The proof that such subtraction can be done by introducing Λ dependent counter-terms is non-trivial. Technically, this can be achieved following a Bogoliubov-Parasiuk-Hepp-Zimmermann (BPHZ) prescription, see [40, 41, 37, 42] for a complete proof in the relativistic case.

[14] The matching can be done to experimental data or to the same set of observables computed in another model supposed to be valid e.g. an underlying EFT.

Diagrams contributing to $G^{(0,2)}$		
$\mathcal{G}^{(0,2)}$	$D(\mathcal{G}^{(0,2)})$	$p(\mathcal{G}^{(0,2)})$
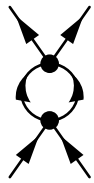	1	-1
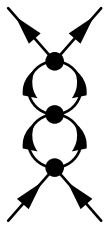	2	-1
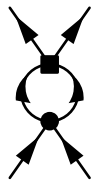	3	0
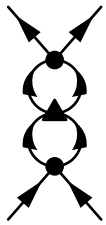	4	2

Diagrams contributing to $G^{(0,3)}$		
$\mathcal{G}^{(0,3)}$	$D(\mathcal{G}^{(0,3)})$	$p(\mathcal{G}^{(0,3)})$
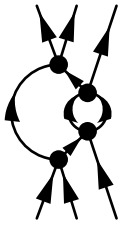	0	-4
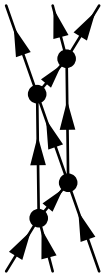	0	-4
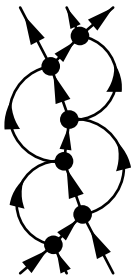	2	-4
	4	-4

Table 2.1. Examples of UV divergent diagrams contributing to $G^{(0,k)}$ for $k = 2, 3$. Associated superficial degree of divergence $D(\mathcal{G}^{(0,k)})$ and counting index $p(\mathcal{G}^{(0,k)})$ are given.

2.1.4. Power-counting rules

Rationale

EFTs exploit the separation between the low-energy scale $M_{\rm lo}$ characteristic of the observables of interest and a higher-energy scale M_b at which the EFT breaks down. For $\not\pi$EFT the low scale is the typical momentum $Q \sim M_{\rm lo}$ of a non-relativistic nucleon so that $Q \ll 1$ GeV. Experimentally, the binding energy per particle of nuclei is $B \sim 8$ MeV so that $Q \lesssim \sqrt{2mB} \sim$ 120 MeV.

The hope of $\not\pi$EFT is that the high-energy (or breakdown) scale M_b, is sufficiently large[15] to justify an expansion of the k-body Green's function in powers of $\frac{M_{\rm lo}}{M_b}$ [6]

$$G^{(\mathrm{A},k)}_{\substack{\mu_1\ldots\mu_k\\ \nu_1\ldots\nu_k}} = \sum_p \left(\frac{M_{\rm lo}}{M_b}\right)^p \mathcal{F}\left(\frac{M_{\rm lo}}{\Lambda}, C_0(\Lambda), C_2(\Lambda), \ldots\right) \ , \tag{2.21}$$

where $\mathcal{F}$ is a function of order one. The problem is then to estimate which subset of Feynman diagrams $\mathcal{G}^{(\mathrm{A},k)}$ contributes to the order p. Such an estimation is done graph by graph[16] by approximating the value of the non-analytic part of their associated amplitude. To this extent, the counting index $p(\mathcal{G}^{(\mathrm{A},k)})$ is defined such that

$$\mathcal{A}^{\mathcal{G}^{(\mathrm{A},k)}}_{\substack{\mu_1\ldots\mu_k\\ \nu_1\ldots\nu_k}} \sim \left(\frac{M_{\rm lo}}{M_b}\right)^{p(\mathcal{G}^{(\mathrm{A},k)})} \ . \tag{2.22}$$

The index p depends in general on the nature of the unperturbed one-body Green's function $G^{(\mathrm{A},1)0}_{\mu\nu}$, on the number of loops in $\mathcal{G}^{(\mathrm{A},k)}$ and on the type of vertices. The rules to obtain p for any $\mathcal{G}^{(\mathrm{A},k)}$ are referred to as the *power-counting rules*. The contributions with the lowest possible p define the so-called leading order (LO), the first corrections with the second lowest p define the next-to-leading order (NLO) and so on. Consequently, the size of the contributions ignored at a given order can be evaluated and employed to stipulate the theoretical error of the EFT at that order. Note that for the EFT to be practical, $p(\mathcal{G}^{(\mathrm{A},k)})$ needs to be bounded from below when considering diagrams with a fixed number of external legs.

While, in principle, power-counting rules could be studied for any perturbation theory, they have been typically stipulated for the particular perturbation theory associated with the partitioning (2.10) and using the particle vacuum as a reference, i.e. for Feynman diagrams $\mathcal{G}^{(\mathrm{A},k)}$ with $\mathrm{A} = 0$ and lines corresponding to the free propagator given in Eq. (2.13).

To estimate the relative size of these Feynman integrals, the size of the coupling constants needs first to be assumed. For example, the naturalness assumption consists in assuming all coupling constants to scale with a given power of M_b, according to their dimensionality. For $\not\pi$EFT this reads [43]

$$C_0 \sim \frac{1}{M_b} \quad , \quad C_2 \sim \frac{1}{M_b^3} \quad , \quad C_2' \sim \frac{1}{M_b^3} \quad , \quad D_0 \sim \frac{1}{M_b^4} \quad , \quad \ldots \ . \tag{2.23}$$

[15] Usually it assumed to be below the pion mass so that $M_b \sim 150$ MeV.

[16] Estimating the size of each graph individually yields an upper bound on the size of their sum. Such bound neglects possible cancellations between them but is usually sufficient.

This leads to the naïve dimensional analysis (NDA) power counting. In this case the power counting is simplified as all $M_{\rm lo}$ contributions come from Q factors.[17] For $\not\pi$EFT, using, as in [44], the counting

$$G^{(0,1)0} \sim Q^{-2} \quad , \quad \mathrm{d}\omega\ \mathrm{d}^3\vec{p} \sim Q^5 \quad , \quad \nabla \sim Q \ , \tag{2.24}$$

the order of magnitude of the amplitude associated to $\mathcal{G}^{(0,k)}$ corresponds to

$$p^{\rm NDA}(\mathcal{G}^{(0,k)}) = 5L - 2I + \sum_i\ 2i\ V_{2i}\ . \tag{2.25}$$

More rigorously, $p^{\rm NDA}(\mathcal{G}^{(0,k)})$ can be derived in NDA by application of the asymptotic theorem [35] which also gives the asymptotic behavior of Feynman integrals in external momentum Q.[18] Using the topology identity $L = I - \sum_i V_{2i} + 1$,

$$p^{\rm NDA}(\mathcal{G}^{(0,k)}) = 3L + 2 + \sum_i\ (2i-2)\ V_{2i}\ . \tag{2.26}$$

A lower bound on $p^{\rm NDA}$ can then be derived using the relation

$$2I + 2k \geq 4\sum_i\ V_{2i}\ , \tag{2.27}$$

leading to

$$p^{\rm NDA}(\mathcal{G}^{(0,k)}) \geq 5 - 3k + \sum_i\ (2i+1)\ V_{2i} \geq 6 - 3k\ . \tag{2.28}$$

In NDA there is only a finite number of diagrams contributing at each order. In the case of nuclear systems, the experimental evidence of non-perturbative physics associated with bound and virtual two-body states imposes that any EFT relying on nucleonic degrees of freedom must in fact depart from NDA. Consequently, at least one coupling constant in $\not\pi$EFT must be assumed to be un-naturally large. Since the scattering length ($a_0 = -18.9$ fm) of two neutrons in the S-wave is un-naturally large, compared to $\frac{1}{M_b} \lesssim \frac{1}{140}$ MeV^{-1} $\sim$ 1.4 fm, at least one two-body coupling constant in the S-wave needs to be un-natural. From such considerations the typical size of two-body coupling constants connecting S-waves are modified to[19]

$$C_0 \sim \frac{1}{M_{\rm lo}} \quad C_2 \sim \frac{1}{M_{\rm lo}^2 M_b} \quad C_2' \sim \frac{1}{M_b^3} \quad \ldots\ . \tag{2.29}$$

At this stage, the new power counting promotes *all* diagrams containing only C_0 vertices at LO.

[17] Associated M_b factor (coming from coupling constants) follows by dimensional analysis so that a factor $\frac{M_{\rm lo}}{M_b}$ is obtained.

[18] This procedure is similar to the one to obtain the superficial degree of divergence. Neglecting potential divergent sub-diagrams leads to the NDA ansatz so that $p^{\rm NDA}(\mathcal{G}^{(0,k)}) = D(\mathcal{G}^{(0,k)})$.

[19] The following power counting is equivalent to considering $\frac{1}{a_0} \sim M_{\rm lo}$ and other parameters such as the effective range r_e to be small in the sense that $\frac{1}{r_e} \sim M_b$ [43].

Renormalization invariance of observables

Power-counting rules require to sum up a certain subset of diagrams to compute the contribution to the k-body Green's function at order p. However, there is no guarantee that all UV divergences appearing at order p can be compensated by counter-terms estimated to appear at the same order. If this is not the case, the power-counting is said to be inconsistent and typically leads to cut-off-dependent observables. Conversely, the requirement of renormalization invariance of any observable O computed at fixed order p can be used to modify power-counting rules such that, at any order p, k-body Green's functions converge in inverse power of Λ in the limit $\Lambda \to +\infty$ i.e.

$$\frac{\Lambda}{O_0^{\mathrm{N}^p\mathrm{LO}}(\Lambda, C_0(\Lambda), C_2(\Lambda), \dots)} \frac{\partial}{\partial \Lambda} O_0^{\mathrm{N}^p\mathrm{LO}}(\Lambda, C_0(\Lambda), C_2(\Lambda), \dots) = O\left(\frac{Q}{\Lambda}\right) \ . \tag{2.30}$$

In the case of $\not\pi$EFT, the renormalization of diagrams contributing to the three-body Green's function $G^{(0,3)}$ at LO, such as those displayed in Tab. 2.1, requires to promote diagrams containing any number of vertices D_0 to LO [45] (while diagrams containing any vertex D_{2i} with $i > 0$ remains a SLO contribution). For example, the size of D_0 can be assumed to be

$$D_0 \sim \frac{1}{M_{\mathrm{lo}}^4} \ . \tag{2.31}$$

Eventually, the counting for diagrams containing vertices C_{2i} and D_0 is modified to

$$p(\mathcal{G}^{(0,k)}) = 3L + 2 + \sum_i (i-3)\ V_{C_{2i}} - 6V_{D_0} \geq 5 - 3k \ . \tag{2.32}$$

For diagrams $\bar{\mathcal{G}}^{(0,k)}$ containing only C_0 and D_0 vertices, one has

$$2I + 2k = 4V_{C_0} + 6V_{D_0} \ , \tag{2.33a}$$

$$L = I - (V_{C_0} + V_{D_0}) + 1 \ , \tag{2.33b}$$

$$p(\bar{\mathcal{G}}^{(0,k)}) = 3L + 2 - 3(V_{C_0} + 2V_{D_0}) \ , \tag{2.33c}$$

so that

$$p(\bar{\mathcal{G}}^{(0,k)}) = 5 - 3k = p^{\mathrm{LO}} \ . \tag{2.34}$$

Computing observables at LO in $\not\pi$EFT is, thus, equivalent to solving the A-body Schrödinger equation exactly for a truncated potential containing only C_0 and D_0 interactions.

Simplified problem

The inclusion of a three-body contact interaction at LO, though relevant for reproducing the phenomenology of nuclear systems with $A \geq 3$, introduces complications to study the renormalization invariance of many-body observables. To simplify the problem while keeping the complexity of a non-perturbative system, it is convenient to restrict the study to pure neutron systems at first. In this case, diagrams containing any number of C_0 vertices contribute at LO to all k-body Green's function $G^{(0,k)}$ whereas, because of Pauli's exclusion principle,

contributions from the three-body contact interaction vanish. The power counting for neutron systems in $\not\pi$EFT thus simplifies to

$$\begin{aligned} p(\mathcal{G}^{(0,k)}) &= 3L + 2 + \sum_i \, (i-3) \; V_{2i} \\ &= 5 - 3k + \sum_i \; i \; V_{2i} \; , \end{aligned} \tag{2.35}$$

for $\mathcal{G}^{(0,k)}$ containing C_{2i} vertices. For diagrams $\tilde{\mathcal{G}}^{(0,k)}$ containing only C_0 vertices,

$$p(\tilde{\mathcal{G}}^{(0,k)}) = 5 - 3k = p^{\mathrm{LO}} \; . \tag{2.36}$$

Eventually, computing LO contributions to the k-body Green's function in pure neutron systems is equivalent to solving the k-body Schrödinger equation exactly for a simplified potential that reads, in terms of antisymmetric two-body matrix elements,

$$V_{\not\pi}^{\mathrm{LO}} \equiv \frac{1}{(2!)^2} \sum_{\substack{\sigma_1'\sigma_2' \\ \sigma_1\sigma_2}} \sum_{\substack{\vec{p}_1'\vec{p}_2' \\ \vec{p}_1\vec{p}_2}} h^{22\ \mathrm{LO}}_{\vec{p}_1'\vec{p}_2'\vec{p}_1\vec{p}_2} \; s^{22\ \mathrm{LO}}_{\sigma_1'\sigma_2'\sigma_1\sigma_2} \; a^\dagger_{\vec{p}_1'\sigma_1} a^\dagger_{\vec{p}_2'\sigma_2} a_{\vec{p}_2\sigma_2} a_{\vec{p}_1\sigma_1} \; , \tag{2.37a}$$

$$h^{22\ \mathrm{LO}}_{\vec{p}_1'\vec{p}_2'\vec{p}_1\vec{p}_2} \equiv (2\pi)^3 \; \delta\left(\vec{p}_1' + \vec{p}_2' - \vec{p}_1 - \vec{p}_2\right) \; C_0 \; , \tag{2.37b}$$

$$s^{22\ \mathrm{LO}}_{\sigma_1'\sigma_2'\sigma_1\sigma_2} \equiv \; \delta_{\sigma_1'\sigma_1}\delta_{\sigma_2'\sigma_2} - \delta_{\sigma_1'\sigma_2}\delta_{\sigma_2'\sigma_1} \; . \tag{2.37c}$$

Contributions associated to the first term of $s^{22\ \mathrm{LO}}_{\sigma_1'\sigma_2'\sigma_1\sigma_2}$ is referred to as the direct contribution while the second term is referred to as the exchange contribution.

Working now with the potential (2.37a), ultraviolet divergences can be studied more easily. Using the relation for a graph $\mathcal{G}_n^{(0,k)}$ containing n vertices C_0

$$2I + 2k = 4n \; , \tag{2.38}$$

the superficial degree of divergence (2.16) simplifies to[20]

$$D(\mathcal{G}_n^{(0,k)}) = 5 - 3k + n \; . \tag{2.39}$$

Typical sets of diagrams contributing to 2- and 3-body Green's functions $G^{(0,k)}$ at LO with their superficial degree of divergence are given in Tab. 2.1.

Discussion

In the present section, renormalization and power-counting rules have been discussed for Feynman diagrams derived in a perturbation theory formulated with respect to the particle vacuum and employing the kinetic Hamiltonian as the unperturbed Hamiltonian.

Because of the un-naturally large scattering length a_0 of two interacting neutrons in the S-wave, power-counting rules require at LO to exactly solve the A-body Schrödinger equation for the potential $V_{\not\pi}^{\mathrm{LO}}$ and to compute SLOs in perturbation relatively to the LO solution. Solving exactly the A-body Schrödinger equation for the potential $V_{\not\pi}^{\mathrm{LO}}$ is manageable for

[20] Similar simplification can be found for graphs containing also D_0 vertices but are not considered here as they do not contribute in the case of pure neutron systems.

A $= 2, 3, 4$ [45, 10] but is impractical for many-body systems where A $\gg 10$. For large A, expanding and truncating the exact solution of the Schrödinger equation is mandatory. This can be done either non-perturbatively, e.g. on the basis of SCGF [11, 12], CC [13, 14] or IM-SRG [15, 16], or in perturbation, via MBPT [17, 18]. It happens that MBPT in particular has recently been shown to yield accurate estimates of nuclear observables, such as ground-state energies, when combined with SRG-evolved Hamiltonians [46, 47].

Traditionally, and in agreement with power-counting rules (2.35), $V_{\not\pi}^{\mathrm{LO}}$ is thus renormalized exactly in 2- and 3-body sectors. As mentioned above, this happens to be technically feasible. However, given both the phenomenological success of approximate many-body schemes and the impossibility to generate exact calculations in large A sectors, this thesis aims at investigating the calculation of many-body observables at LO in $\not\pi$EFT in connection with particular many-body truncations.

To perform consistent $\not\pi$EFT calculations in large A sectors, one must pay attention to the renormalization invariance of observables. At LO, in particular, one may question how much the approximate solving of the Schrödinger equation, on the basis of a previously renormalized potential via an all-order calculation in the two-body sector, compromises the renormalization invariance. Obviously, the extent by which the renormalization invariance is compromised is likely to be function of the severity/nature of the approximation employed to compute A-body observables. It is indeed difficult to design a priori arguments as to what many-body truncation scheme might be best suited. One may for instance argue in favor of solving the A-body Schrödinger equation "as accurately as possible" in order to be "as close as possible" to fulfilling the power counting rule. Working with one specific many-body method, e.g. SCGF, this argument will lead to resumming the largest (infinite) possible set of MBPT diagrams. Another argument might be that a minimal set of diagrams needs to be resummed such that the truncation scheme is exact in the two-body sector and thus corresponds to the calculation done to renormalize the two-body contact interaction in the first place. Employing such a consistency argument between few- and many-body sectors, one might advocate to degrade the calculation employed to renormalize the potential in the two-body sector in order to match whatever truncation is used in the many-body calculation. This would however be done at the cost of compromising the capacity of the EFT to capture the physics associated with the large scattering length (even more so in the unitary limit) that is (at least) known to be crucial in the few-body sector and in low-density neutron matter.

In order to proceed to our investigation in the next chapters, we now describe the renormalization of $V_{\not\pi}^{\mathrm{LO}}$ in the two-body sector at various orders, i.e. tree-level, one-loop and exactly. These renormalized interactions are used in the remainder of the thesis to test the consistency of a renormalization scheme set in few-body sectors and extrapolated to many-body sectors on the basis of various truncations performed within the frame of SCGF or MBPT.

2.2. Renormalization in the two-body sector

This section is devoted to the computation of the two-body Green's function $G^{(0,2)}$ associated to two neutrons on top of the particle vacuum. This is done at tree-level, one-loop and exactly for the LO $\not\pi$EFT potential. Renormalization is discussed via the introduction of a cut-off

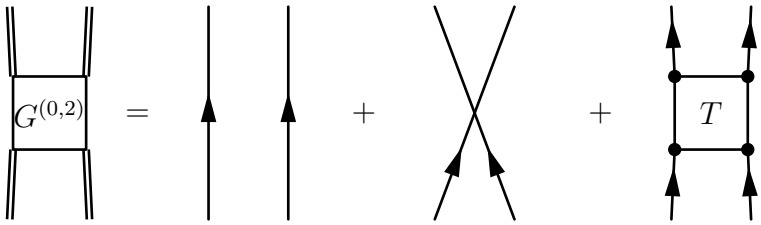

Figure 2.2. Diagrammatic representation of Eq. (2.41).

regulator, i.e.

$$h^{22\ \mathrm{LO}}_{\Lambda\ \vec{p}_1'\vec{p}_2'\vec{p}_1\vec{p}_2} = (2\pi)^3\ \delta\left(\vec{p}_1' + \vec{p}_2' - \vec{p}_1 - \vec{p}_2\right)\ h^{22\ \mathrm{LO}}_{\Lambda\ \vec{q}'\vec{q}}\ , \tag{2.40a}$$

$$h^{22\ \mathrm{LO}}_{\Lambda\ \vec{q}'\vec{q}} \equiv v_\Lambda(2q')C_0(\Lambda)v_\Lambda(2q)\ . \tag{2.40b}$$

Eventually, $C_0(\Lambda)$ is matched to reproduce the experimental S-wave neutron-neutron scattering length ($a_0 = -18.9$ fm).

It is convenient to introduce the T-matrix[21] defined, in the time representation, by

$$\begin{aligned} G^{(0,2)}_{\substack{\mu_1\mu_2\\ \nu_1\nu_2}}(t_{\mu_1}t_{\mu_2}, t_{\nu_1}t_{\nu_2}) &\equiv G^{(0,1)0}_{\mu_1\nu_1}(t_{\mu_1}, t_{\nu_1})G^{(0,1)0}_{\mu_2\nu_2}(t_{\mu_2}, t_{\nu_2}) - G^{(0,1)0}_{\mu_2\nu_1}(t_{\mu_2}, t_{\nu_1})G^{(0,1)0}_{\mu_1\nu_2}(t_{\mu_1}, t_{\nu_2}) \\ &+(-i)\sum_{\substack{\lambda_1\lambda_2\\ \lambda_3\lambda_4}}\int \mathrm{d}t_{\lambda_1}\mathrm{d}t_{\lambda_2}\mathrm{d}t_{\lambda_3}\mathrm{d}t_{\lambda_4}\ G^{(0,1)0}_{\lambda_3\nu_1}(t_{\lambda_3}, t_{\nu_1})G^{(0,1)0}_{\lambda_4\nu_2}(t_{\lambda_4}, t_{\nu_2}) \\ &\qquad \times T_{\substack{\lambda_1\lambda_2\\ \lambda_3\lambda_4}}\ (t_{\lambda_1}t_{\lambda_2}, t_{\lambda_3}t_{\lambda_4})G^{(0,1)0}_{\mu_1\lambda_1}(t_{\mu_1}, t_{\lambda_1})G^{(0,1)0}_{\mu_2\lambda_2}(t_{\mu_2}, t_{\lambda_2})\ . \end{aligned} \tag{2.41}$$

Eq. (2.41) is represented diagrammatically in Fig. 2.2. As $H_1 = V^{\mathrm{LO}}_{\not\pi}$ depends only on the relative momentum $\vec{q}$ so it is for $T_{\substack{\lambda_1\lambda_2\\ \lambda_3\lambda_4}}(t_{\lambda_1}t_{\lambda_2}, t_{\lambda_3}t_{\lambda_4})$. As a shorthand, Fourier-transformed T-matrix elements are denoted by $T_{\vec{q}\vec{q}'}(\omega_1, \omega_2, \omega_3, \omega_4)$. Taking into account conservation of energy, momentum, as well as rotational invariance in the S-wave, the on-shell T-matrix only depends on the modulus of one relative momentum q and energy E and is denoted as $T_q(E)$. The on-shell T-matrix is eventually parametrized by the S-wave phase shift $\delta_0(q)$ as[22]

$$T_q\left(E = \frac{P^2 + q^2}{m}\right) = -\frac{4\pi}{m}\frac{1}{q\cot\delta_0(q) - iq}\ , \tag{2.42}$$

where $\delta_0(q)$ is related to a_0 by

$$\lim_{q\to 0} q\cot\delta_0(q) = -\frac{1}{a_0} + O\left(q^2\right)\ . \tag{2.43}$$

[21] In the two-body sector this corresponds to the exact two-body vertex function. In a general A-body sector, the (two-body) T-matrix is referred to as the ladder approximation of the two-body vertex function.

[22] Note that in Eq. (2.42) T is in the energy representation.

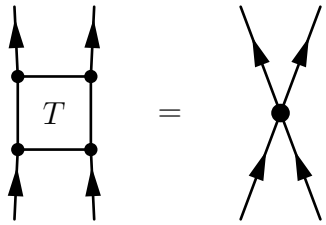

Figure 2.3. T-matrix at tree-level order.

In the low-momentum limit, the on-shell T-matrix can be expanded as

$$\begin{aligned} T_q\left(E=\frac{P^2+q^2}{m}\right) &= -\frac{4\pi}{m}\frac{1}{-\frac{1}{a_0}-iq+O\left(q^2\right)} \\ &= -\frac{4\pi}{m}\frac{1}{-\frac{1}{a_0}-iq}\frac{1}{1+O\left(q^2\right)} \\ &= \frac{4\pi}{m}a_0\left(1-iqa_0\right)+O(q^2)\ . \end{aligned} \tag{2.44}$$

Matching $C_0(\Lambda)$ to the physical scattering length is done by computing directly diagrams contributing to the T-matrix in the energy representation.

2.2.1. Tree-level renormalization

Tree-level approximation means that only Fig. 2.3 contributes to T, i.e.

$$T_q(E) = h^{22\ \mathrm{LO}}_{\Lambda\ \vec{q}\vec{q}}\ . \tag{2.45}$$

Matching to experimental data in the limit $q \to 0$ using (2.42) and (2.43) one has

$$C_0(\Lambda) = \frac{4\pi}{mv^2_\Lambda(0)}a_0 \tag{2.46}$$

and in the case of the Gaussian regulator,

$$C_0(\Lambda) = \frac{4\pi}{m}a_0\ , \tag{2.47}$$

such that the Λ dependence of $C_0(\Lambda)$ is trivial. There is indeed no UV divergence to cancel at tree-level.

If the aim of this calculation was to compute a nuclear observable in the two-body sector, such an approximation would not be pertinent because of the un-naturally large scattering length a_0. In the unitary limit, where $|a_0| \to +\infty$, it is clear that $|T_q(E)| \to +\infty$ and the tree-level approximation breaks down. However, anticipating discussions in Chap. 3, certain many-body truncations, adapted to particular nuclear systems lying in large A-body sectors, require renormalization of $C_0(\Lambda)$ at this order in the two-body sector (e.g. infinite neutron matter at intermediate densities).

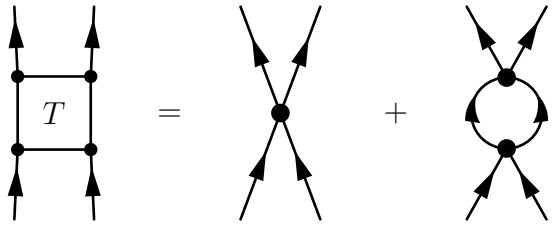

Figure 2.4. T-matrix at one-loop order.

2.2.2. One-loop renormalization

In this section, T includes the one-loop contribution. Diagrams contributing are represented in Fig. 2.4. Any exchange contribution is equal to the direct one such that only the direct contribution needs to be computed. The one-loop contribution reads

$$T_q\left(E\right) = h^{22\ \mathrm{LO}}_{\Lambda\ \vec{q}\vec{q}} - i\int_{-\infty}^{+\infty}\frac{\mathrm{d}l_0}{2\pi}\int\frac{\mathrm{d}^3\vec{l}}{(2\pi)^3}\ h^{22\ \mathrm{LO}}_{\Lambda\ \vec{q}\ \vec{l}}\ G^{(0,1)0}_{\vec{P}+\vec{l}}\left(\frac{E}{2}+l_0\right)G^{(0,1)0}_{\vec{P}-\vec{l}}\left(\frac{E}{2}-l_0\right)h^{22\ \mathrm{LO}}_{\Lambda\ \vec{l}\ \vec{q}}\ . \tag{2.48}$$

Replacing unperturbed one-body propagators with (2.13), integrating the angle of $\vec{l}$ and l_0 around the $+i\epsilon$ pole, one obtains

$$\begin{aligned} T_q\left(E\right) = C_0(\Lambda)v_\Lambda(2q)^2 - C_0(\Lambda)^2 v_\Lambda(2q)^2\ m \\ \times\int_0^{+\infty}\frac{\mathrm{d}l}{2\pi^2}\ \frac{l^2}{l^2-(mE-(P^2+q^2)+q^2)-i\epsilon}v_\Lambda(2l)^2\ . \end{aligned} \tag{2.49}$$

Eventually, the T-matrix reads as

$$\begin{aligned} T_q\left(E\right) = C_0(\Lambda)v_\Lambda(2q)^2 - \frac{m}{2\pi^2}\ C_0(\Lambda)^2 v_\Lambda(2q)^2\ \times\Bigg[\int_0^{+\infty}\mathrm{d}l\ v_\Lambda^2(2l) \\ +\sqrt{mE-(P^2+q^2)+q^2}\ i\frac{\pi}{2}v_\Lambda^2\left(2\sqrt{mE-(P^2+q^2)+q^2}\right)\Bigg]\ . \end{aligned} \tag{2.50}$$

To match $C_0(\Lambda)$ at order a_0^2 , its Λ dependence is assumed to take the form

$$C_0(\Lambda) = a_0\ f(\Lambda) + a_0^2\ g(\Lambda)\ , \tag{2.51}$$

which, inserted in Eq. (2.50) with the on-shell condition $E = \frac{P^2+q^2}{m}$, is matched to Eq. (2.44) for

$$f(\Lambda) = \frac{4\pi}{m v_\Lambda^2(0)}\ , \tag{2.52a}$$

$$g(\Lambda) = \frac{8}{m v_\Lambda^4(0)}\int_0^{+\infty}\mathrm{d}l\ v_\Lambda^2(2l)\ . \tag{2.52b}$$

For the Gaussian regulator,

$$v_\Lambda(0) = 1\ , \tag{2.53a}$$

$$\int_0^{+\infty}\mathrm{d}l\ v_\Lambda^2(2l) = \frac{\Lambda\sqrt{\pi}}{2\sqrt{2}}\ , \tag{2.53b}$$

so that

$$C_0(\Lambda) = \frac{4\pi}{m}\, a_0 + \frac{4\pi}{m}\, \frac{1}{\sqrt{2\pi}}\, a_0^2\, \Lambda \ . \tag{2.54}$$

Compared to (2.47) $C_0(\Lambda)$ includes a Λ dependence that diverges for $\Lambda \to +\infty$. By construction, this divergence exactly cancels the divergence originating from the integral associated to the one-loop diagram.

As in the tree-level approximation, the T-matrix diverges in the unitary limit, which rules out the one-loop approximation to compute observables in the two-body sector. However, for the same reason as for the renormalization at tree-level, one-loop renormalization of $C_0(\Lambda)$ might be pertinent for nuclear systems where employed many-body truncations require such a renormalization.

2.2.3. Exact renormalization

In this section, T is computed exactly. This corresponds to summing all diagrams displayed in Fig. 2.5, which are referred to as ladder diagrams. As for the tree and one-loop diagrams, exchange and direct contributions are equal such that only direct diagrams are to be computed. The summation if all ladder diagrams can be recast into an implicit equation for the T-matrix

$$T_q\,(E) = h_{\Lambda\ \vec{q}\vec{q}}^{22\ \mathrm{LO}} - i \int_{-\infty}^{\infty} \frac{\mathrm{d}l_0}{2\pi} \int \frac{\mathrm{d}^3\vec{l}}{(2\pi)^3}\, h_{\Lambda\ \vec{q}\ \vec{l}}^{22\ \mathrm{LO}}\, G_{\vec{P}+\vec{l}}^{(0,1)0}\left(\frac{E}{2}+l_0\right) G_{\vec{P}-\vec{l}}^{(0,1)0}\left(\frac{E}{2}-l_0\right)\, T_{\vec{l}\ \vec{q}}(E) \ . \tag{2.55}$$

T-matrix computation

To simplify the computation of the T-matrix, it is convenient to introduce the integrated[23] free two-body propagator

$$\mathscr{G}_{ll'}^{(0,2)0}\,(E,P) \equiv \frac{-m\ l^2}{l^2 - (mE - (P^2+q^2) + q^2) - i\epsilon}\delta(l-l') \ . \tag{2.56}$$

Equation (2.55) is rewritten in a matrix notation as

$$T = h_\Lambda^{22\ \mathrm{LO}} + h_\Lambda^{22\ \mathrm{LO}}\ \mathscr{G}^{(0,2)0}\ T \ , \tag{2.57}$$

where the matrix product is defined for two kernels $A_{ll'}$ and $B_{ll'}$ as

$$(AB)_{ll'} = \int_0^{+\infty} \frac{\mathrm{d}k}{2\pi^2}\ A_{lk}B_{kl'} \ . \tag{2.58}$$

As $h_\Lambda^{22\ \mathrm{LO}}$ is separable in l

$$\forall M\ ,\ \mathrm{rank}\left(h_\Lambda^{22\ \mathrm{LO}} M\right) = 1\ , \tag{2.59}$$

and in particular, $\mathrm{rank}\left(h_\Lambda^{22\ \mathrm{LO}}\mathscr{G}^{(0,2)0}\right) = 1$. This is a useful property as for any matrix M of rank one holds an inversion relation, namely[24]

$$(1-M)^{-1} = 1 + \frac{1}{1-\mathrm{Tr}(M)} M \ . \tag{2.60}$$

[23] The integration is performed both on the energy and the angle of the relative momentum.

[24] This approach can be extended in a straightforward way to cases where $\mathrm{rank}\left(h_\Lambda^{22\ \mathrm{LO}}\mathscr{G}^{(0,2)0}\right)$ is a generic integer by generalizing the inversion formula.

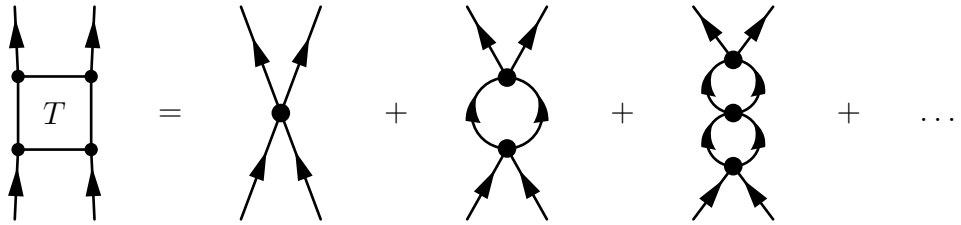

Figure 2.5. Exact T-matrix equation. The dots denote the summation on all Ladder diagrams.

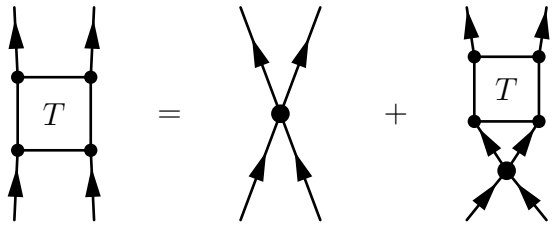

Figure 2.6. Exact T-matrix equation in its implicit form.

Using this relation, an explicit expression of the T matrix can be achieved as

$$\begin{aligned} T &= h_\Lambda^{22\ \mathrm{LO}} + h_\Lambda^{22\ \mathrm{LO}}\ \mathscr{G}^{(0,2)0}\ T \\ &= \left(1 - h_\Lambda^{22\ \mathrm{LO}}\ \mathscr{G}^{(0,2)0}\right)^{-1}\ h_\Lambda^{22\ \mathrm{LO}} \\ &= \frac{1}{1 - \mathrm{Tr}(h_\Lambda^{22\ \mathrm{LO}}\ \mathscr{G}^{(0,2)0})}\ h_\Lambda^{22\ \mathrm{LO}}\ . \end{aligned} \tag{2.61}$$

In an integral form, Eq. (2.61) reads

$$T_q(E) = \frac{h_{\Lambda\ \vec{q}\vec{q}}^{22\ \mathrm{LO}}}{1 - \int_0^{+\infty} \frac{\mathrm{d}l}{2\pi^2}\ h_{\Lambda\ ll}^{22\ \mathrm{LO}}\ \mathscr{G}_{ll}^{(0,2)0}(E)}\ . \tag{2.62}$$

Replacing the potential and integrated free two-body propagator, one obtains

$$\begin{aligned} T_q(E) &= \frac{C_0(\Lambda) v_\Lambda^2(2q)}{1 + mC_0(\Lambda) \int_0^{+\infty} \frac{\mathrm{d}l}{2\pi^2} \frac{l^2 v_\Lambda^2(2l)}{l^2 - (mE - (P^2+q^2) + q^2) - i\epsilon}} \\ &= \frac{C_0(\Lambda) v_\Lambda^2(2q)}{1 + \frac{mC_0(\Lambda)}{2\pi^2}\left[\int_0^{+\infty} \mathrm{d}l\ v_\Lambda^2(2l) + i\frac{\pi}{2}\sqrt{mE - (P^2+q^2) + q^2}\ v_\Lambda^2\left(2\sqrt{mE - (P^2+q^2) + q^2}\right)\right]}\ . \end{aligned} \tag{2.63}$$

Eventually, the on-shell T-matrix reads as

$$T_q\left(E = \frac{P^2+q^2}{m}\right) = \frac{C_0(\Lambda) v_\Lambda^2(2q)}{1 + \frac{mC_0(\Lambda)}{2\pi^2}\left[\int_0^{+\infty} \mathrm{d}l\ v_\Lambda^2(2l) + i\frac{\pi}{2} q\ v_\Lambda^2(2q)\right]}\ . \tag{2.64}$$

Matching $C_0(\Lambda)$ to the scattering length

As for the one-loop calculation, T-matrix elements in Eq. (2.64) are matched to Eq. (2.42), i.e. $C_0(\Lambda)$ is such that

$$-\frac{4\pi}{m}\frac{1}{q\cot\delta_0(q)-iq}=\frac{-\dfrac{4\pi}{m}}{-\dfrac{4\pi}{mC_0(\Lambda)v_\Lambda^2(2q)}-\dfrac{2}{\pi v_\Lambda^2(2q)}\displaystyle\int_0^{+\infty}\mathrm{d}l\ v_\Lambda^2(2l)-iq}\ . \tag{2.65}$$

Using (2.43), $C_0(\Lambda)$ is obtained as

$$\frac{1}{C_0(\Lambda)}=v_\Lambda^2(0)\frac{m}{4\pi}\left[\frac{1}{a_0}-\frac{2}{\pi}\int_0^{+\infty}\mathrm{d}l\ v_\Lambda^2(2l)\right]\ . \tag{2.66}$$

In the case of a Gaussian regulator, using (2.53), Eq. (2.66) reads

$$\frac{1}{C_0(\Lambda)}=\frac{m}{4\pi}\left[\frac{1}{a_0}-\frac{\Lambda}{\sqrt{2\pi}}\right]\ . \tag{2.67}$$

For this exact calculation, the on-shell T-matrix converges in the unitary limit so that among the three different approximations considered in this section, only the exact calculation is justified to compute observables in the two-body sector (in agreement with power-counting rules derived in (2.35) for large S-wave scattering length). That is why, traditionally, $\not\pi$EFT Hamiltonians at LO are renormalized exactly in 2- and 3-body sectors prior to being used in many-body calculations [9]. Again such a renormalization is pertinent for certain many-body truncations. In general, further developments depending on the many-body approximation are necessary to justify a particular renormalization (see Sec. 4.3.1 for an explicit example in the case of the random phase approximation).

Chapter 3.

Equation of state of neutron matter

In the previous chapter $\not\pi$EFT has been introduced leading to the requirement to solve exactly the A-body Schrödinger equation for the LO Hamiltonian defined in Eq. (2.37a). As this thesis deals with issues arising in A-body sectors characterised by $A \gg 10$, focus is put on computing the equation of state (EoS) of infinite nuclear matter. Calculations for infinite matter also have the advantage of being less numerically involved than for finite nuclei as further symmetries such as translation invariance are preserved. For this many-body system, exact techniques to compute the energy, such as Faddeev-Yakubovsky [48, 49], are not feasible. Because of their numerical complexity, Monte-Carlo methods can provide important benchmarks but are not suitable for systematic and explorative calculations (see [50] for a review applied to nuclear physics). In general, further truncations specific to many-body sectors are required to compute the equation of state of infinite nuclear matter. To further simplify the problem, focus is put here on infinite neutron matter as only a two-body contact interaction enters the potential at LO. For convenience, the LO superscript is dropped in this chapter. As it will be argued later, conclusions drawn from such a study will be generalizable to interactions containing N-body parts.

Regarding infinite neutron matter, there are still many different many-body approximations that can be employed. As power-counting rules of $\not\pi$EFT require to solve exactly the LO part of $H_{\not\pi}$, the focus is first put on non-perturbative methods. SCGF formalism is an appropriate tool of choice as it enables to formulate non-perturbative many-body truncations while keeping thermodynamic consistency [51, 52]. Furthermore, the re-expression of the approximations considered in this chapter as the resummation of an infinite number of Feynman diagrams will eventually facilitate the consistency analysis with the renormalizations of $H_{\not\pi}$ considered in Chap. 2.

To analyse the UV divergences coming out of SCGF calculations, the general SCGF framework is first introduced in Secs. 3.1-3.2 where emphasis is put on its relation to MBPT framework. Next, in Sec. 3.4, the structure of a state-of-the-art numerical code is briefly recalled before analysing numerical results that have been produced with it. Eventually, an analytical calculation performed within the framework of MBPT with the resummation of an infinite set of diagrams is detailed in Sec. 3.5. This enables us to analyse the consequences of the conclusions drawn from the numerical analysis, to test the numerical sensitivity of the SCGF code, and to study the consistency of another many-body approximation with the renormalization of $H_{\not\pi}$.

3.1. Infinite neutron matter

In this section, the perturbation theory used for many-body calculations in infinite matter is introduced. Infinite neutron matter in the canonical ensemble at temperature $T = 0$ is considered. Eventually, the procedure to compute the energy per particle is detailed.

3.1.1. Perturbation theory

Infinite neutron matter is a statistical quantum system assumed to be in the thermodynamical limit. At temperature $T = 0$, it reduces to a deterministic quantum system described by an eigenstate of $H_{\not{t}}$ and A.

Unperturbed system

The same partitioning of the Hamiltonian as in Chap. 2 is used to set up the perturbation theory i.e.

$$H_{\not{t}} = H_0 + H_1 \ , \tag{3.1a}$$

$$H_0 \equiv \sum_{\vec{p}\sigma} \frac{p^2}{2m} a^\dagger_{\vec{p}\sigma} a_{\vec{p}\sigma} \ , \tag{3.1b}$$

$$H_1 \equiv \sum_{\sigma_1\sigma_2} \sum_{\substack{\vec{p}_1\vec{p}_2 \\ \vec{p}'_1\vec{p}'_2}} h^{22}_{\vec{p}_1\vec{p}_2\vec{p}'_1\vec{p}'_2} \ a^\dagger_{\vec{p}'_1\sigma_1} a^\dagger_{\vec{p}'_2\sigma_2} a_{\vec{p}_1\sigma_1} a_{\vec{p}_2\sigma_2} \ , \tag{3.1c}$$

such that the unperturbed Hamiltonian H_0 is again the kinetic Hamiltonian and the associated single-particle energies read as single-particle kinetic energies of a free particle of momentum $\vec{p}$ i.e.

$$e_{\vec{p}\sigma} = \frac{p^2}{2m} \ . \tag{3.1d}$$

However, the reference state is not the particle vacuum $|0\rangle$ but the Slater determinant defined as

$$|\Phi^\rho_0\rangle = \prod_{\sigma, p<k_F} a^\dagger_{\vec{p}\sigma} |0\rangle \ , \tag{3.1e}$$

where the superscript ρ denotes the number of particle per unit volume and k_F is the Fermi momentum associated to ρ (see Eq. (3.11c)).

The associated unperturbed many-body basis, as defined in Eqs. (1.42) and (1.43), reads as

$$|\Phi^\rho_0\rangle = \prod_{\sigma, p<k_F} a^\dagger_{\vec{p}\sigma} |0\rangle \ , \tag{3.2a}$$

$$\left|\Phi^{ab\ldots}_{ij\ldots}\right\rangle = a^\dagger_a a^\dagger_b \ldots a_i a_j \ldots |\Phi^\rho_0\rangle \ , \tag{3.2b}$$

where $a \equiv (\vec{p}_a\sigma_a)$, $b \equiv (\vec{p}_b\sigma_b)$, ... are particle states such that[1] $p_a, p_b, \cdots > k_F$ and $i \equiv (\vec{p}_i\sigma_i)$, $j \equiv (\vec{p}_j\sigma_j)$, ... are hole states such that $p_i, p_j, \cdots < k_F$. Their associated unperturbed energies,

[1] Presently dealing with spin unpolarized neutron matter, both spin states associated to a given momentum $\vec{p}$ are either occupied or unoccupied. Presently dealing with a spherical Fermi sea, all momenta $\vec{p}$ with the same magnitude p are either occupied or unoccupied.

as defined in (1.44), read as

$$\epsilon_0^\rho = \sum_\sigma \sum_{p<k_F} e_{\vec{p}\sigma} \ , \tag{3.2c}$$

$$\epsilon_{ij\dots}^{ab\dots} = \epsilon_0^\rho + \sum_{p\in\{p_a,p_b,\dots\}} e_{\vec{p}\sigma} - \sum_{p\in\{p_i,p_j,\dots\}} e_{\vec{p}\sigma} \ . \tag{3.2d}$$

where the sums on momenta are to be understood as integrals on $\vec{p}$, e.g.

$$\sum_{p<k_F} \longleftrightarrow \int_{|\vec{p}|<k_F} \frac{\mathrm{d}^3\vec{p}}{(2\pi)^3} \ . \tag{3.3}$$

Using Eq. (3.1d) and similarly as for Eq. (1.52b), the unperturbed one-body Green's function in time representation reads as

$$\begin{aligned} iG^{(\rho,1)0}_{\vec{p}\sigma\vec{p}'\sigma'}(t,t') = \Big[&\theta(t-t')\ \theta(p-k_F)e^{-ie_{\vec{p}\sigma}(t-t')} \\ &- \theta(t'-t)\ \theta(k_F-p)e^{-ie_{\vec{p}\sigma}(t'-t)}\Big]\ (2\pi)^3\delta\left(\vec{p}-\vec{p}'\right)\delta_{\sigma\sigma'} \ , \end{aligned} \tag{3.4}$$

such that its energy representation becomes

$$iG^{(\rho,1)0}_{\vec{p}\sigma\vec{p}'\sigma'}(\omega) = i\left[\frac{\theta\left(p-k_F\right)}{\omega-\frac{p^2}{2m}+i\eta} + \frac{\theta\left(k_F-p\right)}{\omega-\frac{p^2}{2m}-i\eta}\right](2\pi)^3\delta\left(\vec{p}-\vec{p}'\right)\ \delta_{\sigma\sigma'} \ . \tag{3.5}$$

Contrary to the perturbation theory introduced in Sec. 2.1.2, the one-body Green's function contains poles associated both to single-particle ($p > k_F$) and single-hole ($p < k_F$) states. Incidentally, the topology of the Feynman diagrams contributing to $G^{(\rho,k)}$ is richer than in the perturbation theory developed in Chap. 2. This point will be elaborated on Chap. 4.

3.1.2. Energy per particle

The one-body momentum density distribution is associated to the operator

$$n\left(\vec{p}\right) \equiv \sum_\sigma a^\dagger_{\vec{p}\sigma} a_{\vec{p}\sigma} \ . \tag{3.6}$$

Using Eq. (1.27), its expectation value is related to the equal-time one-body Green's function as

$$n\left(\vec{p}\right)_0 = \frac{\langle\Psi_0^\rho|\sum_\sigma a^\dagger_{\vec{p}\sigma}a_{\vec{p}\sigma}|\Psi_0^\rho\rangle}{\langle\Psi_0^\rho|\Psi_0^\rho\rangle} = -i\sum_\sigma G^{(\rho,1)}_{\vec{p}\sigma\vec{p}\sigma}(t,t^+) \ . \tag{3.7}$$

The (number) density operator ρ and its expectation value in the ground state are respectively defined as the integral of $n(\vec{p})$ and of $n(\vec{p})_0$[2], i.e.

$$\rho \equiv \sum_{\vec{p}} n(\vec{p}) = \sum_{\vec{p}\sigma} a^\dagger_{\vec{p}\sigma}a_{\vec{p}\sigma} \ , \tag{3.8a}$$

$$\rho_0 \equiv \sum_{\vec{p}} n(\vec{p})_0 = -i\sum_{\vec{p}\sigma} G^{(\rho,1)}_{\vec{p}\sigma\vec{p}\sigma}(t,t^+) \ . \tag{3.8b}$$

[2] ρ_0 should not be confused with the saturation density.

Similarly the energy density is obtained using Eq. (1.28) with

$$e_\mu \equiv \frac{p_\mu^2}{2m} \ , \tag{3.9a}$$

$$\breve{h}^{11}_{\mu\nu} \equiv 0 \ , \tag{3.9b}$$

$$h^{22} \equiv h^{22}_{\not\pi} \ , \tag{3.9c}$$

so that

$$E_0 = -\frac{1}{(1!)^2}\sum_{\vec{p}\sigma}\frac{p^2}{2m}\ iG^{(\rho,1)}_{\vec{p}\sigma\vec{p}\sigma}(t,t^+) + \frac{1}{(2!)^2}\sum_{\sigma_1\sigma_2}\sum_{\substack{\vec{p}_1\vec{p}_2\\ \vec{p}_1'\vec{p}_2'}} h^{22}_{\vec{p}_1\vec{p}_2\vec{p}_1'\vec{p}_2'}\ i^2 G^{(\rho,2)}_{\substack{\vec{p}_1\sigma_1\vec{p}_2\sigma_2\\ \vec{p}_1'\sigma_1\vec{p}_2'\sigma_2}}(t,t,t^+,t^+) \ . \tag{3.10}$$

Using the unperturbed one-body Green's function (3.4), the unperturbed energy density, momentum distribution and (number) density are related to the Fermi momentum respectively as

$$\epsilon_0^\rho = \frac{k_F^5}{5\pi^2 2m} \ , \tag{3.11a}$$

$$n(\vec{p})_0^0 = 2\theta(k_F - p) \ , \tag{3.11b}$$

$$\rho_0^0 = \frac{k_F^3}{3\pi^2} \ . \tag{3.11c}$$

Consequently, the energy per particle reads in the unperturbed case

$$\frac{\epsilon_0^\rho}{\rho_0^0} = \frac{3}{5}\frac{k_F^2}{2m} \ . \tag{3.12}$$

To compute the energy per particle of neutron matter beyond the unperturbed case, corrections to the one- and two-body Green's functions are required as input to Eqs. (3.10) and (3.8b). In the next section, the framework of Self-Consistent Green's Functions (SCGF) is introduced to compute (non-perturbative) approximations of exact Green's functions.

3.2. Self-consistent Green's functions

In the context of nuclear many-body calculations applied to infinite matter, non-perturbative schemes based on the SCGF formalism provide state-of-the-art results. Such a technique has the advantage of dealing with the non-perturbative character of nuclear systems while keeping, under certain conditions, the thermodynamic consistency of observables i.e. the validity of thermodynamic identities [51, 52]. The many-body scheme can be related to perturbation theory as its outcome can be reformulated in terms of an infinite sum of Feynman amplitudes. Being able to correctly renormalize the $\not\pi$EFT interaction with respect to a generic SCGF calculation would be an important step forward in the development of an EFT for nuclear matter. That is why, in this thesis, SCGF is the first many-body scheme to be employed to test the renormalization of $H_{\not\pi}$ at LO. To this aim, SCGF theory is introduced in this section via the use of *equations of motion* with an emphasis on its link to MBPT diagrams. As SCGF calculations must eventually be done numerically, the numerical implementation is discussed in Sec. 3.4 with a focus on specific numerical approximations that can hamper the study of renormalization invariance of observables.

3.2.1. Equations of motion

The equations of motion denote a set of coupled differential equations fulfilled by exact k-body Green's functions[3]. They can be derived from the time-dependence of creation and annihilation operators [24]. For a Hamiltonian composed of up to N-body operators, the equations of motion couple the k-body Green's function to $(k-N+1)$- , . . . , $(k+N-1)$-body Green's functions. In the present case where $H_{\not t}$ is a two-body operator, the equation involving the one-body Green's function reads in position space as

$$\left(i\frac{\partial}{\partial t_1}+\frac{\nabla_r^2}{2m}\right) G^{(\rho,1)}_{\vec{r}_1\sigma_1\vec{r}_3\sigma_3}(t_1,t_3) = \delta(t_1-t_3)\delta(\vec{r}_1-\vec{r}_3) \; - i\sum_{\sigma_2}\int \mathrm{d}^3\vec{r}_2 \; h^{22}_{\vec{r}_1\vec{r}_2\vec{r}_1\vec{r}_2} \; G^{(\rho,2)}_{\substack{\vec{r}_1\sigma_1\vec{r}_2\sigma_2\\ \vec{r}_3\sigma_3\vec{r}_2\sigma_2}}(t_1,t_1,t_3,t_3^+) \; . \quad (3.13)$$

Given that, the full hierarchy of equations of motion cannot be solved for $H_{\not t}$ in practice, truncations must be introduced.

Truncations presently considered consist in approximations performed at the level of $G^{(\rho,2)}$. By introducing the self-energy $\Sigma^{(\rho)}_{\vec{r}_1\sigma_1\vec{r}_2\sigma_2}(t_1,t_2)$, defined implicitly via

$$\sum_{\sigma_2}\int \mathrm{d}^3\vec{r}_2\mathrm{d}t_2 \; \Sigma^{(\rho)}_{\vec{r}_1\sigma_1\vec{r}_2\sigma_2}(t_1,t_2) \; G^{(\rho,1)}_{\vec{r}_2\sigma_2\vec{r}_3\sigma_3}(t_2,t_3) \equiv - i\sum_{\sigma_2}\int \mathrm{d}^3\vec{r}_2 \; h^{22}_{\vec{r}_1\vec{r}_2\vec{r}_1\vec{r}_2} \; G^{(\rho,2)}_{\substack{\vec{r}_1\sigma_1\vec{r}_2\sigma_2\\ \vec{r}_3\sigma_3\vec{r}_2\sigma_2}}(t_1,t_1,t_3,t_3^+) \; , \quad (3.14)$$

approximations on $G^{(\rho,2)}$ can be conveniently expressed as approximations on $\Sigma^{(\rho)}$, with the advantage of working at the one-body level. Substituting (3.14) in (3.13) leads to Dyson's equation

$$G^{(\rho,1)}_{\vec{r}\sigma\vec{r}'\sigma'}(t,t') = G^{(\rho,1)0}_{\vec{r}\sigma\vec{r}'\sigma'}(t,t') + \sum_{\sigma_1\sigma_2}\int \mathrm{d}t_1\mathrm{d}^3\vec{r}_1 \; \mathrm{d}t_3\mathrm{d}^3\vec{r}_2 \; G^{(\rho,1)}_{\vec{r}\sigma\vec{r}_1\sigma_1}(t,t_1) \; \Sigma^{(\rho)}_{\vec{r}_1\sigma_1\vec{r}_2\sigma_2}(t_1,t_2) \; G^{(\rho,1)0}_{\vec{r}_2\sigma_2\vec{r}'\sigma'}(t_2,t') \; , \quad (3.15)$$

which is represented diagrammatically in Fig. 3.1. Equation (3.15) is conveniently rewritten in a matrix notation as

$$G^{(\rho,1)} = G^{(\rho,1)0} + G^{(\rho,1)} \; \Sigma^{(\rho)} \; G^{(\rho,1)0} \; , \quad (3.16)$$

where the matrix product is both with respect to the one-body basis and to the time-dependence.

The self-energy can be expanded in terms of unperturbed one-body Green's functions and two-body vertices. In terms of Feynman diagrams, the self-energy is the sum of all one-particle irreducible (1PI) diagrams. All one-particle reducible diagrams are then generated by iteration within Dyson equation (see Fig. 3.2 for a diagrammatic representation). Therefore approximations on the self-energy can be seen as truncations on the corresponding set of 1PI diagrams.

In the case of *self-consistent* Green's functions, the self-energy is expanded in terms of the *dressed* one-body Green's function itself (rather than unperturbed ones), which is the unknown

[3]Equations of motion are also referred to as Martin-Schwinger [24] or BBGYK hierarchy [53, 54, 55, 56].

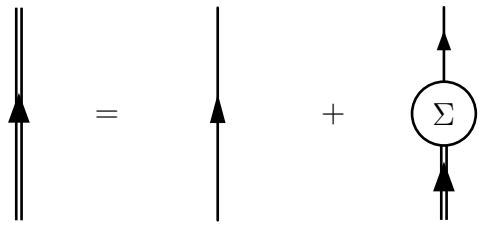

Figure 3.1. Diagrammatic representation of the self-consistent Dyson equation (3.15).

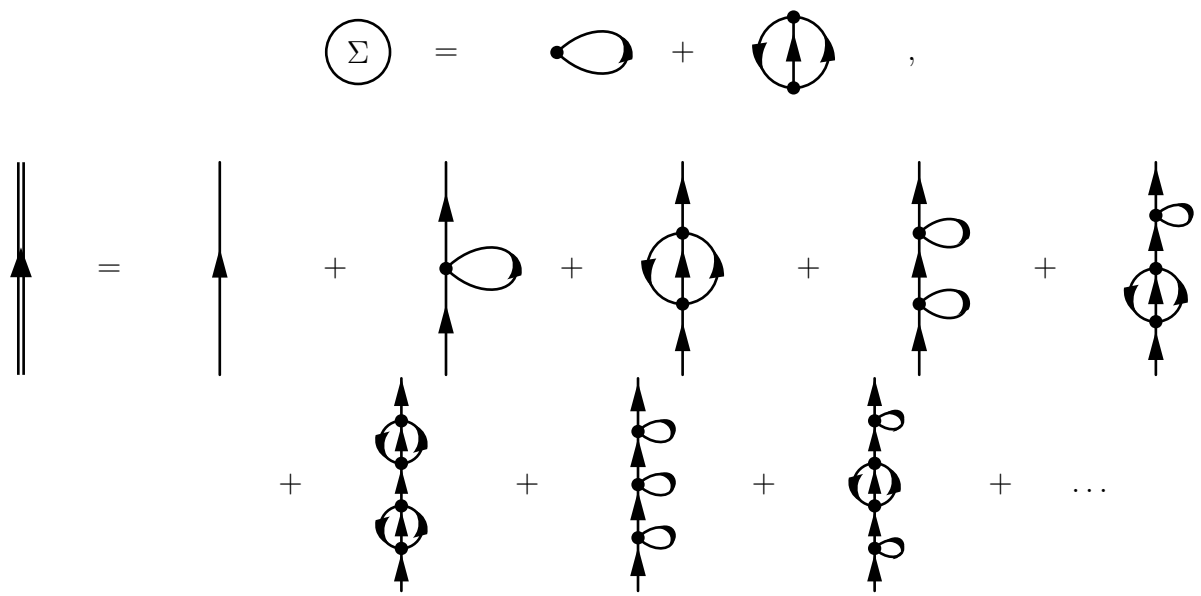

Figure 3.2. Example of an approximation of $\Sigma^{(\rho)}$ in terms of 1PI diagrams (with undressed propagators) and summed diagrams contributing to $G^{(\rho,1)}$ in this approximation.

of the problem[4]. In this case, the dressed one-body Green's function is exact if and only if the self-energy is the sum of all 2PI diagrams [11][5]. Therefore, SCGF approximations consist in truncations of the set of 2PI diagrams with dressed propagators. An example of such an approximation on the self-energy and the diagrams resummed are displayed in Fig. 3.3.

To compute the approximated one-body Green's function, the Dyson equation (3.15) together with the approximative ansatz on the self-energy are solved iteratively. Examples of such approximations are discussed in Sec. 3.3. In practice, this is done by working on the spectral functions of the one-body Green's function[6] and on the self-energy, as discussed in the Sec. 3.2.2. Before turning to that, the relation between MBPT and SCGF formalisms is made explicitly.

Relation to Many-Body Perturbation Theories

The link between MBPT and SCGF can be made explicit by decomposing the self-energy $\Sigma^{(\rho)}$ as

$$\Sigma^{(\rho)} = \Sigma^{(\rho)(0)} + \Sigma^{(\rho)(1)} + \Sigma^{(\rho)(2)} + \dots \ , \tag{3.17}$$

where $\Sigma^{(\rho)(p)}$ denotes the order p component of the self-energy i.e. the sum of all 1PI diagrams (in terms of unperturbed propagator) with p vertices[7]. Similarly, the dressed propagator is decomposed as

$$G^{(\rho,1)} = G^{(\rho,1)(0)} + G^{(\rho,1)(1)} + G^{(\rho,1)(2)} + \dots \ , \tag{3.18}$$

where $G^{(\rho,1)(p)}$ denotes the order p component of the dressed one-body propagator i.e. the sum of all diagrams (in terms of unperturbed propagator) with p vertices and one incoming/outgoing external line.[8]. Using Dyson's equation (3.15), contribution at order p in MBPT to the one-body Green's function reads recursively as

$$G^{(\rho,1)(0)} \equiv G^{(\rho,1)0} \ , \tag{3.19a}$$

$$G^{(\rho,1)(1)} \equiv G^{(\rho,1)(0)} \ \Sigma^{(\rho)(1)} \ G^{(\rho,1)(0)} \ , \tag{3.19b}$$

$$G^{(\rho,1)(2)} \equiv G^{(\rho,1)(0)} \ \Sigma^{(\rho)(2)} \ G^{(\rho,1)(0)} + G^{(\rho,1)(1)} \ \Sigma^{(\rho)(1)} \ G^{(\rho,1)0} \ , \tag{3.19c}$$

$$\dots$$

$$G^{(\rho,1)(p)} \equiv \sum_{j=1}^{p} G^{(\rho,1)(p-j)} \ \Sigma^{(\rho)(j)} \ G^{(\rho,1)0} \ . \tag{3.19d}$$

Consequently, contributions at order p in MBPT to the one-body Green's function are included in SCGF formalism for a self-energy approximated with all 1PI diagrams containing at least p vertices. In the case of a self-energy approximated in terms of 2PI diagrams with dressed propagators, formulas are more involved and are not displayed explicitly here.

[4]This is enough to compute the energy per particle thanks to the GMK sum rule (1.40).

[5]The 2PI character avoids any double counting of Feynman diagrams when iterating the Dyson equation via self-energy insertion. If *dressed vertices* are used as well (by means of a Bethe-Salpeter equation [57]) in the development of the self-energy, only skeleton diagrams are to be considered to avoid double counting [58].

[6]Unless precise otherwise, spectral function refers in the following to the one-body spectral function as defined in Eq. (1.36)

[7]The self-energy at order $p = 0$ is defined as $\Sigma^{(\rho)(0)} \equiv 0$.

[8]The dressed propagator at order $p = 0$ is defined as the unperturbed propagator ; see Eq (3.19a).

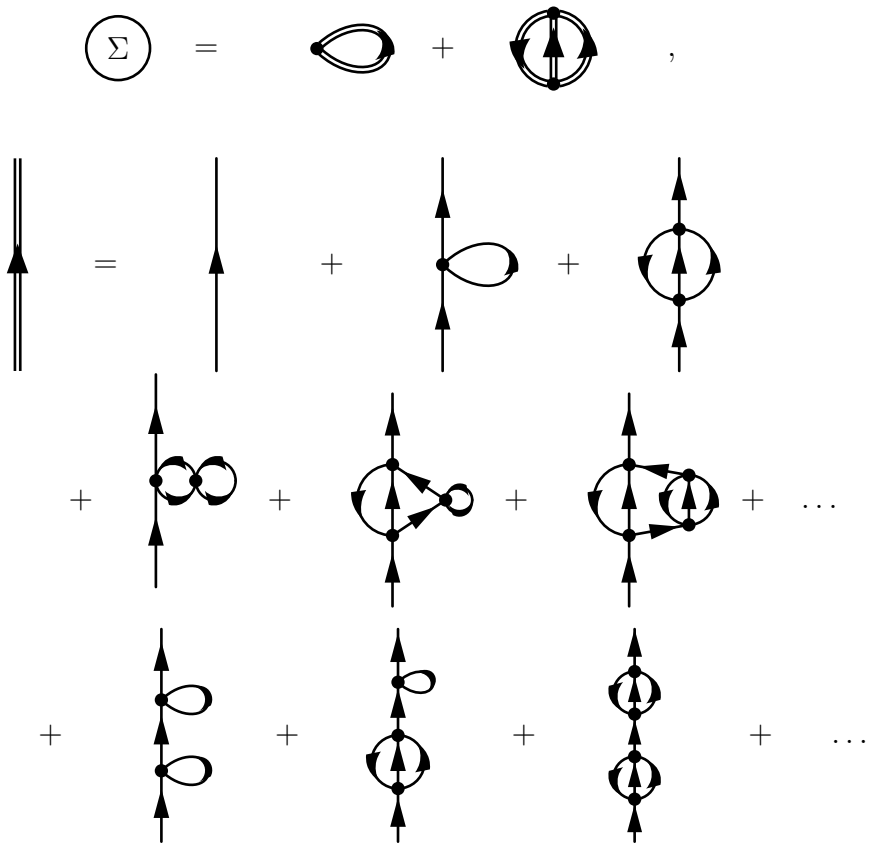

Figure 3.3. Example of an approximation of $\Sigma^{(\rho)}$ in terms of 2PI diagrams (with dressed propagators) and summed diagrams (with unperturbed diagrams) contributing to $G^{(\rho,1)}$ in this approximation.

3.2.2. Spectral function in the iterative procedure

The calculation starts with a particular ansatz on the spectral function. Typically, the initial spectral function is the unperturbed one reading from (1.35) and (1.36) as

$$S^{(\rho,1)+0}_{\vec{p}\sigma\vec{p}'\sigma'}(\omega) = \theta(p-k_F)\ (2\pi)\delta\left(\omega - \frac{p^2}{2m}\right)\ \delta_{\sigma\sigma'}\ , \tag{3.20a}$$

$$S^{(\rho,1)-0}_{\vec{p}\sigma\vec{p}'\sigma'}(\omega) = \theta(k_F-p)\ (2\pi)\delta\left(\omega - \frac{p^2}{2m}\right)\ \delta_{\sigma\sigma'}\ , \tag{3.20b}$$

$$S^{(\rho,1)0}_{\vec{p}\sigma\vec{p}'\sigma'}(\omega) = (2\pi)\delta\left(\omega - \frac{p^2}{2m}\right)\ \delta_{\sigma\sigma'}\ . \tag{3.20c}$$

Note that compared to the general case (1.35), the Fermi energies $E_0^{\pm 1}$ are presently degenerated and correspond to the unperturbed chemical potential μ^0 verifying

$$\mu^0 \equiv \frac{k_F^2}{2m}\ . \tag{3.21}$$

Using the spectral function, the imaginary part of retarded and advanced one-body Green's functions are obtained using (1.39), which leads to

$$\mathrm{Im}\, G^{(\rho,1)+}_{\vec{p}\sigma\vec{p}'\sigma'}(\omega) = -\frac{1}{2} S^{(\rho,1)}_{\vec{p}\sigma\vec{p}'\sigma'}(\omega)\ , \tag{3.22a}$$

$$\mathrm{Im}\, G^{(\rho,1)-}_{\vec{p}\sigma\vec{p}'\sigma'}(\omega) = +\frac{1}{2} S^{(\rho,1)}_{\vec{p}\sigma\vec{p}'\sigma'}(\omega)\ . \tag{3.22b}$$

Next, the real parts are obtained thanks to the dispersion relations derived from (1.39) namely

$$\mathrm{Re}\, G^{(\rho,1)+}_{\vec{p}\sigma\vec{p}'\sigma'}(\omega) = -2\ \mathcal{P}\int_{-\infty}^{+\infty} \frac{\mathrm{d}\omega'}{2\pi}\ \frac{\mathrm{Im}\, G^{(\rho,1)+}_{\vec{p}\sigma\vec{p}'\sigma'}(\omega')}{\omega-\omega'}\ , \tag{3.23a}$$

$$\mathrm{Re}\, G^{(\rho,1)-}_{\vec{p}\sigma\vec{p}'\sigma'}(\omega) = +2\ \mathcal{P}\int_{-\infty}^{+\infty} \frac{\mathrm{d}\omega'}{2\pi}\ \frac{\mathrm{Im}\, G^{(\rho,1)-}_{\vec{p}\sigma\vec{p}'\sigma'}(\omega')}{\omega-\omega'}\ . \tag{3.23b}$$

Given a truncation for the self-energy $\Sigma^{(\rho)}$, its real and imaginary parts are computed using the one-body Green's function derived in the previous step. Eventually, the new spectral function is actualized using Dyson's equation, which leads to

$$S^{(\rho,1)}_{\vec{p}\sigma\vec{p}'\sigma'}(\omega) = \frac{-2\,\mathrm{Im}\,\Sigma^{(\rho)+}_{\vec{p}\sigma\vec{p}'\sigma'}(\omega)}{\left[\omega - \frac{p^2}{2m} - \mathrm{Re}\,\Sigma^{(\rho)+}_{\vec{p}\sigma\vec{p}'\sigma'}(\omega)\right]^2 + \left[\mathrm{Im}\,\Sigma^{(\rho)+}_{\vec{p}\sigma\vec{p}'\sigma'}(\omega)\right]^2}\ (2\pi)^3\delta\left(\vec{p}-\vec{p}'\right)\ , \tag{3.24}$$

where $\Sigma^{(\rho)+}$ corresponds to the retarded self-energy, defined in analogy with the retarded one-body Green's function.

At this level, and before iterating further with the new spectral function computed in (3.24),

the chemical potential[9] μ is adjusted to obtain the targeted density ρ_0 using

$$n(\vec{p})_0 = \sum_{\sigma} \int_{-\infty}^{+\infty} \frac{\mathrm{d}\omega}{2\pi} \; S^{(\rho,1)}_{\vec{p}\sigma\vec{p}\sigma}(\omega)\theta\left(\mu - \omega\right) \;, \tag{3.25a}$$

$$\rho_0 = \int \frac{\mathrm{d}^3\vec{p}}{(2\pi)^3} \; n(\vec{p})_0 \;. \tag{3.25b}$$

Note that (3.25), by updating the chemical potential, enables to disentangle the hole and the particle component of the spectral function as

$$S^{(\rho,1)+}_{\vec{p}\sigma\vec{p}\sigma}(\omega) = S^{(\rho,1)}_{\vec{p}\sigma\vec{p}\sigma}(\omega)\theta\left(\omega - \mu\right) \;, \tag{3.26a}$$

$$S^{(\rho,1)-}_{\vec{p}\sigma\vec{p}\sigma}(\omega) = S^{(\rho,1)}_{\vec{p}\sigma\vec{p}\sigma}(\omega)\theta\left(\mu - \omega\right) \;. \tag{3.26b}$$

The different steps in the iterative procedure are recapitulated in Tab. 3.1. To fully define an approximation in a SCGF framework, one needs to specify the approximation on the self-energy. In the following section, Hartree-Fock, 2nd Born and ladder approximations, which are used in the numerical calculations presented in Sec. 3.4, are introduced.

3.3. Self-energy approximations

Approximations considered here are based on a truncation of the set of dressed Feynman diagrams.

3.3.1. Hartree-Fock approximation

The Hartree-Fock (HF) approximation consists in the first order (in term of number of vertices) contribution to the self-energy. The HF self-energy is non-zero only for $t = t'$ which is why it is characterized as instantaneous. Consequently, the energy representation is actually energy independent. Evaluating the Feynman amplitude of diagrams in Fig. 3.4, the Hartree-Fock self-energy reads as

$$\Sigma^{(\rho)\mathrm{HF}}_{\vec{p}_1\sigma_1\vec{p}_1'\sigma_1'}(t,t') = \sum_{\sigma\sigma'}\sum_{\vec{p}\vec{p}'} h^{22}_{\vec{p}_1\vec{p}\vec{p}_1'\vec{p}} \; s^{22}_{\sigma_1\sigma\sigma_1'\sigma'} \; (-i)G^{(\rho,1)}_{\vec{p}'\sigma'\vec{p}\sigma}(t,t^+) \; \delta(t-t') \;, \tag{3.27}$$

which gives in the energy representation

$$\Sigma^{(\rho)\mathrm{HF}}_{\vec{p}_1\sigma_1\vec{p}_1'\sigma_1'} = \left(\delta_{\sigma_1\sigma_1'}\sum_{\vec{p}} h^{22}_{\vec{p}_1\vec{p}\vec{p}_1'\vec{p}} \; n(\vec{p})_0 - \sum_{\vec{p}} \; h^{22}_{\vec{p}_1\vec{p}\vec{p}\vec{p}_1'} \; iG^{(\rho,1)}_{\vec{p}\sigma_1\vec{p}\sigma_1'}(t,t^+)\right) \; (2\pi)^3\delta\left(\vec{p}_1 - \vec{p}_1'\right) \;, \tag{3.28}$$

where the first (second) term in (3.28) corresponds to the direct (exchange) contribution. Comparing with the perturbation theory developed in Chap. 2, at first order there are already loop diagrams contributing to k-body Green's functions. Furthermore, exchange and direct contributions are no longer identical. This is due to the presence of a hole component in the one-body Green's function (dressed or unperturbed).

[9] If the spectral function is iterated, at fixed $\mu = \mu^0$, the density is in general modified and does not match the targeted one anymore.

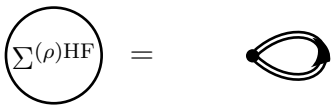

Figure 3.4. Diagrams contributing to $\Sigma^{(\rho)\mathrm{HF}}$ in terms of dressed propagators.

As the initial Green's function considered in the iteration (the unperturbed one) is diagonal in spin-isospin and in momentum space, and given that the two-body interaction is spin- and isospin-independent and conserves the total momentum, the dressed propagator obtained after any number of iterations verifies

$$G^{(\rho,1)}_{\vec{p}\sigma\vec{p}'\sigma'}(t,t') \equiv G^{(\rho,1)}_{\vec{p}\sigma}(t,t')\ (2\pi)^3\delta(\vec{p}-\vec{p}')\ \delta_{\sigma\sigma'}\ . \tag{3.29a}$$

Similarly, the self-energy and the spectral function can also be reduced to their diagonal part i.e.

$$\Sigma^{(\rho)}_{\vec{p}\sigma\vec{p}'\sigma'}(\omega) \equiv \Sigma^{(\rho)}_{\vec{p}\sigma}(\omega)\ (2\pi)^3\delta(\vec{p}-\vec{p}')\ \delta_{\sigma\sigma'}\ , \tag{3.29b}$$

$$S^{(\rho,1)}_{\vec{p}\sigma\vec{p}'\sigma'}(\omega) \equiv S^{(\rho,1)}_{\vec{p}\sigma}(\omega)\ (2\pi)^3\delta(\vec{p}-\vec{p}')\ \delta_{\sigma\sigma'} \tag{3.29c}$$

Consequently, (3.28) further simplifies to

$$\Sigma^{(\rho)\mathrm{HF}}_{\vec{p}_1\sigma_1} = \left(\sum_{\vec{p}} h^{22}_{\vec{p}_1\vec{p}\vec{p}_1\vec{p}}\ n(\vec{p})_0 - \sum_{\vec{p}}\ h^{22}_{\vec{p}_1\vec{p}\vec{p}\vec{p}_1}\ iG^{(\rho,1)}_{\vec{p}\sigma_1}(t,t^+)\right)\ . \tag{3.30}$$

In the HF approximation, the dressed one-body Green's function $G^{(\rho,1)\mathrm{HF}}$ can be computed easily as the self-energy is energy independent. From Dyson's equation (3.16),

$$\left(G^{(\rho,1)\mathrm{HF}}\right)^{-1} = \left(G^{(\rho,1)0}\right)^{-1} - \Sigma^{(\rho)\mathrm{HF}}\ , \tag{3.31}$$

so that

$$G^{(\rho,1)\mathrm{HF}}_{\vec{p}\sigma}(\omega) = \frac{\theta\left(p-k_F\right)}{\omega - e^{\mathrm{HF}}_{\vec{p}\sigma} + i\eta} + \frac{\theta\left(k_F-p\right)}{\omega - e^{\mathrm{HF}}_{\vec{p}\sigma} - i\eta}\ , \tag{3.32}$$

where

$$e^{\mathrm{HF}}_{\vec{p}\sigma} \equiv \frac{p^2}{2m} + \Sigma^{(\rho)\mathrm{HF}}_{\vec{p}\sigma}\ . \tag{3.33}$$

In the HF approximation, the one-body Green's function is the same as the unperturbed one with modified single-particle energies $e^{\mathrm{HF}}_{\vec{p}\sigma}$.

3.3.2. Second Born approximation

The 2nd Born approximation sums all diagrams at 1st and 2nd order contributing to the self-energy. Diagrams contributing in 2nd Born approximation are represented in Fig. 3.5. The

Figure 3.5. Diagrams contributing to $\Sigma^{(\rho)2\mathrm{B}}$ in terms of dressed propagators.

self-energy reads, in the energy representation, as

$$\begin{aligned}\Sigma^{(\rho)2\mathrm{B}}_{\vec{p}\sigma}(\omega) = \Sigma^{(\rho)\mathrm{HF}}_{\vec{p}\sigma} \\ + \frac{(-i)}{2!}\frac{1}{2}\sum_{\sigma_1\sigma_2\sigma_3}\sum_{\vec{l}_1\vec{l}_2}\int_{-\infty}^{+\infty}\frac{\mathrm{d}\omega_1}{2\pi}\frac{\mathrm{d}\omega_2}{2\pi}\, h^{22}_{(\frac{\vec{p}}{2}+\vec{l}_1)(\frac{\vec{p}}{2}-\vec{l}_2)(\vec{p})(\vec{l}_2-\vec{l}_1)}\, s^{22}_{\sigma_1\sigma_2\sigma\sigma_3} \\ \times\, iG^{(\rho,1)}_{\frac{\vec{p}}{2}+\vec{l}_1\ \sigma_1}\left(\frac{\omega}{2}+\omega_1\right) iG^{(\rho,1)}_{\frac{\vec{p}}{2}-\vec{l}_2\ \sigma_2}\left(\frac{\omega}{2}-\omega_1\right) \\ \times\, iG^{(\rho,1)}_{\vec{l}_2-\vec{l}_1\ \sigma_3}(\omega_2-\omega_1)\, h^{22}_{(\vec{p})(\vec{l}_2-\vec{l}_1)(\frac{\vec{p}}{2}+\vec{l}_1)(\frac{\vec{p}}{2}-\vec{l}_2)} s^{22}_{\sigma\sigma_3\sigma_1\sigma_2}\ .\end{aligned} \tag{3.34}$$

Contrary to the Hartree-Fock case, $\Sigma^{(\rho)2\mathrm{B}}$ is not independent of the energy and is complex-valued. Both are general features of the self-energy. In general, the energy-dependent part of the self-energy $\Sigma^{(\rho)}_d(\omega)$ is referred to as the dynamic self-energy while the energy independent part $\Sigma^{(\rho)}_s \equiv \Sigma^{(\rho)\mathrm{HF}}$ is referred to as the static self energy, i.e.

$$\Sigma^{(\rho)}(\omega) = \Sigma^{(\rho)}_s + \Sigma^{(\rho)}_d(\omega)\ . \tag{3.35}$$

Following from the Dyson equation (3.15) and the analytic properties of the one-body Green's function, the self-energy verifies, in the approximations considered in this thesis and in the exact case, the dispersion relations [59]

$$\mathrm{Re}\,\Sigma^{(\rho)+}_{\vec{p}\sigma\vec{p}'\sigma'}(\omega) = \Sigma^{(\rho)\mathrm{HF}}_{\vec{p}\sigma\vec{p}'\sigma'} - 2\,\mathcal{P}\int_{-\infty}^{+\infty}\frac{\mathrm{d}\omega'}{2\pi}\,\frac{\mathrm{Im}\,\Sigma^{(\rho)+}_{\vec{p}\sigma\vec{p}'\sigma'}(\omega')}{\omega-\omega'}\ , \tag{3.36a}$$

$$\mathrm{Re}\,\Sigma^{(\rho)-}_{\vec{p}\sigma\vec{p}'\sigma'}(\omega) = \Sigma^{(\rho)\mathrm{HF}}_{\vec{p}\sigma\vec{p}'\sigma'} + 2\,\mathcal{P}\int_{-\infty}^{+\infty}\frac{\mathrm{d}\omega'}{2\pi}\,\frac{\mathrm{Im}\,\Sigma^{(\rho)-}_{\vec{p}\sigma\vec{p}'\sigma'}(\omega')}{\omega-\omega'}\ . \tag{3.36b}$$

In practice, the HF self-energy and the imaginary part of the dynamic self-energy are first computed. The real part of the self energy is then evaluated using (3.36).

3.3.3. Ladder approximation

Eventually, the last approximation considers calculations based on SCGF is the ladder or T-matrix approximation. The ladder approximation consists in summing all ladder diagrams as shown in Fig. 3.6. The ladder approximation is of great interest for calculating observables of

Figure 3.6. Diagrams contributing to $\Sigma^{(\rho)\mathrm{L}}$ in terms of dressed propagators.

infinite nuclear matter. Analogously to HF and 2nd Born approximations, it has the advantage of keeping thermodynamic consistency. Furthermore, in terms of Feynman diagrams, the ladder approximation resums all-order two-body scattering vertices, traditionally important to handle the strong repulsive core of the nuclear interaction [60]. Regarding $\not\pi$EFT power counting at LO, it does not meet in general the requirement of exactly computing the self-energy. However, observables computed in the two-body sector within the ladder approximation are indeed exact. This motivates further investigations on both the renormalization of the ladder approximation and on its accuracy to compute nuclear observables.

In practice, one first computes the (in-medium) T-matrix defined as the solution of the implicit equation represented diagrammatically in Fig. 3.7. Conservation of the total momentum and the factorization of the spin components as in Sec. 2.2 allow one to use the shorthand notation

$$T^{(\rho)}_{\substack{\vec{p}_1\sigma_1\vec{p}_2\sigma_2\\ \vec{p}_1{}'\sigma_1'\vec{p}_2{}'\sigma_2'}}(\omega) \equiv T^{(\rho)}_{\vec{P}\ \vec{q}\vec{q}'}(\omega)\ s^{22}_{\sigma_1\sigma_2\sigma_1'\sigma_2'}\ (2\pi)^3\delta(\vec{p}_1+\vec{p}_2-\vec{p}_1{}'-\vec{p}_2{}')\ , \tag{3.37}$$

where $\vec{P}$, $\vec{q}$ and $\vec{q}'$ are the total and relative momenta defined in (2.8).

With these notations, the implicit equation satisfied by the T-matrix reads as

$$T^{(\rho)}_{\vec{P}\ \vec{q}\vec{q}'}(\omega) = h^{22}_{\vec{q}'\vec{q}} + \frac{(-i)}{2}\int_{-\infty}^{\infty}\frac{\mathrm{d}\omega_l}{2\pi}\int\frac{\mathrm{d}^3\vec{l}}{(2\pi)^3}\ h^{22}_{\vec{q}\ \vec{l}}\,G^{(\rho,1)}_{\vec{P}+\vec{l}}\left(\frac{\omega}{2}+\omega_l\right)G^{(\rho,1)}_{\vec{P}-\vec{l}}\left(\frac{\omega}{2}-\omega_l\right)\ T^{(\rho)}_{\vec{P}\ \vec{l}\vec{q}'}(\omega)\ . \tag{3.38}$$

Eventually, the self-energy is computed from the closure (by one dressed propagator) of the T-matrix i.e.

$$\Sigma^{(\rho)\mathrm{L}}_{\vec{p}\sigma}(\omega) = \sum_{\sigma'}\sum_{\vec{p}'}\int\frac{\mathrm{d}\omega}{2\pi}\ T^{(\rho)}_{\frac{\vec{p}+\vec{p}'}{2}\ \frac{\vec{p}-\vec{p}'}{2}\ \frac{\vec{p}-\vec{p}'}{2}}(\omega+\omega')\ s^{22}_{\sigma\sigma'\sigma\sigma'}\ iG^{(\rho,1)}_{\vec{p}'\sigma'}(\omega')\ , \tag{3.39}$$

which is represented diagrammatically in Fig. 3.8. As for the 2nd Born approximation, in practical calculations, only the imaginary part of the retarded/advanced self-energy are computed before using the dispersion relations (3.36) to access the real part.

3.3.4. Renormalization in self-consistent Green's functions

Many-body calculations within SCGF theory rely on approximations of the equation of motions for k-body Green's functions. In the three different approximations considered above, the fact that the self-energy is approximated via the sum of dressed Feynman amplitudes allows

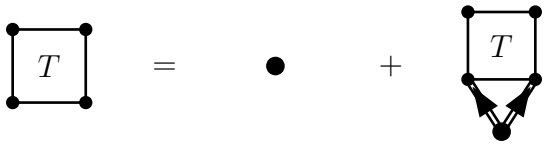

Figure 3.7. Diagrammatic representation of the self-consistent equation satisfied by the T-matrix.

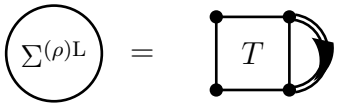

Figure 3.8. Diagrammatic representation of the relation between the Self-energy $\Sigma^{(\rho)\mathrm{L}}$ and the T-matrix.

one to make a direct connection to Feynman diagrams introduced in Chap. 1. While MBPT calculations of the one-body Green's function at order n consist of summing all Feynman diagrams with at most n vertices, the three approximations above can be restated as a resummation of an infinite number of Feynman diagrams expressed in terms of the unperturbed propagator used in MBPT diagrams. For example, typical Feynman diagrams with unperturbed propagators contributing to the 2nd Born approximation are represented in Fig. 3.3.

The re-expression of such approximations in terms of unperturbed Feynman diagrams allows one to study explicit UV divergences that can occur. This has been thoroughly studied in the particular case of Φ-derivable approximations [11, 51, 61, 62, 63] for a relativistic ϕ^4 theory [64, 65, 66, 67, 68]. The main outcome of such studies is that additional counter-terms can be necessary to renormalize the interaction compared to the naïve renormalization obtained by using equivalent diagrams but with unperturbed propagators in the particle vacuum. However, it is still unclear whether such a conclusion holds in the case of a non-relativistic theory such as $\not{\pi}$EFT. For example, a dressed (or unperturbed) hole propagator has no obvious counterpart in the perturbation theory employing the particle vacuum as the reference state. Hence, it would be of interest to extend such studies to the non-relativistic case, in view of developing consistently renormalized calculations of observables in $\not{\pi}$EFT within e.g. a SCGF framework. To the best of our knowledge, such analytical investigations are yet to be done. As a first step into that direction, numerical investigations can provide new insight into the renormalization of the $H_{\not{\pi}}$ for many-body observables computed in a SCGF framework.

In the next section, numerical calculations are detailed. After introducing the close set of equations to be solved consistently, emphasis is put on the numerical approximations necessary for practical calculations. Eventually, numerical results are discussed.

3.4. Numerical computations

3.4.1. Self-consistent Green's function numerical scheme

The HF, 2nd Born and ladder approximations can all be recast as three different approximations of the T-matrix. The HF consists in taking into account only the first diagram (a simple vertex) in Fig. 3.7. The 2nd Born approximation truncates the T-matrix at second order i.e. only the simple vertex and the one-loop diagrams contribute to the T-matrix. The ladder approximation takes into account the T-matrix solving exactly Fig. 3.7. In this section the close set of equation solved numerically is made explicit for the exact T-matrix. HF and 2nd Born approximations are then retrieved by only adapting the equation used to compute the T-matrix.

Following Sec. 3.2.2 the imaginary and real parts of the dressed one-body Green's function are computed from Eq. (3.22) and Eq. (3.23). Then, the T-matrix must be computed using Eq. (3.38) with the consistently dressed propagator. In practice the T-matrix is derived from the spectral function by computing the retarded two-time reduced two-body Green's function $G^{(\rho,2)+}$ as an intermediate object. $G^{(\rho,2)+}$ and the spectral function $S^{(\rho,1)}$ are related in the energy representation via

$$\operatorname{Im} G^{(\rho,2)+}_{\substack{\vec{p}_1\sigma_1\vec{p}_2\sigma_2\\ \vec{p}_1\sigma_1\vec{p}_2\sigma_2}}(\Omega) = -\frac{1}{2}\int_{-\infty}^{+\infty}\frac{\mathrm{d}\omega}{2\pi}\; S^{(\rho,1)}_{\vec{p}_1\sigma_1}(\omega)S^{(\rho,1)}_{\vec{p}_2\sigma_2}(\Omega-\omega)\;\left[1-\theta(\mu-\omega)-\theta\left(\mu-(\Omega-\omega)\right)\right]\;, \tag{3.40}$$

whereas the real part reads from the dispersion relation as

$$\operatorname{Re} G^{(\rho,2)+}_{\substack{\vec{p}_1\sigma_1\vec{p}_2\sigma_2\\ \vec{p}_1\sigma_1\vec{p}_2\sigma_2}}(\Omega) = -2\,\mathcal{P}\int_{-\infty}^{+\infty}\frac{\mathrm{d}\Omega'}{2\pi}\;\frac{\operatorname{Im} G^{(\rho,2)+}_{\substack{\vec{p}_1\sigma_1\vec{p}_2\sigma_2\\ \vec{p}_1\sigma_1\vec{p}_2\sigma_2}}(\Omega')}{\Omega-\Omega'}\;. \tag{3.41}$$

Then Eq. (3.38) is reformulated in terms of the two-time reduced two-body Green's function integrated on the angle of the relative momentum and the energy $\mathscr{G}^{(\rho,2)+}$, namely

$$\mathscr{G}^{(\rho,2)+}_{\vec{P}\;qq'}(\Omega)\;\delta_{\sigma_1\sigma_1'}\delta_{\sigma_2\sigma_2'}\;(2\pi^2)\delta\left(q-q'\right) \equiv \int_{-1}^{+1}\mathrm{d}\left(\cos\theta\right)G^{(\rho,2)+}_{\substack{\vec{p}_1\sigma_1\vec{p}_2\sigma_2\\ \vec{p}_1'\sigma_1'\vec{p}_2\sigma_2'}}(\Omega)\;, \tag{3.42}$$

where θ denotes the angle between the total momentum $\vec{P}$ and the relative momentum $\vec{q}$. As in Sec. 2.2.3 the retarded T-matrix is solution of the matrix equation (at fixed total momentum $\vec{P}$ and total energy Ω)[10]

$$T^{(\rho)+}_{\vec{P}}(\Omega) = h^{22}_{\Lambda} + h^{22}_{\Lambda}\mathscr{G}^{(\rho,2)+}_{\vec{P}}(\Omega)T^{(\rho)+}_{\vec{P}}(\Omega)\;, \tag{3.43}$$

which is solved by matrix inversion. In Eq. (3.43) matrix notations are used for the retarded T-matrix $T^{(\rho)+}_{\vec{P}}(\Omega)$, the interaction potential h^{22} and the integrated two-time reduced two-body

[10]The spin trace is compensated by the symmetry $\frac{1}{2}$ due to the two equivalent lines in the loop.

Green's function $\mathscr{G}^{(\rho,2)+}_{\vec{P}}(\Omega)$, i.e.

$$\left(T^{(\rho)+}_{\vec{P}}(\Omega)\right)_{qq'} \equiv T^{(\rho)+}_{\vec{P}\ qq'}(\Omega) \ , \tag{3.44a}$$

$$\left(\mathscr{G}^{(\rho,2)+}_{\vec{P}}(\Omega)\right)_{qq'} \equiv \mathscr{G}^{(\rho,2)+}_{\vec{P}\ qq'}(\Omega) \ , \tag{3.44b}$$

$$\left(h^{22}_{\Lambda}\right)_{qq'} \equiv h^{22}_{\Lambda\ qq'} \ . \tag{3.44c}$$

The retarded self-energy follows from Eq. (3.39) which, expressed in terms of the retarded T-matrix and of the spectral function $S^{(\rho,1)}$ reads for the imaginary part as

$$\begin{aligned}\mathrm{Im}\,\Sigma^{(\rho)+}_{\vec{p}\sigma}(\omega) = \frac{1}{2}\sum_{\sigma'}\sum_{\vec{p}'}\int_{-\infty}^{+\infty}\frac{\mathrm{d}\omega'}{2\pi}\,\mathrm{Im}\,T^{(\rho)+}_{\frac{(\vec{p}+\vec{p}')}{2})\ (\frac{\vec{p}-\vec{p}'}{2})(\frac{\vec{p}-\vec{p}'}{2})}(\omega+\omega') \\ \times\, s^{22}_{\sigma\sigma'\sigma\sigma'}\ S^{(\rho,1)}_{\vec{p}'\sigma'}(\omega')\left[\theta(\mu-\omega')-\theta(2\mu-(\omega+\omega'))\right] \ .\end{aligned} \tag{3.45}$$

The real part of the retarded self-energy follows from the dispersion relation (3.36) and the HF part computed directly from the spectral function by rewriting Eq. (3.30)

$$\Sigma^{(\rho)\mathrm{HF}}_{\vec{p}\sigma} = \frac{1}{2}\sum_{\vec{p}'}\sum_{\sigma'}\int_{-\infty}^{+\infty}\frac{\mathrm{d}\omega'}{2\pi}\ h^{22}_{\Lambda\ \vec{p}\vec{p}'\vec{p}\vec{p}'}\ S^{(\rho,1)}_{\vec{p}'\sigma'}(\omega')\ \theta(\mu-\omega') \ . \tag{3.46}$$

Eventually, from the retarded self-energy, the spectral function is actualized using (3.24) and the chemical potential is actualized using (3.25). The global set of equations to be solved is displayed in Tab. 3.1. All those equations are solved self-consistently i.e. iteratively until the spectral function $S^{(\rho,1)}$, the retarded T-matrix $T^{(\rho)+}$, the retarded self-energy $\Sigma^{(\rho)+}$ and the chemical potential μ reach convergence.

Equations in Tab. 3.1 can only be solved numerically and require numerical approximations. Such approximations are detailed in the next section.

3.4.2. Numerical approximations

Equations in Tab. 3.1 are solved numerically by a Fortran code. Such a code relies on three main numerical approximations which are briefly discussed here as they play an important role when attempting to draw conclusions about the consistency of the renormalization of $H_{\not\pi}$ through the calculation of the energy per particle of infinite neutron matter. Further discussions about the numerical aspects of codes can be found in [69, 70, 12, 71, 72].

The first numerical approximation consists in the discretization of the continuous integrals on the energy and on the momenta e.g. in Eq. (3.45). This is done by introducing discretization steps Δ_p, Δ_θ and Δ_ω respectively on the momentum modulus, the angle between the relative and the total momentum and on the energy. Additionally, numerical cut-offs C_p and C_ω are necessary to terminate the infinite integrals on momenta and energies. For example, the integral on the energy of a generic function $f(\omega)$ is realized numerically as

$$\int_{-\infty}^{+\infty}\frac{\mathrm{d}\omega}{2\pi}\ f(\omega) \longleftrightarrow \sum_{i=-\frac{C_\omega}{\Delta_\omega}}^{+\frac{C_\omega}{\Delta_\omega}}\frac{\Delta_\omega}{2\pi}\ f\left(i\times\Delta_\omega\right) \ . \tag{3.47}$$

Fixed	Step	Eq.	Instruction
μ and $S^{(\rho,1)}$	1	(3.40)	$\operatorname{Im} G^{(\rho,2)+}_{\substack{\vec{p}_1\sigma_1\vec{p}_2\sigma_2\\ \vec{p}_1\sigma_1\vec{p}_2\sigma_2}}(\Omega) = -\frac{1}{2}\int_{-\infty}^{+\infty}\frac{\mathrm{d}\omega}{2\pi}\, S^{(\rho,1)}_{\vec{p}_1\sigma_1}(\omega) S^{(\rho,1)}_{\vec{p}_2\sigma_2}(\Omega-\omega) \times \left[1-\theta(\mu-\omega)-\theta\left(\mu-(\Omega-\omega)\right)\right]$
	2	(3.41)	$\operatorname{Re} G^{(\rho,2)+}_{\substack{\vec{p}_1\sigma_1\vec{p}_2\sigma_2\\ \vec{p}_1\sigma_1\vec{p}_2\sigma_2}}(\Omega) = -2\,\mathcal{P}\int_{-\infty}^{+\infty}\frac{\mathrm{d}\Omega'}{2\pi}\,\frac{\operatorname{Im} G^{(\rho,2)+}_{\substack{\vec{p}_1\sigma_1\vec{p}_2\sigma_2\\ \vec{p}_1\sigma_1\vec{p}_2\sigma_2}}(\Omega')}{\Omega-\Omega'}$
	3	(3.42)	$\mathscr{G}^{(\rho,2)+}_{\vec{P}\ qq'}(\Omega)\ \delta_{\sigma_1\sigma_1'}\delta_{\sigma_2\sigma_2'}\ (2\pi^2)\delta\left(q-q'\right) = \int_{-1}^{+1}\mathrm{d}\left(\cos\theta\right) G^{(\rho,2)+}_{\substack{\vec{p}_1\sigma_1\vec{p}_2\sigma_2\\ \vec{p}_1'\sigma_1'\vec{p}_2\sigma_2'}}(\Omega)$
	4	(3.43)	$T^{(\rho)+}_{\vec{P}}(\Omega) = h^{22}_{\Lambda} + h^{22}_{\Lambda}\,\mathscr{G}^{(\rho,2)+}_{\vec{P}}(\Omega)\ T^{(\rho)+}_{\vec{P}}(\Omega)$
	5	(3.45)	$\operatorname{Im}\Sigma^{(\rho)+}_{\vec{p}\sigma}(\omega) = \frac{1}{2}\sum_{\sigma'}\sum_{\vec{p}'}\int_{-\infty}^{+\infty}\frac{\mathrm{d}\omega'}{2\pi}\operatorname{Im} T^{(\rho)+}_{\frac{(\vec{p}+\vec{p}')}{2})\ (\frac{\vec{p}-\vec{p}'}{2})(\frac{\vec{p}-\vec{p}'}{2})}(\omega+\omega') \times s^{22}_{\sigma\sigma'\sigma\sigma'}\ S^{(\rho,1)}_{\vec{p}'\sigma'}(\omega')\left[\theta(\mu-\omega')-\theta(2\mu-(\omega+\omega'))\right]$
	6	(3.46)	$\Sigma^{(\rho)\mathrm{HF}}_{\vec{p}\sigma} = \frac{1}{2}\sum_{\vec{p}'}\sum_{\sigma'}\int_{-\infty}^{+\infty}\frac{\mathrm{d}\omega'}{2\pi}\ h^{22}_{\Lambda\ \vec{p}\vec{p}'\vec{p}\vec{p}'}\ S^{(\rho,1)}_{\vec{p}'\sigma'}(\omega')\ \theta(\mu-\omega')$
	7	(3.36)	$\operatorname{Re}\Sigma^{(\rho)+}_{\vec{p}\sigma\vec{p}'\sigma'}(\omega) = \Sigma^{(\rho)\mathrm{HF}}_{\vec{p}\sigma\vec{p}'\sigma'} - 2\,\mathcal{P}\int_{-\infty}^{+\infty}\frac{\mathrm{d}\omega'}{2\pi}\,\frac{\operatorname{Im}\Sigma^{(\rho)+}_{\vec{p}\sigma\vec{p}'\sigma'}(\omega')}{\omega-\omega'}$
$\Sigma^{(\rho)+}$	8	(3.24)	$S^{(\rho,1)}_{\vec{p}\sigma}(\omega) = \frac{-2\operatorname{Im}\Sigma^{(\rho)+}_{\vec{p}\sigma}(\omega)}{\left[\omega-\frac{p^2}{2m}-\operatorname{Re}\Sigma^{(\rho)+}_{\vec{p}\sigma}(\omega)\right]^2+\left[\operatorname{Im}\Sigma^{(\rho)+}_{\vec{p}\sigma}(\omega)\right]^2}$
$T^{(\rho)+}$	9	(3.25)	$\rho_0 = \sum_{\sigma}\int\frac{\mathrm{d}^3\vec{p}}{(2\pi)^3}\int_{-\infty}^{+\infty}\frac{\mathrm{d}\omega}{2\pi}\ S^{(\rho,1)}_{\vec{p}\sigma}(\omega)\theta\left(\mu-\omega\right)$

Table 3.1. Self-consistent equations solved numerically in the self-consistent ladder scheme.

Furthermore, in the case of a general potential, an angle-averaging approximation is introduced on the two-time reduced two-body Green's function. This enables to decouple partial-wave contributions in (3.43) by replacing $G^{(\rho,2)}_{\vec{p}\sigma\vec{p}'\sigma'}(\omega)$ in the T-matrix calculation by

$$\bar{G}^{(\rho,2)}_{\vec{P}q\sigma\sigma'}(\omega) \equiv \frac{1}{2}\int_{-1}^{+1} \mathrm{d}\left(\cos\theta\right)\ G^{(\rho,2)}_{(\vec{P}+\vec{q})\sigma(\vec{P}-\vec{q})\sigma'}(\omega)\ , \tag{3.48}$$

which depends only on the total momentum $\vec{P}$, the module of the relative momentum q and spin indices σ, σ'. A more detailed discussion on the angle-averaging procedure can be found in [70, 71]. This is a common approximation in SCGF codes that has been checked to lead to minor errors of the computed energy in [73, 74, 75]. However, it is not clear if the angle-averaging approximation affects or not the renormalization invariance of the energy per particle.

Eventually, in numerical applications of SCGF code, a key problem is to deal with the stiffness of the spectral function $S^{(\rho,1)}$ around the Fermi surface. Indeed, the spectral function diplays in most cases a peak characterizing a quasi-particle behaviour [69, 72, 71, 70, 12]. Numerically different strategies have been implemented. In this thesis the code uses a decomposition of the spectral function in a quasi-particle and a background component [69, 70] i.e. as

$$S^{(\rho,1)}_{\vec{p}\sigma}(\omega) \equiv B^{(\rho,1)}_{\vec{p}\sigma}(\omega) + Z_p(2\pi)\delta\left(\omega-\omega_p\right)\ , \tag{3.49}$$

where $B^{(\rho,1)}$ denotes the background spectral function, ω_p the position of the quasiparticle peak and Z_p the strength of the peak. This decomposition is controlled by an external parameter s as

$$B^{(\rho,1)}_{\vec{p}\sigma}(\omega) = \begin{cases} \frac{-2\,\mathrm{Im}\,\Sigma^{(\rho)+}_{\vec{p}\sigma}(\omega)}{\left(\omega-\frac{p^2}{2m}-\mathrm{Re}\,\Sigma^{(\rho)+}_{\vec{p}\sigma}(\omega)\right)^2+\left(\mathrm{Im}\,\Sigma^{(\rho)+}_{\vec{p}\sigma}(\omega)\right)^2} & \text{if } \left(\omega-\frac{p^2}{2m}-\mathrm{Re}\,\Sigma^{(\rho)+}_{\vec{p}\sigma}(\omega)\right)^2+\left(\mathrm{Im}\,\Sigma^{(\rho)+}_{\vec{p}\sigma}(\omega)\right)^2 \geq s \\ \frac{-2\,\mathrm{Im}\,\Sigma^{(\rho)+}_{\vec{p}\sigma}(\omega)}{s} & \text{if } \left(\omega-\frac{p^2}{2m}-\mathrm{Re}\,\Sigma^{(\rho)+}_{\vec{p}\sigma}(\omega)\right)^2+\left(\mathrm{Im}\,\Sigma^{(\rho)+}_{\vec{p}\sigma}(\omega)\right)^2 < s \end{cases} . \tag{3.50}$$

At fixed $\vec{p}$, a quasiparticle peak is introduced if the threshold s is reached for a certain ω. In this case, the position of the peak ω_p is defined as the solution of

$$\omega_p \equiv \frac{p^2}{2m} + \mathrm{Re}\,\Sigma^{(\rho)+}_{\vec{p}\sigma}(\omega_p)\ , \tag{3.51}$$

and the strength Z_p is adapted such that the one-body spectral function verifies the sum rule (1.37).

With the numerical approximations introduced in this section the equations can be solved numerically by iterating equations in Tab. 3.1 until convergence is reached. In the next section, numerical results are discussed on the renormalization invariance of the energy per particle computed in the approximations introduced in Sec. 3.3.

3.4.3. Numerical results

Numerical convergence

In order to assess the numerical accuracy of the code, the convergence of the energy per particle with increasing numerical precision must be checked. To ensure the validity of the

conclusions drawn on the renormalization invariance of the energy per particle, numerical convergence is checked for the whole range of Λ spanned by the numerical calculations.

For example, Fig. 3.9 displays the energy per particle in the ladder approximation for $C_p \in [1\text{ GeV}, 3\text{ GeV}]$, $\Lambda \in [k_F, 6k_F]$ and $\Delta_p \in [10\text{ MeV}, 20\text{ MeV}]$. Similarly, another typical plot characterized by $C_\omega \in \{600\text{ MeV}, 2\text{ GeV}, 5\text{ GeV}\}$ and $\Lambda \in [k_F, 8k_F]$ is depicted in Fig. 3.10. As a complementary check, the energy per particle is computed both with (1.28) and with the GMK sum rule (1.40). Fig. 3.11 shows a good agreement between both when numerical convergence is reached. The substantial difference in Fig. 3.11 for high-density ($k_F = 331$ MeV) and high Λ ($\gtrsim 1$ GeV) is explained by a too low energy cut-off $C_\omega = 2$ GeV.

From these plots testing numerical convergence, it is clear that assessing the renormalization invariance numerically requires significant computational ressources as increasing Λ at fixed k_F requires to take large numerical cut-off (C_p, C_ω) while keeping sufficiently low $(\Delta_p, \Delta_\omega)$. For instance, numerical convergence (with respect to parameters (C_p, Δ_p)) have been verified empirically for

$$\Delta_p \lesssim \frac{\Lambda}{200} \ , \quad \Delta_p \lesssim \frac{k_F}{2} \ , \quad C_p \gtrsim \Lambda \ , \quad C_p \gtrsim 2k_F \ , \tag{3.52}$$

where the "numerical convergence" relates to an estimated error of 0.5 MeV on the energy per particle. In practice to reach this numerical precision the Fortran code has been fully parallelized using MPI and is run on a supercomputer with up to 100 nodes per calculation (at fixed Λ).

Renormalization invariance

Once the numerical accuracy of the Fortran code has been characterised, the renormalization invariance of the energy per particle can be assessed. Self-consistent calculations in the HF, the 2nd Born and the ladder approximations, with $H_{\not\pi}$ renormalized exactly in the two-body sector, are shown in Fig. 3.12 for $k_F = 263$ MeV. The energy per particle shows a clear Λ dependence, regardless of the many-body approximation, leading to shift of more than 5 MeV. This variation is one order of magnitude larger than the numerical uncertainty.

At this point, either the renormalization of $H_{\not\pi}$ is inconsistent with the three tested many-body approximations, or the Fortran code to implement SCGF schemes is insufficiently accurate. Because the numerical accuracy has already been tested, it only remains to test the additional approximations used in the Fortran code namely the angle-averaging and the quasiparticle-background decomposition.

To investigate these approximations, one focuses on simpler non-self-consistent approximations i.e. without iterating equations in Tab. 3.1. In this case, the outcomes of the Fortran code can be compared with exact calculations. The initial spectral function in non-self-consistent calculations is the unperturbed one as in Eq. (3.20), which is strongly peaked. Thus non-self-consistent calculations enable to test the quasiparticle treatment in the Fortran code. In the next section, the non-self-consistent HF results from the Fortran code is compared to a calculation with the sole angle-averaging approximation realized on Mathematica. Eventually, results from the Fortran code are compared to exact analytical calculations for the non-self-consistent HF, 2nd Born and ladder approximations in Sec. 3.5. Thanks to this extensive comparison, clear conclusions are eventually drawn in Sec. 3.5.3.

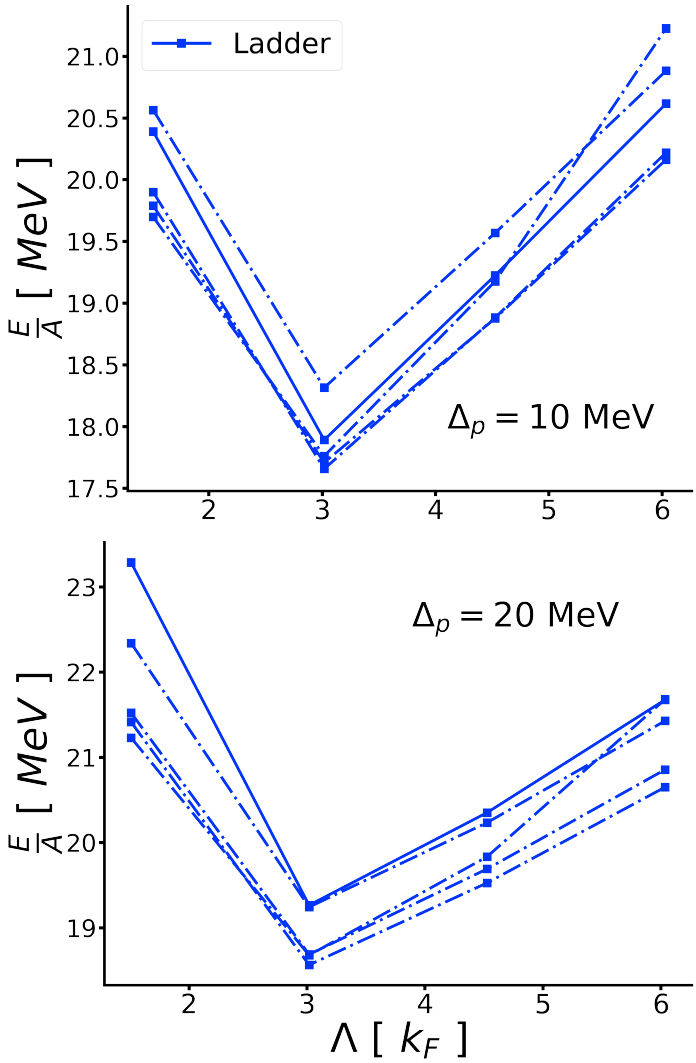

Figure 3.9. Energy per particle in the ladder approximation for $\Lambda \in [k_F, 6k_F]$ at $k_F = 331$ MeV. Dashed lines represent calculations with $C_p = 1$, 1.5, 2, 2.5 GeV and the plain line with $C_p = 3$ GeV. The upper-panel corresponds to $\Delta_p = 10$ MeV and the lower-panel to $\Delta_p = 20$ MeV.

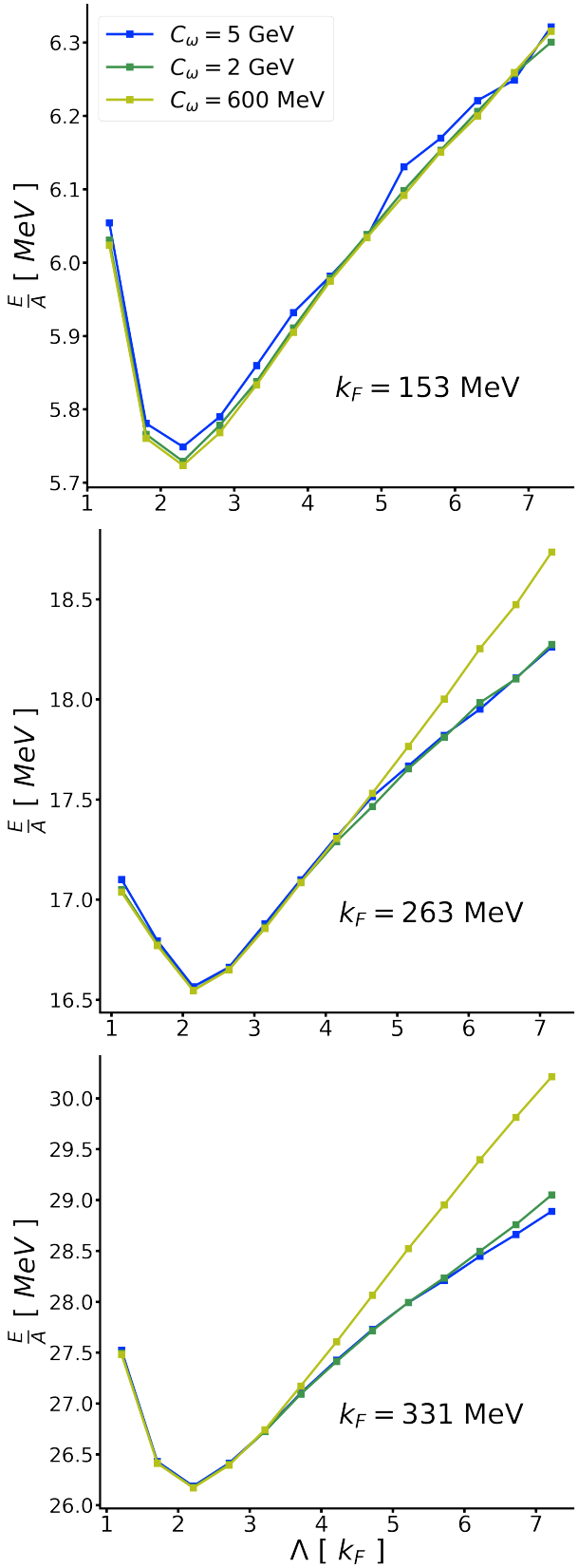

Figure 3.10. Energy per particle in the ladder approximation for $\Lambda \in [k_F, 8k_F]$. The curves represent calculations for $C_\omega = 600$, 2000, 5000 MeV. The upper-panel corresponds to $k_F = 153$ MeV, the middle-panel to $k_F = 263$ MeV and the lower-panel to $k_F = 331$ MeV.

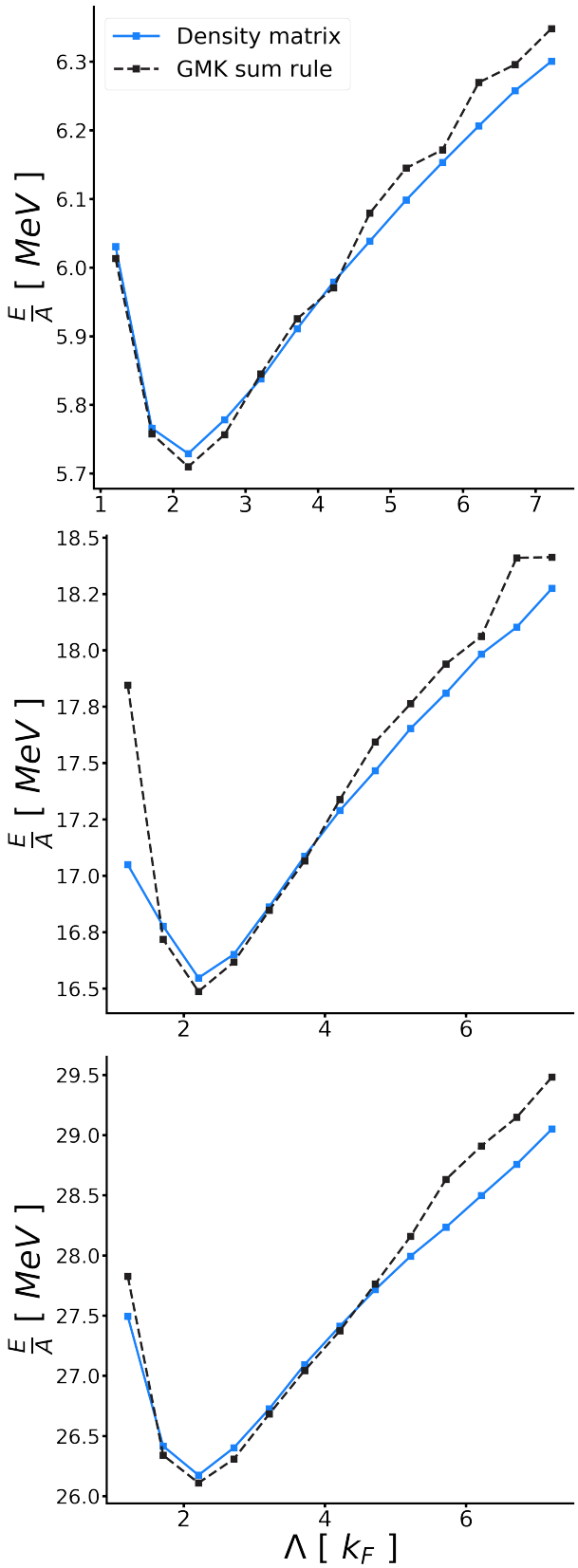

Figure 3.11. Energy per particle in the ladder approximation. Dashed lines represent computations using the GMK relation while the plain line represent computations using (1.28). The upper-panel corresponds to $k_F = 153$ MeV, the middle-panel to $k_F = 263$ MeV and the lower-panel to $k_F = 331$ MeV.

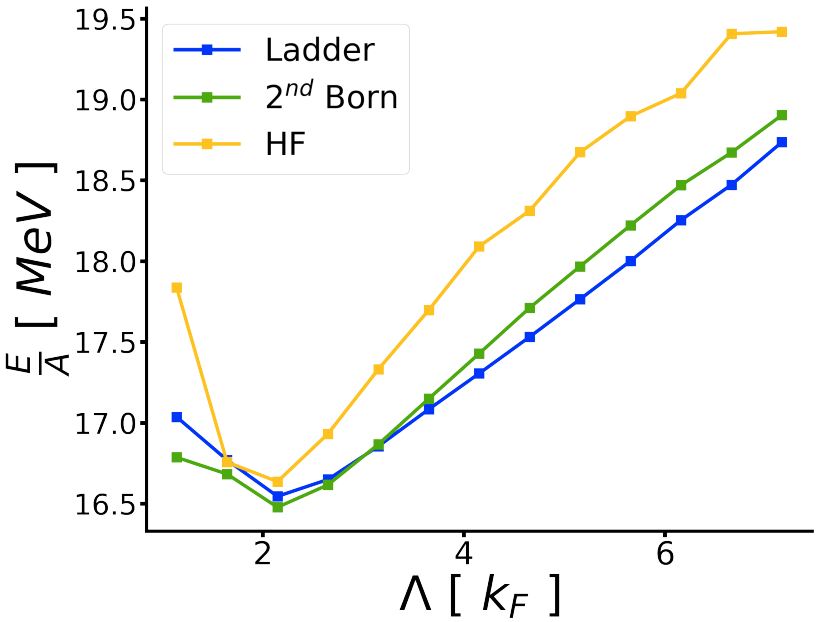

Figure 3.12. Energy per particle in the HF, the 2nd Born and the ladder approximations at density $\rho_0 = 0.08$ fm^{-3} ($k_F = 263$ MeV).

3.4.4. Non-self consistent Hartree-Fock calculation

In this section, the energy per particle in the non-self-consistent HF approximation is computed with only the angle-averaging approximation. This has been realized in a Mathematica code following the exact same steps as the Fortran code in order to trace potential numerical instabilities in the Fortran code. Each step is realized analytically apart from the calculation of the energy per particle from the T-matrix which is done numerically[11].

Comparing non-self-consistent HF results from the Mathematica and the Fortran code yields an agreement for $\Lambda \in [k_F, 8k_F]$ up to the numerical accuracy of 0.5 MeV as illustrated in Fig. 3.13. This comparison confirms the numerical accuracy of the Fortran code as well as the quasiparticle treatment of the peaked spectral function in the HF approximation. However, similar calculations could not be realized in the non-self-consistent 2nd Born and ladder approximations.

In order to assess the validity of 2nd Born and ladder calculations in the Fortran code, and bypass limitations of Mathematica, the exact result (in the non-self-consistent case) is derived fully analytically in the next section. This allows one to test the validity of the angle-averaging approximation as well as the validity of the background-quasiparticle decomposition in the 2nd Born and in the ladder approximations as implemented in the Fortran code.

[11]The algorithm used in the Mathematica code checks the convergence of this last step done numerically so that it can be considered as computed exactly.

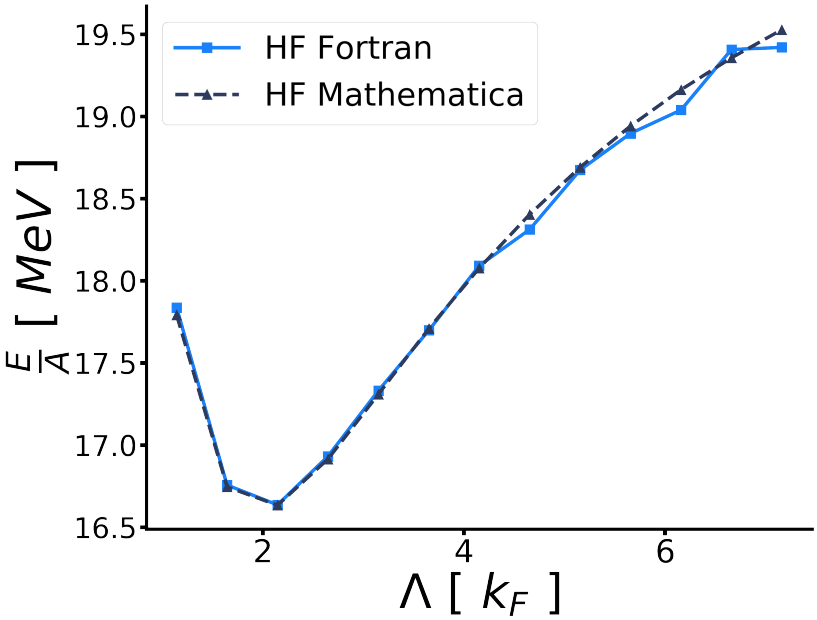

Figure 3.13. Energy per particle in the HF approximation for $\rho_0 = 0.08$ fm^{-3} ($k_F = 263$ MeV). Dashed lines represent computations using the Mathematica code while the plain line represent computations using the Fortran.

3.5. Analytical calculations

As discussed previously, numerical results obtained from the state-of-the-art SCGF code used in this thesis are difficult to interpret. The reproduction of the HF results in the Mathematica code in Sec. 3.4.4 rules out any numerical accuracy due to discretization and numerical cut-off and checks the validity of the background-quasiparticle decomposition in the HF approximation.

In the next section, the calculation of the energy per particle of pure neutron matter is derived in the undressed HF, 2nd Born and ladder approximations fully analytically. Eventually, the comparison with the outcomes from the Fortran and the Mathematica codes in Sec. 3.4.3 allows one to conclude regarding the numerical instability of SCGF calculations performed by means of the Fortran code.

3.5.1. Analytical calculation in the ladder approximation

In this section, the computation of the energy per particle is realized fully analytically for the HF, the 2nd Born and the ladder approximations, implemented on the basis of unperturbed propagators. This is most conveniently achieved by introducing a vacuum/medium decomposition of the one-body propagator. Such a strategy follows mainly from [76, 77], with the difference that a cut-off regularization is presently used instead of a dimensional one. The use of a cut-off regularization is crucial to assess the accuracy of the Fortran code at different Λ and to obtain clear enough information to localize potential numerical artefacts. The ladder calculation is detailed first so that HF and 2nd Born approximations can be easily retrieved as its 1st and 2nd order (in the coupling constant) reductions. Contrarily to numerical calculations,

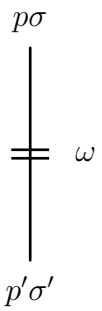

Figure 3.14. Diagrammatic representation of $G^{(M,1)0}_{p\sigma p'\sigma'}(\omega)$.

no approximation such as angle-averaging or discretization is involved.

In-medium formalism

The vacuum/medium decomposition of the unperturbed propagator consists in rewriting the one-body propagator (3.5) in the energy-representation

$$iG^{(\rho,1)0}_{\vec{p}\sigma\vec{p}'\sigma'}(\omega) = i\left[\frac{\theta\left(p-k_F\right)}{\omega-\frac{p^2}{2m}+i\eta}+\frac{\theta\left(k_F-p\right)}{\omega-\frac{p^2}{2m}-i\eta}\right](2\pi)^3\delta\left(\vec{p}-\vec{p}'\right)\ \delta_{\sigma\sigma'}\ ,$$

using the identity (1.34)

$$\frac{1}{\omega\pm i\eta} = \mathcal{P}\frac{1}{\omega}\mp i\pi\delta(\omega)\ .$$

This leads to

$$iG^{(\rho,1)0}_{\vec{p}\sigma\vec{p}'\sigma'}(\omega) = \left[\frac{i}{\omega-\frac{p^2}{2m}+i\eta}-2\pi\delta\left(\omega-\frac{p^2}{2m}\right)\theta\left(k_F-p\right)\right](2\pi)^3\delta\left(\vec{p}-\vec{p}'\right)\ \delta_{\sigma\sigma'}\ , \tag{3.53a}$$

$$\equiv iG^{(0,1)0}_{\vec{p}\sigma\vec{p}'\sigma'}(\omega)+iG^{(M,1)0}_{\vec{p}\sigma\vec{p}'\sigma'}(\omega)\ , \tag{3.53b}$$

where $G^{(0,1)0}$ and $G^{(M,1)0}$ denote the vacuum propagator and the medium-insertion, respectively. The diagrammatic representation of $G^{(M,1)0}$ is displayed in Fig. 3.14. The strategy to compute ladder diagrams is to expand them in the sum of diagrams containing vacuum propagators and medium insertions. First, the loops with 0, 1 and 2 medium insertion are explicitly computed. Then the resummation of ladder diagrams is performed, taking care of the non-trivial combinatorics of the diagrams. Eventually, the energy per particle is retrieved from the two-body Green's function by using (1.28).

In the following, B_i refers to the ratio of one-loop diagrams with i medium insertions and the tree diagram made of one vertex h^{22}. This way the diagrams with n loops is nothing but the product of n factors B_i and of one vertex h^{22}.[12] Similarly to the T-matrix in Sec. 2.2, B_i depends only on the external relative momentum q, the total momentum P and on the total energy E. Moreover, to compute the energy per particle, only the on-shell part of B_i is necessary which only depends on q and P. In the following $B_i(P,q)$ denotes the on-shell value of B_i for an external relative momentum q and a total momentum P. To further simplify

[12]Without such ratio, the product of B_i factors would double-count vertices.

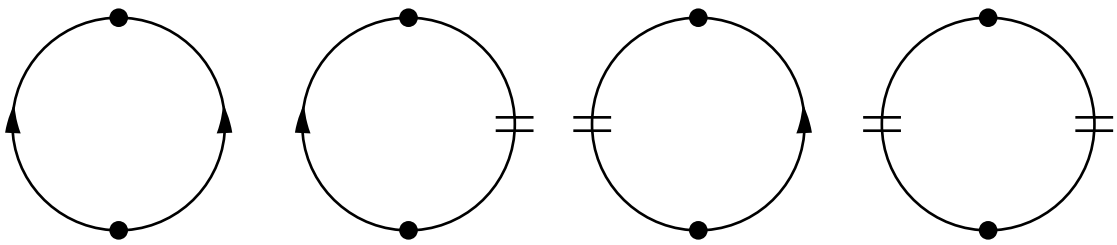

Figure 3.15. Diagrammatic representation of loops with 0, 1 and 2 medium-insertion.

the calculation, one can assume the incoming neutrons to occupy hole states i.e. $p_1 \leq k_F$ and $p_2 \leq k_F$ which limits the values q and P can reach. Loops with 0, 1 and 2 medium-insertion are represented in Fig. 3.15.

Loop with no medium insertion

Without medium insertion, the one-loop diagram is the same as in (2.48) which only depends on q. Without forgetting to divide by the one-vertex contribution,

$$\begin{aligned} B_0(q) = & \frac{-1}{(-i)C_0(\Lambda)v_\Lambda(2q)v_\Lambda(2q)} \\ & \times \int_{-\infty}^{\infty} \frac{\mathrm{d}l_0}{2\pi} \int \frac{\mathrm{d}^3\vec{l}}{(2\pi)^3}(-i)C_0(\Lambda)v_\Lambda(2q)v_\Lambda(2l)\frac{i}{\frac{(p_1^2+p_2^2)}{4m} + l_0 - \frac{(\vec{P}+\vec{l})^2}{2m} + i\eta} \\ & \times (-i)C_0(\Lambda)v_\Lambda(2l)v_\Lambda(2q)\frac{i}{\frac{(p_1^2+p_2^2)}{4m} - l_0 - \frac{(\vec{P}-\vec{l})^2}{2m} + i\eta} \ . \end{aligned} \tag{3.54}$$

After simplifications and integrating over l_0 by closing the contour of integration around the $+i\eta$ pole, $B_0(q)$ reads as

$$\begin{aligned} B_0(q) &= -iC_0(\Lambda)mi \int \frac{\mathrm{d}^3\vec{l}}{(2\pi)^3}\frac{v_\Lambda^2(2l)}{\vec{q}^2 - \vec{l}^2 + i\eta} \\ &= -\frac{mC_0(\Lambda)}{2\pi^2}\int_0^\infty \mathrm{d}l \frac{v_\Lambda^2(2l)l^2}{l^2 - q^2 - i\eta} \\ &= -\frac{mC_0(\Lambda)}{2\pi^2}\left\{\int_0^\infty \mathrm{d}l\ v_\Lambda^2(2l) + q^2\int_0^\infty \mathrm{d}l \frac{v_\Lambda^2(2l)}{(l-q-i\eta)(l+q+i\eta)}\right\} \\ &= -\frac{mC_0(\Lambda)}{2\pi^2}\left\{\int_0^\infty \mathrm{d}l\ v_\Lambda^2(2l) + i\frac{\pi}{2}qv_\Lambda^2(2q)\right\} \ . \end{aligned} \tag{3.55}$$

Loop with one medium insertion

The loop diagram with one medium insertion on the right (on the left) is denoted as $B_1^R(P,q)$ ($B_1^L(P,q)$). $B_1^R(P,q)$, reads as

$$\begin{aligned}
B_1^R(P,q) = &\frac{1}{(-i)C_0(\Lambda)v_\Lambda(2q)v_\Lambda(2q)} \\
&\times \int_{-\infty}^{\infty} \frac{\mathrm{d}l_0}{2\pi} \int \frac{\mathrm{d}^3\vec{l}}{(2\pi)^3} (-i)C_0(\Lambda)v_\Lambda(2q)v_\Lambda(2l) \frac{i}{\frac{(p_1^2+p_2^2)}{4m} + l_0 - \frac{(\vec{P}+\vec{l})^2}{2m} + i\eta} \\
&\qquad \times (-i)C_0(\Lambda)v_\Lambda(2l)v_\Lambda(2q) \\
&\qquad \times \left[-2\pi\delta\left(\frac{(p_1^2+p_2^2)}{4m} - l_0 - \frac{(\vec{P}-\vec{l})^2}{2m} \right) \theta(k_F - |\vec{P}-\vec{l}|\,) \right] \\
= &\, mC_0(\Lambda) \int \frac{\mathrm{d}^3\vec{l}}{(2\pi)^3} \frac{v_\Lambda^2(2l)}{l^2-q^2-i\eta} \theta(k_F - |\vec{P}-\vec{l}|\,) \ . \qquad (3.56)
\end{aligned}$$

Similarly, the medium insertion on the left reads as

$$B_1^L(P,q) = mC_0(\Lambda) \int \frac{\mathrm{d}^3\vec{l}}{(2\pi)^3} \frac{v_\Lambda^2(2l)}{l^2-q^2-i\eta} \theta(k_F - |\vec{P}+\vec{l}|\,) \ , \qquad (3.57)$$

such that, the sum is eventually given by

$$B_1(P,q) = mC_0(\Lambda) \int \frac{\mathrm{d}^3\vec{l}}{(2\pi)^3} \frac{v_\Lambda^2(2l)}{l^2-q^2-i\eta} \left[\theta(k_F - |\vec{P}-\vec{l}|\,) + \theta(k_F - |\vec{P}+\vec{l}|\,) \right] \ . \qquad (3.58)$$

Using spherical coordinates and integrating over the azimuthal angle provides,

$$\begin{aligned}
B_1(P,q) = \frac{mC_0(\Lambda)}{(2\pi)^2} \int_{-1}^{1} \mathrm{d}y \Bigg\{ &\int_0^{Py+\sqrt{(Py)^2+k_F^2-P^2}} \mathrm{d}l \frac{v_\Lambda^2(2l)l^2}{l^2-q^2-i\eta} \\
&+ \int_0^{-Py+\sqrt{(Py)^2+k_F^2-P^2}} \mathrm{d}l \frac{v_\Lambda^2(2l)l^2}{l^2-q^2-i\eta} \Bigg\}
\end{aligned}$$

where y is the cosine of the polar angle.

To compute $B_1(P,q)$ it is convenient to introduce the integral $\mathcal{I}_\Lambda(y)$ through

$$k_F\mathcal{I}_\Lambda(y) \equiv \int_0^{Py+\sqrt{(Py)^2+k_F^2-P^2}} \mathrm{d}l \frac{v_\Lambda^2(2l)l^2}{l^2-q^2-i\eta} \ , \qquad (3.59)$$

and to introduce the reduced variables s, κ as

$$s \equiv \frac{P}{k_F} \ , \qquad (3.60a)$$

$$\kappa \equiv \frac{q}{k_F} \ . \qquad (3.60b)$$

Assuming that $p_{1,2} \leq k_F$, s, κ verify the three inequalities

$$0 \leq s \leq 1 \ , \tag{3.61a}$$
$$0 \leq \kappa \leq 1 \ , \tag{3.61b}$$
$$0 \leq s^2 + \kappa^2 \leq 1 \ . \tag{3.61c}$$

In terms of reduced variables, Eq. (3.59) reads as

$$\mathcal{I}_\Lambda(y) = \int_0^{sy+\sqrt{(sy)^2+1-s^2}} \mathrm{d}\mu \ v_\Lambda^2(2\ k_F\mu) \ + \ \kappa \int_0^{\frac{sy+\sqrt{(sy)^2+1-s^2}}{\kappa}} \mathrm{d}\mu \ \frac{v_\Lambda^2(2\kappa\ k_F\mu)}{\mu^2 - 1 - i\eta} \tag{3.62}$$
$$\equiv \mathcal{I}_\Lambda^{(1)}(y;s) + \mathcal{I}_\Lambda^{(2)}(y;s,\kappa) \ . \tag{3.63}$$

To avoid lengthy notations, the regulator is assumed to be Gaussian as defined in (2.19). For convenience $M(y;s)$ is introduced as

$$M(y;s) \equiv sy + \sqrt{(sy)^2 + 1 - s^2} \ . \tag{3.64}$$

The first integral in Eq. (3.62) then reads as

$$\begin{aligned}\mathcal{I}_\Lambda^{(1)}(y;s) &= \int_0^{M(y;s)} \mathrm{d}\mu \ e^{-8(\frac{k_F}{\Lambda})^2\mu^2} \\ &= \frac{\Lambda}{\sqrt{8}k_F}\frac{\sqrt{\pi}}{2}\,\mathrm{Erf}\left(\frac{2\sqrt{2}k_F}{\Lambda}M(y;s)\right) \ ,\end{aligned}$$

which can be expanded in the limit $\Lambda \gg 2\sqrt{2}k_F M(y;s)$ thanks to[13]

$$\mathrm{Erf}\,(x) = \frac{2}{\sqrt{\pi}}\left\{x - \frac{x^3}{3} + O(x^5)\right\} \ . \tag{3.65}$$

This eventually gives

$$\mathcal{I}_\Lambda^{(1)}(y;s) = M(y;s) - \left(\frac{2\sqrt{2}k_F}{\Lambda}\right)^2 M(y;s)^3 + O\left(\left(\frac{2\sqrt{2}k_F}{\Lambda}\right)^4 M(y;s)^5\right) \ . \tag{3.66}$$

The second integral in Eq. (3.62) is less trivial to compute. To expand it in the limit $\Lambda \gg 2\sqrt{2}k_F$ the regulator is expanded in $\frac{2\sqrt{2}k_F}{\Lambda}$ as

$$v_\Lambda^2(2\kappa\ k_F\mu) = 1 - \left(\frac{2\sqrt{2}k_F}{\Lambda}\right)^2 \kappa^2\mu^2 + O\left(\left(\frac{2\sqrt{2}k_F}{\Lambda}\right)^4 \kappa^4\right) \tag{3.67}$$

[13] One can assume Λ being large in front of any fixed quantities as one are interested in the limit $\Lambda \to +\infty$.

such that

$$\begin{aligned}
\mathcal{I}_\Lambda^{(2)}(y;s,\kappa) &= \kappa\left\{\int_0^{\frac{M(y;s)}{\kappa}} \mathrm{d}\mu\ \frac{1}{\mu^2-1-i\eta} - \left(\frac{2\sqrt{2}k_F}{\Lambda}\right)^2 \kappa^2 \int_0^{\frac{M(y;s)}{\kappa}} \mathrm{d}\mu \frac{\mu^2}{\mu^2-1-i\eta}\right. \\
&\qquad\qquad \left. + O\left(\left(\frac{2\sqrt{2}k_F}{\Lambda}\right)^4\right)\right\} \\
&= \kappa\left\{-\mathrm{Argth}\frac{M(y;s)}{\kappa} - \left(\frac{2\sqrt{2}k_F}{\Lambda}\right)^2 \kappa^2 \left[\int_0^{\frac{M(y;s)}{\kappa}} \mathrm{d}\mu + \int_0^{\frac{M(y;s)}{\kappa}} \mathrm{d}\mu\ \frac{1}{\mu^2-1-i\eta}\right]\right. \\
&\qquad\qquad \left. + O\left(\left(\frac{2\sqrt{2}k_F}{\Lambda}\right)^4\right)\right\} \\
&= -\kappa\mathrm{Argth}\frac{M(y;s)}{\kappa} + \left(\frac{2\sqrt{2}k_F}{\Lambda}\right)^2 \kappa^2 \left[\kappa\mathrm{Argth}\frac{M(y;s)}{\kappa} - M(y;s)\right] \\
&\qquad\qquad + O\left(\left(\frac{2\sqrt{2}k_F}{\Lambda}\right)^4\right) . \qquad (3.68)
\end{aligned}$$

Gathering the expansion of $\mathcal{I}_\Lambda^{(1)}(y;s,\kappa)$ and $\mathcal{I}_\Lambda^{(2)}(y;s,\kappa)$, the real part of $B_1(P,q)$ reads as

$$\begin{aligned}
\mathrm{Re}\, B_1(P,q) &= \frac{mC_0(\Lambda)}{(2\pi)^2} k_F \int_{-1}^{1} \mathrm{d}y\, \mathrm{Re}\left\{\mathcal{I}_\Lambda^{(1)}(y;s) + \mathcal{I}_\Lambda^{(1)}(-y;s) + \mathcal{I}_\Lambda^{(2)}(y;s,\kappa) + \mathcal{I}_\Lambda^{(2)}(-y;s,\kappa)\right\} \\
&\equiv \frac{mC_0(\Lambda)}{(2\pi)^2} k_F \left\{R_0(s,\kappa) + \left(\frac{2\sqrt{2}k_F}{\Lambda}\right)^2 R_1(s,\kappa) + R_r\left(s,\kappa;\frac{k_F}{\Lambda}\right)\left(\frac{2\sqrt{2}k_F}{\Lambda}\right)^4\right\} \\
&\equiv \frac{mC_0(\Lambda)}{(2\pi)^2} k_F\ R_{\frac{k_F}{\Lambda}}(s,\kappa) .
\end{aligned}$$

As the calculation of the imaginary part of $B_1(P,q)$ turns out not to be necessary to compute the energy per particle, it is not displayed here. All details of the calculation of the R functions can be found in Appendix B. In the end, the following equations are sufficient for any further derivation

$$\mathrm{Re}\, B_1(P,q) = \frac{mC_0(\Lambda)}{(2\pi)^2} k_F R_{\frac{k_F}{\Lambda}}(s,\kappa) , \qquad (3.69a)$$

$$R_{\frac{k_F}{\Lambda}}(s,\kappa) = R_0(s,\kappa) - \left(\frac{2\sqrt{2}k_F}{\Lambda}\right)^2 \left[4+\kappa^2 R_0(s,\kappa)\right] + R_r\left(s,\kappa;\frac{k_F}{\Lambda}\right)\left(\frac{2\sqrt{2}k_F}{\Lambda}\right)^4 , \qquad (3.69b)$$

$$R_0(s,\kappa) = 2 + \frac{1}{2s}\left[1-(s+\kappa)^2\right]\ln\frac{1+s+\kappa}{|1-s-\kappa|} + \frac{1}{2s}\left[1-(s-\kappa)^2\right]\ln\frac{1+s-\kappa}{1-s+\kappa} . \qquad (3.69c)$$

Loop with two medium insertions

Similarly to B_0 and B_1, $B_2(P,q)$ reads as

$$B_2(q) = -iC_0(\Lambda)\int_{-\infty}^{\infty}\frac{\mathrm{d}l_0}{2\pi}\int\frac{\mathrm{d}^3\vec{l}}{(2\pi)^3}\ v_\Lambda(2l)\left[-2\pi\delta\left(\frac{(p_1^2+p_2^2)}{4m} + l_0 - \frac{(\vec{P}+\vec{l})^2}{2m}\right)\theta(k_F - |\vec{P}+\vec{l}|\,)\right]$$

$$\times\, v_\Lambda(2l)\left[-2\pi\delta\left(\frac{(p_1^2+p_2^2)}{4m}-l_0-\frac{(\vec{P}-\vec{l})^2}{2m}\right)\theta(k_F-|\vec{P}-\vec{l}|)\right] .$$

Integrating on l_0 and the angle between $\vec{l}$ and $\vec{P}$, the two medium insertion loop reads as

$$B_2(P,q) = -i\frac{mC_0(\Lambda)}{\pi}\int_0^{+\infty}\mathrm{d}l\ \frac{l^2}{2q}v_\Lambda^2(2l)\delta\left(l-q\right)\bar{Q}(s,\kappa)\ , \tag{3.70}$$

where $\bar{Q}(s,\kappa)$ is the Pauli-Blocking factor and reads

$$\bar{Q}(s,\kappa) \equiv \int\frac{\mathrm{d}\Omega}{4\pi}\ \theta(k_F-|\vec{P}-\vec{l}|)\theta(k_F-|\vec{P}+\vec{l}|)\ , \tag{3.71}$$

$$= \begin{cases} 1 & \text{if} \quad 0\le\kappa\le 1-s \\ \frac{1-s^2-\kappa^2}{2s\kappa} & \text{if} \quad 1-s\le\kappa\le\sqrt{1-s^2} \end{cases} . \tag{3.72}$$

Eventually $B_2(P,q)$ can be written as

$$B_2(P,q) = -i\frac{mC_0(\Lambda)}{2\pi}\ k_F\ I_{\frac{k_F}{\Lambda}}(s,\kappa)\ , \tag{3.73}$$

where $I_{\frac{k_F}{\Lambda}}(s,\kappa)$ is defined through

$$I_{\frac{k_F}{\Lambda}}(s,\kappa) \equiv \kappa\bar{Q}(s,\kappa)v_\Lambda^2(2\kappa\ k_F)\ . \tag{3.74}$$

Imaginary part of one loop contributions

As stated before, $\mathrm{Im}(B_1)$ is not necessary for further computation. However, one needs to compute $\mathrm{Im}(B_0+B_1+B_2)$, which turns out to be simpler to accomplished. Indeed, using the Sokhotski-Plemelj theorem on vacuum propagators, $\mathrm{Im}(B_0+B_1+B_2)(P,q)$ reads as

$$\begin{aligned}\mathrm{Im}(B_0+B_1+B_2)(P,q) = &-\frac{C_0(\Lambda)}{m}\int\frac{\mathrm{d}^3\vec{l}}{(2\pi)^3}\ v_\Lambda^2(2l)\pi\delta(l^2-q^2)\\ &\times\Big\{1-\theta(k_F-|\vec{P}-\vec{l}|)-\theta(k_F-|\vec{P}+\vec{l}|)\\ &\quad+2\ \theta(k_F-|\vec{P}-\vec{l}|)\theta(k_F-|\vec{P}+\vec{l}|)\Big\}\\ = &-\frac{C_0(\Lambda)}{m}\int\frac{\mathrm{d}^3\vec{l}}{(2\pi)^3}\ v_\Lambda^2(2l)\pi\delta(l^2-q^2)\\ &\times\Big\{\Big[1-\theta(k_F-|\vec{P}-\vec{l}|)\Big]\Big[1-\theta(k_F-|\vec{P}+\vec{l}|)\Big]\\ &\quad+\theta(k_F-|\vec{P}-\vec{l}|)\theta(k_F-|\vec{P}+\vec{l}|)\Big\}\ .\end{aligned}$$

The first term in the bracket gives zero after integration because if $|\vec{P} \pm \vec{l}| \geq k_F$ and remembering that $|\vec{p}_{1,2}| \leq k_F$, then

$$\begin{aligned}\frac{q^2}{2m} &= \frac{p_1^2 + p_2^2}{4m} - \frac{(\vec{P}+\vec{l})^2 + (\vec{P}-\vec{l})^2}{4m} \\ &\leq \frac{k_F^2}{2m} - \frac{k_F^2}{2m} \\ &\leq 0 \ .\end{aligned}$$

Therefore its contribution is null whenever $q \neq 0$ [14] so that,

$$\begin{aligned}\mathrm{Im}(B_0 + B_1 + B_2)(P,q) &= \frac{1}{2}\,\mathrm{Im}(B_2)(P,q) \\ &= -\frac{mC_0(\Lambda)}{4\pi}\ k_F\ I_{\frac{k_F}{\Lambda}}(s,\kappa)\ .\end{aligned}$$

Eventually, combining all results, the three main identities read as

$$B_0(q) + B_1(P,q) + B_2(P,q) = \frac{mC_0(\Lambda)}{(2\pi)^2}\ k_F\ \left[\tilde{R}_{\frac{k_F}{\Lambda}}(s,\kappa) - i\pi I_{\frac{k_F}{\Lambda}}(s,\kappa)\right]\ , \tag{3.75a}$$

$$B_0(q) + B_1(P,q) = \frac{mC_0(\Lambda)}{(2\pi)^2}\ k_F\ \left[\tilde{R}_{\frac{k_F}{\Lambda}}(s,\kappa) + i\pi I_{\frac{k_F}{\Lambda}}(s,\kappa)\right]\ , \tag{3.75b}$$

$$B_2(P,q) = -i\frac{mC_0(\Lambda)}{2\pi}\ k_F I_{\frac{k_F}{\Lambda}}(s,\kappa)\ , \tag{3.75c}$$

where

$$\tilde{R}_{\frac{k_F}{\Lambda}}(s,\kappa) = R_{\frac{k_F}{\Lambda}}(s,\kappa) - \frac{2}{k_F}\int_0^\infty \mathrm{d}l\ v_\Lambda^2(2l)\ . \tag{3.76}$$

Ladder resummation

In the case of the vacuum/medium decomposition, at least one loop with two medium-insertions is necessary to obtain a non zero contribution to $G^{(\rho,2)}(t,t^+)$ in (1.28)[15]. In this section the ladder kernel $L(s,\kappa)$ to be closed by one loop with two medium-insertion is computed.

Any diagrams contributing to $L(s,\kappa)$ and containing j loops with double medium insertion lead to double-counting when closed by an additional loop with two medium insertions. To compensate such an over counting, an additional factor of $(j+1)^{-1}$ is necessary[16].

In general the computation of multi-loop diagrams is highly non-trivial. However, in this case, the particular choice of a separable regulator decouples the loop calculations such that the contribution to the ladder kernel $L(s,\kappa)$ with j double medium-insertion loops inside a total of $n-1$ loops reads as

$$\frac{1}{j+1}\binom{n-1}{j}(B_0+B_1)^{n-1-j}B_2^j\ . \tag{3.77}$$

[14] Actually its contribution will still be 0 for $q = 0$ because of the integrand being proportional to q.

[15] Otherwise $G^{(\rho,2)}(t,t')$ would be purely causal as it is the case for $G^{(0,2)}(t,t')$.

[16] See [76] for a more detailed explanation.

Eventually, the ladder kernel at order $n-1$ (with $n-1$ vertices) reads as

$$\begin{aligned} L_{n-1} &\equiv \sum_{j=0}^{n-1} \frac{1}{j+1}\binom{n-1}{j}(B_0+B_1)^{n-1-j}B_2^j \\ &= \frac{1}{B_2 n}\sum_{j=1}^{n}\binom{n}{j}(B_0+B_1)^{n-j}B_2^j \\ &= \frac{1}{B_2 n}\left\{(B_0+B_1+B_2)^n-(B_0+B_1)^n\right\} \ . \end{aligned} \tag{3.78}$$

Using Eqs. (3.75)

$$\begin{aligned} L_{n-1} = \frac{1}{-i\frac{mC_0(\Lambda)}{2\pi}\ k_F I_{\frac{k_F}{\Lambda}}(s,\kappa)n}&\left\{\left(\frac{mC_0(\Lambda)}{(2\pi)^2}\ k_F\ \left[\tilde{R}_{\frac{k_F}{\Lambda}}(s,\kappa)-i\pi I_{\frac{k_F}{\Lambda}}(s,\kappa)\right]\right)^n\right. \\ &\left.-\left(\frac{mC_0(\Lambda)}{(2\pi)^2}\ k_F\ \left[\tilde{R}_{\frac{k_F}{\Lambda}}(s,\kappa)+i\pi I_{\frac{k_F}{\Lambda}}(s,\kappa)\right]\right)^n\right\} \end{aligned} \tag{3.79a}$$

$$\begin{aligned} = \frac{1}{2i\pi}\left(\frac{mC_0(\Lambda)}{(2\pi)^2}\ k_F\right)^{n-1}\frac{1}{-I_{\frac{k_F}{\Lambda}}(s,\kappa)n}&\left\{\left(\tilde{R}_{\frac{k_F}{\Lambda}}(s,\kappa)-i\pi I_{\frac{k_F}{\Lambda}}(s,\kappa)\right)^n\right. \\ &\left.-\left(\tilde{R}_{\frac{k_F}{\Lambda}}(s,\kappa)+i\pi I_{\frac{k_F}{\Lambda}}(s,\kappa)\right)^n\right\} \end{aligned} \tag{3.79b}$$

$$= \frac{1}{\pi}\left(\frac{mC_0(\Lambda)}{(2\pi)^2}\ k_F\right)^{n-1}\frac{1}{-I_{\frac{k_F}{\Lambda}}(s,\kappa)n}\,\mathrm{Im}\left\{\left(\tilde{R}_{\frac{k_F}{\Lambda}}(s,\kappa)+i\pi I_{\frac{k_F}{\Lambda}}(s,\kappa)\right)^n\right\} \ . \tag{3.79c}$$

Eq. (3.79c) shows without ambiguity that L_{n-1} is real. However, to resum easily all L_{n-1} contributions it is convenient to use Eq. (3.79b), which leads to

$$\begin{aligned} L &\equiv \sum_{n=1}^{+\infty} L_{n-1} \\ &= \sum_{n=1}^{+\infty}\frac{1}{2i\pi}\left(\frac{mC_0(\Lambda)}{(2\pi)^2}\ k_F\right)^{n-1}\frac{1}{-I_{\frac{k_F}{\Lambda}}(s,\kappa)n}\left\{\left(\tilde{R}_{\frac{k_F}{\Lambda}}(s,\kappa)-i\pi I_{\frac{k_F}{\Lambda}}(s,\kappa)\right)^n\right. \\ &\qquad\left.-\left(\tilde{R}_{\frac{k_F}{\Lambda}}(s,\kappa)+i\pi I_{\frac{k_F}{\Lambda}}(s,\kappa)\right)^n\right\} \\ &= \frac{1}{-2i\pi\frac{mC_0(\Lambda)}{(2\pi)^2}\ k_F\ I_{\frac{k_F}{\Lambda}}(s,\kappa)}\left\{\sum_{n=1}^{+\infty}\frac{(-1)^{n+1}}{n}\left(\frac{-mC_0(\Lambda)}{(2\pi)^2}\ k_F\ \left[\tilde{R}_{\frac{k_F}{\Lambda}}(s,\kappa)+i\pi I_{\frac{k_F}{\Lambda}}(s,\kappa)\right]\right)^n\right. \\ &\qquad\left.-\sum_{n=1}^{+\infty}\frac{(-1)^{n+1}}{n}\left(\frac{-mC_0(\Lambda)}{(2\pi)^2}\ k_F\ \left[\tilde{R}_{\frac{k_F}{\Lambda}}(s,\kappa)-i\pi I_{\frac{k_F}{\Lambda}}(s,\kappa)\right]\right)^n\right\} \\ &= \frac{1}{-2i\pi\frac{mC_0(\Lambda)}{(2\pi)^2}\ k_F\ I_{\frac{k_F}{\Lambda}}(s,\kappa)}\left\{\ln\left(1-\frac{mC_0(\Lambda)}{(2\pi)^2}\ k_F\ \left[\tilde{R}_{\frac{k_F}{\Lambda}}(s,\kappa)+i\pi I_{\frac{k_F}{\Lambda}}(s,\kappa)\right]\right)\right. \end{aligned}$$

$$- \ln\left(1 - \frac{mC_0(\Lambda)}{(2\pi)^2}\ k_F\ \left[\tilde{R}_{\frac{k_F}{\Lambda}}(s,\kappa) - i\pi I_{\frac{k_F}{\Lambda}}(s,\kappa)\right]\right)\Bigg\}$$

$$= \frac{1}{-2i\pi\frac{mC_0(\Lambda)}{(2\pi)^2}\ k_F\ I_{\frac{k_F}{\Lambda}}(s,\kappa)} \ln\left(\frac{1 - \frac{mC_0(\Lambda)}{(2\pi)^2}\ k_F\ \left[\tilde{R}_{\frac{k_F}{\Lambda}}(s,\kappa) + i\pi I_{\frac{k_F}{\Lambda}}(s,\kappa)\right]}{1 - \frac{mC_0(\Lambda)}{(2\pi)^2}\ k_F\ \left[\tilde{R}_{\frac{k_F}{\Lambda}}(s,\kappa) - i\pi I_{\frac{k_F}{\Lambda}}(s,\kappa)\right]}\right) ,$$

where ln is the principal branch of the complex logarithm i.e.

$$\ln(x+iy) = \ln|x+iy| + 2i\arctan\frac{y}{x+\sqrt{x^2+y^2}} . \tag{3.80}$$

Eventually, the full ladder kernel reads as

$$L(s,\kappa) = \frac{4\pi}{-mC_0(\Lambda)\ k_F\ I_{\frac{k_F}{\Lambda}}(s,\kappa)} \arctan\left\{\frac{\frac{-mC_0(\Lambda)}{(2\pi)^2}k_F\pi I_{\frac{k_F}{\Lambda}}(s,\kappa)}{1 - \frac{mC_0(\Lambda)}{(2\pi)^2}k_F\tilde{R}_{\frac{k_F}{\Lambda}}(s,\kappa)}\right\} . \tag{3.81}$$

Energy per particle in the ladder approximation

To compute the energy density, it only remains to close the ladder kernel with an additional loop containing 2 medium-insertions (without forgetting the additional vertex). It is also convenient to use the following formula from [76] valid for any function $F(s,\kappa)$

$$\int_{|\vec{p}_{1,2}|<k_F} \frac{\mathrm{d}^3p_1\mathrm{d}^3p_2}{(2\pi)^6}\ F(s,\kappa) = \frac{2k_F^6}{\pi^4}\int_0^1 \mathrm{d}s\ s^2 \int_0^{\sqrt{1-s^2}} \mathrm{d}\kappa\ \kappa\ I_0(s,\kappa)F(s,\kappa) . \tag{3.82}$$

Consequently, the energy per particle in the ladder approximation reads as

$$\begin{aligned}
\frac{E_\Lambda^{Ld}}{A}(k_F) &= \frac{\epsilon_0^\rho}{\rho_0^0} + \frac{1}{\rho_0^0}\int_{|\vec{p}_{1,2}|<k_F} \frac{\mathrm{d}^3p_1\mathrm{d}^3p_2}{(2\pi)^6} L(s,\kappa)\ C_0(\Lambda)v_\Lambda^2(2\kappa\ k_F) \\
&= \frac{3}{5}\frac{k_F^2}{2m} + C_0(\Lambda)\frac{2k_F^6 3\pi^2}{k_F^3\pi^4}\int_0^1 \mathrm{d}s\ s^2\int_0^{\sqrt{1-s^2}} \mathrm{d}\kappa\ \kappa\ I_0(s,\kappa)\ v_\Lambda^2(2\kappa\ k_F)\ L(s,\kappa) \\
&= \frac{3}{5}\frac{k_F^2}{2m} - \frac{k_F^2}{2m}\frac{48}{\pi}\int_0^1 \mathrm{d}s\ s^2\int_0^{\sqrt{1-s^2}} \mathrm{d}\kappa\ \kappa\arctan\left\{\frac{-\frac{mC_0(\Lambda)}{(2\pi)^2}k_F\pi I_{\frac{k_F}{\Lambda}}(s,\kappa)}{1 - \frac{mC_0(\Lambda)}{(2\pi)^2}k_F\tilde{R}_{\frac{k_F}{\Lambda}}(s,\kappa)}\right\} ,
\end{aligned}$$

and eventually,

$$\frac{E_\Lambda^{Ld}}{A}(k_F) = \frac{k_F^2}{2m}\left\{\frac{3}{5} - \frac{48}{\pi}\int_0^1 \mathrm{d}s\ s^2\int_0^{\sqrt{1-s^2}} \mathrm{d}\kappa\ \kappa\arctan\left(\frac{k_F I_{\frac{k_F}{\Lambda}}(s,\kappa)}{\frac{-4\pi}{mC_0(\Lambda)} + \frac{k_F}{\pi}\tilde{R}_{\frac{k_F}{\Lambda}}(s,\kappa)}\right)\right\} . \tag{3.83}$$

3.5.2. Reduction to Hartree-Fock and second Born approximations

Hartree-Fock approximation

The full ladder having been computed, it can conveniently be degraded down to the Hartree-Fock calculation of the energy per particle. To do so, the ladder kernel is computed with 0

loop i.e.

$$
\begin{aligned}
L_{HF}(s,\kappa) &= L_0(s,\kappa) && (3.84)\\
&= \frac{1}{2i\pi}\left(\frac{mC_0(\Lambda)}{(2\pi)^2}\ k_F\right)^{1-1}\frac{1}{-I_{\frac{k_F}{\Lambda}}(s,\kappa)1}\left\{\left(\tilde{R}_{\frac{k_F}{\Lambda}}(s,\kappa)-i\pi I_{\frac{k_F}{\Lambda}}(s,\kappa)\right)^1\right.\\
&\qquad\left.-\left(\tilde{R}_{\frac{k_F}{\Lambda}}(s,\kappa)+i\pi I_{\frac{k_F}{\Lambda}}(s,\kappa)\right)^1\right\} && (3.85)\\
&= \frac{-1}{2i\pi}\frac{1}{I_{\frac{k_F}{\Lambda}}(s,\kappa)}\left\{-2i\pi I_{\frac{k_F}{\Lambda}}(s,\kappa)\right\} && (3.86)\\
&= 1\ . && (3.87)
\end{aligned}
$$

Eventually, using Eq. (3.82) again, the energy per particle in the HF approximation reads as

$$
\begin{aligned}
\frac{E_\Lambda^{HF}}{A}(k_F) &= \frac{\epsilon_0^\rho}{\rho_0^0}+\frac{1}{\rho_0^0}\int_{|\vec{p}_{1,2}|<k_F}\frac{\mathrm{d}^3p_1\mathrm{d}^3p_2}{(2\pi)^6}L_{HF}(s,\kappa)\ C_0(\Lambda)v_\Lambda^2(2\kappa\ k_F)\\
&= \frac{3}{5}\frac{k_F^2}{2m}+\frac{6C_0(\Lambda)k_F^3}{\pi^2}\int_0^1\mathrm{d}s\ s^2\int_0^{\sqrt{1-s^2}}\mathrm{d}\kappa\ \kappa\ I_0(s,\kappa)\ v_\Lambda^2(2\kappa\ k_F)\\
&= \frac{3}{5}\frac{k_F^2}{2m}+\frac{6C_0(\Lambda)k_F^3}{\pi^2}\left\{\int_0^1\mathrm{d}s\ s^2\int_0^{1-s}\mathrm{d}\kappa\ \kappa^2\ v_\Lambda^2(2\kappa\ k_F)\right.\\
&\qquad\left.+\int_0^1\mathrm{d}s\ s\int_{1-s}^{\sqrt{1-s^2}}\mathrm{d}\kappa\ \kappa\ \frac{1-s^2-\kappa^2}{2}v_\Lambda^2(2\kappa\ k_F)\right\}\ .
\end{aligned}
$$

In particular, for a Gaussian regulator

$$
\begin{aligned}
\frac{E_\Lambda^{HF}}{A}(k_F) = \frac{k_F^2}{2m}&\left\{\frac{3}{5}+\frac{mC_0(\Lambda)}{(2\pi)^2}8k_F\left(\frac{\Lambda}{2\sqrt{2}k_F}\right)^6\right.\\
&\times\left[1-\frac{3}{2}\left(\frac{2\sqrt{2}k_F}{\Lambda}\right)^2-e^{-\left(\frac{2\sqrt{2}k_F}{\Lambda}\right)^2}\left(1-\frac{1}{2}\left(\frac{2\sqrt{2}k_F}{\Lambda}\right)^2\right)\right.\\
&\left.\left.+\frac{1}{2}\left(\frac{2\sqrt{2}k_F}{\Lambda}\right)^3\sqrt{\pi}\,\mathrm{Erf}\left(\frac{2\sqrt{2}k_F}{\Lambda}\right)\right]\right\}\ . \qquad (3.88)
\end{aligned}
$$

Second Born approximation

Similarly to the calculation in the HF approximation, the energy density in the 2nd Born approximation can be computed by taking into account 0 and 1 loop order. Consequently, the

ladder kernel in this approximation reads as

$$
\begin{aligned}
L_{2B}(s,\kappa) &= L_0(s,\kappa) + L_1(s,\kappa) \\
&= 1 + \frac{1}{2i\pi}\left(\frac{mC_0(\Lambda)}{(2\pi)^2}\ k_F\right)^{2-1} \frac{1}{-I_{\frac{k_F}{\Lambda}}(s,\kappa)2}\left\{\left(\tilde{R}_{\frac{k_F}{\Lambda}}(s,\kappa) - i\pi I_{\frac{k_F}{\Lambda}}(s,\kappa)\right)^2\right. \\
&\qquad\qquad \left. - \left(\tilde{R}_{\frac{k_F}{\Lambda}}(s,\kappa) + i\pi I_{\frac{k_F}{\Lambda}}(s,\kappa)\right)^2\right\} \\
&= 1 - \frac{1}{4i\pi}\frac{1}{I_{\frac{k_F}{\Lambda}}(s,\kappa)}\frac{mC_0(\Lambda)}{(2\pi)^2}\ k_F\left\{-2i\pi I_{\frac{k_F}{\Lambda}}(s,\kappa)\times 2\tilde{R}_{\frac{k_F}{\Lambda}}(s,\kappa)\right\} \\
&= 1 + \frac{mC_0(\Lambda)}{(2\pi)^2}\ k_F\tilde{R}_{\frac{k_F}{\Lambda}}(s,\kappa)\ . \qquad (3.89)
\end{aligned}
$$

Eventually, the energy per particle in the 2nd Born approximation reads as

$$
\begin{aligned}
\frac{E^{2B}_\Lambda}{A}(k_F) &= \frac{\epsilon^\rho_0}{\rho^0_0} + \frac{1}{\rho^0_0}\int_{|\vec{p}_{1,2}|<k_F}\frac{\mathrm{d}^3p_1\mathrm{d}^3p_2}{(2\pi)^6}L_{2B}(s,\kappa)\ C_0(\Lambda)v^2_\Lambda(2\kappa\ k_F) \\
&= \frac{3}{5}\frac{k_F^2}{2m} + \frac{6C_0(\Lambda)k_F^3}{\pi^2}\int_0^1 \mathrm{d}s\ s^2\int_0^{\sqrt{1-s^2}}\mathrm{d}\kappa\ \kappa\ I_0(s,\kappa)\ v^2_\Lambda(2\kappa\ k_F) \\
&\qquad\qquad \times\left[1 + \frac{mC_0(\Lambda)}{(2\pi)^2}\ k_F\tilde{R}_{\frac{k_F}{\Lambda}}(s,\kappa)\right] \\
&= \frac{3}{5}\frac{k_F^2}{2m} + \frac{6C_0(\Lambda)k_F^3}{\pi^2}\int_0^1 \mathrm{d}s\ s^2\int_0^{\sqrt{1-s^2}}\mathrm{d}\kappa\ \kappa^2\ \bar{Q}(s,\kappa)\ v^2_\Lambda(2\kappa\ k_F)\frac{mC_0(\Lambda)}{4\pi} \\
&\qquad\qquad \times\left[\frac{4\pi}{mC_0(\Lambda)} + \frac{k_F}{\pi}\tilde{R}_{\frac{k_F}{\Lambda}}(s,\kappa)\right]\ . \qquad (3.90)
\end{aligned}
$$

3.5.3. Comparative study

In the previous section, the energy per particle of infinite neutron matter described in $\not{\pi}$EFT at LO (regularized by a momentum cut-off $v_\Lambda(q)$) has been derived in the Hartree-Fock, 2nd Born and ladder approximations.

In this section, the convergence of $\frac{E_\Lambda}{A}$ for $\Lambda \to +\infty$ is assessed for the three different renormalizations of $H_{\not{\pi}}$ in the two-body sector. Then the result are compared to numerical results from the Fortran code in order to conclude on its numerical sensitivity.

Renormalization invariance in the ladder approximation

To study the convergence of $\frac{E^{Ld}_\Lambda}{A}$ in Eq. (3.83) only the argument of the arctan needs to be investigated. Replacing $I_{\frac{k_F}{\Lambda}}(s,\kappa)$ and $\tilde{R}_{\frac{k_F}{\Lambda}}(s,\kappa)$ by their full expressions as well as $C_0(\Lambda)$ by the exact renormalization as displayed in Eq. (2.66), one has

$$
\frac{k_F I_{\frac{k_F}{\Lambda}}(s,\kappa)}{-\frac{4\pi}{mC_0(\Lambda)} + \frac{k_F}{\pi}\tilde{R}_{\frac{k_F}{\Lambda}}(s,\kappa)} = \frac{k_F I_0(s,\kappa)v^2_{\frac{\Lambda}{k_F}}(2\kappa)}{-\frac{1}{a_0} + \frac{k_F}{\pi}R_{\frac{k_F}{\Lambda}}(s,\kappa)}\ ,
$$

so that

$$\lim_{\Lambda\to+\infty} \frac{k_F I_{\frac{k_F}{\Lambda}}(s,\kappa)}{-\frac{4\pi}{mC_0(\Lambda)} + \frac{k_F}{\pi}\tilde{R}_{\frac{k_F}{\Lambda}}(s,\kappa)} = \frac{k_F I_0(s,\kappa)}{-\frac{1}{a_0} + \frac{k_F}{\pi}R_0(s,\kappa)} \ .$$

Consequently, the energy per particle in the ladder approximation computed in connection with the exact renormalization of $C_0(\Lambda)$ in the two-body sector converges to

$$\lim_{\Lambda\to+\infty} \frac{E_\Lambda^{Ld}}{A}(k_F) = \frac{E_\infty^{Ld}}{A}(k_F) = \frac{k_F^2}{2m}\left\{\frac{3}{5} - \frac{48}{\pi}\int_0^1 \mathrm{d}s\ s^2 \int_0^{\sqrt{1-s^2}} \mathrm{d}\kappa\ \kappa \arctan\left(\frac{k_F I_0(s,\kappa)}{-\frac{1}{a_0} + \frac{k_F}{\pi}R_0(s,\kappa)}\right)\right\} \ . \tag{3.91}$$

Conversely, for a renormalisation of $C_0(\Lambda)$ performed in the two-body sector at the tree-level (Eq. (2.47)) or in the one-loop approximation (Eq. (2.54)), the energy per particle converges to the trivial limit of the free Fermi gas i.e.

$$\lim_{\Lambda\to+\infty} \frac{E_\Lambda^{Ld}}{A}(k_F) = \frac{\epsilon_0^\rho}{\rho_0^0} \ . \tag{3.92}$$

Therefore, it is concluded that a *ladder calculation of the energy per particle requires to renormalize the two-body Hamiltonian $H_{\not\pi}^{LO}$ exactly in the two-body sector*. If it is not the case, the energy per particle converges to a trivial limit as depicted in Fig. 3.16.

Once the renormalization of the Hamiltonian has been fixed in the advocated way, the unitary limit can be studied in the ladder approximation as in [76]. In particular the energy per particle converges to

$$\lim_{a_0\to-\infty} \frac{E_\infty^{Ld}}{A}(k_F) = \xi^{Ld}\frac{\epsilon_0^\rho}{\rho_0^0} \ , \tag{3.93}$$

where the Bertsch parameter reads as

$$\xi^{Ld} \equiv 1 - \frac{80}{\pi}\int_0^1 \mathrm{d}s\ s^2 \int_0^{\sqrt{1-s^2}} \mathrm{d}\kappa\ \kappa\ \arctan\left(\frac{\pi I_0(s,\kappa)}{R_0(s,\kappa)}\right) \ , \tag{3.94}$$

and numerically, $\xi^{Ld} \simeq 0.506654$. Compared to recent experimental estimations $\xi^{\mathrm{Exp}} = 0.376(4)$ [78] the estimation appears reasonable yet away from the exact value, as expected from a many-body approximation not fulfilling PC rules.

Renormalization invariance in the Hartree-Fock approximation

In order to study the convergence of $\frac{E_\Lambda^{HF}}{A}$ one uses the expansion of Erf and exp in the limit $\Lambda \gg 2\sqrt{2}k_F$ to derive

$$\frac{E_\Lambda^{HF}}{A}(k_F) = \frac{k_F^2}{2m}\left\{\frac{3}{5} + \frac{mC_0(\Lambda)}{(2\pi)^2}8k_F\left[\frac{1}{12} + O\left(\left(\frac{2\sqrt{2}k_F}{\Lambda}\right)^2\right)\right]\right\} \ . \tag{3.95}$$

Consequently, using $C_0(\Lambda)$ renormalized exactly in the two-body sector as in Eq. (2.66), the energy per particle converges to

$$\lim_{\Lambda\to+\infty} \frac{E_\Lambda^{HF}}{A}(k_F) = \frac{\epsilon_0^\rho}{\rho_0^0} \ . \tag{3.96}$$

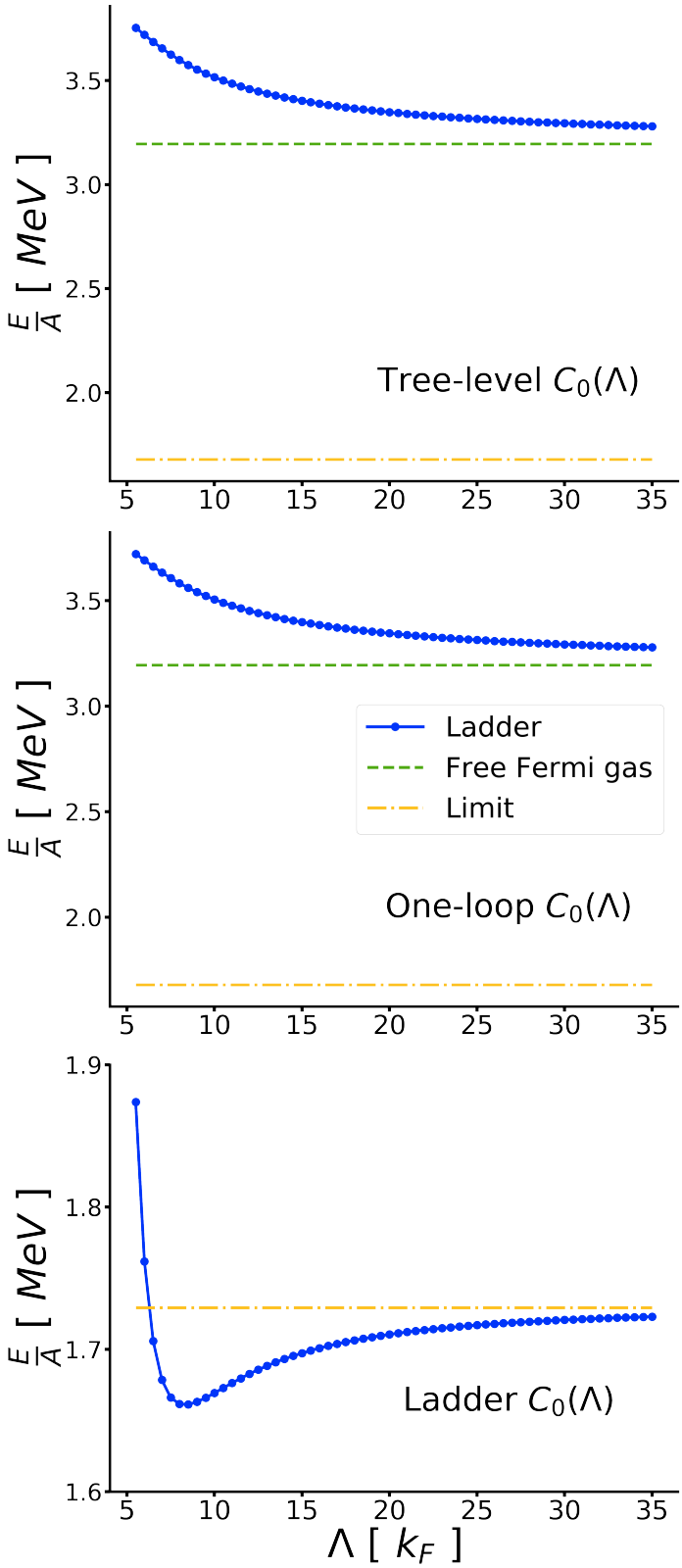

Figure 3.16. Energy per particle in the (non-self consistent) ladder approximation for $k_F =$ 100 MeV. The upper-panel uses a $C_0(\Lambda)$ computed at tree-level. The middle-panel takes into account the counter-term computed at one-loop as in Eq. (3.102). The lower-panel uses $C_0(\Lambda)$ from an exact renormalization in the two-body sector.

Rather using $C_0(\Lambda)$ renormalized at one-loop order in the two-body sector as in Eq. (2.54), one obtains

$$\lim_{\Lambda\to+\infty} \frac{E_\Lambda^{HF}}{A}(k_F) = \infty \ . \tag{3.97}$$

However, for the renormalization of $C_0(\Lambda)$ at tree-level i.e. for Eq. (2.47), the energy per particle converges to a non-trivial value, i.e.

$$\lim_{\Lambda\to+\infty} \frac{E_\Lambda^{HF}}{A}(k_F) = \frac{E_\infty^{HF}}{A}(k_F) = \frac{k_F^2}{2m}\left\{\frac{3}{5} + \frac{2k_F}{3\pi}a_0\right\} \ . \tag{3.98}$$

Again, the energy per particle converges either to a trivial limit or to an unphysical value when the renormalization of $H_{\not\pi}$ is not consistent with the employed many-body approximation. The cut-off dependence of the energy per particle in the HF approximation is explicitly displayed in Fig. 3.17 for the three different renormalization of $C_0(\Lambda)$. In this case, *using the Hartree-Fock approximation to compute many-body observables requires to renormalize the two-body Hamiltonian $H_{\not\pi}^{LO}$ at tree-level in the two-body sector to converge to a non-trivial limit.*

Once the renormalization is performed according to the many-body approximation of interest, one can discuss how relevant such an approximation is to describe a particular system. In the case of the Hartree-Fock approximation, a system near the unitary limit is badly approximated as

$$\lim_{a_0\to-\infty} \frac{E_\infty^{HF}}{A}(k_F) = -\infty \ , \tag{3.99}$$

such that, while being properly renormalized, the employed scheme is not physically relevant, at least in some particular situations.

Renormalization invariance in the 2nd Born approximation

A similar study follows for the energy per particle computed in the 2nd Born approximation. For $C_0(\Lambda)$ renormalized exactly in the two-body sector,

$$\lim_{\Lambda\to+\infty} \frac{E_\Lambda^{2B}}{A}(k_F) = \frac{\epsilon_0^\rho}{\rho_0^0} \ , \tag{3.100}$$

while for $C_0(\Lambda)$ renormalized at tree-level,

$$\lim_{\Lambda\to+\infty} \frac{E_\Lambda^{2B}}{A}(k_F) = +\infty \ . \tag{3.101}$$

Conversely, for $C_0(\Lambda)$ renormalized at one-loop order in the two-body sector, one obtains

$$\begin{aligned}\frac{E_\Lambda^{2B}}{A}(k_F) = \frac{k_F^2}{2m}\Bigg\{&\frac{3}{5} + \left[\frac{2}{3\pi} - \frac{1}{5\pi}\left(\frac{2\sqrt{2}k_F}{\Lambda}\right)^2 + O\left(\left(\frac{2\sqrt{2}k_F}{\Lambda}\right)^4\right)\right](a_0k_F) \\ &+ \left[\frac{4}{35\pi^2}(11-\ln 2) - \frac{2957-96\ln 2}{945\pi^2}\left(\frac{2\sqrt{2}k_F}{\Lambda}\right)^2 + O\left(\left(\frac{2\sqrt{2}k_F}{\Lambda}\right)^4\right)\right](a_0k_F)^2\Bigg\} \ ,\end{aligned} \tag{3.102}$$

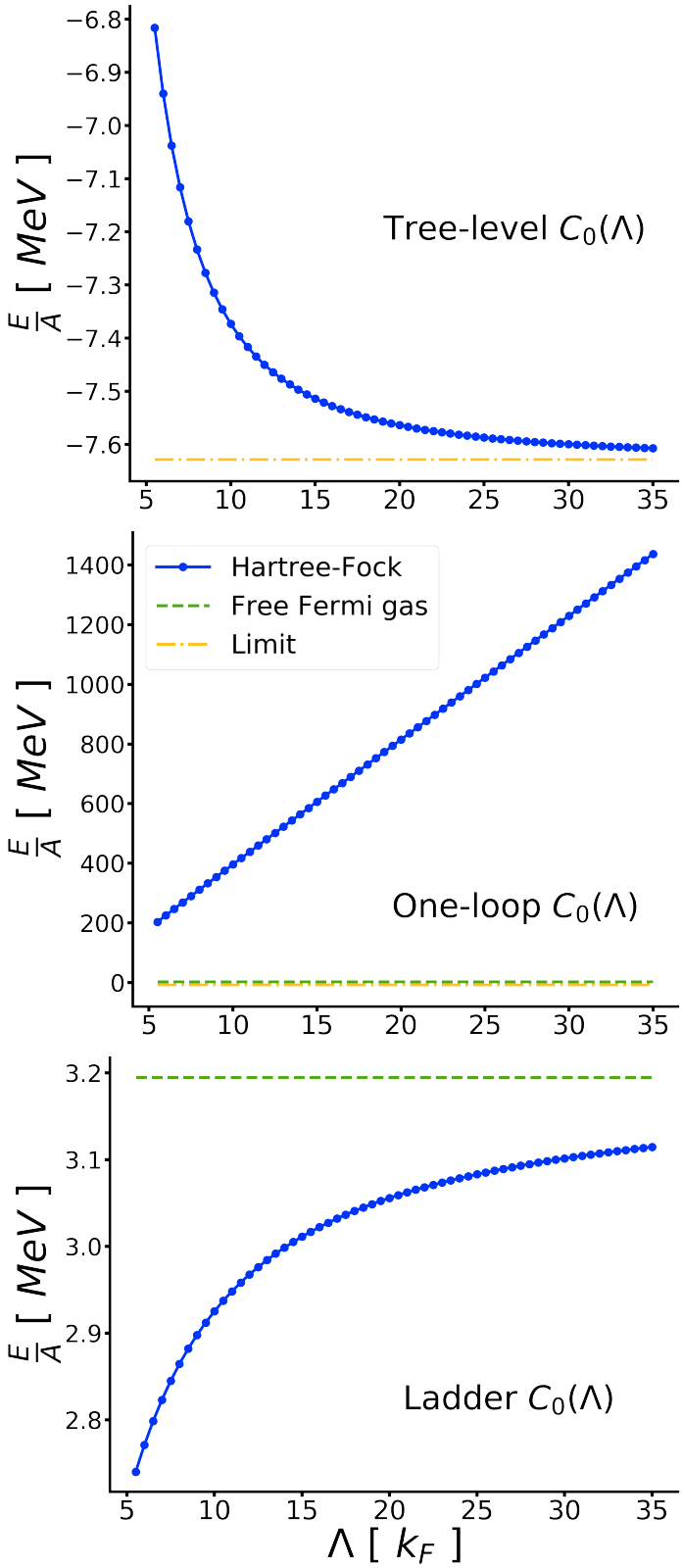

Figure 3.17. Energy per particle in the (non-self consistent) Hartree-Fock approximation for $k_F = 100$ MeV. The upper-panel uses a $C_0(\Lambda)$ computed at tree-level. The middle-panel takes into account the counter-term computed at one-loop as in Eq. (3.102). The lower-panel uses $C_0(\Lambda)$ from an exact renormalization in the two-body sector.

so that,

$$\lim_{\Lambda\to+\infty}\frac{E^{2B}_{\Lambda}}{A}(k_F)=\frac{E^{2B}_{\infty}}{A}(k_F)=\frac{k_F^2}{2m}\left\{\frac{3}{5}+\frac{2}{3\pi}(a_0k_F)+\frac{4}{35\pi^2}(11-\ln 2)(a_0k_F)^2\right\}\ , \tag{3.103}$$

which corresponds to the first orders of the Lee-Yang expansion [79, 80, 81]. As for the HF and the ladder approximations, the conclusion drawn from Eqs. (3.100), (3.101) and (3.103) is that *the computation of many-body observables in the* 2nd *Born approximation requires to renormalize the two-body Hamiltonian* $H^{LO}_{\not\pi}$ *at one-loop order in the two-body sector to converge to a non-trivial limit.* Typical cut-off dependences of the energy per particle computed in the 2nd Born approximation are displayed in Fig. 3.18 for the three renormalizations computed in Chap. 2.

Similarly, having the Hamiltonian consistently renormalized within the 2nd Born approximation, one can conclude that the 2nd Born approximation breaks down in the unitary limit as

$$\lim_{a_0\to-\infty}\frac{E^{2B}_{\infty}}{A}(k_F)=\infty\ . \tag{3.104}$$

Numerical analysis

The exact calculations of the energy per particle derived in Sec. 3.5.1 and Sec. 3.5.2 are compared to the results obtained from the Fortran and the Mathematica code. In Fig. 3.19 calculations are plotted in the HF and the ladder approximations for $\Lambda\in[4k_F,8k_F]$ and $\rho_0=0.08,\ 0.16\ \text{fm}^{-3}$ on the basis of an exact renormalization in the two-body sector[17]. Regarding the Hartree-Fock approximation, the perfect agreement confirms the numerical accuracy and stability of the Fortran code in this case. The HF calculation in the Fortran code is, thus, accurate up to the numerical precision tested to be of the order of 0.5 MeV in Sec. 3.4.3. However, the analytical results obtained in the ladder approximation disagree by more than 5 MeV per particle from the numerical calculation in the Fortran code. This disagreement is an order of magnitude larger than the numerical precision. Consequently, the implementation of the ladder approximation in the Fortran code is not sufficiently accurate to conclude about the Λ dependence of the energy per particle.

One can however use the cross-check with analytical calculations to detect the source of numerical inaccuracy of the Fortran code. In the algorithms, the only differences between the HF and the ladder approximations are localized in the T-matrix computation. Analysing HF calculations, as presented in Tab. 3.1, it turns out that the real part of $G^{(\rho,2)+}(\Omega)$ is actually not necessary to compute the energy per particle as the T-matrix is purely real [70]. Conversely, in the ladder approximation $\mathrm{Re}\,G^{(\rho,2)+}(\Omega)$ is crucial both to compute the T-matrix and the energy per particle. As this is the only main difference between HF and ladder calculations, Eq. (3.41) used to compute $\mathrm{Re}\,G^{(\rho,2)+}(\Omega)$ is further analysed.

The dispersion relation (3.41) is largely used in the different state-of-the-art implementations of SCGF for nuclear matter [12, 69, 70, 71, 72]. However the code used here relies heavily on the background-quasiparticle decomposition of the spectral function. Analytical calculations

[17]The choice of $\Lambda>4k_F$ is made to ensure that the expansion in $\frac{2\sqrt{2}k_F}{\Lambda}$, used in analytical derivations, is well justified.

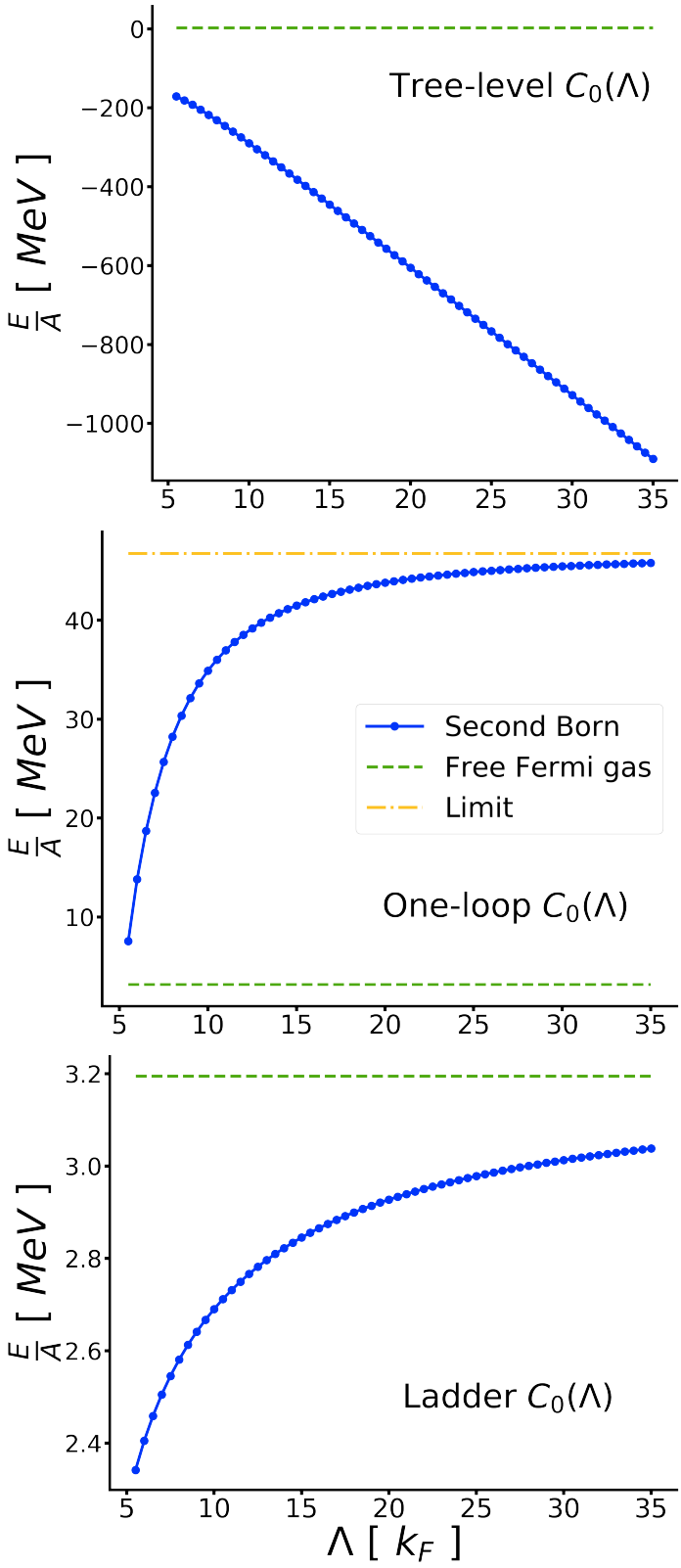

Figure 3.18. Second Born (non-self consistent) computation of the energy per particle for $k_F = 100$ MeV. The upper-panel uses a $C_0(\Lambda)$ computed at tree-level. The middle-panel takes into account the counter-term computed at one-loop as in Eq. (3.102). The lower-panel uses $C_0(\Lambda)$ from an exact renormalization in the two-body sector.

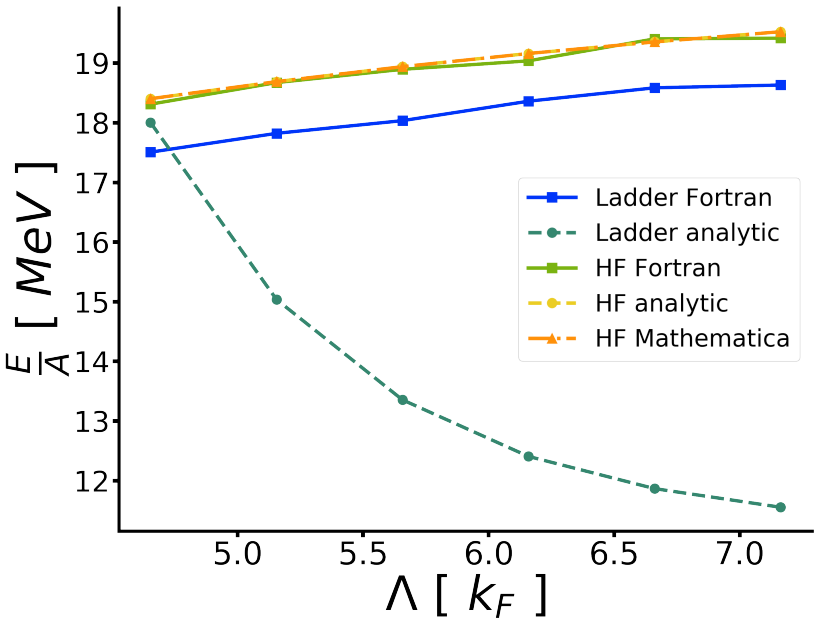

Figure 3.19. Energy per particle in the HF and the ladder approximations at $\rho_0 = 0.08$ fm^{-3} ($k_F = 263$ MeV) with $C_0(\Lambda)$ renormalized exactly in the two-body sector. Λ is varied in the range $[4k_F, 8k_F]$.

are realized for the unperturbed spectral function i.e. with the Dirac spectral function in (3.20). In this case the analytical treatment of quasiparticle peaks in the Fortran code is critical. A careful analysis of the Fortran code reveals that such treatment is indeed done analytically at every step except for the evaluation of the dispersion relation (3.41). In the case of a Dirac spectral function (3.20), Eq. (3.41) reads as

$$\mathrm{Re}\, G^{(\rho,2)+}_{\substack{\vec{p}_1\sigma_1\vec{p}_2\sigma_2\\ \vec{p}_1\sigma_1\vec{p}_2\sigma_2}}(\Omega) = \mathcal{P}\int_{-\infty}^{+\infty}\frac{\mathrm{d}\Omega'}{2\pi}\,\frac{(2\pi)\delta\left(\Omega' - \frac{p^2}{m}\right)}{\Omega - \Omega'} \times\left[1 - \theta\left(\mu - \frac{p^2}{2m}\right) - \theta\left(\mu + \frac{p^2}{m} - \Omega'\right)\right]\delta_{\sigma_1\sigma_1'}\delta_{\sigma_2\sigma_2'}\ , \quad (3.105)$$

which is mathematically ill-defined. Consequently, it is concluded that the Fortran code presents a critical numerical instability in relation to Eq. (3.41). In order to bypass this instability, the calculation of $G^{(\rho,2)+}(\Omega)$ for a quasiparticle propagator should be done analytically using the relation

$$\left(\frac{1}{x + i\eta}\right)^2 = \mathcal{P}\frac{1}{x^2} + i\pi\delta'(x)\ , \quad (3.106)$$

as mentioned in [82]. Alternatively, the instability can be understood as the presence of a pole in the two-body Green's function which could be addressed using numerical tricks as in Brueckner-Hartree-Fock calculations, see e.g. [74]. Such an implementation is however out of the scope of this thesis.

As discussed in this section, numerical accuracy is key to ensure the renormalization invariance of observables computed numerically. The cancellations between counter-terms introduced

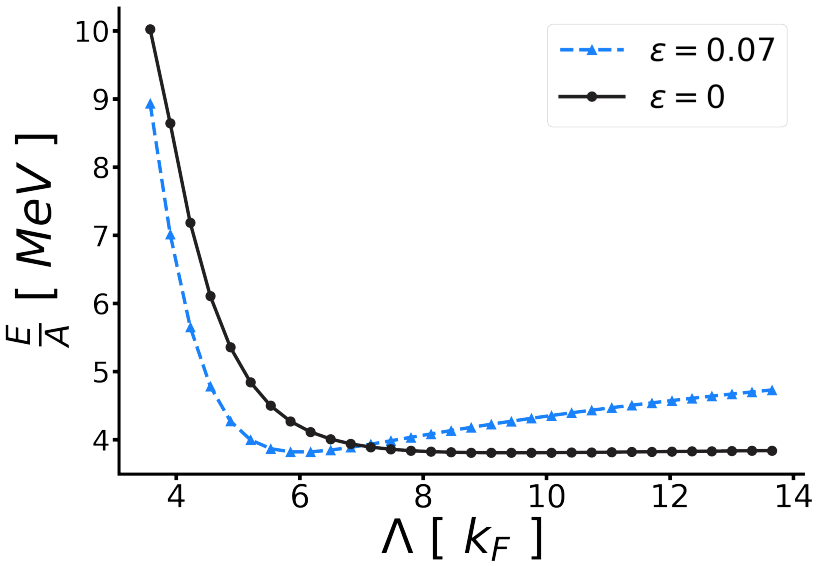

Figure 3.20. Energy per particle in the ladder approximations for $\Lambda \in [3k_F, 14k_F]$ at $\rho_0 = 0.016$ fm^{-3} ($k_F = 153$ MeV) and $C_0(\Lambda)$ renormalized exactly in the two-body sector. Dashed line represent the calculation for $\epsilon = 0.07$ in Eq. (3.107).

in $C_0(\Lambda)$ and the UV divergences must be treated with care in order to extrapolate the calculation in the limit $\Lambda \to +\infty$. In this respect, testing the renormalization invariance of observables provides a powerful tool to assess numerical instability which might have remained un-noticed. In general, numerical computations of renormalization invariant observables put strong constraints on the necessary numerical accuracy of the implementation.

To illustrate this numerical sensitivity Fig. 3.20 displays the Λ dependence of the energy per particle calculated analytically in the ladder approximation with/without a small artificial error introduced in the ladder calculation. To simulate an artificial error similar to the one in the Fortran code, a factor $(1-\epsilon)$ is introduced in front of the one-loop calculations prior to performing the resummation i.e. B_i is replaced by

$$B_i^{\text{err}} \equiv (1-\epsilon)B_i \ . \tag{3.107}$$

As soon as $\epsilon \neq 0$ the energy per particle converges to the free Fermi gas limit as in Eq. (3.92) instead of converging to the non-trivial limit (3.91). Furthermore, this error does not only compromise the large Λ behaviour but also significantly modifies the result for small Λ values.

It is a difficult task to estimate numerically if the Hamiltonian $H_{\not\pi}$ is renormalized consistently with the many-body approximation without further *a priori* knowledge. In the next chapter, a systematic procedure is derived to renormalize the Hamiltonian $H_{\not\pi}$ consistently with many-body approximations expressed as a truncation on Feynman diagrams in terms of vacuum/medium insertion or in terms of particle/hole propagators.

Chapter 4.

Ultraviolet divergences of many-body diagrams

In the previous chapter, numerical SCGF calculations demonstrated the criticality of the numerical accuracy to assess the renormalization invariance of many-body observables. Deriving *a priori* the set of counter-terms necessary to renormalize SCGF calculations would be an important step forward to test the validity of sophisticated many-body approximations within the frame of $\not{\pi}$EFT. As a matter of fact, analytical calculations with different renormalizations of $H_{\not{\pi}}$ seems to indicate the possibility to derive a systematic procedure to lead to renormalization invariant many-body observables.

The object of this chapter is to investigate such systematic procedures. In Sec. 4.1, UV divergences arising from diagrams in the in-medium formalism and their consequences on the renormalization of the Hamiltonian are studied in a systematic way. In Sec. 4.2, the study is extended to diagrams in the more general particle-hole formalism. This opens the path to renormalize consistently the Hamiltonian with various many-body approximations, namely whenever they can be expressed as a sum of particle-hole diagrams. Eventually, practical examples are studied in Sec. 4.3 before discussing some of the consequences of the present work in Sec. 4.4.

4.1. Ultraviolet divergences in many-body calculations

In this section, the general problem of the renormalization of the Hamiltonian when computing many-body observables is introduced. Then, a general procedure is derived in the medium-insertion formalism used in Sec. 3.5. The focus is on UV divergences so that any potential problem occurring in the infrared (IR) limit is neglected and considered out of the scope of this thesis.

4.1.1. General problem

The perturbation theory used in Secs. 4.1-4.2 is the one described in Sec. 3.1.1 so that the Hamiltonian is partitioned as in Eqs. (3.1), i.e.

$$H_{\not{\pi}}^{\mathrm{LO}} = H_0 + H_1^{\mathrm{LO}} \ ,$$
$$H_0 \equiv \sum_{\vec{p}\sigma} \frac{p^2}{2m} a^\dagger_{\vec{p}\sigma} a_{\vec{p}\sigma} \ ,$$

$$H_1^{\rm LO} \equiv \sum_{\sigma_1\sigma_2} \sum_{\substack{\vec{p}_1\vec{p}_2 \\ \vec{p}_1'\vec{p}_2'}} h^{22}_{\vec{p}_1\vec{p}_2\vec{p}_1'\vec{p}_2'} \; a^\dagger_{\vec{p}_1'\sigma_1} a^\dagger_{\vec{p}_2'\sigma_2} a_{\vec{p}_1\sigma_1} a_{\vec{p}_2\sigma_2} \; .$$

The goal is to find a general procedure to compute counter-terms appearing in $H_1^{\rm LO}$ that are necessary to take into account in the computation of many-body observables for a particular many-body approximation. In order to comply with the *ab initio* philosophy, counter-terms should be independent of the nuclear system studied, i.e. they should not depend on the A-body sector studied[1]. In the case of infinite neutron matter this constrains counter-terms to be independent of the density ρ_0 or equivalently of the Fermi momentum k_F[2].

On a more fundamental level, the EFT approach decouples UV effects by incorporating them in the coupling constants. Introducing medium-dependent counter-terms would entangle UV effects integrated in the coupling constant with collective low momentum effects. Such a mixing would obscure the naturalness assumptions regarding the scaling of coupling constants in power of the breakdown scale as in Eq. (2.23). In this case NDA power-counting rules (and its modification) are no longer trivial to justify. Eventually, regarding practical aspects, the computation of counter-terms is in general simpler in few-body sectors and could even be realized analytically for $\not\pi$EFT. Conversely, many-body calculations often rely on numerically involved approximations and computing counter-terms at this order would be both numerically involved and error prone. For instance, the case of the ladder resummation in Sec. 3.5.1 is illuminating. The energy per particle of infinite neutron matter in Eq. (3.83) could be used to compute directly counter-terms in $C_0(\Lambda)$ by matching Eq. (3.83) to the experimental value at a fixed density. However, beside introducing a k_F dependence in $C_0(\Lambda)$ (thus in $H_{\not\pi}$), it is much easier to compute the necessary counter-terms as in Sec. 2.2.3.

In the next subsection, an example of such a systematic procedure is derived on the basis of many-body approximations that can be recast as a set of Feynman diagrams made out of vacuum propagators and medium-insertions as described in Sec. 3.5.

4.1.2. Analysis of medium-insertion diagrams

In this subsection, we focus on the computation of the k-body Green's function in the perturbation theory defined in Eqs. (3.1). The reference state is the Slater determinant $|\Phi_0^\rho\rangle$ and the unperturbed propagator is conveniently written as a vacuum and a medium-insertion component as in Eq. (3.53a), i.e.

$$\begin{aligned} iG^{(\rho,1)0}_{\vec{p}\sigma\vec{p}'\sigma'}(\omega) &= \left[\frac{i}{\omega - \frac{p^2}{2m} + i\eta} - 2\pi\delta\left(\omega - \frac{p^2}{2m}\right)\theta\left(k_F - p\right)\right](2\pi)^3\delta\left(\vec{p}-\vec{p}'\right)\;\delta_{\sigma\sigma'} \\ &\equiv iG^{(0,1)0}_{\vec{p}\sigma\vec{p}'\sigma'}(\omega) + iG^{(M,1)0}_{\vec{p}\sigma\vec{p}'\sigma'}(\omega) \; . \end{aligned}$$

[1]Of course, this statement does not concern counter-terms that are strictly zero in certain A-body sectors and non-zero in others. For example, the three-body counter-term appearing at LO in $\not\pi$EFT cannot be identified in the two-body systems as it is strictly zero by construction.

[2]More generally counter-terms must be independent of the medium. For instance, they must also be independent of the temperature T of the system.

General integrals

Formally, the exact k-body Green's function reads as

$$i^k G^{(\rho,k)}_{\substack{\mu_1\dots\mu_k\\ \nu_1\dots\nu_k}}(\omega_{\mu_1}\dots\omega_{\mu_k},\omega_{\nu_1}\dots\omega_{\nu_k}) = \sum_{\mathcal{G}^{(\rho,k)}\in\mathcal{S}^{(\rho,k)}_{\text{Exact}}} \mathcal{A}^{\mathcal{G}^{(\rho,k)}}_{\substack{\mu_1\dots\mu_k\\ \nu_1\dots\nu_k}}(\omega_{\mu_1}\dots\omega_{\mu_k},\omega_{\nu_1}\dots\omega_{\nu_k}) \ , \tag{4.1}$$

where $\mathcal{S}^{(\rho,k)}_{\text{Exact}}$ is the set of all diagrams, made out of the complete unperturbed propagator $iG^{(\rho,1)0}$. Expanding the propagator in Eq. (1.62) on the basis of Eq. (3.53a), each Feynman amplitude corresponds to the sum of amplitudes associated to diagrams made out of vacuum propagators $iG^{(0,1)0}$ and medium-insertions $iG^{(M,1)0}$. Many-body approximations considered here consist in choosing a subset $\mathcal{S}^{(\rho,k)}_{\text{MB}}$ of all possible diagrams made out of vacuum propagators and medium-insertions so that the approximate k-body Green's function is computed as

$$i^k G^{(\rho,k)\text{MB}}_{\substack{\mu_1\dots\mu_k\\ \nu_1\dots\nu_k}}(\omega_{\mu_1}\dots\omega_{\mu_k},\omega_{\nu_1}\dots\omega_{\nu_k}) \equiv \sum_{\mathcal{G}^{(\rho,k)}\in\mathcal{S}^{(\rho,k)}_{\text{MB}}} \mathcal{A}^{\mathcal{G}^{(\rho,k)}}_{\substack{\mu_1\dots\mu_k\\ \nu_1\dots\nu_k}}(\omega_{\mu_1}\dots\omega_{\mu_k},\omega_{\nu_1}\dots\omega_{\nu_k}) \ . \tag{4.2}$$

Focusing on one diagram $\mathcal{G}^{(\rho,k)}_n$ with n vertices belonging to $\mathcal{S}^{(\rho,k)}_{\text{MB}}$, the associated amplitude reads from Eq. (1.62) as

$$\begin{aligned}
&\mathcal{A}^{\mathcal{G}^{(\rho,k)}_n}_{\substack{\mu_1\dots\mu_k\\ \nu_1\dots\nu_k}}(\omega_{\mu_1}\dots\omega_{\mu_k},\omega_{\nu_1}\dots\omega_{\nu_k}) = \\
&(-1)^\sigma \frac{(-i)^n}{n!}\sum_\lambda \frac{h^{22}_{\lambda\dots\lambda}}{(2!)^2}\dots\frac{h^{22}_{\lambda\dots\lambda}}{(2!)^2}\int\frac{\mathrm{d}\omega_\lambda}{2\pi}\dots\prod_{i=1}^n 2\pi\delta\left(\pm\omega_\lambda\dots-\omega_\mu\dots+\omega_\nu\dots\right) \\
&\qquad\times\prod_{e\in I^{(0)}} iG^{(0,1)0}_{\lambda\lambda}(\omega_\lambda)\prod_{e\in E^{(0)}_{in}} iG^{(0,1)0}_{\lambda\nu}(\omega_\nu)\prod_{e\in E^{(0)}_{out}} iG^{(0,1)0}_{\mu\lambda}(\omega_\mu) \\
&\qquad\times\prod_{e\in I^{(M)}} iG^{(M,1)0}_{\lambda\lambda}(\omega_\lambda)\prod_{e\in E^{(M)}_{in}} iG^{(M,1)0}_{\lambda\nu}(\omega_\nu)\prod_{e\in E^{(M)}_{out}} iG^{(M,1)0}_{\mu\lambda}(\omega_\mu) \ ,
\end{aligned} \tag{4.3}$$

where the distinction between vacuum propagators $iG^{(0,1)0}$ and medium-insertions $iG^{(M,1)0}$ is made explicitly via the set of internal vacuum (medium-insertion) lines $I^{(0)}$ ($I^{(M)}$), the set of external incoming vacuum (medium-insertion) lines $E^{(0)}_{in}$ ($E^{(M)}_{in}$) and the set of external outgoing vacuum (medium-insertion) lines $E^{(0)}_{out}$ ($E^{(M)}_{out}$).

Isolation of ultraviolet subdivergences with cut diagrams

The medium insertions involved in the amplitude Eq. (4.3) are non-zero only in a finite volume of the $(\omega,\vec{p})$ vector space and thus cannot generate UV divergences. Consequently, to prove the UV convergence of Eq. (4.3), it is sufficient to prove the convergence of the sub-integral with respect to the sole vacuum propagators. Formally, the sub-integral is isolated

by rewriting Eq. (4.3) as

$$
\begin{aligned}
&\mathcal{A}^{\mathcal{G}_n^{(\rho,k)}}_{\substack{\mu_1\dots\mu_k\\ \nu_1\dots\nu_k}}(\omega_{\mu_1}\dots\omega_{\mu_k},\omega_{\nu_1}\dots\omega_{\nu_k}) = (-1)^{\sigma}\frac{(-i)^n}{n!}\\
&\quad\times\sum_{\lambda^{(M)}}\frac{h^{22}_{\lambda^{(M)}\dots\lambda^{(M)}}}{(2!)^2}\dots\frac{h^{22}_{\lambda^{(M)}\dots\lambda^{(M)}}}{(2!)^2}\\
&\qquad\times\int\frac{\mathrm{d}\omega_{\lambda^{(M)}}}{2\pi}\dots\prod_{i=1}^{n^{(M)}}2\pi\delta\left(\pm\omega_{\lambda^{(M)}}\dots-\omega_{\mu^{(M)}}\dots+\omega_{\nu^{(M)}}\dots\right)\\
&\qquad\quad\prod_{e\in I^{(M)}}iG^{(M,1)0}_{\lambda^{(M)}\lambda^{(M)}}(\omega_{\lambda^{(M)}})\prod_{e\in E^{(M)}_{in}}iG^{(M,1)0}_{\lambda^{(M)}\nu^{(M)}}(\omega_{\nu^{(M)}})\prod_{e\in E^{(M)}_{out}}iG^{(M,1)0}_{\mu^{(M)}\lambda^{(M)}}(\omega_{\mu^{(M)}})\\
&\qquad\quad\sum_{\lambda^{(0)}}\frac{h^{22}_{\lambda\dots\lambda}}{(2!)^2}\dots\frac{h^{22}_{\lambda\dots\lambda}}{(2!)^2}\int\frac{\mathrm{d}\omega_{\lambda^{(0)}}}{2\pi}\dots\prod_{i=1}^{n-n^{(M)}}2\pi\delta\left(\pm\omega_{\lambda}\dots-\omega_{\mu}\dots+\omega_{\nu}\dots\right)\\
&\qquad\qquad\times\prod_{e\in I^{(0)}}iG^{(0,1)0}_{\lambda^{(0)}\lambda^{(0)}}(\omega_{\lambda^{(0)}})\prod_{e\in E^{(0)}_{in}}iG^{(0,1)0}_{\lambda^{(0)}\nu^{(0)}}(\omega_{\nu^{(0)}})\prod_{e\in E^{(0)}_{out}}iG^{(0,1)0}_{\mu^{(0)}\lambda^{(0)}}(\omega_{\mu^{(0)}})\ ,
\end{aligned}
\tag{4.4}
$$

where labels with superscript (0) ((M)) are related to vacuum propagators (medium-insertion) and labels without superscript refer indifferently to labels attached to a vacuum propagator or a medium-insertion. In particular $n^{(M)}$ denotes the number of vertices to which only medium-insertions are attached. The sub-integrals containing the potential UV divergences then read as

$$
\begin{aligned}
&\sum_{\lambda}\frac{h^{22}_{\lambda\dots\lambda}}{(2!)^2}\dots\frac{h^{22}_{\lambda\dots\lambda}}{(2!)^2}\int\frac{\mathrm{d}\omega_{\lambda}}{2\pi}\dots\prod_{i=1}^{n-n^{(M)}}2\pi\delta\left(\pm\omega_{\lambda}\dots-\omega_{\mu}\dots+\omega_{\nu}\dots\right)\\
&\qquad\times\prod_{e\in I^{(0)}}iG^{(0,1)0}_{\lambda\lambda}(\omega_{\lambda})\prod_{e\in E^{(0)}_{in}}iG^{(0,1)0}_{\lambda\nu}(\omega_{\nu})\prod_{e\in E^{(0)}_{out}}iG^{(0,1)0}_{\mu\lambda}(\omega_{\mu})\ ,
\end{aligned}
\tag{4.5}
$$

where all labels with a superscript (M) inside the sub-integral are now written as external labels, i.e. they are rewritten as[3]

$$\lambda^{(M)}\longrightarrow\mu\text{ or }\nu \tag{4.6a}$$
$$\mu^{(M)}\longrightarrow\mu \tag{4.6b}$$
$$\nu^{(M)}\longrightarrow\nu\ , \tag{4.6c}$$

and labels with a superscript (0) are rewritten as

$$\lambda^{(0)}\longrightarrow\lambda \tag{4.6d}$$
$$\mu^{(0)}\longrightarrow\mu \tag{4.6e}$$
$$\nu^{(0)}\longrightarrow\nu\ . \tag{4.6f}$$

The substitution (4.6) is introduced to make manifest the relation of the potentially UV divergent sub-integral (4.5) to the amplitude of a Feynman diagram made out of vacuum

[3] $\lambda^{(M)}$ label becomes a μ (ν) label if it corresponds to an outgoing (incoming) line of its associated vertex.

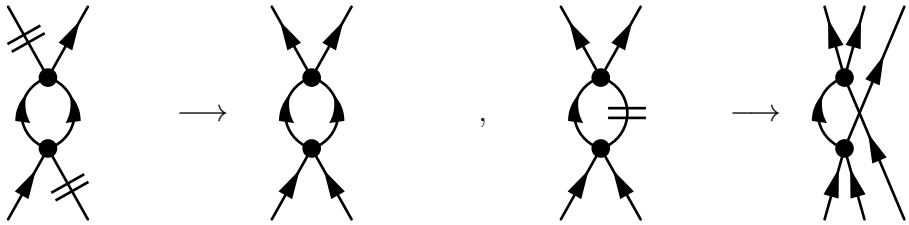

Figure 4.1. Examples of the procedure described in Sec. 4.1.2 to translate diagrams $\mathcal{G}^{(\rho,k)}$ into diagrams $\mathcal{G}^{(0,k+p)}$.

propagators $iG^{(0,1)0}$. To do so let us define the Feynman diagram made out of the same n vertices but with incoming lines $E_{in} \cup I^{(M)}$, outgoing lines $E_{out} \cup I^{(M)}$ and internal lines $I^{(0)}$. As each line in the aforementioned diagram corresponds to a vacuum propagator $iG^{(0,1)0}$, the diagram is denoted in the following as $\mathcal{G}_n^{(0,k+p)}$ where $p \equiv \#I^{(M)}$. Diagrammatically, $\mathcal{G}_n^{(0,k+p)}$ is obtained from the original diagram by cutting all internal medium-insertions in $\mathcal{G}_n^{(\rho,k)}$ and replacing them by an incoming and an outgoing external vacuum propagator. Additionally, external medium-insertions are replaced by external vacuum propagators to obtain a Feynman diagram contributing to the $(k+p)$-body Green's function[4]. In the following, this procedure is referred to as the *cutting procedure*. The amplitude of the cut diagram $\mathcal{G}_n^{(0,k+p)}$ reads as

$$\begin{aligned}
&\mathcal{A}^{\mathcal{G}_n^{(0,k+p)}}_{\substack{\mu_1\dots\mu_k\\ \nu_1\dots\nu_k}}(\omega_{\mu_1}\dots\omega_{\mu_k},\omega_{\nu_1}\dots\omega_{\nu_k}) = \\
&(-1)^{\sigma}\frac{(-i)^n}{n!}\sum_{\lambda}\frac{h^{22}_{\lambda\dots\lambda}}{(2!)^2}\dots\frac{h^{22}_{\lambda\dots\lambda}}{(2!)^2}\int\frac{\mathrm{d}\omega_\lambda}{2\pi}\dots\prod_{i=1}^{n}2\pi\delta\left(\pm\omega_\lambda\cdots-\omega_\mu\cdots+\omega_\nu\dots\right) \\
&\qquad\qquad\times\prod_{e\in I^{(0)}}iG^{(0,1)0}_{\lambda\lambda}(\omega_\lambda)\prod_{e\in E_{in}\cup I^{(M)}}iG^{(0,1)0}_{\lambda\nu}(\omega_\nu)\prod_{e\in E_{out}\cup I^{(M)}}iG^{(0,1)0}_{\mu\lambda}(\omega_\mu)\,.
\end{aligned} \tag{4.7}$$

The only difference between Eq. (4.5) and Eq. (4.7) consists of a product of the additional external propagator $iG^{(0,1)0}$ (obtained from the cutting procedure) and of $n^{(M)}$ vertex factors (the one that were only attached to medium-insertions). Those additional factors do not affect the UV behaviour as they are constant with respect to integrals on internal momenta/energies. Examples of this procedure are depicted in Fig. 4.1. The sets of diagrams $\mathcal{G}_n^{(0,k+p)}$ obtained for a range of p values (see below) from the set of diagrams $\mathcal{G}_n^{(\rho,k)} \in \mathcal{S}_{\mathrm{MB}}^{(\rho,k)}$ are denoted by $\mathcal{S}_{\mathrm{MB}}^{(0,k+p)}$. Any diagram $\mathcal{G}_n^{(0,k+p)} \in \mathcal{S}_{\mathrm{MB}}^{(0,k+p)}$ is ensured to remain linked as the cut of any internal line generates a pair of additional external lines.

Renormalization in $(k+p)$-body sectors

Consequently, $\mathcal{G}_n^{(0,k+p)}$ correspond to Feynman diagrams contributing to the $(k+p)$-body Green's function with respect to the particle vacuum $|0\rangle$ and the problem of renormalization invariance of the k-body Green's function with respect to the reference state $|\Phi_0^\rho\rangle$ is reduced

[4]One could avoid the replacement of external medium-insertion by considering directly amputated diagrams but this would introduce additional non-necessary notations.

to a renormalization problem for $(k+p)$-body Green's functions with respect to $|0\rangle$. Such a renormalization can typically be realized via a Bogoliubov-Parasiuk-Hepp-Zimmermann (BPHZ) procedure [83, 36, 37], which introduces counter-terms in the Hamiltonian to cancel UV divergences (see App. C for a brief overview of the procedure ; more details can be found in [37]).

Applying the BPHZ procedure for a diagram $\mathcal{G}_n^{(0,k+p)}$ consists of replacing the Feynman amplitude $\mathcal{A}^{\mathcal{G}_n^{(0,k+p)}}$ by its UV-finite counterpart $R^{\mathcal{G}_n^{(0,k+p)}}$ at the price of introducing counter-terms in the Hamiltonian. The BPHZ procedure corresponds to adding new diagrams to $\mathcal{G}_n^{(0,k+p)}$ (containing Λ dependent vertices, i.e. counter-terms) so that UV divergences cancel out. These additional diagrams correspond to Feynman amplitudes with vacuum propagators. The UV-finite Feynman amplitude reads as

$$R^{\mathcal{G}_n^{(0,k+p)}} = \mathcal{A}^{\mathcal{G}_n^{(0,k+p)}} + \sum_{\mathscr{F}\in\mathcal{F}_R(\mathcal{G}_n^{(0,k+p)})} \Omega^{\mathscr{F}} \ , \tag{4.8}$$

where the sum is realized on the set of non-empty restricted i-forest $\mathcal{F}_R(\mathcal{G}_n^{(0,k+p)})$ of $\mathcal{G}_n^{(0,k+p)}$[5] as defined in App. C. Any term in the sum corresponds to a Feynman diagram with at least one vertex corresponding to a counter-term. The amplitude associated to $\Omega^{\mathscr{F}}$ corresponds to the amplitude associated to the diagram $\mathcal{G}_n^{(0,k+p)}$ where each connected component of $\mathscr{F}$ is replaced by a counter-term with the same number of incoming/outgoing lines[6]. In particular, if $\mathscr{F}$ is made of only one A′-body renormalization part γ, $\Omega^{\mathscr{F}}$ corresponds to the amplitude associated to the diagram $\mathcal{G}_n^{(0,k+p)}$ where γ has been replaced by a A′-body vertex (being polynomial in external momenta of at most degree $D(\gamma)$, see for example Sec. 5.8 of Ref [84]). From now, as a shorthand notation, a diagram where an i-forest $\mathscr{F}$ is pictured with boxes will represent directly the amplitude $\Omega^{\mathscr{F}}$. See Fig. 4.2 for an example on a one-loop diagram. The sets of additional diagrams containing counter-terms generated by the BPHZ procedure are denoted as $\mathcal{S}_{\mathrm{MB,ct}}^{(0,k+p)}$. Considering the total function $R^{\mathcal{G}_n^{(0,k+p)}}$ (instead of $\mathcal{A}^{\mathcal{G}_n^{(0,k+p)}}$) results in lowering the superficial degree of divergence of any UV divergent sub-diagram γ made of internal lines from $D(\gamma)\geq 0$ to $D^{\mathrm{BPHZ}}(\gamma)<0$ [35]. Following this procedure for any diagram $\mathcal{G}_n^{(0,k+p)}$ obtained by the cutting procedure leads to renormalization-invariant and UV-finite $(k+p)$-body Green's functions with respect to $|0\rangle$ while using only counter-terms computed in the $(k+p)$-body sector. To finish the renormalization procedure, one only needs to match the calculation of $(k+p)$-body Green's functions to experimental observables. For instance, as detailed in Sec. 1.2.2, poles of the two-time reduction of $(k+p)$-body Green's functions correspond to the eigenspectrum of the $(k+p)$-body nuclear system so that the matching equations read as

$$\lim_{\Lambda\to+\infty}\left(\sum_{\mathcal{G}^{(0,k+p)}\in\mathcal{S}_{\mathrm{MB}}^{(0,k+p)}\cup\mathcal{S}_{\mathrm{MB,ct}}^{(0,k+p)}} \mathcal{A}^{\mathcal{G}_n^{(0,k+p)}}_{\substack{\mu_1\ldots\mu_k\\ \nu_1\ldots\nu_k}}\right)^{-1}\left(\omega = E_m^{+(k+p)}\right) = 0 \ . \tag{4.9}$$

In practice, however, it is often more convenient to use only the topology of the diagrams with counter-terms generated by the BPHZ procedure and to computing both the Λ dependence and

[5]Here the original amplitude $\mathcal{A}^{\mathcal{G}_n^{(0,k+p)}}$ is made explicit to clarify that $R^{\mathcal{G}_n^{(0,k+p)}}$ is a sum of original and newly-generated Feynman diagrams.

[6]Diagrammatically, it means that each outermost box of the i-forest $\mathscr{F}$ is replaced by a counter-term.

the constant part directly with the matching equations of the $(k+p)$-body Green's functions (as done in Chap. 2 for the two-body Green's function) by requiring, for example,

$$\left(\sum_{\mathcal{G}^{(0,k+p)}\in\mathcal{S}_{\rm MB}^{(0,k+p)}\cup\mathcal{S}_{\rm MB,ct}^{(0,k+p)}} \mathcal{A}^{\mathcal{G}_n^{(0,k+p)}}_{\substack{\mu_1\ldots\mu_k\\ \nu_1\ldots\nu_k}}\right)^{-1}\left(\omega = E_m^{+(k+p)}\right) = 0\ . \tag{4.10}$$

Denoting as $p^{\max}$ the maximum[7] number of internal medium insertions for the complete set of diagrams $\mathcal{G}_n^{(\rho,k)} \in \mathcal{S}_{\rm MB}^{(\rho,k)}$, the renormalization invariance must be ensured for $(k+p)$-body Green's function with respect to $|0\rangle$ with $0 \leq p \leq p^{\max}$. For instance, the ladder summation considered in Sec. 3.5.1 considers diagrams with arbitrary large number of internal medium-insertions so that the renormalization problem concerns A′-body Green's function with A′ arbitrary large. Matching equations (4.9) or (4.10) seem, thus, not practical as they imply calculations in inconveniently large A′-body sectors.

However, in practice, the BPHZ procedure stipulates that only 1PI sub-diagrams that are superficially divergent, the so-called *renormalization parts*, must be considered. Considering only the set of renormalization parts can greatly simplify the renormalization problem. In the case where renormalization parts are A′-body sub-diagrams with $\mathrm{A}'_{\min} \leq \mathrm{A}' \leq \mathrm{A}'_{\max}$ the hope would be to find new matching equations such that calculations to compute counter-terms are confined in few-body sectors, ideally in A′-body sectors with $\mathrm{A}' \lesssim \mathrm{A}'_{\max}$. Then, all $(k+p)$-body Green's functions could be made renormalization invariant, regardless of the initial A-body system studied (provided $\mathrm{A}'_{\max}$ is independent of A). Due to a lack of time, this problem is out of the scope of this thesis and proper and explicit investigations remain to be done for the largest class of many-body approximations possible.

In the ladder approximation $\mathrm{A}'_{\max} = \mathrm{A}'_{\min} = 2$ and the problem is reduced back to the computation of counter-terms in the two-body sector, in agreement with the analytical results discussed in Sec. 3.5.3. An example of a two-body renormalization part included in a diagram $\mathcal{G}^{(0,2+1)}$ is depicted in Fig. 4.3. In fact in this particular case, the sum of diagrams with counter-terms can be absorbed by a redefinition of the bare two-body vertex into an effective two-body vertex incorporating all UV-divergences and all Λ dependent counter-terms as depicted in Fig. 4.4. Any cut diagram in the ladder approximation is then expressed as a tree diagram with effective two-body vertices. Thus, for any p the $(2+p)$-body Green's function is renormalization-invariant as it is expressed in terms of a sum of tree diagrams with only well-renormalized effective two-body vertices. Eventually, only two-body counter-terms were computed in the two-body sector (for example as in Sec. 2.2.3) to obtain renormalization-invariant $(2+p)$-body Green's functions[8].

Renormalization-invariant many-body observables

The diagrams obtained by the cutting procedure are made finite by adding diagrams generated via the BPHZ procedure. In order to transport the cancellation realized in $G^{(0,k+p)}$ back to $G^{(\rho,k)}$,

[7]Using two-body vertices only as is done here, $p^{\max}$ for a $n^{\rm th}$ order diagram of the k-body Green's function is bounded as $p^{\max} \leq 2n-k$.

[8]Similar reduction could be found for more complicated sets of diagrams $\mathcal{S}_{\rm MB}^{(0,k+p)}$ by introducing, similarly, the notion of effective vertices. Their detailed study is however out of the scope of this thesis.

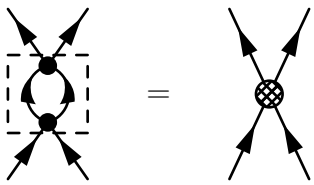

Figure 4.2. Representation, in the case of a one-loop diagram, of the amplitude $\Omega^{\mathscr{F}}$ both with the i-forest pictured on the original diagram and with an explicit counter-term vertex. The filled dot represents the bare vertex whereas the hatched vertex represents the counter-term associated to the i-forest represented by a box on the left-hand side diagram.

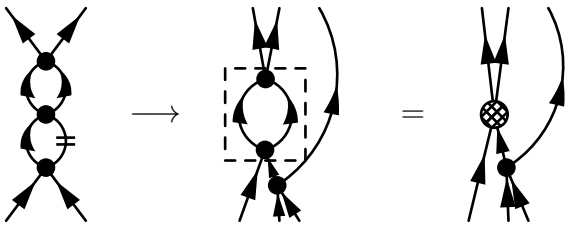

Figure 4.3. On the left, an example of a two-loop diagram contributing to $\mathcal{G}_3^{(\rho,2)}$ in the ladder approximation. In the middle, the diagram obtained by applying the cutting procedure to the diagram on the left. It corresponds to a third order three-body diagram $\mathcal{G}_3^{(0,2+1)}$. The only renormalization part of the diagram on the right is surrounded by a box and corresponds to a two-body sub-diagram i.e. it has only two incoming and two outgoing external lines. On the right, the corresponding second-order three-body diagram including the two-body counter-term is depicted.

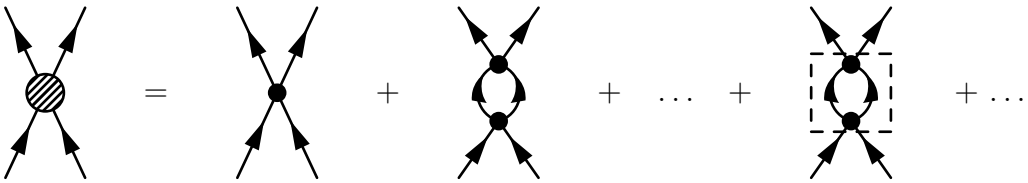

Figure 4.4. Representation of the effective two-body vertices discussed in the case of the ladder approximation. The shaded (full) vertex represents the effective (bare) vertex. The first ... denotes the sum of all ladders while the second ... denotes the sum of all diagrams with counter-terms, necessary to cancel out the UV-divergences.

one only needs to reverse the procedure by re-introducing medium-insertions. Algebraically, this consists in replacing the UV divergent sub-integral (4.5) by a UV finite renormalized amplitude in the full Feynman amplitude (4.4). Diagrammatically, this is done by closing previously cut lines by medium-insertions and by replacing external vacuum propagators with external medium-insertions as originally. Regarding additional diagrams generated through the BPHZ procedure, medium-insertions can be introduced identically as diagrams with counter-terms possess the same external legs as the original UV-divergent diagram[9]. Following this general prescription leads to renormalization-invariant k-body Green's functions with respect to $|\Phi_0^\rho\rangle$. Note that everything that has been done for $G^{(\rho,k)}$ remains true for $G^{(\mathrm{A},k)}$ with $\mathrm{A} \geq 1$.

Renormalization procedure for many-body Green's functions

The complete procedure to derive a renormalization-invariant k-body Green's function in a many-body approximation characterised by the set of Feynman diagrams $\mathcal{S}_{\mathrm{MB}}^{(\rho,k)}$ is now recapitulated. For any diagram $\mathcal{G}^{(\rho,k)} \in \mathcal{S}_{\mathrm{MB}}^{(\rho,k)}$

1. Apply the cutting procedure to $\mathcal{G}^{(\rho,k)}$ containing p ($0 \leq p \leq p^{\max}$), internal medium-insertions i.e. cut internal medium-insertions into external vacuum propagators and replace external medium-insertions by vacuum propagators. From this first step the associated diagram $\mathcal{G}^{(0,k+p)}$ is obtained.

2. Apply the BPHZ procedure to $\mathcal{G}^{(0,k+p)}$, which generates additional diagrams $\mathcal{G}_{\mathrm{MB,ct}}^{(0,k+p)}$ to cancel out UV divergences of $\mathcal{G}^{(0,k+p)}$. The set of diagrams $\mathcal{G}_{\mathrm{MB,ct}}^{(0,k+p)}$ is denoted as $\mathcal{S}_{\mathrm{MB,ct}}^{(0,k+p)}$.

3. Compute the counter-terms by matching the $(k+p)$-body Green's functions to observables in their approximations defined by $\mathcal{S}_{\mathrm{MB}}^{(0,k+p)} \cup \mathcal{S}_{\mathrm{MB,ct}}^{(0,k+p)}$.

4. For any diagram $\mathcal{G}_{\mathrm{MB,ct}}^{(0,k+p)} \in \mathcal{S}_{\mathrm{MB,ct}}^{(0,k+p)}$, external lines obtained via the cut (replacement) of internal medium-insertions are closed (replaced) by a medium-insertion leading to the diagram $\mathcal{G}_{\mathrm{ct}}^{(\rho,k)}$. The set of diagrams $\mathcal{G}_{\mathrm{ct}}^{(\rho,k)}$ is referred to as $\mathcal{S}_{\mathrm{MB,ct}}^{(\rho,k)}$.

5. The approximated UV-finite k-body Green's function eventually reads as

$$i^k G^{(\rho,k)\mathrm{MB}}_{\substack{\mu_1\ldots\mu_k\\ \nu_1\ldots\nu_k}}(\omega_{\mu_1}\ldots\omega_{\mu_k},\omega_{\nu_1}\ldots\omega_{\nu_k}) \equiv \sum_{\mathcal{G}^{(\rho,k)}\in\mathcal{S}_{\mathrm{MB}}^{(\rho,k)}\cup\mathcal{S}_{\mathrm{MB,ct}}^{(\rho,k)}} \mathcal{A}^{\mathcal{G}^{(\rho,k)}}_{\substack{\mu_1\ldots\mu_k\\ \nu_1\ldots\nu_k}}(\omega_{\mu_1}\ldots\omega_{\mu_k},\omega_{\nu_1}\ldots\omega_{\nu_k}) \ . \tag{4.11}$$

To illustrate this procedure, it is now applied to the second Born approximation.

[9] As a matter of fact, the whole procedure can be realized directly on the diagrams $\mathcal{G}_n^{(\rho,k)}$ by following the BPHZ procedure. Important modifications are that only sub-diagrams made out of vacuum propagators must be considered and that counter-terms to renormalization parts *must* be computed on diagrams resulting from the cutting procedure.

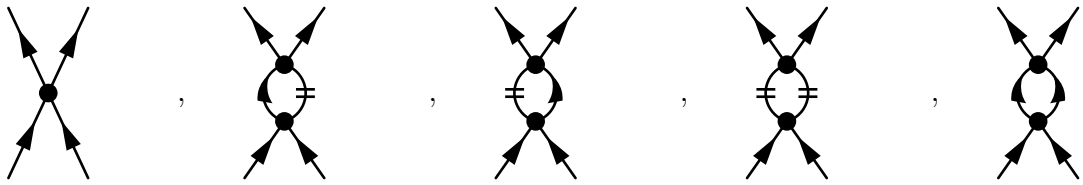

Figure 4.5. Diagrammatic representation of contributions to the two-body Green's function with respect to $|\Phi_0^\rho\rangle$ for the second Born approximation, before introducing counter-terms in the Hamiltonian.

Application to the second Born approximation

In the second Born approximation, the energy per particle is computed from the equal-time one- and two-body Green's function using Eq. (1.28). This is equivalent to computing one- and two-body Green's function at second order (in number of vertices) and closing external lines with additional medium-insertions. The additional closure with medium-insertions does not induce additional UV-divergences so that one can focus on the renormalization of one- and two-body Green's function at second order. No loop made of vacuum propagators can contribute to the one-body Green's function (by conservation of the number of particle). Let us, thus, now focus on the UV divergences in the two-body Green's function.

The set $\mathcal{S}_{2B}^{(\rho,2)}$ of diagrams contributing to the two-body Green's function with respect to $|\Phi_0^\rho\rangle$ are depicted in Fig. 4.5. Following step 1, the cutting procedure is applied. The sets of cut diagrams $\mathcal{S}_{2B}^{(0,2+p)}$ with $p = 0$, 1 and 2, are pictured in Fig. 4.6. In this example, the cutting procedure generates diagrams that are disconnected but always linked, hence ensuring that they do contribute to the $(2+p)$-body Green's function with respect to $|0\rangle$. Next, in step 2, the BPHZ procedure is applied to diagrams in $\mathcal{S}_{2B}^{(0,2+p)}$. Only the diagram with a loop contains a renormalization part (itself) and, thus, generates a new diagram with its associated counter-term. For step 3, the counter-term corresponds to the pure contact counter-term (without any derivative) computed in Sec. 2.2.2 and used in Sec. 3.5.3 to lead to a renormalization invariant energy per particle in the second Born approximation. The UV divergent diagram and the additional diagram generated by the BPHZ procedure are depicted in Fig. 4.7[10]. Step 4 and step 5 are trivial in this case as the only UV-divergent diagram contained 0 medium-insertions.

Eventually, as already derived in Sec. 3.5.3, the energy per particle obtained from the renormalized one- and two-body Green's functions corresponds to the second order approximation of the Lee-Yang expansion [79, 80, 81], i.e.

$$\frac{E^{2\mathrm{B}}}{A}(k_F) = \frac{k_F^2}{2m}\left\{\frac{3}{5} + \frac{2}{3\pi}(a_0 k_F) + \frac{4}{35\pi^2}(11 - \ln 2)(a_0 k_F)^2\right\} . \tag{4.12}$$

[10] One could have worked directly on vacuum-to-vacuum diagrams associated to the energy rather than on one- and two-body Green's functions. In this case, the complete set of diagrams resulting from the procedure derived above is pictured in Fig. 4.8.

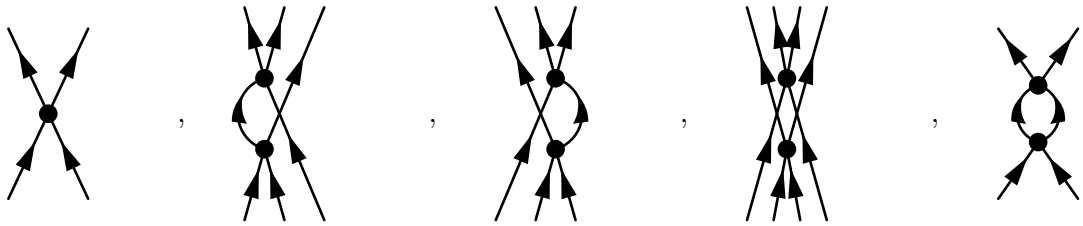

Figure 4.6. Diagrams obtained by applying the cutting procedure to the diagrams contributing to the two-body Green's function with respect to $|\Phi_0^\rho\rangle$ for the second Born approximation.

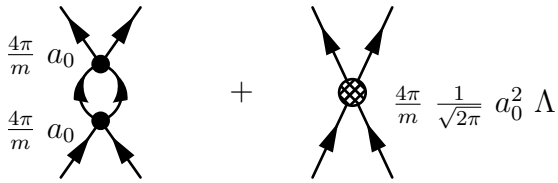

Figure 4.7. Diagrammatic representation of the sole UV divergent diagram in the second Born approximation and the additional diagram generated by the BPHZ procedure. The expression of the different vertices are displayed explicitly. The hatched vertex represents the counter-term computed in Eq. (2.54) while the filled vertex represents the bare two-body interaction (i.e. without any Λ dependent counter-term included).

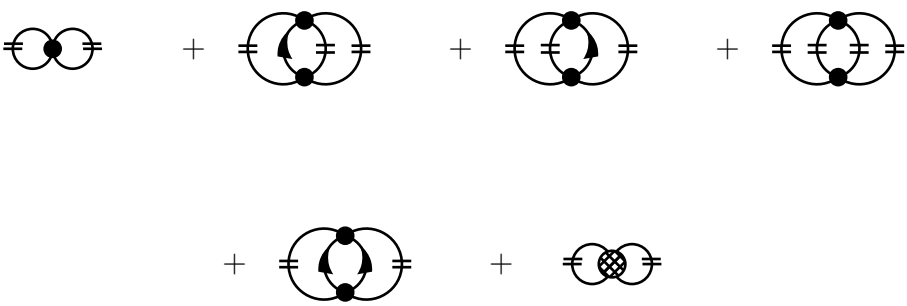

Figure 4.8. Diagrammatic representation of contributions to the energy per particle in the second Born approximation, after introducing the counter-term in the Hamiltonian following the procedure derived in Sec. 4.1. For clarity counter-terms and bare vertices are explicitly separated. The filled (hatched) vertex represents the bare (counter-term) two-body interaction.

Discussion

In this section a systematic procedure has been derived to renormalize the Hamiltonian $H_{\not{\pi}}$ consistently with many-approximations that can be recast as a set of Feynman diagrams made out of vacuum propagators and medium-insertions. However, the decomposition of the unperturbed one-body propagator as a vacuum part and a trivial medium-insertion part (Eq. (3.53a)) only holds in the particular framework considered here, i.e. the kinetic Hamiltonian as the unperturbed Hamiltonian and a Slater determinant as a reference state. Furthermore, many-body approximations cannot necessarily be recast as a truncation on diagrams made of vacuum propagators and medium-insertions (e.g. Brückner-Goldstone theory, see [85] for a review). In order to extend the analysis, a procedure based directly on particle-hole diagrams is now investigated. Such a decomposition is indeed more general as it holds for any partitioning of the Hamiltonian thanks to the Lehmann representation in Eq. (1.32). As a first step into that direction, the next section highlight a procedure to renormalize particle-hole diagrams for the same partitioning of the Hamiltonian and the same reference state as before.

4.2. Analysis of particle-hole diagrams

In this section, we focus again on the computation of the k-body Green's function in the perturbation theory defined in Eqs. (3.1) with $|\Phi_0^\rho\rangle$ as the reference state. However the unperturbed propagator is now kept in its particle-hole form (3.5), i.e.

$$\begin{aligned} iG^{(\rho,1)0}_{\vec{p}\sigma\vec{p}'\sigma'}(\omega) &= i\left[\frac{\theta\left(p-k_F\right)}{\omega-\frac{p^2}{2m}+i\eta}+\frac{\theta\left(k_F-p\right)}{\omega-\frac{p^2}{2m}-i\eta}\right](2\pi)^3\delta\left(\vec{p}-\vec{p}'\right)\ \delta_{\sigma\sigma'} \\ &\equiv iG^{(\rho,1)0+}_{\vec{p}\sigma\vec{p}'\sigma'}(\omega)+iG^{(\rho,1)0)-}_{\vec{p}\sigma\vec{p}'\sigma'}(\omega)\ . \end{aligned}$$

4.2.1. General integrals

Let us recall that the exact k-body Green's function reads as

$$i^k G^{(\rho,k)}_{\substack{\mu_1\ldots\mu_k\\ \nu_1\ldots\nu_k}}(\omega_{\mu_1}\ldots\omega_{\mu_k},\omega_{\nu_1}\ldots\omega_{\nu_k}) = \sum_{\mathcal{G}^{(\rho,k)}\in\mathcal{S}^{(\rho,k)}_{\text{Exact}}} \mathcal{A}^{\mathcal{G}^{(\rho,k)}}_{\substack{\mu_1\ldots\mu_k\\ \nu_1\ldots\nu_k}}(\omega_{\mu_1}\ldots\omega_{\mu_k},\omega_{\nu_1}\ldots\omega_{\nu_k})\ ,$$

where $\mathcal{S}^{(\rho,k)}_{\text{Exact}}$ is the set of Feynman diagrams made out of the complete unperturbed propagator $iG^{(\rho,1)0}$. Any diagram $\mathcal{G}^{(\rho,k)}\in\mathcal{S}^{(\rho,k)}_{\text{Exact}}$ is referred to as a *time-unordered diagram*. Similarly as in Sec. 4.1.2, expanding the complete unperturbed propagator $iG^{(\rho,1)0}$ with Eq.(3.5), the amplitude associated to a time-unordered diagram corresponds to the sum of amplitudes associated to particle-hole diagrams i.e. diagrams made out of particle $iG^{(\rho,1)0+}$ and hole $iG^{(\rho,1)0-}$ propagators. As opposed to time-unordered diagrams, particle-hole diagrams are referred to as *time-ordered diagrams*. Time-ordered diagrams are pictured similarly as time-unordered diagrams except that ascending (descending) lines now referred to as a particle (hole) propagator $iG^{(\rho,1)0+}$ ($iG^{(\rho,1)0-}$), see Fig. 4.9 for example of time-ordered diagrams.

Formally, the exact k-body Green's function reads as

$$i^k G^{(\rho,k)}_{\substack{\mu_1\ldots\mu_k\\ \nu_1\ldots\nu_k}}(\omega_{\mu_1}\ldots\omega_{\mu_k},\omega_{\nu_1}\ldots\omega_{\nu_k}) = \sum_{\mathcal{G}^{(\rho,k)}\in\tilde{\mathcal{S}}^{(\rho,k)}_{\text{Exact}}} \mathcal{A}^{\mathcal{G}^{(\rho,k)}}_{\substack{\mu_1\ldots\mu_k\\ \nu_1\ldots\nu_k}}(\omega_{\mu_1}\ldots\omega_{\mu_k},\omega_{\nu_1}\ldots\omega_{\nu_k})\ , \tag{4.13}$$

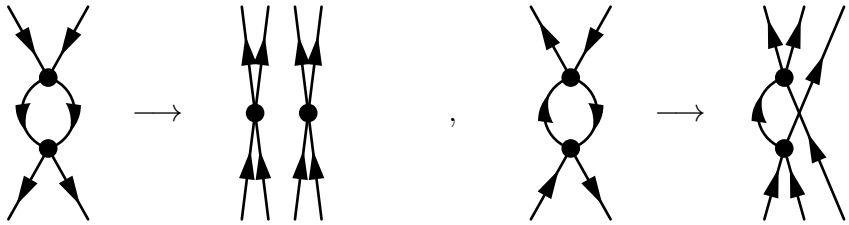

Figure 4.9. Examples of the cutting procedure applied to particle-hole diagrams $\mathcal{G}_2^{(\rho,k)}$ and resulting diagrams $\mathcal{G}_2^{(\rho,k+p)}$, with $p = 2$ (left) and $p = 1$ (right).

where $\tilde{\mathcal{S}}^{(\rho,k)}_{\text{Exact}}$ is the set of all time-ordered diagrams contributing to the k-body Green's function. Many-body approximations considered here consist of a choice of a subset $\tilde{\mathcal{S}}^{(\rho,k)}_{\text{MB}} \subset \tilde{\mathcal{S}}^{(\rho,k)}_{\text{Exact}}$ so that the approximated k-body Green's function reads as

$$i^k G^{(\rho,k)\text{MB}}_{\substack{\mu_1\dots\mu_k\\ \nu_1\dots\nu_k}}(\omega_{\mu_1}\dots\omega_{\mu_k},\omega_{\nu_1}\dots\omega_{\nu_k}) \equiv \sum_{\mathcal{G}^{(\rho,k)}\in\tilde{\mathcal{S}}^{(\rho,k)}_{\text{MB}}} \mathcal{A}^{\mathcal{G}^{(\rho,k)}}_{\substack{\mu_1\dots\mu_k\\ \nu_1\dots\nu_k}}(\omega_{\mu_1}\dots\omega_{\mu_k},\omega_{\nu_1}\dots\omega_{\nu_k}) \ . \tag{4.14}$$

Focusing on one diagram $\mathcal{G}_n^{(\rho,k)}$ with n vertices in $\tilde{\mathcal{S}}^{(\rho,k)}_{\text{MB}}$, the associated amplitude to $\mathcal{G}_n^{(\rho,k)}$ reads from Eq. (1.62) as

$$\begin{aligned}
&\mathcal{A}^{\mathcal{G}_n^{(\rho,k)}}_{\substack{\mu_1\dots\mu_k\\ \nu_1\dots\nu_k}}(\omega_{\mu_1}\dots\omega_{\mu_k},\omega_{\nu_1}\dots\omega_{\nu_k}) = \\
&(-1)^\sigma \frac{(-i)^n}{n!}\sum_\lambda \frac{h^{22}_{\lambda\dots\lambda}}{(2!)^2}\dots\frac{h^{22}_{\lambda\dots\lambda}}{(2!)^2}\int\frac{\mathrm{d}\omega_\lambda}{2\pi}\dots\prod_{i=1}^n 2\pi\delta\left(\pm\omega_\lambda\cdots-\omega_\mu\cdots+\omega_\nu\dots\right)\\
&\qquad\times\prod_{e\in I^+} iG^{(\rho,1)0+}_{\lambda\lambda}(\omega_\lambda)\prod_{e\in E^+_{in}} iG^{(\rho,1)0+}_{\lambda\nu}(\omega_\nu)\prod_{e\in E^+_{out}} iG^{(\rho,1)0+}_{\mu\lambda}(\omega_\mu)\\
&\qquad\times\prod_{e\in I^-} iG^{(\rho,1)0-}_{\lambda\lambda}(\omega_\lambda)\prod_{e\in E^-_{in}} iG^{(\rho,1)0-}_{\lambda\nu}(\omega_\nu)\prod_{e\in E^-_{out}} iG^{(\rho,1)0-}_{\mu\lambda}(\omega_\mu)\ ,
\end{aligned} \tag{4.15}$$

where the distinction between hole propagators $iG^{(\rho,1)0-}$ and particle propagators $iG^{(\rho,1)0+}$ is made explicitly via the set of internal particle (hole) lines I^+ (I^-), the set of external incoming particle (hole) lines E^+_{in} (E^-_{in}) and the set of external outgoing particle (hole) lines E^+_{out} (E^-_{out}).

As in Sec. 4.1.2, a cutting procedure can be carried out to isolate UV divergent components of the amplitude (4.15). Here, the only difference is that the cutting procedure is applied to hole lines instead of medium-insertions. To simplify the analysis, the cutting procedure is modified so that external hole propagators are replaced by particle propagators instead of vacuum propagators. This does not affect the analysis of UV divergences as it concerns only external propagators. An example of the cutting procedure applied to particle-hole diagrams is pictured in Fig. 4.9.

However, unlike in Sec. 4.1.2, the diagrams resulting from the cutting procedure are no longer diagrams contributing to $(k+p)$-body Green's functions with respect to $|0\rangle$ (where p denotes the number of internal hole lines that have been cut) but diagrams contributing to

$(k+p)$-body Green's functions with respect to $|\Phi_0^\rho\rangle$ hence denoted $\mathcal{G}^{(\rho,k+p)}$. Indeed, the lines of the resulting diagram denote now particle propagators $iG^{(\rho,1)0+}$ instead of vacuum propagators $iG^{(0,1)0}$ as in Sec. 4.1.2.

In order to relate the UV divergences of the resulting diagram $\mathcal{G}^{(\rho,k+p)}$ to those of a diagram $\mathcal{G}^{(0,k+p)}$, it is necessary to introduce a strong version of the power-counting theorem stated in Sec. 2.1.2, i.e. as derived by Weinberg [35]. In this case, the proof of convergence (after renormalization) of Feynman amplitudes is only dependent on the asymptotic coefficients of the propagators. In the next subsection, the definition of asymptotic coefficients of a multivariate function is briefly recalled, Weinberg's asymptotic theorem is stated in its general form and applied to Feynman amplitudes.

4.2.2. Asymptotic theorem

The UV convergence of Feynman amplitudes is analysed as the convergence problem of a multidimensional integral of a multivariate function. Here the main ingredients to the understanding of Weinberg's asymptotic theorem are introduced for a generic multivariate function. Eventually, Weinberg's asymptotic theorem is stated both in terms of general integrals and in terms of diagrams. For the complete proof and further discussion on Weinberg's asymptotic theorem see [35].

Asymptotic coefficients and multidimensional integrals

Let us first introduce the definition of asymptotic coefficients (provided they exist) of a function $f:\mathbb{R}^n\to\mathbb{C}$ as given in [35]. For any vector subspace $S=\left\{\vec{L}_1,\dots,\vec{L}_m\right\}$[11] of $\mathbb{R}^n$ with $m\leq n$ and $\vec{L}_1,\dots,\vec{L}_m$ being m independent $\mathbb{R}^n$-vectors, and any compact region $W\subset\mathbb{R}^n$, the asymptotic coefficients are defined as the numbers $\alpha\left(\left\{\vec{L}_1,\dots,\vec{L}_r\right\}\right)$ and $\beta\left(\vec{L}_1,\dots,\vec{L}_r\right)$ (with $1\leq r\leq m$) such that for every $\vec{C}\in W$

$$f\left(\eta_1\dots\eta_m\vec{L}_1+\eta_2\dots\eta_m\vec{L}_2+\dots+\eta_m\vec{L}_m+\vec{C}\right)= O\left(\eta_1^{\alpha(\{\vec{L}_1\})}(\ln\eta_1)^{\beta(\{\vec{L}_1\})}\,\eta_2^{\alpha(\{\vec{L}_1,\vec{L}_2\})}(\ln\eta_2)^{\beta(\{\vec{L}_1,\vec{L}_2\})}\times\dots \dots\times\eta_m^{\alpha(\{\vec{L}_1,\dots,\vec{L}_m\})}(\ln\eta_m)^{\beta(\{\vec{L}_1,\dots,\vec{L}_m\})}\right)\,, \tag{4.16}$$

if $\eta_1\dots\eta_m$ go independently to infinity. The asymptotic coefficients $\alpha(S)$ and $\beta(S)$ can be interpreted as the asymptotic coefficients $\alpha\left(\left\{\vec{L}\right\}\right)$ and $\beta\left(\left\{\vec{L}\right\}\right)$ for $\vec{L}$ a "typical" vector in S i.e. fixing $\eta_1\dots\eta_{m-1}$ sufficiently large and $\vec{C}\in W$,

$$f\left(\left[\eta_1\dots\eta_{m-1}\vec{L}_1+\eta_2\dots\eta_{m-1}\vec{L}_2+\dots+\eta_{m-1}\vec{L}_{m-1}+\vec{L}_m\right]\eta_m+\vec{C}\right)=O\left(\eta_m^{\alpha(S)}(\ln\eta_m)^{\beta(S)}\right)\,, \tag{4.17}$$

when η_m goes to infinity.

[11] For convenience, in this section, the bracket notation $\{\dots\}$ denotes the vector space spanned by the set of vectors considered.

Considering now integrals of a function f, the integration along the directions $\vec{L}_1, \dots, \vec{L}_r$ is defined as

$$f_{\vec{L}_1,\dots,\vec{L}_r}\left(\vec{X}\right) \equiv \int_{-\infty}^{+\infty} \mathrm{d}y_1 \ \dots \int_{-\infty}^{+\infty} \mathrm{d}y_r \ f\left(\vec{X} + y_1\vec{L}_1 + \dots + y_r\vec{L}_r\right) \ , \tag{4.18}$$

where $\vec{X}$ is a vector in $\mathbb{R}^n$. Thanks to Fubini's theorem, if $f_{\vec{L}_1,\dots,\vec{L}_r}\left(\vec{X}\right)$ exists (in the sense that the integral is absolutely convergent), the integration depends only on the vector space $I = \left\{\vec{L}_1, \dots, \vec{L}_r\right\}$ so that one defines

$$f_I\left(\vec{X}\right) \equiv \int_{\vec{Y}\in I} \mathrm{d}^r\vec{Y} \ f(\vec{X} + \vec{Y}) \equiv f_{\vec{L}_1,\dots,\vec{L}_r}\left(\vec{X}\right) \ . \tag{4.19}$$

Furthermore, $f_I\left(\vec{X}\right)$ depends only on the projection of $\vec{X}$ along I[12]. Choosing a subspace E such that $\mathbb{R}^n = I \oplus E$, the domain of definition of the function $f_I\left(\vec{X}\right)$ can be restricted to E.

In the case of a Feynman amplitude, the general integrand depends on $(\omega_1, \vec{p}_1, \dots)$ and is integrated on the internal energies and momenta. Therefore in this case, I denotes the vector space of internal (one-body) energies and momenta whereas the vector space E denotes the space of external (one-body) energies and momenta[13]. The general vector space $\mathbb{R}^n = I \oplus E$ denotes the vector space of all (one-body) energies and momenta (internal and external).

As an example, the asymptotic coefficients $\alpha\left(S\right)$ of the vacuum propagator

$$iG^{(0,1)0}_{\vec{p}\sigma}(\omega) = \frac{i}{\omega - \frac{p^2}{2m} + i\eta} \ ,$$

are now extracted. The vacuum propagator $iG^{(0,1)0}_{\vec{p}\sigma}(\omega)$ is interpreted as a multivariate function on $\mathbb{R}^4 = \{\vec{e}_\omega, \vec{e}_{p_x}, \vec{e}_{p_y}, \vec{e}_{p_z}\}$, so that[14]

$$f(\omega\vec{e}_\omega + p_x\vec{e}_{p_x} + p_y\vec{e}_{p_y} + p_z\vec{e}_{p_z}) \equiv iG^{(0,1)0}_{\vec{p}\sigma}(\omega) \ . \tag{4.20}$$

One can show that in this case, the asymptotic coefficients of the vacuum propagator α^0, read as

$$\alpha^0\left(S\right) = \begin{cases} -1 & \text{if } S = \{\vec{e}_\omega\} \\ -2 & \text{if } S = \{\vec{L}\} \text{ with } \vec{L} \notin \{\vec{e}_\omega\} \\ -2 & \text{if } \dim S \geq 2 \end{cases} \ . \tag{4.21}$$

Asymptotic theorem

With all the notations introduced before, the general asymptotic theorem follows.

If a function $f\left(\vec{X}\right)$ possesses asymptotic coefficients $\alpha\left(S\right), \beta\left(S\right)$ for any non-null subspace $S \subset \mathbb{R}^n$, if $f(\vec{X})$ is integrable for any finite region of $\mathbb{R}^n$ and if $D_I < 0$ where

$$D_I \equiv \max_{S'\subseteq I}\left[\alpha\left(S'\right) + \dim S'\right] \ , \tag{4.22}$$

[12]Any component of $\vec{X}$ in I can be absorbed in $\vec{Y}$ by a change of variable in the integral on I.

[13]Finite sum on spin-isospin indices are omitted here as they introduce only a finite linear combination of integrals on energies and momenta so that the conclusion on the UV behaviour is not impacted.

[14]The label σ is just considered as a fixed parameter so that it is dropped in the definition of $f(\omega\vec{e}_\omega + p_x\vec{e}_{p_x} + p_y\vec{e}_{p_y} + p_z\vec{e}_{p_z})$.

then $f_I\left(\vec{X}\right)$ *exists i.e. is absolutely convergent.*[15]

In order to apply this theorem easily to the convergence of Feynman amplitudes, it is rewritten in terms of Feynman sub-diagrams as detailed in [35]. This is done by associating to any sub-space of integration $S' \subseteq I$ a sub-diagram $\gamma \subseteq \mathcal{G}$. In particular $S' = I$ corresponds to the sub-diagram γ made of $\mathcal{G}$ itself without its external lines. The quantity $\alpha\left(S'\right) + \dim S'$ corresponds to the superficial degree of divergence of the associated sub-diagram γ of $\mathcal{G}$ so that having $D_I < 0$ is equivalent to having $D(\gamma) < 0$ for all $\gamma \subseteq \mathcal{G}$. Consequently, from Weinberg's asymptotic theorem, the power-counting theorem of Sec. 2.1.2 follows. *The Feynman amplitude associated to* $\mathcal{G}$ *is finite if* $D(\gamma) < 0$ *for any sub-diagram* $\gamma \subseteq \mathcal{G}$ *made of internal lines of* $\mathcal{G}$.

This theorem was already stated in Chap. 2. However, Zimmermann's proof of convergence of Feynman amplitudes relies on the particular expression of the propagator and can be applied only to the perturbation theory defined in Chap. 2. Conversely, Weinberg's asymptotic theorem is very powerful as it proves the convergence of Feynman amplitudes *with the sole knowledge of the asymptotic coefficients* $\alpha\left(S\right)$ *associated with the propagator*. It is crucial for applications to MBPT diagrams (such as $\mathcal{G}_n^{(\rho,k)}$) as the actual content of the propagator depends on the partitioning of the Hamiltonian and/or on the reference state. In the next subsection, the asymptotic theorem is used to complete the derivation of a systematic procedure to obtain renormalization invariant k-body Green's functions when computed in many-body approximations considered in Eq. (4.14).

4.2.3. General procedure

Reduction to a diagram $\mathcal{G}^{(0,k+p)}$

As discussed above, the cutting procedure introduced for diagrams made of vacuum propagators and medium-insertions can similarly be applied to particle-hole diagrams where hole lines play the same role as medium-insertions. However the resulting diagram contributes now to the $(k+p)$-body Green's functions (where p is the number of cut hole-line) computed with respect to $|\Phi_0^\rho\rangle$.

To go further one must notice that the unperturbed particle one-body Green's function $iG^{(\rho,1)0+}$ possesses the same asymptotic coefficients $\alpha\left(S\right)$ as the vacuum one-body Green's function $iG^{(0,1)0}$, i.e. for any sub-space S of $\{\vec{e}_\omega, \vec{e}_{p_x}, \vec{e}_{p_y}, \vec{e}_{p_z}\}$

$$\alpha^+\left(S\right) = \alpha^0\left(S\right) \ , \tag{4.23}$$

where $\alpha^+\left(S\right)$ correspond to the asymptotic coefficients of $iG_{\vec{p}\sigma}^{(\rho,1)0+}(\omega)$. Consequently, *any diagram made solely of unperturbed particle propagators is UV convergent if and only if the same diagram made of vacuum propagators is UV convergent.* Thanks to Weinberg's asymptotic theorem one can now focus on the study of a diagram $\mathcal{G}^{(0,k+p)}$ associated to $\mathcal{G}^{(\rho,k+p)}$ where the unperturbed particle propagators have been replaced by vacuum propagators. The resulting diagram contributes to the $(k+p)$-body Green's function with respect to $|0\rangle$.

As in Sec. 4.1.2, the UV divergences are canceled out by additional diagrams, containing counter-terms, generated by the BPHZ procedure. Similarly as in Eq. (4.8), the UV-finite

[15] In the original paper [35], further implications on the asymptotic behaviour of the integral $f_I\left(\vec{X}\right)$ are deduced but they are not stated here as they are not necessary for the developments in this thesis.

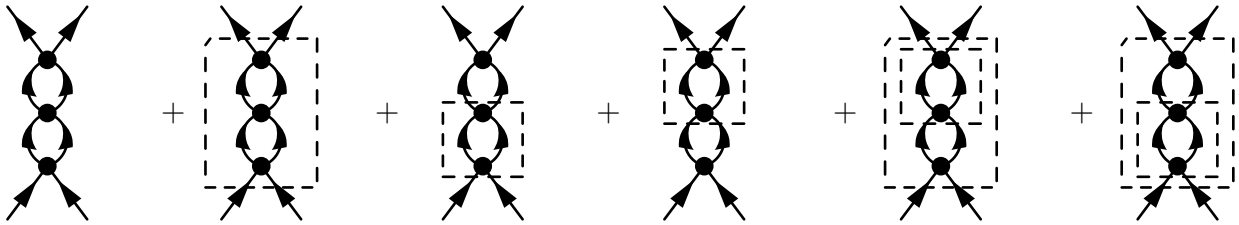

Figure 4.10. An example of renormalization of a two-loop diagram made of unperturbed particle propagators as in Eq. (4.25). To avoid multiplying notations for counter-terms, only i-forests are pictured with dashed boxes.

Feynman amplitude reads as

$$R^{\mathcal{G}^{(0,k+p)}} = \mathcal{A}^{\mathcal{G}^{(0,k+p)}} + \sum_{\mathscr{F}\in\mathcal{F}_R(\mathcal{G}^{(0,k+p)})} \Omega^{\mathscr{F}} \ . \tag{4.24}$$

In order to transport the cancellation of UV divergences to the diagram $\mathcal{G}^{(\rho,k+p)}$ made of unperturbed particle propagators, one introduces the amplitude

$$R^{\mathcal{G}^{(\rho,k+p)}} \equiv \mathcal{A}^{\mathcal{G}^{(\rho,k+p)}} + \sum_{\mathscr{F}\in\mathcal{F}_R(\mathcal{G}^{(\rho,k+p)})} \Omega^{(\rho)\mathscr{F}} \ , \tag{4.25}$$

where $\Omega^{(\rho)\mathscr{F}}$ denotes the amplitude associated to the same Feynman diagram as for $\Omega^{\mathscr{F}}$ except that lines denoting vacuum propagators are replaced by unperturbed particle propagators. Therefore, the additional Feynman amplitudes $\Omega^{(\rho)\mathscr{F}}$ contains the same counter-terms as in $\Omega^{\mathscr{F}}$ i.e. counter-terms computed, for instance, through a set of matching equations in the $(k+p)$-body sector via Eq. (4.10). An example of a two-loop UV divergent diagram along with the diagrams needed to cancel UV-divergences (both made of unperturbed particle propagators) are pictured in Fig. 4.10.

Thanks to Eq. (4.23), $R^{\mathcal{G}^{(\rho,k+p)}}$ is UV-finite if and only if $R^{\mathcal{G}^{(0,k+p)}}$ is UV-finite. Following this procedure leads to renormalization-invariant and UV-finite $(k+p)$-body Green's functions with respect to $|\Phi_0^\rho\rangle$ while using only counter-terms computed in the $(k+p)$-body sector. As mentioned in Sec. 4.1.2, counter-terms can, in some particular cases, be computed in A'-body sectors with $\mathrm{A}' < k+p$. Hopefully, for reasonable many-body approximations, $\mathrm{A}'_{\max} \lesssim 10$ with $\mathrm{A}'_{\max} \equiv \max \mathrm{A}'$. Eventually, as in Sec. 4.1.2, previously cut internal hole lines are closed whereas previously replaced external hole lines are re-introduced as originally in order to obtained UV finite k-body Green's function with respect to $|\Phi_0^\rho\rangle$.

General procedure

Let us recapitulate the full procedure to derive UV-finite k-body Green's functions with respect to $|\Phi_0^\rho\rangle$, in a many-body approximation defined by a truncated set of particle-hole diagrams $\tilde{\mathcal{S}}_{\mathrm{MB}}^{(\rho,k)}$, with counter-terms in the Hamiltonian computed in few-body sectors. For any diagram $\mathcal{G}^{(\rho,k)} \in \tilde{\mathcal{S}}_{\mathrm{MB}}^{(\rho,k)}$ with p internal hole lines,

1. Apply the cutting procedure to $\mathcal{G}^{(\rho,k)}$, i.e. cut internal hole lines into external particle propagators and replace external hole lines by particle propagators. From this first step the associated diagram $\mathcal{G}^{(\rho,k+p)}$ is obtained.

2. Replace all particle propagators by vacuum propagators in $\mathcal{G}^{(\rho,k+p)}$ leading to the diagram $\mathcal{G}^{(0,k+p)}$ contributing to the $(k+p)$-body Green's function with respect to $|0\rangle$.

The sets of diagrams $\mathcal{G}^{(0,k+p)}$ obtained is denoted as $\tilde{\mathcal{S}}^{(0,k+p)}_{\mathrm{MB}}$.

3. The renormalization of the Hamiltonian can be carried on as usually on $(k+p)$-body Green's functions with respect to $|0\rangle$ leading to the introduction of an additional set of diagrams with counter-terms denoted $\tilde{\mathcal{S}}^{(0,k+p)}_{\mathrm{MB,ct}}$. The counter-terms are typically computed by matching the $(k+p)$-body Green's functions to observables in their approximations defined by $\tilde{\mathcal{S}}^{(0,k+p)}_{\mathrm{MB}} \cup \tilde{\mathcal{S}}^{(0,k+p)}_{\mathrm{MB,ct}}$.

Then, for any diagram $\mathcal{G}^{(0,k+p)}_{\mathrm{ct}} \in \tilde{\mathcal{S}}^{(0,k+p)}_{\mathrm{MB,ct}}$,

4. Replace each vacuum propagator with a particle propagator. This generates the diagram $\mathcal{G}^{(\rho,k+p)}_{\mathrm{ct}}$.

5. External lines obtained via the cut (replacement) of internal hole lines are closed (replaced) by a hole line. This leads to the diagram $\mathcal{G}^{(\rho,k)}_{\mathrm{ct}}$.

The set of all diagrams $\mathcal{G}^{(\rho,k)}_{\mathrm{ct}}$ obtained is denoted as $\tilde{\mathcal{S}}^{(\rho,k)}_{\mathrm{MB,ct}}$.

6. The approximated UV-finite k-body Green's function eventually reads as

$$i^k G^{(\rho,k)\mathrm{MB}}_{\substack{\mu_1\ldots\mu_k\\ \nu_1\ldots\nu_k}}(\omega_{\mu_1}\ldots\omega_{\mu_k},\omega_{\nu_1}\ldots\omega_{\nu_k}) \equiv \sum_{\mathcal{G}^{(\rho,k)}\in\tilde{\mathcal{S}}^{(\rho,k)}_{\mathrm{MB}}\cup\tilde{\mathcal{S}}^{(\rho,k)}_{\mathrm{MB,ct}}} \mathcal{A}^{\mathcal{G}^{(\rho,k)}}_{\substack{\mu_1\ldots\mu_k\\ \nu_1\ldots\nu_k}}(\omega_{\mu_1}\ldots\omega_{\mu_k},\omega_{\nu_1}\ldots\omega_{\nu_k}) \ . \tag{4.26}$$

Again, the analysis realized for particle-hole diagrams $\mathcal{G}^{(\rho,k)}$ remains valid for particle-hole diagrams $\mathcal{G}^{(\mathrm{A},k)}$.

In the next section, the general procedure described in this section is applied to typical examples of practical interest for many-body calculations of nuclear observables.

4.3. Example of applications

In this section, as a first example of the procedure described in Sec. 4.2.3, the counter-terms for the one-body Green's function $iG^{(\rho,1)\mathrm{RPA}}$ computed in the Random Phase Approximation (RPA) are worked out[16]. As a second example, an extension of the procedure derived in Sec. 4.2.3 for a different partitioning of the Hamiltonian is investigated.

[16]In the literature, it is sometimes referred to as *particle-hole RPA* in order to distinguish it from other approximations such as particle-particle RPA.

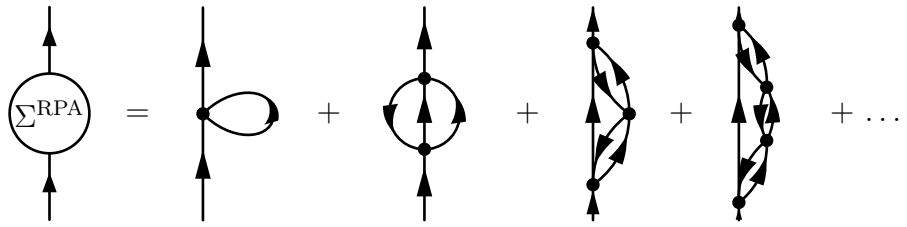

Figure 4.11. Examples of 1PI time-unordered diagrams (with undressed propagators) contributing to the one-body Green's function in the RPA approximation.

4.3.1. Random phase approximation

Historically, the RPA was first introduced in Ref. [86] as a way to deal with collective phenomena such as charge screening effect in electronic gas. Later, it was reformulated in Refs. [87, 88] as a particular resummation of Feynman diagrams, namely successive particle-hole excitations. Regarding nuclear systems, RPA and its extensions play an important role to take into account the coupling to collective excitations [89].

Here the Hamiltonian is partitioned as in Eqs. (3.1) and the reference state is chosen to be $|\Phi_0^\rho\rangle$ as defined in (3.1e). The RPA is formulated as an approximation to the self-energy in the Dyson equation (3.15). The 1PI time-unordered Feynman diagrams (in terms of unperturbed propagators) contributing to the self-energy in this approximation consist of the so-called ring diagrams. Examples of contributions at first, second, third and fourth orders (in terms of number of vertices) to the self-energy are pictured in Fig. 4.11. Once the counter-terms are correctly taken into account for the 1PI part of the one-body Green's function, no additional UV-divergences appear in the full (1PR) one-body Green's function. Thus, in the following, we focus only on 1PI diagrams.

Each 1PI time-unordered diagram contributing to the one-body Green's function is decomposed in a sum of time-ordered diagrams. In a time-unordered diagram, each line refers to the complete unperturbed propagator $iG^{(\rho,1)0}$. In a time-ordered diagram, an ascending (descending) line refers to the unperturbed particle (hole) propagator $iG^{(\rho,1)0+}$ ($iG^{(\rho,1)0-}$). Example of this decomposition is represented in Fig. 4.12. Consequently, the RPA can be recast as a truncation on the sum of particle-hole diagrams.

Applying the procedure in Sec. 4.2.3 to 1PI time-ordered Feynman diagrams contributing to the one-body Green's function, the set of diagrams with p hole lines, belonging to $\tilde{\mathcal{S}}_{\mathrm{RPA}}^{(\rho,1+p)}$, is explicitly pictured for examples at second, third and fourth orders in Tab. 4.1 and Tab. 4.2. In the RPA approximation, the resulting diagrams at n^{th} order in Tab. 4.2 contain no loop and, thus, are free of any UV-divergences. However, the resulting diagrams at n^{th} order in Tab. 4.1 read as one-loop diagrams (made of n internal lines) contributing to the n-body Green's function with respect to $|0\rangle$. With the notations of Sec. 4.2.3,

$$k = 1 \ , \tag{4.27a}$$

$$p = n - 1 \ . \tag{4.27b}$$

Following the BPHZ procedure for a diagram $\mathcal{G}_n^{(0,n)} \in \tilde{\mathcal{S}}_{\mathrm{RPA}}^{(0,n)}$ is straightforward. As $\mathcal{G}_n^{(0,n)}$ contains only one loop, any potential renormalization part γ must contain at least all n internal

Order n	$\mathcal{G}_n^{(\rho,1)} \in \tilde{\mathcal{S}}_{\mathrm{RPA}}^{(\rho,1)}$	p	$\mathcal{G}_n^{(0,1+p)} \in \tilde{\mathcal{S}}_{\mathrm{RPA}}^{(0,1+p)}$	$D(\mathcal{G}_n^{(0,1+p)})$
2		1	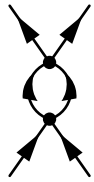	1
3		2	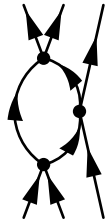	-1
3	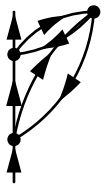	2		-1
4		3	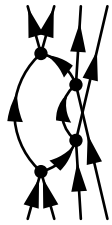	-3
4		3	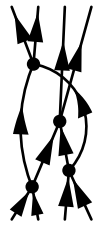	-3

Table 4.1. Examples of diagrams $\mathcal{G}_n^{(\rho,1)}$, with p hole lines and one particle loop, contributing to $G^{(\rho,1)}$ in the RPA approximation. Associated cut diagrams $\mathcal{G}_n^{(0,1+p)}$ and their superficial degree of divergence $D(\mathcal{G}_n^{(0,1+p))})$ are given.

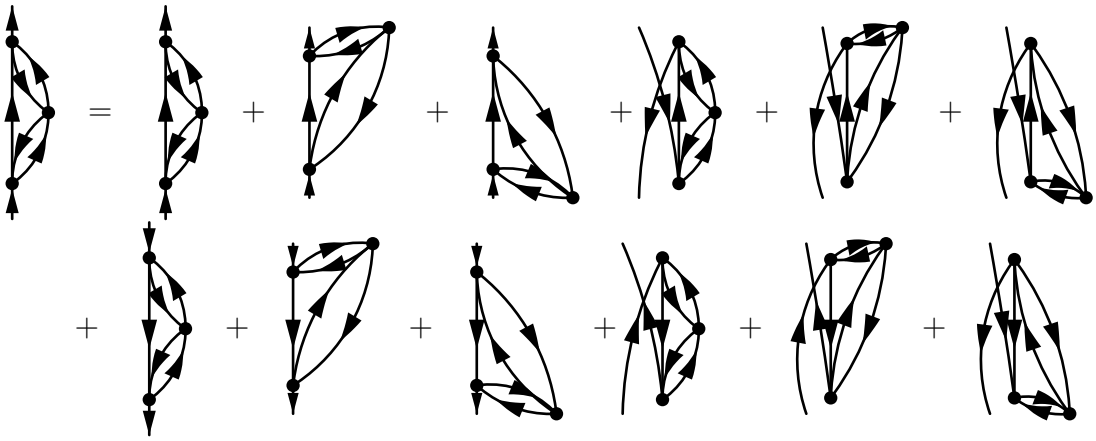

Figure 4.12. Example of decomposition of a time-unordered diagram into a sum of time-ordered diagrams. In a time-unordered diagram, any line refers to the complete propagator $iG^{(\rho,1)0}$. In a time-ordered diagram, any ascending (descending) line refers to the unperturbed particle (hole) propagator $iG^{(\rho,1)0+}$ ($iG^{(\rho,1)0-}$). Time-ordered diagrams in the first row contain one loop made of unperturbed particle propagators whereas time-ordered diagrams in the second row contain zero loop made of unperturbed particle propagators. Due to conservation of momentum, diagrams with one particle and one hole external leg vanish so that they are not represented. However, for a general partitioning of the Hamiltonian this is no longer the case.

Order n	$\mathcal{G}_n^{(\rho,1)} \in \tilde{\mathcal{S}}_{\mathrm{RPA}}^{(\rho,1)}$	p	$\mathcal{G}_n^{(0,1+p)} \in \tilde{\mathcal{S}}_{\mathrm{RPA}}^{(0,1+p)}$
2		2	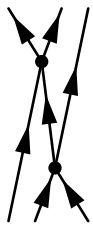
3		3	

Table 4.2. Examples of diagrams $\mathcal{G}_n^{(\rho,1)}$, with p hole lines and no particle loop, contributing to $G^{(\rho,1)}$ in the RPA approximation. Associated cut diagrams $\mathcal{G}_n^{(0,1+p)}$ are given.

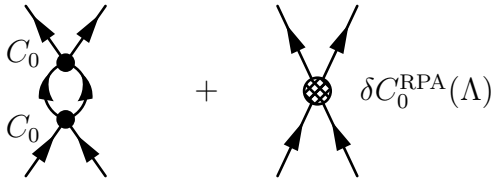

Figure 4.13. The only UV divergent diagram appearing in the RPA. Its associated counter-terms is added. The filled vertex represents the bare coupling constant C_0 while the hatched vertex represents the counter-term $\delta C_0^{\mathrm{RPA}}(\Lambda)$.

lines building the loop so that

$$L^\gamma = 1 \ , \tag{4.28a}$$
$$I^\gamma \geq n \ , \tag{4.28b}$$
$$n^\gamma \leq n \ , \tag{4.28c}$$

where L^γ is the number of loops, I^γ the number of internal lines and n^γ the number of vertices of γ. Using the topological identity $L^\gamma = I^\gamma - n^\gamma + 1$ implies that

$$L^\gamma = 1 \ , \tag{4.29a}$$
$$I^\gamma = n \ , \tag{4.29b}$$
$$n^\gamma = n \ . \tag{4.29c}$$

Eventually, the only potential renormalization part of $\mathcal{G}_n^{(0,n)}$ is $\mathcal{G}_n^{(0,n)}$ itself. From Eq. (2.39), the superficial degree of divergence of $\mathcal{G}_n^{(0,n)}$ for $n \geq 2$ reads as

$$D(\mathcal{G}_n^{(0,n)}) = 5 - 2n \ . \tag{4.30}$$

The only solution to $D(\mathcal{G}_n^{(0,n)}) \geq 0$ is to take $n = 2$. Consequently, there is only one UV divergent diagram which is pictured in Fig. 4.13 with its additional counter-term. This is actually the same diagram as in the case of the second Born approximation.

Eventually, from the application of the procedure derived in Sec. 4.2.3, one concludes that when applying the RPA to compute the one-body Green's function in $\not{\pi}$EFT at LO for neutron matter, an additional diagram is required with the pure contact counter-term

$$\delta C_0^{\mathrm{RPA}}(\Lambda) \equiv \frac{4\pi}{m} \frac{1}{\sqrt{2\pi}} \, a_0^2 \, \Lambda \ . \tag{4.31}$$

RPA 1PI time-unordered diagrams contributing to the one-body Green's function are pictured in Fig. 4.14 where the additional diagram cancelling the UV divergence is added. The result derived for $G^{(\rho,1)\mathrm{RPA}}$ can be carried on similarly for $G^{(\mathrm{A},1)\mathrm{RPA}}$ with $\mathrm{A} \geq 2$.

4.3.2. Hartree-Fock perturbation theory

Up to now all many-body approximations considered were formulated in a framework where the kinetic Hamiltonian was used as the unperturbed Hamiltonian. In this section, a different

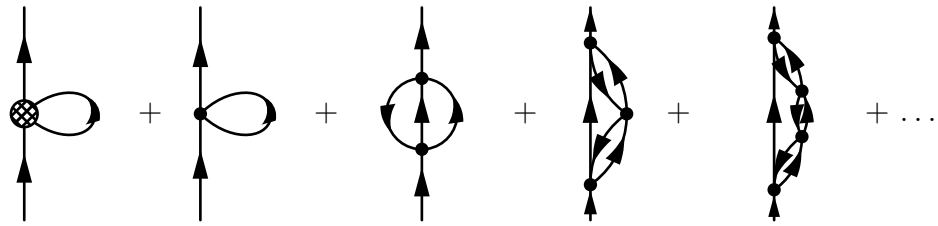

Figure 4.14. Time-unordered 1PI diagrams contributing to the one-body Green's function in the RPA approximation with the additional counter-terms derived following the procedure in Sec. 4.2.3.

partitioning of the Hamiltonian is considered to illustrate the flexibility of the procedure derived in Sec. 4.2.3.

Another partitioning of the Hamiltonian that plays an important role in nuclear physics is

$$H_{\not{\pi}} = H_0 + H_1 \ , \tag{4.32a}$$

$$H_0 \equiv \sum_{\vec{p}\sigma} e^{\rm HF}_{\vec{p}\sigma} a^\dagger_{\vec{p}\sigma} a_{\vec{p}\sigma} \ , \tag{4.32b}$$

$$H_1 \equiv \sum_{\vec{p}\sigma} \left(\frac{p^2}{2m} - e^{\rm HF}_{\vec{p}\sigma} \right) a^\dagger_{\vec{p}\sigma} a_{\vec{p}\sigma} + \sum_{\sigma_1\sigma_2} \sum_{\substack{\vec{p}_1\vec{p}_2 \\ \vec{p}_1'\vec{p}_2'}} h^{22}_{\vec{p}_1\vec{p}_2\vec{p}_1'\vec{p}_2'} \ a^\dagger_{\vec{p}_1'\sigma_1} a^\dagger_{\vec{p}_2'\sigma_2} a_{\vec{p}_1\sigma_1} a_{\vec{p}_2\sigma_2} \ , \tag{4.32c}$$

where $e^{\rm HF}_{\vec{p}\sigma}$ is defined in Eq. (3.30), namely

$$e^{\rm HF}_{\vec{p}\sigma} \equiv \frac{p^2}{2m} + \Sigma^{(\rho){\rm HF}}_{\vec{p}\sigma} \ ,$$

and the self-energy $\Sigma^{(\rho){\rm HF}}_{\vec{p}\sigma}$ is chosen to be the HF self-energy, i.e. solution of

$$\Sigma^{(\rho){\rm HF}}_{\vec{p}\sigma} = \frac{1}{2} \sum_{\vec{p}'} \sum_{\sigma'} \int_{-\infty}^{+\infty} \frac{{\rm d}\omega'}{2\pi} \ h^{22}_{\vec{p}\vec{p}'\vec{p}\vec{p}'} \ S^{(\rho,1){\rm HF}}_{\vec{p}'\sigma'}(\omega') \ \theta(\mu - \omega') \ , \tag{4.33a}$$

$$S^{(\rho,1){\rm HF}}_{\vec{p}\sigma}(\omega) = 2\pi\delta\left(\omega - (p^2 + \Sigma^{(\rho){\rm HF}}_{\vec{p}\sigma})\right) \ . \tag{4.33b}$$

MBPT with the partitioning (4.32) consists in expanding the k-body Green's function with respect to $|\Phi_0^\rho\rangle$ as a sum of Feynman diagrams with the HF propagator $iG^{(\rho,1){\rm HF}}$ as the unperturbed propagator, i.e. as a sum of amplitudes

$$\begin{aligned} &\mathcal{A}^{\mathcal{G}^{(\rho,k)}_n}_{\substack{\mu_1\ldots\mu_k \\ \nu_1\ldots\nu_k}}(\omega_{\mu_1}\ldots\omega_{\mu_k},\omega_{\nu_1}\ldots\omega_{\nu_k}) = \\ &(-1)^\sigma \frac{(-i)^n}{n!} \sum_\lambda \frac{h^{p_1q_1}_{\lambda\ldots\lambda}}{p_1!q_1!} \cdots \frac{h^{p_nq_n}_{\lambda\ldots\lambda}}{p_n!q_n!} \int \frac{{\rm d}\omega_\lambda}{2\pi} \cdots \prod_{i=1}^n 2\pi\delta\left(\pm\omega_\lambda \cdots - \omega_\mu \cdots + \omega_\nu \ldots\right) \\ &\qquad\qquad \times \prod_{e\in I} iG^{(\rho,1){\rm HF}}_{\lambda\lambda}(\omega_\lambda) \prod_{e\in E_{in}} iG^{(\rho,1){\rm HF}}_{\lambda\nu}(\omega_\nu) \prod_{e\in E_{out}} iG^{(\rho,1){\rm HF}}_{\mu\lambda}(\omega_\mu) \ , \end{aligned} \tag{4.34}$$

where the propagator $iG^{(\rho,1){\rm HF}}$ is defined in Eq. (3.32), namely

$$G^{(\rho,1){\rm HF}}_{\vec{p}\sigma}(\omega) = \frac{\theta\left(p - k_F\right)}{\omega - e^{\rm HF}_{\vec{p}\sigma} + i\eta} + \frac{\theta\left(k_F - p\right)}{\omega - e^{\rm HF}_{\vec{p}\sigma} - i\eta} \ .$$

More precisely, HF-MBPT(n) is defined as the many-body approximation for which the approximated k-body Green's function reads as

$$i^k G^{(\rho,k)\text{HF-MBPT}(n)}_{\substack{\mu_1\dots\mu_k\\ \nu_1\dots\nu_k}}(\omega_{\mu_1}\dots\omega_{\mu_k},\omega_{\nu_1}\dots\omega_{\nu_k}) \equiv \sum_{\mathcal{G}^{(\rho,k)}\in\tilde{\mathcal{S}}^{(\rho,k)}_{\text{HF-MBPT}(n)}} \mathcal{A}^{\mathcal{G}^{(\rho,k)}}_{\substack{\mu_1\dots\mu_k\\ \nu_1\dots\nu_k}}(\omega_{\mu_1}\dots\omega_{\mu_k},\omega_{\nu_1}\dots\omega_{\nu_k}) \ , \tag{4.35}$$

where $\tilde{\mathcal{S}}^{(\rho,k)}_{\text{HF-MBPT}(n)}$ is the set of particle-hole diagrams (with the propagator $iG^{(\rho,1)\text{HF}}$) with at most n vertices. More detail on HF-MBPT(n) can be found in classical textbooks such as [58].

In this section we study the UV behaviour of a diagram $\mathcal{G}^{(\rho,k)} \in \tilde{\mathcal{S}}^{(\rho,k)}_{\text{HF-MBPT}(n)}$ in order to derive the counter-terms required for HF-MBPT(n). To do so, the asymptotic coefficients $\alpha^{\text{HF}}(S)$ of $iG^{(\rho,1)\text{HF}}$ are computed. In the case of $\not\pi$EFT at LO for the neutron matter, $h^{22}_{\vec{p}\vec{p}',\vec{p}\vec{p}'} = C_0$ so that Eqs. (4.33) can be solved exactly with the ansatz

$$\Sigma^{(\rho)\text{HF}}_{\vec{p}\sigma} = \Sigma^{(\rho)\text{HF}} \ , \tag{4.36}$$

where $\Sigma^{(\rho)\text{HF}}$ is a constant[17]. The fact that $\Sigma^{(\rho)\text{HF}}_{\vec{p}\sigma}$ is a constant leads to

$$\alpha^{\text{HF}}(S) = \begin{cases} -1 & \text{if } S = \{\vec{e}_\omega\} \\ -2 & \text{if } S = \{\vec{L}\} \text{ with } \vec{L} \notin \{\vec{e}_\omega\} \\ -2 & \text{if } \dim S \geq 2 \end{cases} \ . \tag{4.37}$$

Eventually, as $\alpha^{\text{HF}}(S) = \alpha^{+}(S)$, the procedure described in Sec. 4.2.3 can be applied directly, without any modification, on diagrams contributing in the approximation HF-MBPT(n).

4.4. Discussion

Starting from the derivation of a Hamiltonian H describing the interaction between nucleons within an EFT approach (namely $\not\pi$EFT), the power-counting rules proposed to compute observables at LO require to exactly solve the A-body Schrödinger equation for a truncated Hamiltonian H^{LO}. However, as discussed previously, in large A-body sectors (A $\gg$ 10) exact calculations remain intractable. In order to overcome this tension, the idea pursued here is to test the largest class of many-body approximations so that one could identify one (or several) approximations that would lead to accurate estimation of nuclear many-body observables. If that was the case, this might indicate the possibility to find new power-counting rules better suited to the exploration of nuclear many-body sectors.

Before that, however, it is necessary to be able to renormalize the Hamiltonian consistently with the many-body approximation. It has been argued in Sec. 4.1.1 that the computation of counter-terms appearing in the Hamiltonian should be done only in few-body sectors. On top of that, for a given many-body approximation, the A-body sectors considered must be bounded (in A) as low as possible to keep the best predictive power.

In Chap. 4, a systematic procedure to renormalize the Hamiltonian has been derived for different classes of many-body approximations. This procedure has the nice property to

[17] Plugging the ansatz (4.36) into Eqs. (4.33) leads to a cubic equation solved by $\Sigma^{(\rho)\text{HF}}$.

introduce counter-terms computed in A′-body sectors independently of the number A of nucleons composing the nuclear system under study. If no *a piori* upper bound has been derived on A′, it appears, in practice, that the A′-body sectors necessary to consider for the computation of counter-terms fulfill in general $\mathrm{A}' \ll \mathrm{A}$. For example, considering either RPA, ladder approximation or second Born approximation lead to $\mathrm{A}' \leq 2$ (for LO calculations applied to neutron matter). This drastic reduction follows from the necessity of considering only renormalization parts in the cut diagrams. From $D(\gamma_n^{(0,\mathrm{A}')}) = 5 - 3\mathrm{A}' + n$ one can see that, at fixed number of vertices, increasing A′ will eventually result in a non UV-divergent sub-diagram so that renormalization parts do not tend to proliferate in large A′-body sectors[18].

Last but not least, the different tools used along Chap. 4 i.e. Weinberg's asymptotic theorem combined with BPHZ, show a great flexibility in their use. This was illustrated in the quite trivial example of Sec. 4.3.2 which considers a different partitioning of the Hamiltonian where the unperturbed Hamiltonian H_0 is no longer the kinetic Hamiltonian. Following this general approach, it is hoped that similar developments will be achieved in less trivial cases. The case of SCGF seems to be a first non-trivial application as from the work of [64, 65, 66, 67, 68] additional counter-terms might be necessary (compared to a naïve application of BPHZ i.e. in absence of the dressing of the propagators). Further extensions, such as considering partitions of the Hamiltonian where H_0 breaks specific symmetries of H would be an other interesting development. For example, breaking translation symmetry by choosing the unperturbed system to be an harmonic oscillator is crucial to tackle finite nuclei in *ab-initio* approaches. As another example, the use of a partitioning that breaks particle number symmetry has enabled recently an accurate treatment of superfluid nuclei while keeping a low order perturbative approximation in the computation of observables [47, 90].

[18] Yet this is only an heuristic argument and, without further knowledge, it might be possible that particular many-body approximations lead to arbitrarily high A′.

Conclusion

Following the EFT program for nuclear systems in arbitrarily large A-body sectors, the present thesis has focused on the particular case of $\not\pi$EFT. As for χEFT, the power-counting rules require to exactly solve the Schrödinger equation in any A-body sector for the leading order Hamiltonian $H_{\not\pi}^{\mathrm{LO}}$. Despite the relative simplicity of $H_{\not\pi}^{\mathrm{LO}}$, exact calculations remains, to this day, out of reach for many-body sectors i.e. with $A \gg 10$. Consequently, many-body approximations *must* be considered to make predictions for large A nuclear systems. The main goal of the present thesis was, thus, to investigate the implications of many-body approximations on the renormalization invariance of A-body observables computed at LO. This study constitutes only a first step as SLOs will have to be investigated as well in the future.

Following this goal, the calculation of the equation of state of neutron matter (i.e. the energy per particle as a function of the density) has been computed using SCGF theory on the basis of a $\not\pi$EFT potential at LO, previously renormalized exactly in the two-body sector in adequacy with power-counting rules. Attempting to fulfill power-counting rules as well, "as exact as possible" SCGF calculations were performed by using one of the most advanced truncation scheme available numerically to this day i.e. the "self-consistent ladder approximation". However, after testing extensively the available state-of-the-art numerical implementation of the self-consistent ladder approximation, it has been demonstrated to be insufficiently precise in its implementation to draw any conclusion about the renormalization invariance of observables. A critical numerical instability has indeed been revealed through a comparison with analytical calculations in the simpler non-self-consistent ladder approximation. This instability relates to the calculation of the real part of the two-body Green's function on the basis of a dispersion relation. More precisely, the numerical instability occurs when combined with the quasiparticle treatment of the peak of the spectral function. This numerical instability *must* be addressed before performing calculations in the self-consistent ladder approximation, especially for codes implementing a quasiparticle-background decomposition. In the meantime, analytical calculations performed to benchmark the numerical implementation of the self-consistent ladder approximation, have revealed to be consistent with a particular renormalization of $H_{\not\pi}^{\mathrm{LO}}$ in the two-body sector. In particular, non-self consistent ladder approximation is consistent with the exact renormalization of $H_{\not\pi}^{\mathrm{LO}}$ in the two-body sector. Conversely, Hartree-Fock and second Born approximations require counter-terms computed respectively at first (tree-level) or second order (one-loop) in the bare coupling constants.

In order to extend the analysis realised in Sec. 3.5.3, a systematic procedure (for a large class of many-body approximations) has been derived in Chap. 4 to compute necessary counter-terms to cancel out any potential UV divergences, hence leading to renormalization-invariant many-body observables. The first class of many-body approximations considered is based on the truncation of the set of Feynman diagrams expressed in terms of vacuum propagators and medium-insertions. The systematic procedure has been successfully carried out thanks to the

powerful BPHZ procedure that enables to deal with overlapping divergences. More precisely, the BPHZ procedure is applied on diagrams resulting from a cutting procedure. This allows one to renormalize $H_{\not\pi}^{\mathrm{LO}}$ solely in A′-body sectors with $\mathrm{A}' \leq \mathrm{A}'_{max}$ where A'_{max} is independent of the A-body sector of interest. In practice, (for RPA, the ladder approximation and the second Born approximation) it was found that $\mathrm{A}'_{max} \leq 2$ (even though no *a priori* bound has been derived). This comforts the idea that one can renormalize $H_{\not\pi}^{\mathrm{LO}}$ in few-body sectors even for non-trivial many-body approximations. With the help of Weinberg's asymptotic theorem, a similar procedure has been derived for many-body approximations based on the truncation of the set of particle-hole diagrams contributing to k-body Green's functions. As the particle-hole representation of the unperturbed propagator is general (thanks to the Lehmann representation), it opens the path to further generalizations in nuclear physics for different many-body approximations (such as CC or SCGF) and/or different partitioning of the Hamiltonian. Finally, all the considerations in the procedures derived in Chap. 4 were fairly agnostic regarding the Hamiltonian employed. It would be interesting to study extensions of the present work to different Hamiltonians such as the one derived in χEFT.

Appendices

Appendix A.

Feynman rules for k-body Green's functions

In this appendix, Feynman rules associated with the diagrams arising in the perturbative expansion of Eq. (1.59). The rules are given both in time and energy representation for antisymmetrized vertices.

For the k-body Green's function, contributions at n^{th}-order in perturbation theory are represented by a diagram with $2k$ external lines and n vertices, all connected by means of oriented fermion lines. These fermion lines represent contractions between annihilation and creation operators when applying the time-dependent Wick theorem [27] with respect to $\left|\Phi_0^{\text{A}}\right\rangle$. As a result of the Wick theorem, the nth-order contribution is derived from the following Feynman rules.

Rule 1 Draw all unlabelled, topologically distinct and linked diagrams with n vertices, k incoming and k outgoing external lines, using directed arrows.

Rule 2 Each oriented fermion line represents a Wick contraction, leading to the unperturbed propagator $iG_{\mu\nu}^{(\text{A},1)0}(t_\mu, t_\nu)$ (or $iG_{\mu\nu}^{(\text{A},1)0}(\omega_\lambda)$). In time formulation, the t_μ and t_ν label the times of the vertices at the end and at the beginning of the line. In energy formulation, ω_λ denotes the energy carried by the propagator.

Rule 3 Each fermion line starting from and ending at the *same* vertex is an equal-time propagator, $-iG_{\mu\nu}^{(\text{A},1)0}(t, t^+) = \rho_{\mu\nu}^{(\text{A},1)0}$.

Rule 4 For each one- or two-body vertex, write down a factor $(-i)\breve{h}_{\mu\nu}^{11}$ or $(-i)h_{\alpha\beta\gamma\delta}^{22}$ respectively.

Rule 5 Include a factor $(-1)^{\sigma(P)+n_L}$ where n_L is the number of closed fermion loops and $\sigma(P)$ is the signature of the permutation connecting incoming and outgoing external lines. The sign $(-1)^{n_L}$ comes from the odd permutation of operators needed to create a loop and does not include loops of a single propagator, already accounted for by Rule 3.

Rule 6 For a diagram representing a k-body Green's function, add a factor $(-i)^k$, whereas for a k-body vertex without external lines (such as $\Sigma^{(\rho)}$ or T) add a factor i.

The next two rules require a distinction between the time and the energy representation. In the time representation:

Rule 7 Label each vertex with a time t_λ. All the fermion lines connected to the same vertex share the same time, t_λ.

Rule 8 Sum over all the internal quantum numbers and integrate over all internal times from $-\infty$ to $+\infty$ i.e. $\int_{-\infty}^{+\infty} \mathrm{d}t_\lambda$.

Alternatively, in energy representation:

Rule 7' Label each fermion line with an energy ω_λ, under the *constraint* that the total incoming energy equals the total outgoing energy at each vertex, i.e. $\sum_\lambda \omega_\lambda^{in} = \sum_\lambda \omega_\lambda^{out}$.

Rule 8' Sum over all the internal quantum numbers and integrate over each independent internal energy, from $-\infty$ to $+\infty$ i.e. $\int_{-\infty}^{+\infty} \frac{\mathrm{d}\omega_\lambda}{2\pi}$.

Eventually, each diagram is multiplied by a combinatorial factor S that originates from the number of equivalent Wick contractions that lead to it. In the present thesis, only symmetry from equivalent lines or exchange of vertices appear hence the last Feynman rule

Rule 9 A factor $\frac{1}{n_e!}$ must be considered for each group of n_e equivalent lines namely lines that begin and end at the same vertices. A factor $\frac{1}{n_s}$ must be considered where n_s is the number of ways of exchanging vertices of the labelled diagram leading to a topologically equivalent labelled diagram.

For an extended discussion on how to calculate this combinatorial factor see [91].

Appendix B.

Calculation of R functions

In this appendix the calculation of the R functions used in the one medium-insertion loop is detailed.

B.1. R_0

In this document $R_0(s,\kappa)$ is defined in an integral form as

$$R_0(s,\kappa) \equiv \int_{-1}^{1} \mathrm{d}y \left\{ [M(y;s) + M(-y;s)] - \kappa \left[\mathrm{Argth}\frac{M(y;s)}{\kappa} + \mathrm{Argth}\frac{M(-y;s)}{\kappa} \right] \right\} . \tag{B.1}$$

B.1.1. $M(y;s)$ integrals

To derive an explicit form of R_0 the two auxiliary integrals are first computed

$$\int_{-1}^{1} \mathrm{d}y \ [M(y;s) + M(-y;s)] \ , \tag{B.2}$$

$$\int_{-1}^{1} \mathrm{d}y \ \left[\mathrm{Argth}\frac{M(y;s)}{\kappa} + \mathrm{Argth}\frac{M(-y;s)}{\kappa} \right] \ , \tag{B.3}$$

where Eq. (3.64) is recalled namely

$$M(y;s) \equiv sy + \sqrt{(sy)^2 + 1 - s^2} \ .$$

Integral (B.2) is trivial and reads

$$\int_{-1}^{1} \mathrm{d}y \ [M(y;s) + M(-y;s)] = 2 - \frac{1-s^2}{s} \ln \frac{1-s}{1+s} \ . \tag{B.4}$$

Integral (B.3) is a bit more involved and a software such as Mathematica is not sufficient to compute it directly. The derivation of its real part is detailed here.

$$\mathrm{Re} \int_{-1}^{1} \mathrm{d}y \ \left[\mathrm{Argth}\frac{M(y;s)}{\kappa} + \mathrm{Argth}\frac{M(-y;s)}{\kappa} \right] = - \int_{-1}^{1} \mathrm{d}y \ \frac{1}{2} \ln \left| 1 + \frac{2}{\frac{\kappa^2 - s^2 + 1}{2\kappa\sqrt{(sy)^2 + 1 - s^2}} - 1} \right| , \tag{B.5}$$

then, making the change of variable $u = \sqrt{(sy)^2 + 1 - s^2}$ one obtains

$$\begin{aligned}
&\mathrm{Re}\int_{-1}^{1} \mathrm{d}y \ \left[\mathrm{Argth}\frac{M(y;s)}{\kappa} + \mathrm{Argth}\frac{M(-y;s)}{\kappa}\right] \\
&\quad = -\frac{2}{s}\,\mathrm{Re}\int_{\sqrt{1-s^2}}^{1} \mathrm{d}u \ \frac{u}{\sqrt{u^2+s^2-1}}\mathrm{Argth}\frac{\kappa^2-s^2+1}{2\kappa u} \\
&\quad = \frac{2}{s}\left\{\int_{\sqrt{1-s^2}}^{1} \mathrm{d}u \ \partial_u\left(\sqrt{u^2+s^2-1}\right)\right. \\
&\qquad \left. \times\left(-\frac{1}{2}\right)\left(\ln\left|\frac{\kappa^2-s^2+1}{2\kappa}+u\right| - \ln\left|\frac{\kappa^2-s^2+1}{2\kappa}-u\right|\right)\right\} \\
&\quad = \frac{2}{s}\left\{-\frac{s}{2}\ln\left|\frac{(\kappa+1)^2-s^2}{(\kappa-1)^2-s^2}\right| - \frac{\kappa^2-s^2+1}{2\kappa}\int_{\sqrt{1-s^2}}^{1}\mathrm{d}u\frac{\sqrt{u^2+s^2-1}}{u^2-\left(\frac{\kappa^2-s^2+1}{2\kappa}\right)^2}\right\} .
\end{aligned}$$

Changing again of variable with $v = \frac{u}{\sqrt{1-s^2}}$, one obtains

$$\begin{aligned}
&\mathrm{Re}\int_{-1}^{1} \mathrm{d}y \ \left[\mathrm{Argth}\frac{M(y;s)}{\kappa} + \mathrm{Argth}\frac{M(-y;s)}{\kappa}\right] \\
&\quad = \frac{2}{s\kappa}\left\{-\frac{s\kappa}{2}\left[\ln\frac{1+s+\kappa}{|1-s-\kappa|} + \ln\left|\frac{1-s+\kappa}{1+s-\kappa}\right|\right]\right. \\
&\qquad\qquad \left. -\frac{\kappa^2-s^2+1}{2}\int_{1}^{\frac{1}{\sqrt{1-s^2}}}\mathrm{d}v\frac{\sqrt{v^2-1}}{v^2-\left(\frac{\kappa^2-s^2+1}{2\kappa\sqrt{1-s^2}}\right)^2}\right\} \\
&\quad = \frac{2}{s\kappa}\left\{-\frac{s\kappa}{2}\left[\ln\frac{1+s+\kappa}{|1-s-\kappa|} + \ln\left|\frac{1-s+\kappa}{1+s-\kappa}\right|\right] - \frac{\kappa^2-s^2+1}{2}\frac{1}{2}\ln\left(\frac{1+s}{1-s}\right)\right. \\
&\qquad\qquad \left. +\frac{1}{2}\frac{1-(\kappa^2+s^2)}{2}\ln\left(\frac{1-s}{1+s}\left|\frac{(1+s)^2-\kappa^2}{(1-s)^2-\kappa^2}\right|\right)\right\} \\
&\quad = \frac{2}{s\kappa}\left\{\frac{1-s^2}{2}\ln\left(\frac{1+s}{1-s}\right) + \frac{1-(\kappa+s)^2}{2}\ln\frac{1+s+\kappa}{|1-s-\kappa|}\right. \\
&\qquad\qquad \left. +\frac{1-(\kappa-s)^2}{2}\ln\left|\frac{1-s+\kappa}{1+s-\kappa}\right|\right\} \qquad \text{(B.6)}
\end{aligned}$$

where Eq. (B.8) is used to replace the last integral on v.

Finally, putting Eq.(B.6) and Eq.(B.4) together into Def. (B.1)

$$R_0(s,\kappa) = 2 + \frac{1}{2s}\left[1-(s+\kappa)^2\right]\ln\frac{1+s+\kappa}{|1-s-\kappa|} + \frac{1}{2s}\left[1-(s-\kappa)^2\right]\ln\frac{1+s-\kappa}{1-s+\kappa} \qquad \text{(B.7)}$$

B.1.2. v integral

For the sake of completeness, the above integral on v is derived. Starting with the change of variable $v = \mathrm{ch}(t)$,

$$\int_{1}^{\frac{1}{\sqrt{1-s^2}}}\mathrm{d}v\frac{\sqrt{v^2-1}}{v^2-\left(\frac{\kappa^2-s^2+1}{2\kappa\sqrt{1-s^2}}\right)^2}$$

$$
\begin{aligned}
&= \int_0^{\mathrm{Argch}\frac{1}{\sqrt{1-s^2}}} \mathrm{d}t \frac{\mathrm{sh}(t)^2}{\mathrm{ch}(t)^2 - \left(\frac{\kappa^2-s^2+1}{2\kappa\sqrt{1-s^2}}\right)^2} \\
&= \int_0^{\frac{1}{2}\ln\left(\frac{1+s}{1-s}\right)} \mathrm{d}t \frac{\mathrm{ch}(t)^2 - \left(\frac{\kappa^2-s^2+1}{2\kappa\sqrt{1-s^2}}\right)^2 + \left(\frac{\kappa^2-s^2+1}{2\kappa\sqrt{1-s^2}}\right)^2 - 1}{\mathrm{ch}(t)^2 - \left(\frac{\kappa^2-s^2+1}{2\kappa\sqrt{1-s^2}}\right)^2} \\
&= \frac{1}{2}\ln\left(\frac{1+s}{1-s}\right) + \left[\left(\frac{\kappa^2-s^2+1}{2\kappa\sqrt{1-s^2}}\right)^2 - 1\right] \int_0^{\frac{1}{2}\ln\left(\frac{1+s}{1-s}\right)} \mathrm{d}t \frac{1}{\mathrm{ch}(t)^2 - \left(\frac{\kappa^2-s^2+1}{2\kappa\sqrt{1-s^2}}\right)^2} \\
&= \frac{1}{2}\ln\left(\frac{1+s}{1-s}\right) + \left(\frac{\kappa^2+s^2-1}{2\kappa\sqrt{1-s^2}}\right)^2 \frac{1}{2\left(\frac{\kappa^2-s^2+1}{2\kappa\sqrt{1-s^2}}\right)^2} \\
&\qquad \times \int_0^{\frac{1}{2}\ln\left(\frac{1+s}{1-s}\right)} \mathrm{d}t \left[\frac{1}{\mathrm{ch}(t) - \left(\frac{\kappa^2-s^2+1}{2\kappa\sqrt{1-s^2}}\right)} - \frac{1}{\mathrm{ch}(t) + \left(\frac{\kappa^2-s^2+1}{2\kappa\sqrt{1-s^2}}\right)}\right] .
\end{aligned}
$$

Simplifying and changing again of variable with $z = e^t$, one get back to simpler rationale fraction integrals

$$
\begin{aligned}
&\int_1^{\frac{1}{\sqrt{1-s^2}}} \mathrm{d}v \frac{\sqrt{v^2-1}}{v^2 - \left(\frac{\kappa^2-s^2+1}{2\kappa\sqrt{1-s^2}}\right)^2} \\
&\quad = \frac{1}{2}\ln\left(\frac{1+s}{1-s}\right) + \frac{1}{\kappa^2-s^2+1} \frac{\left(1-(\kappa^2+s^2)\right)^2}{2\kappa\sqrt{1-s^2}} \\
&\qquad \times \int_1^{\sqrt{\frac{1+s}{1-s}}} \mathrm{d}z \left[\frac{1}{z^2 - 2z\left(\frac{\kappa^2-s^2+1}{2\kappa\sqrt{1-s^2}}\right) + 1} - \frac{1}{z^2 + 2z\left(\frac{\kappa^2-s^2+1}{2\kappa\sqrt{1-s^2}}\right) + 1}\right] .
\end{aligned}
$$

Combining with inequalities (3.60), an expression using Argth function is derived as

$$
\begin{aligned}
&\int_1^{\frac{1}{\sqrt{1-s^2}}} \mathrm{d}v \frac{\sqrt{v^2-1}}{v^2 - \left(\frac{\kappa^2-s^2+1}{2\kappa\sqrt{1-s^2}}\right)^2} \\
&\quad = \frac{1}{2}\ln\left(\frac{1+s}{1-s}\right) - \frac{1-(\kappa^2+s^2)}{\kappa^2-s^2+1} \\
&\qquad \times \left\{ \mathrm{Argth}\left(\frac{2\kappa(1+s) - \kappa^2 - \sqrt{1-s^2}^2}{1-(\kappa^2+s^2)}\right) - \mathrm{Argth}\left(\frac{-(\kappa-\sqrt{1-s^2})^2}{1-(\kappa^2+s^2)}\right) \right. \\
&\qquad \left. -\mathrm{Argth}\left(\frac{2\kappa(1+s) + \kappa^2 + \sqrt{1-s^2}^2}{1-(\kappa^2+s^2)}\right) + \mathrm{Argth}\left(\frac{(\kappa+\sqrt{1-s^2})^2}{1-(\kappa^2+s^2)}\right) \right\} ,
\end{aligned}
$$

and eventually,

$$
\begin{aligned}
&\int_1^{\frac{1}{\sqrt{1-s^2}}} \mathrm{d}v \frac{\sqrt{v^2-1}}{v^2 - \left(\frac{\kappa^2-s^2+1}{2\kappa\sqrt{1-s^2}}\right)^2} \\
&\qquad = \frac{1}{2}\ln\left(\frac{1+s}{1-s}\right) - \frac{1}{2}\,\frac{1-(\kappa^2+s^2)}{\kappa^2-s^2+1} \ln\left(\frac{1-s}{1+s}\left|\frac{(1+s)^2-\kappa^2}{(1-s)^2-\kappa^2}\right|\right) . \qquad \text{(B.8)}
\end{aligned}
$$

B.2. R_1

R_1 is defined as

$$R_1(s,\kappa) \equiv \int_{-1}^{1} \mathrm{d}y \left\{ -\left[M(y;s)^3 + M(-y;s)^3\right] \right.$$
$$\left. -\kappa^2 \left[(M(y;s) + M(-y;s)) - \kappa \left(\mathrm{Argth}\frac{M(y;s)}{\kappa} + \mathrm{Argth}\frac{M(-y;s)}{\kappa} \right) \right] \right\} . \tag{B.9}$$

In this case the calculation uses integrals in R_0 calculation plus the following one

$$\int_{-1}^{1} \mathrm{d}y \ \left[M(y;s)^3 + M(-y;s)^3\right] . \tag{B.10}$$

It turns out

$$\int_{-1}^{1} \mathrm{d}y \ \left[M(y;s)^3 + M(-y;s)^3\right] = 4 , \tag{B.11}$$

so that,

$$R_1(s,\kappa) = -\left(4 + \kappa^2 R_0(s,\kappa)\right) . \tag{B.12}$$

Note that it is only a particular case to having the full s dependence in $R_0(s,\kappa)$. Indeed if one try to go to higher order one will need to compute more general integrals as

$$\int_{-1}^{1} \mathrm{d}y \ [M(y;s)^n + M(-y;s)^n] \tag{B.13}$$

which are not independent of s for $n \geq 4$ since

$$\forall n \neq 1 , \int_{-1}^{1} \mathrm{d}y \ [M(y;s)^n + M(-y;s)^n] = \frac{2}{(n^2-1)s} \left[(1+s)^n(n-s) - (1-s)^n(n+s)\right] . \tag{B.14}$$

Appendix C.

BPHZ renormalization procedure

In this appendix, the Bogoliubov-Parasiuk-Hepp-Zimmermann (BPHZ) procedure to make UV finite Feynman diagrams arising in the perturbative expansion of the k-body Green's function $G^{(0,k)}$ (where the Hamiltonian is partitioned as in Eqs. (3.1) and the reference state is $|0\rangle$) is briefly recalled. For an extensive discussion and the complete proof of the procedure, the reader is referred to Refs. [40, 41, 37, 42]. Before describing the BPHZ procedure applied to a generic diagram $\mathcal{G}$, several useful definitions must be recalled.

A sub-diagram γ of $\mathcal{G}$ is defined as a subset of lines and vertices contained in $\mathcal{G}$ where end points of the lines of γ belong to its vertices. A diagram $\mathcal{G}_1$ is said to be included in $\mathcal{G}_2$ and denoted as $\mathcal{G}_1 \subseteq \mathcal{G}_2$ if their set of lines verify the same inclusion relation. In particular, a sub-diagram γ of $\mathcal{G}$ verifies $\gamma \subseteq \mathcal{G}$. The sub-diagram generated by the intersection of lines of two sub-diagrams γ_1 and γ_2 defines a sub-diagram γ and is denoted as

$$\gamma \equiv \gamma_1 \cap \gamma_2 \ . \tag{C.1}$$

Two sub-diagrams γ_1 and γ_2 that have neither lines nor vertices in common are said to be *disjoint* and the result is denoted as

$$\gamma_1 \cap \gamma_2 = \emptyset \ . \tag{C.2}$$

If neither $\gamma_1 \subseteq \gamma_2$ nor $\gamma_2 \subseteq \gamma_1$ and $\gamma_1 \cap \gamma_2 \neq \emptyset$ they are said to be *overlapping*. Otherwise they are said to be non-overlapping. As a shorthand, "γ_1 and γ_2 overlaps" is often written as $\gamma_1 \circ \gamma_2$. For a set of non-overlapping sub-diagrams $\gamma_1, \gamma_2, \ldots, \gamma_n$ of $\mathcal{G}$, the *reduced diagram* $\mathcal{G} \setminus \{\gamma_1, \gamma_2, \ldots, \gamma_n\}$ is defined by the diagram resulting from $\mathcal{G}$ after contracting all lines of $\gamma_1, \gamma_2, \ldots, \gamma_n$ to a point.

A sub-diagram γ of $\mathcal{G}$ is referred to as a *renormalization part* if it is a 1PI diagram with a superficial degree of divergence greater than or equal to 0, i.e. if

$$D(\gamma) \geq 0 \ . \tag{C.3}$$

The Feynman amplitude associated to $\mathcal{G}$ is denoted as $\mathcal{A}^{\mathcal{G}}$. For a set of mutually disjoint sub-diagrams $\gamma_1, \gamma_2, \ldots, \gamma_n$ the Feynman amplitude is expressed in terms of the Feynman amplitudes of the sub-diagrams $\mathcal{A}^{\gamma_j}$ and the remainder is denoted as $\mathcal{A}^{\mathcal{G}\setminus\{\gamma_1,\ldots,\gamma_n\}}$ with $\mathcal{G} \setminus \{\gamma_1, \ldots, \gamma_n\}$ corresponding to the reduced diagram as defined above. With these definitions,

$$\mathcal{A}^{\mathcal{G}} = \mathcal{A}^{\mathcal{G}\setminus\{\gamma_1,\ldots,\gamma_n\}} \prod_{j=1}^{n} \mathcal{A}^{\gamma_j}. \tag{C.4}$$

The BPHZ procedure defines recursively a renormalized amplitude $R^{\mathcal{G}}$ associated to the diagram $\mathcal{G}$. If the amplitude associated to $\mathcal{G}$ is convergent

$$R^{\mathcal{G}} \equiv \mathcal{A}^{\mathcal{G}} \ . \tag{C.5}$$

If the diagram does not contain any renormalization part but is superficially divergent it is called *primitively divergent*. In that case the renormalized amplitude is defined by

$$R^{\mathcal{G}} \equiv (1 - t_{\mathcal{G}})\mathcal{A}^{\mathcal{G}} \ , \tag{C.6}$$

where $t_{\mathcal{G}}$ is the operator of the Taylor expansion with respect to the external momenta[1] around 0 up to the order of the dimension $D(\gamma)$ of the divergent diagram, i.e.

$$t_\gamma \mathcal{A}^{\gamma}_{\substack{p_1,\dots,p_k \\ p'_1,\dots,p'_k}} \equiv \sum_{j=0}^{D(\gamma)} \frac{1}{j!} \sum_{\substack{s_1+\dots+s'_k \geq 0 \\ s_1+\dots+s'_k = j}} \frac{\partial^j \mathcal{A}^{\gamma}}{\partial p_1^{s_1} \cdots \partial p_k^{s_k} \partial p_1'^{s'_1} \cdots \partial p_k'^{s'_k}} \bigg|_{p_1=\dots=p'_k=0} p_1^{s_1} \cdots p_k'^{s'_k} \tag{C.7}$$

If $\mathcal{G}$ is superficially divergent and contains divergent sub-diagrams the renormalized amplitude is defined as

$$R^{\mathcal{G}} \equiv (1 - t_{\mathcal{G}})\bar{R}^{\mathcal{G}} \ , \tag{C.8}$$

where $\bar{R}^{\mathcal{G}}$ corresponds to the Feynman amplitude where all sub-divergences have already been subtracted. The subtraction by the Taylor operator t_γ corresponds to adding the amplitude associated to a diagram where the divergent sub-diagram γ has been replaced by a vertex so-called a *counter-term*.

The recursion relation (C.8) was solved explicitly by the *forest formula* [37] which is based on the concept of *i-forest* (for inclusion-forest). An i-forest is defined as any set of sub-diagrams (including the empty set and the whole diagram itself) which are mutually non-overlapping. This way, the Hasse diagram[2], for the order relation $\subseteq$ and the mutually non-overlapping sub-diagrams, represents a forest i.e. a set of disconnected tree (see the right panel of Fig. C.1 for an example where the Hasse diagram of the i-forest is made of only one tree). An i-forest is said to be connected if its Hasse diagram is connected. A connected i-forest is also referred to as an *i-tree*. As for regular forest, an i-forest can be decomposed as the set of its connected components (i.e. as a set of i-trees). An i-forest is usually depicted by drawing boxes around the sub-diagrams as represented in the left panel of Fig. C.1. The boxes are, thus, not allowed to overlap but can be nested. An i-forest is *restricted* if each of its boxes contains only renormalization parts. To each restricted i-forest $\mathscr{F}$ one associates again an amplitude, i.e.

$$\Omega^{\mathscr{F}} \equiv \tilde{\prod}_{\gamma \in \mathscr{F}} (-t_\gamma)\mathcal{A}^{\mathcal{G}} \ , \tag{C.9}$$

where the tilde over the product sign stands for the fact that in case of nested diagrams within the i-forest one has to apply the Taylor operators from the innermost to the outermost diagrams

[1] The renormalization point is chosen here to be 0 but could be chosen arbitrarily. In the case of $\not{\pi}$EFT the calculations realized in Sec. 2.2 are equivalent to the choice of a renormalization point at 0 as the coupling constants are matched in the limit $q \to 0$.

[2] A Hasse diagram associated to an order relation is a diagrammatic representation of the ordering between the objects considered.

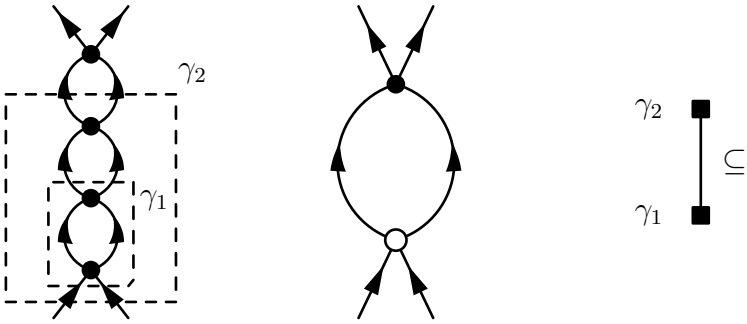

Figure C.1. On the left panel, an example of an i-forest (depicted by boxes) for a three-loop ladder diagram contributing to $G^{(0,2)}$. The middle panel pictures the diagram with the counter-term associated to this i-forest (the vertex with an empty circle denotes the two-body counter-term appearing for this particular i-forest). The associated Hasse diagram is depicted on the right panel.

while for disjoint sub-diagrams the expressions are naturally independent of the order of Taylor operators since

$$\mathcal{A}^{\mathcal{G}} = \mathcal{A}^{\mathcal{G}\setminus\{\gamma_1,\ldots,\gamma_n\}} \prod_{k=1}^{n} \mathcal{A}^{\gamma_k} \ . \tag{C.10}$$

Each i-forest corresponds to a particular diagram with counter-terms[3]. Eventually, the forest formula states that the renormalized amplitude of the diagram $\mathcal{G}$ is given by the sum over all restricted i-forests, i.e.

$$R^{\mathcal{G}} = \sum_{\mathscr{F}\in\mathcal{F}_R(\mathcal{G})} \Omega^{\mathscr{F}} \ , \tag{C.11}$$

where $\mathcal{F}_R(\mathcal{G})$ denotes the set of restricted i-forest and where it is understood that the empty i-forest (i.e. without any box around a sub-diagram) stands for the diagram $\mathcal{G}$ itself. The term with the empty i-forest corresponds to the UV divergent diagram while all other additional terms correspond to diagrams with counter-terms to cancel the original UV divergences.

[3]The topology of the resulting diagram consists of the original diagram $\mathcal{G}$ where the sub-diagrams γ of the i-forest have been contracted to a vertex corresponding to a counter-term. The nature of the counter-terms depends on the i-forest.

Synthèse en français

La physique nucléaire de basse énergie est en train de subir des changements majeurs ces dernières années. Sur Terre, les générations successives des générateurs de faisceau radioactif s'intéressent à des éléments à durée de vie de plus en plus faible, à des isotopes de plus en plus exotiques et repoussent toujours plus loin la frontière de la carte des noyaux observés expérimentalement. Dans l'espace, les explosions de supernovae, les étoiles à neutrons (extrêmement compacts) et leur coalescence constituent un laboratoire unique pour tester les modèles de matière nucléaire dans des conditions extrêmes. D'une manière générale, cette volonté de repousser toujours plus loin la frontière de notre compréhension des systèmes nucléaires nous emmène vers un certain nombre de questions fondamentales qui guident la recherche dans ce domaine de la physique, à savoir

- comment l'interaction entre les protons et neutrons émerge de la théorie quantique des champs qui décrit l'interaction entre les quarks et gluons les composant, à savoir la chromodynamique quantique (QCD) ?
- comment sont liés les nucléons au sein d'un noyau et quelles sont les limites d'existence de ces derniers vis-à-vis de l'interaction forte, en terme de masse, d'asymétrie neutron-proton ou encore de moment angulaire ?
- comment une phénoménologie aussi complexe et riche émerge de l'interaction entre nucléons ?

Pour répondre à ces questions un certain nombre de défis, autant expérimentaux que théoriques, doivent être relevés. Malgré les efforts fournis sur de nombreuses décennies, la physique nucléaire de basse énergie reste encore un problème ouvert et difficile. En particulier, une description précise et systématique des systèmes nucléaires à basse énergie reste, à l'heure actuelle, hors de portée.

Au cours de ces dernières décennies, de nombreuses approches théoriques ont été développées pour répondre au problème à N corps en physique nucléaire, avec leur originalité et hétérogénéité qui reflètent la complexité des systèmes nucléaires. Traditionnellement, ces approches sont séparées en deux catégories : (i) les méthodes *ab initio*, qui reposent sur l'idée que les propriétés du système dans son ensemble peuvent être décrites en terme de nucléons ponctuels en interaction, et (ii) les approches dites *effectives*, qui formulent le problème en terme de degrés de liberté effectifs (par rapport aux nucléons) interagissant entre eux. Bien que la première catégorie de méthodes représente le "graal" de la physique nucléaire de basse énergie, seule la seconde catégorie permet d'accéder à la majorité des noyaux observés.

Au cours de ces dernières années, le flux ininterrompu de données expérimentales sur les noyaux à courte vie ainsi que la demande toujours plus forte d'estimations fiables d'observables nucléaires représentent un défi pour les approches théoriques. L'attention et les efforts pour les

améliorer se tournent maintenant vers des considérations de cohérence interne des théories, de pouvoir de prédictions et vers une estimation précise des erreurs/incertitudes théoriques. D'une part, les approches *effectives*, souvent ajustées pour reproduire une zone particulière de la carte des noyaux ou possédant un biais d'ajustement envers les noyaux stables, rencontrent des problèmes pour produire des prédictions consistantes loin des données déjà expérimentalement connues. D'autre part, les approches *ab initio*, qui cherchent à résoudre l'équation de Schrödinger à N corps en fonction de l'interaction élémentaire entre les nucléons, ont connues des développements majeurs et émergent maintenant comme une méthode de choix pour les noyaux de masse faible à moyenne.

Au cours des vingts dernières années, les méthodes *ab initio* ont subies deux avancées majeures. La première s'est déroulée dans les années 90 grâce à l'apparition des premiers super calculateurs qui ont permis l'utilisation des méthodes Monte-Carlo et des techniques d'interaction de configurations au problème N corps nucléaire [1, 2]. De telles méthodes cherchent à résoudre exactement le problème à N corps en calculant toutes les configurations possibles (directement ou à travers un échantillonnage Monte-Carlo) dans un espace des phases suffisamment grand. Les résultats obtenus reproduisent avec précision les propriétés de structure ainsi que de réaction pour des noyaux légers. Parmi les exemples récents d'un tel succès il y a l'unification de la description de la structure du ^{6}Li et de la dynamique du couple deutérium-^{4}He [3] ainsi que les réponses électromagnétiques et faibles de ^{4}He et du ^{12}C [4]. De telles simulations ont cependant une complexité de calcul exponentielle avec le nombre de particules ce qui les limite aux noyaux les plus légers, contenant au plus une dizaine de nucléons, malgré les infrastructures de calculs les plus modernes.

La deuxième avancée majeure s'est déroulée au cours des dix dernières années avec l'utilisation combinée des interactions chirales évoluées par des méthodes SRG (pour similarity renormalization group)[1] [5] et l'introduction d'approximations contrôlées dans la résolution de l'équation de Schrödinger. Par "contrôlée" il faut entendre ici que l'incertitude engendrée par de telles approximations est *a posteriori* majorée à l'aide de tests de convergences. De telles approximations sont basées sur une troncation du développement en perturbation de la solution du problème à N corps, typiquement exprimée en une série de diagrammes resommés de manière appropriée. Par rapport aux méthodes résolvant exactement le problème à N corps, ces méthodes permettent d'abaisser la complexité de calcul d'exponentielle à polynomiale tout en conservant une incertitude autour de quelques pourcents sur la solution du problème à N corps. Par conséquent, les méthodes *ab initio* peuvent accéder, depuis quelques années, aux noyaux de masse moyenne (contenants plusieurs dizaines de nucléons).

En pratique, les méthodes de résolution du problème à N corps se basent sur la donnée d'un Hamiltonien H et cherchent à calculer les états et valeurs propres dans tous les secteurs à N corps. Le but est donc de résoudre l'équation de Schrödinger

$$H \left|\Psi_m^{\mathrm{A}}\right\rangle = E_m^{\mathrm{A}} \left|\Psi_m^{\mathrm{A}}\right\rangle \ , \tag{1}$$

où m indexe l'ensemble des solutions, le plus précisément possible. Le Hamiltonien, décrivant l'interaction entre nucléons, peut être modélisé de plusieurs manières. Le paradigme actuel

[1] Les méthodes SRG consistent en un changement de base unitaire (laissant donc les observables à N corps inchangées) visant à découpler les composantes de faibles et fortes impulsions de l'interaction entre nucléons. Le problème à N corps devient alors "plus pertubatif".

tente de construire H dans le cadre de la théorie effective des champs chirale (χEFT) [6, 7, 8] de tel sorte qu'il prend la forme d'une série

$$H_\chi \equiv H_\chi^{\mathrm{LO}} + H_\chi^{\mathrm{SL}O} = H_\chi^{\mathrm{LO}} + \sum_{p=1}^{\infty} H_\chi^{\mathrm{N}p\mathrm{LO}} \tag{2}$$

où l'ordre principal (désigné par LO pour leading-order) et les ordres sous-dominants (désignés par SLO pour subleading-orders) sont organisés suivant un ensemble de règles de comptage de puissance (désignées par PC pour power-counting). Le comptage de puissance proposé par Weinberg [7, 8] s'avère être en parfaite adéquation avec l'approche traditionnelle du problème à N corps, cherchant à résoudre le plus exactement possible (1), indépendamment de l'ordre auquel les SLOs sont tronqués. Cependant les règles de comptage proposées par Weinberg ont récemment été rejetées sur la base d'une inadéquation avec une renormalisation (ordre par ordre) et des règles alternatives ont été proposées [9] pour répondre à ce problème. En plus de modifier l'ordre auquel apparaît certaines contributions à l'Hamiltonien, les nouvelles règles de comptage stipulent que si le LO nécessite toujours une résolution exacte de (1), les ordres sous-dominants doivent être calculés en perturbation relativement à la solution obtenue pour l'ordre principal. Il s'avère que dans le cadre de la théorie effective des champs sans pion ($\not\pi$EFT) les PCs ont fait l'objet du même genre de modifications. De plus, la compatibilité avec la renormalisabilité ordre par ordre d'un tel PC alternatif a été vérifiée au LO pour des systèmes nucléaires contenant jusqu'à quatre corps [10].

Au regard de tout ce qui a été évoqué ci-dessus, le but de cette thèse est donc d'étudier l'invariance par la renormalisation des observables dans les secteurs à N corps pour $\not\pi$EFT et notamment dans les cas où $\mathrm{N} \gg 10$. L'espoir étant ensuite d'étendre les leçons tirées de cette étude au cas de χEFT. Le programme se distingue clairement des approches plus traditionnelles du problème à N corps au sens que les contributions SLOs *doivent* être calculées uniquement en perturbation relativement à l'ordre principal soit dans une approximation type onde distordu (DWA pour distorted wave approximation). Comme il a été mentionné ci-dessus, cette approche a été appliquée avec succès aux systèmes contenant jusqu'à quatre nucléons sur la base d'un Hamiltonien $H_{\not\pi}^{\mathrm{LO}}$ contenant des interactions à deux et trois corps. Cependant, pour étendre cette approche aux systèmes à N corps où $\mathrm{N} \gg 10$ un problème majeur doit être surmonté. En effet, si $H_{\not\pi}^{\mathrm{LO}}$ peut être traité exactement pour $\mathrm{N} \sim 4$ cela devient intraitable, analytiquement ou numériquement, pour $\mathrm{N} \gg 10$, et cela probablement pour encore plusieurs décennies à venir. Par conséquent, il est *nécessaire* de mettre au point un développement (et une troncation) supplémentaire pour pouvoir espérer appliquer la première étape du programme EFT aux systèmes nucléaires, consistant à résoudre

$$H_{\not\pi}^{\mathrm{LO}} \left|\Psi_m^{\mathrm{A}}\right\rangle^{(\mathrm{LO})} = E_m^{\mathrm{A(LO)}} \left|\Psi_m^{\mathrm{A}}\right\rangle^{(\mathrm{LO})} \quad . \tag{3}$$

Les troncations les plus répandues dans le cas de système à N corps où $\mathrm{N} \gg 10$ sont actuellement basées sur des approches non-perturbatives telles que les fonctions de Green auto-cohérentes (SCGF) [11, 12], les cluster couplés (CC) [13, 14] et le groupe de renormalisation dans le milieu [15, 16], ou sur des approches perturbatives comme la théorie de perturbation à N corps (MBPT) [17, 18]. Dans cette thèse, les approches SCGF et MBPT sont étudiées en détail. Le but principal est d'étudier les conséquences de devoir résoudre (3) de manière approchée sur l'invariance par renormalisation des observables à N corps. Cela représente seulement une

première étape car l'étude se concentre sur le Hamiltonien au LO. Une fois le problème du LO surmonté, les corrections SLOs devront être étudiées à leur tour.

Pour cela, le présent manuscrit se décompose en quatre chapitres. Chap. 1 et Chap. 2 introduisent respectivement les notations/notions de développement en perturbation du problème à N corps et la théorie effective des champs sans pion. Dans Chap. 2 les divergences ultraviolettes et l'opération de renormalisation sont mises en avant pour sensibiliser le lecteur à l'importance de l'invariance par renormalisation des observables calculées dans le cadre d'une EFT. Dans Chap. 3 l'équation d'état de la matière infinie de neutron est calculée dans le cadre de la théorie SCGF en utilisant $H_{\not\pi}^{\mathrm{LO}}$. La renormalisation du Hamiltonien au LO est explicitée dans Chap. 2 où l'équation de Schrödinger est résolue exactement dans le secteur à deux corps, en accord avec les règles de comptage de puissance. En essayant de résoudre "le plus exactement possible" pour essayer de coller au plus proche du PC, la théorie SCGF est utilisée avec la troncation la plus avancée actuellement accessible, consistant à ressommer l'ensemble des diagrammes en échelle de manière auto-cohérente. Il s'avère que cette approximation est exacte dans le secteur à deux corps ce qui laisse espérer une compatibilité avec la façon dont $H_{\not\pi}^{\mathrm{LO}}$ a été renormalisée. Cependant, après avoir testé en profondeur une implémentation numérique disponible, et au niveau de l'état de l'art, il a été démontré que son implémentation est actuellement insuffisamment précise pour pouvoir tirer des conclusions quant à l'invariance des observables calculées dans cette approche vis-a-vis de la renormalisation. Une instabilité critique a été mise en évidence grâce à une comparaison avec des calculs analytiques dans le cas plus simple des échelles non auto-cohérentes comme observé dans Fig. 3.19. Cette instabilité a été reliée au calcul de la partie réelle de la fonction de Green à deux corps qui repose sur une relation de dispersion. Plus précisément, cette instabilité numérique apparaît lorsque la relation de dispersion est utilisée en même temps que le traitement en quasiparticule des pics de la fonction spectrale. Cette instabilité *doit* être corrigée avant de pouvoir réaliser des calculs dans l'approximation des échelles auto-cohérentes de manière fiable, en particulier pour les codes utilisant une décomposition quasiparticule-background de la fonction spectrale. Les calculs analytiques dérivés initialement pour tester l'implémentation numérique de SCGF ont été aussi utile pour tester, de manière analytique, la compatibilité des approximations non auto-cohérentes avec la renormalisation de $H_{\not\pi}^{\mathrm{LO}}$ dans le secteur à deux corps. En particulier il a été montré explicitement que l'approximation des échelles nécessite de renormaliser exactement $H_{\not\pi}^{\mathrm{LO}}$ dans le secteur à deux corps. À l'inverse, pour les approximations Hartree-Fock et Second Born[2] requièrent des contre-termes calculés respectivement au premier et second ordre (en l'interaction) lors de la renormalisation de $H_{\not\pi}^{\mathrm{LO}}$ dans le secteur à deux corps.

En se basant sur ces résultats, le caractère renormalisable d'un ensemble de diagrammes MBPT est ensuite étudié de manière formelle dans Chap. 4, en faisant particulièrement attention à ce que la renormalisabilité soit indépendante du secteur à N corps considéré. Pour étendre l'analyse (et les conclusions) réalisée dans la section 3.5.3, une procédure systématique (pour une classe importante d'approximation du problème à N corps) est dérivée, permettant de calculer les contre-termes nécessaires à l'annulation des divergences ultraviolettes, de sorte que les observables à N corps sont manifestement invariantes vis-à-vis de la renormalisation. La première classe d'approximations considérée regroupe les sommes d'un ensemble de diagrammes de

[2]Les calculs analytiques Hartree-Fock et Second Born de l'énergie par particule sont obtenus en dégradant la ressommation des échelles respectivement à l'ordre un et deux en l'interaction.

Feynman exprimés en terme de propagateurs dans le vide et d'insertions du milieu. La procédure a pu être dérivée systématiquement grâce au puissant théorème BPHZ [83, 36, 37] (voir App. C pour une brève revue). Ce théorème permet notamment de traiter de manière systématique des divergences ultraviolettes qui s'entremêlent dans un diagramme. Plus précisément, le théorème BPHZ est appliqué à des diagrammes résultant d'une procédure de coupage introduite dans Chap. 4 (voir Tab. 4.1 pour un exemple). Cela permet de procéder à la renormalisation de $H_{\not{t}}^{\mathrm{LO}}$ uniquement dans des secteurs à N′ corps où $\mathrm{N}' \leq \mathrm{N}'_{max}$ avec N'_{max} indépendant du secteur à N corps d'intérêt. Dans la pratique, et les exemples développés, il s'avère que $\mathrm{N}'_{max} \leq 2$ même si aucun majorant n'a été dérivé *a priori*. Cela soutient l'idée qu'il est possible de dériver des approximations du problème à N corps non-trivial tout en limitant la renormalisation de $H_{\not{t}}^{\mathrm{LO}}$ sur des secteurs à N corps avec N petit. La seconde classe d'approximations considérée regroupe les sommes d'un ensemble de diagrammes de Feynman exprimés en terme de propagateurs de particule et de trou. Cela a été possible grâce à un deuxième puissant théorème, le théorème asymptotique de Weinberg [35]. Ce théorème et les outils mathématiques qui l'accompagnent sont brièvement passés en revue dans la section 4.2.2. À l'aide de ce théorème, une procédure systématique est dérivée de manière similaire pour les diagrammes de particule/trou. Comme la décomposition du propagateur non-perturbé en un propagateur de particule et un propagateur de trou est générale (via la représentation de Lehmann), cela ouvre la voie à de futures généralisations pour diverses approximations du problème à N corps (tel que CC ou SCGF) et/ou différentes partitions du Hamiltonien. Parmi les premiers exemples d'intérêt pour la physique nucléaire, mentionnons l'application de la procédure dérivée dans Chap. 4 au cas de la ressommation RPA (pour random phase approximation) et l'extension de la procédure au cas où l'Hamiltonien non-perturbé est l'Hamiltonien Hartree-Fock. Enfin, toutes les considérations faites dans Chap. 4 sont restées en large partie agnostique pour ce qui est de l'Hamiltonien. Dans le futur, il serait donc intéressant de chercher à étendre la présente étude à d'autre Hamiltoniens tels que ceux dérivés dans le cadre de χEFT.

Bibliography

[1] P. Navrátil, J. P. Vary, and B. R. Barrett, "Properties of 12C in the Ab Initio Nuclear Shell Model," *Physical Review Letters* **84** no. 25, (Jun, 2000) 5728–5731. On pages ii and 122.

[2] S. C. Pieper and R. B. Wiringa, "Quantum Monte Carlo Calculations of Light Nuclei," *Annual Review of Nuclear and Particle Science* **51** no. 1, (Dec, 2001) 53–90. On pages ii and 122.

[3] G. Hupin, S. Quaglioni, and P. Navrátil, "Unified Description of Li 6 Structure and Deuterium- 4He Dynamics with Chiral Two- and Three-Nucleon Forces," *Physical Review Letters* **114** no. 21, (May, 2015) 212502. On pages ii and 122.

[4] A. Lovato, S. Gandolfi, J. Carlson, S. C. Pieper, and R. Schiavilla, "Electromagnetic and neutral-weak response functions of 4He and 12C," *Physical Review C* **91** no. 6, (Jun, 2015) 062501. On pages ii and 122.

[5] S. Bogner, R. Furnstahl, and A. Schwenk, "From low-momentum interactions to nuclear structure," *Progress in Particle and Nuclear Physics* **65** no. 1, (Jul, 2010) 94–147. On pages ii and 122.

[6] S. Weinberg, "Phenomenological Lagrangians," *Physica A: Statistical Mechanics and its Applications* **96** no. 1-2, (Apr, 1979) 327–340. On pages ii, 18, 25, and 123.

[7] S. Weinberg, "Nuclear forces from chiral lagrangians," *Physics Letters B* **251** no. 2, (Nov, 1990) 288–292, `arXiv:9910064v1 [nucl-th]`. On pages ii and 123.

[8] S. Weinberg, "Effective chiral lagrangians for nucleon-pion interactions and nuclear forces," *Nuclear Physics, Section B* **363** no. 1, (Sep, 1991) 3–18. On pages ii and 123.

[9] P. F. Bedaque and U. van Kolck, "Effective Field Theory for Few-Nucleon Systems," *Annu. Rev. Nucl. Part. Sci* **52** (Dec, 2002) 339–96, `arXiv:0203055 [nucl-th]`. On pages ii, 35, and 123.

[10] L. Platter, H.-W. Hammer, and U.-G. Meißner, "Four-boson system with short-range interactions," *Physical Review A* **70** no. 5, (Nov, 2004) 052101. On pages iii, 29, and 123.

[11] J. M. Luttinger and J. C. Ward, "Ground-State Energy of a Many-Fermion System. II," *Physical Review* **118** no. 5, (Jun, 1960) 1417–1427. On pages iii, 29, 43, 50, and 123.

[12] T. Frick, *Self-consistent Green's functions in nuclear matter at finite temperature.* PhD thesis, 2004. On pages iii, 29, 52, 54, 76, and 123.

[13] F. Coester, "Bound states of a many-particle system," *Nuclear Physics* **7** (Jun, 1958) 421–424. On pages iii, 29, and 123.

[14] G. Hagen, T. Papenbrock, D. J. Dean, and M. Hjorth-Jensen, "Ab initio coupled-cluster approach to nuclear structure with modern nucleon-nucleon interactions," *Physical Review C* **82** no. 3, (Sep, 2010) 034330. On pages iii, 29, and 123.

[15] K. Tsukiyama, S. K. Bogner, and A. Schwenk, "In-Medium Similarity Renormalization Group For Nuclei," *Physical Review Letters* **106** no. 22, (Jun, 2011) 222502. On pages iii, 29, and 123.

[16] H. Hergert, S. K. Bogner, S. Binder, A. Calci, J. Langhammer, R. Roth, and A. Schwenk, "In-medium similarity renormalization group with chiral two- plus three-nucleon interactions," *Physical Review C* **87** no. 3, (Mar, 2013) 034307. On pages iii, 29, and 123.

[17] J. Goldstone, "Derivation of the Brueckner Many-Body Theory," *Proceedings of the Royal Society A: Mathematical, Physical and Engineering Sciences* **239** no. 1217, (Feb, 1957) 267–279. On pages iii, 29, and 123.

[18] I. Shavitt and R. J. Bartlett, *Many-body methods in chemistry and physics : MBPT and coupled-cluster theory.* Cambridge University Press, 2009. On pages iii, 29, and 123.

[19] P. Navrátil, V. G. Gueorguiev, J. P. Vary, W. E. Ormand, and A. Nogga, "Structure of A = 10 – 13 Nuclei with Two- Plus Three-Nucleon Interactions from Chiral Effective Field Theory," *Physical Review Letters* **99** no. 4, (Jul, 2007) 042501. On page 3.

[20] T. Otsuka, T. Suzuki, J. D. Holt, A. Schwenk, and Y. Akaishi, "Three-body forces and the limit of oxygen isotopes," *Physical Review Letters* **105** no. 3, (Jul, 2010) 032501, `arXiv:0908.2607`. On page 3.

[21] H. Hergert, S. Binder, A. Calci, J. Langhammer, and R. Roth, "Ab initio calculations of even oxygen isotopes with chiral two-plus-three-nucleon interactions," *Physical Review Letters* **110** no. 24, (Jun, 2013) 242501, `arXiv:1302.7294v1`. On page 3.

[22] W. Dickhoff and C. Barbieri, "Self-consistent Green's function method for nuclei and nuclear matter," *Progress in Particle and Nuclear Physics* **52** no. 2, (Apr, 2004) 377–496. On page 7.

[23] V. Galitskii and A. Migdal, "Application of quantum field theory methods to the many body problem," *Sov. Phys. JETP* no. 96, jul. On page 8.

[24] P. C. Martin and J. Schwinger, "Theory of Many-Particle Systems. I," *Physical Review* **115** no. 6, (Sep, 1959) 1342–1373. On pages 8 and 41.

[25] D. S. Koltun, "Total Binding Energies of Nuclei, and Particle-Removal Experiments," *Physical Review Letters* **28** no. 3, (Jan, 1972) 182–185. On page 8.

[26] M. Gell-Mann and F. Low, "Bound states in quantum field theory," *Physical Review* **84** no. 2, (Oct, 1951) 350–354, `arXiv:9907483 [hep-ph]`. On page 12.

[27] J.-P. Blaizot and G. Ripka, *Quantum theory of finite systems*. MIT Press, 1986. On pages 12, 13, and 111.

[28] L. L. Foldy and S. A. Wouthuysen, "On the dirac theory of spin 1/2 particles and its non-relativistic limit," *Physical Review* **78** no. 1, (Apr, 1950) 29–36. On page 18.

[29] E. E. Jenkins and A. V. Manohar, "Baryon chiral perturbation theory using a heavy fermion Lagrangian," *Physics Letters, Section B: Nuclear, Elementary Particle and High-Energy Physics* **255** no. 4, (Feb, 1991) 558–562. On page 18.

[30] A. Gårdestig, K. Kubodera, and F. Myhrer, "Comparison of the heavy-fermion and Foldy-Wouthuysen formalisms at third order," *Physical Review C - Nuclear Physics* **76** no. 1, (Jul, 2007) 014005. On page 18.

[31] M. Luke and A. V. Manohar, "Reparameterisation invariance constraints on heavy particle effective field theories," *Physics Letters B* **286** no. 3, (Jul, 1992) 348 – 354. On page 18.

[32] D. R. Entem and R. Machleidt, "Accurate nucleon-nucleon potential based upon chiral perturbation theory," *Physics Letters, Section B: Nuclear, Elementary Particle and High-Energy Physics* **524** no. 1-2, (Jan, 2002) 93–98, `arXiv:0108057 [nucl-th]`. On page 20.

[33] E. Epelbaum, A. Nogga, W. Glöckle, H. Kamada, U.-G. Meißner, and H. Witała, "Three-Nucleon Forces from Chiral Effective Field Theory," *Physical Review C* **66** no. 6, (Dec, 2002) 064001, `arXiv:0208023 [nucl-th]`. On page 20.

[34] R. Machleidt and D. R. Entem, "Chiral effective field theory and nuclear forces," *Physics Reports* **503** no. 1, (Jun, 2011) 1–75, `arXiv:1105.2919v1`. On page 20.

[35] S. Weinberg, "High-energy behavior in quantum field theory," *Physical Review* **118** no. 3, (May, 1960) 838–849. On pages 22, 26, 86, 94, 96, and 125.

[36] K. Hepp, "Proof of the Bogolyubov-Parasiuk theorem on renormalization," *Communications in Mathematical Physics* **2** no. 1, (Dec, 1966) 301–326. On pages 22, 86, and 125.

[37] W. Zimmermann, "Convergence of Bogoliubov's method of renormalization in momentum space," *Communications in Mathematical Physics* **15** no. 3, (Sep, 1969) 208–234. On pages 22, 23, 86, 117, 118, and 125.

[38] G. t' Hooft and M. Veltman, "Regularization and renormalization of gauge fields," *Nuclear Physics B* **44** no. 1, (Jul, 1972) 189–213, `arXiv:1011.1669v3`. On page 22.

[39] D. R. Phillips, S. R. Beane, and T. D. Cohen, "Nonperturbative Regularization and Renormalization: Simple Examples from Nonrelativistic Quantum Mechanics," *Annals of Physics* **263** no. 2, (Mar, 1998) 255–275, `arXiv:9706070 [hep-th]`. On page 22.

[40] Y. Hahn and W. Zimmermann, "An Elementary Proof of Dyson's Power Counting Theorem," *Communications in Mathematical Physics* **10** no. 4, (Dec, 1968) 330–342. On pages 23 and 117.

[41] W. Zimmermann, "The power counting theorem for Minkowski metric," *Communications in Mathematical Physics* **11** no. 1, (Mar, 1968) 1–8. On pages 23 and 117.

[42] J. H. Lowenstein and W. Zimmermann, "The power counting theorem for Feynman integrals with massless propagators," *Communications in Mathematical Physics* **44** no. 1, (Feb, 1975) 73–86. On pages 23 and 117.

[43] H.-W. Hammer and S. König, "General Aspects of Effective Field Theories and Few-Body Applications," pp. 93–153. Springer, Cham, 2017. On pages 25 and 26.

[44] M. Luke and A. V. Manohar, "Bound states and power counting in effective field theories," *Physical Review D* **55** no. 7, (Apr, 1997) 4129–4140. On page 26.

[45] P. F. Bedaque, H.-W. Hammer, and U. van Kolck, "Renormalization of the Three-Body System with Short-Range Interactions," `arXiv:9809025v2 [nucl-th]`. On pages 27 and 29.

[46] A. Tichai, J. Langhammer, S. Binder, and R. Roth, "Hartree–Fock many-body perturbation theory for nuclear ground-states," *Physics Letters B* **756** (May, 2016) 283–288. On page 29.

[47] A. Tichai, P. Arthuis, T. Duguet, H. Hergert, V. Somà, and R. Roth, "Bogoliubov Many-Body Perturbation Theory for Open-Shell Nuclei," `arXiv:1806.10931 [nucl-th]`. On pages 29 and 105.

[48] L. Faddeev, "Scattering theory for a three particle system," *Zh. Eksp. Teor. Fiz.* **39** (1960) 1459. On page 37.

[49] O. Yakubovsky, "On the integral equations in the theory of n particle scattering," *Sov. J. Nucl. Phys.* **5** (1967) 937. On page 37.

[50] J. Carlson, S. Gandolfi, F. Pederiva, S. C. Pieper, R. Schiavilla, K. Schmidt, and R. Wiringa, "Quantum Monte Carlo methods for nuclear physics," *Reviews of Modern Physics* **87** no. 3, (Sep, 2015) 1067–1118. On page 37.

[51] G. Baym and L. P. Kadanoff, "Conservation Laws and Correlation Functions," *Physical Review* **124** no. 2, (Oct, 1961) 287–299. On pages 37, 40, and 50.

[52] G. Baym, "Self-Consistent Approximations in Many-Body Systems," *Physical Review* **127** no. 4, (Aug, 1962) 1391–1401. On pages 37 and 40.

[53] N. N. Bogolyubov, "The dynamical theory in statistical physics," 1965. On page 41.

[54] M. Born and H. S. Green, "A General Kinetic Theory of Liquids. IV. Quantum Mechanics of Fluids," *Proceedings of the Royal Society A: Mathematical, Physical and Engineering Sciences* **191** no. 1025, (Nov, 1947) 168–181. On page 41.

[55] J. Yvon, "Une méthode d'étude des corrélations dans les fluides quantiques en équilibre," *Nuclear Physics* **4** (Aug, 1957) 1–20. On page 41.

[56] J. G. Kirkwood, "The Statistical Mechanical Theory of Transport Processes I. General Theory," *The Journal of Chemical Physics* **14** no. 3, (Mar, 1946) 180–201. On page 41.

[57] E. E. Salpeter and H. A. Bethe, "A Relativistic Equation for Bound-State Problems," *Physical Review* **84** no. 6, (Dec, 1951) 1232–1242. On page 43.

[58] A. L. Fetter and J. D. Walecka, *Quantum Theory of Many-Particle Systems*. Dover Publications, 1971. On pages 43 and 104.

[59] W. H. Dickhoff and D. Van Neck, *Many-Body Theory Exposed!* World Scientific, May, 2008. On page 48.

[60] K. A. Brueckner, C. A. Levinson, and H. M. Mahmoud, "Two-Body Forces and Nuclear Saturation. I. Central Forces," *Physical Review* **95** no. 1, (Jul, 1954) 217–228. On page 49.

[61] C. De Dominicis and P. C. Martin, "Stationary Entropy Principle and Renormalization in Normal and Superfluid Systems. I. Algebraic Formulation," *Journal of Mathematical Physics* **5** no. 1, (Jan, 1964) 14–30. On page 50.

[62] C. De Dominicis and P. C. Martin, "Stationary Entropy Principle and Renormalization in Normal and Superfluid Systems. II. Diagrammatic Formulation," *Journal of Mathematical Physics* **5** no. 1, (Jan, 1964) 31–59. On page 50.

[63] J. M. Cornwall, R. Jackiw, and E. Tomboulis, "Effective action for composite operators," *Physical Review D* **10** no. 8, (Oct, 1974) 2428–2445. On page 50.

[64] H. van Hees and J. Knoll, "Renormalization in self-consistent approximation schemes at finite temperature: Theory," *Physical Review D - Particles, Fields, Gravitation and Cosmology* **65** no. 2, (Dec, 2002) 025010, `arXiv:0107200 [hep-ph]`. On pages 50 and 105.

[65] H. van Hees and J. Knoll, "Renormalization of self-consistent approximation schemes at finite temperature. II. Applications to the sunset diagram," *Physical Review D - Particles, Fields, Gravitation and Cosmology* **65** no. 10, (Apr, 2002) 14, `arXiv:0111193 [hep-ph]`. On pages 50 and 105.

[66] H. van Hees and J. Knoll, "Renormalization in self-consistent approximation schemes at finite temperature. III. Global symmetries," *Physical Review D - Particles, Fields, Gravitation and Cosmology* **66** no. 2, (Jul, 2002) 2, `arXiv:0203008 [hep-ph]`. On pages 50 and 105.

[67] J. P. Blaizot, E. Iancu, and U. Reinosa, "Renormalization of Φ-derivable approximations in scalar field theories," *Nuclear Physics A* **736** no. 1-2, (May, 2004) 149–200, `arXiv:0312085 [hep-ph]`. On pages 50 and 105.

[68] J. Berges, S. Borsányi, U. Reinosa, and J. Serreau, "Nonperturbative renormalization for 2PI effective action techniques," *Annals of Physics* **320** no. 2, (Dec, 2005) 344–398, `arXiv:0503240 [hep-ph]`. On pages 50 and 105.

[69] P. Bożek, "One-body properties of nuclear matter with off-shell propagation," *Physical Review C* **65** no. 5, (Apr, 2002) 054306. On pages 52, 54, and 76.

[70] V. Somà, *Short range correlations in nuclear matter*. PhD thesis, 2009. On pages 52, 54, and 76.

[71] A. Huguet, *Thermodynamical properties of nuclear matter from a self-consistent Green's function approach*. PhD thesis, 2007. On pages 52, 54, and 76.

[72] C. Barbieri and A. Carbone, "Self-Consistent Green's Function Approaches," pp. 571–644. Springer, Cham, 2017. On pages 52, 54, and 76.

[73] J. E. Irwin, *A detailed investigation of the tensor force and the Pauli exclusion principle in nuclear matter*. PhD thesis, 1963. On page 54.

[74] R. Sartor, "Solution of the Bethe-Goldstone equation with an exact propagator," *Physical Review C* **54** no. 2, (Aug, 1996) 809–814. On pages 54 and 78.

[75] K. Suzuki, R. Okamoto, M. Kohno, and S. Nagata, "Exact treatment of the Pauli exclusion operator in nuclear matter calculation," *Nuclear Physics A* **665** no. 1-2, (Feb, 2000) 92–104. On page 54.

[76] N. Kaiser, "Resummation of fermionic in-medium ladder diagrams to all orders," *Nuclear Physics A* (Jun, 2011) , `arXiv:1102.2154v1`. On pages 60, 67, 69, and 72.

[77] N. Kaiser, "Resummation of in-medium ladder diagrams: S-wave effective range and P-wave interaction," *European Physical Journal A* (Sep, 2012) , `arXiv:1210.0783v1`. On page 60.

[78] M. J. H. Ku, A. T. Sommer, L. W. Cheuk, and M. W. Zwierlein, "Revealing the superfluid lambda transition in the universal thermodynamics of a unitary fermi gas," *Science* **335** no. 6068, (Feb, 2012) 563–567. On page 72.

[79] T. D. Lee and C. N. Yang, "Many-Body Problem in Quantum Mechanics and Quantum Statistical Mechanics," *Physical Review* **105** no. 3, (Feb, 1957) 1119–1120. On pages 76 and 90.

[80] G. A. Baker, "Singularity Structure of the Perturbation Series for the Ground-State Energy of a Many-Fermion System," *Reviews of Modern Physics* **43** no. 4, (Oct, 1971) 479–531. On pages 76 and 90.

[81] R. Bishop, "Ground-state energy of a dilute fermi gas," *Annals of Physics* **77** no. 1-2, (May, 1973) 106–138. On pages 76 and 90.

[82] M. Le Bellac, *Thermal field theory*. Cambridge University Press, 2000. On page 78.

[83] N. N. Bogoliubov and O. S. Parasiuk, "On the multiplication of the causal function in the quantum theory of fields," *Acta Mathematica* **97** (1957) 227–266. On pages 86 and 125.

[84] J. C. Collins, *Renormalization: an introduction to renormalization, the renormalization group and the operator-product expansion.* Cambridge university press, 1985. On page 86.

[85] B. D. Day, "Elements of the Brueckner-Goldstone Theory of Nuclear Matter," *Reviews of Modern Physics* **39** no. 4, (Oct, 1967) 719–744. On page 92.

[86] D. Bohm and D. Pines, "A Collective Description of Electron Interactions: III. Coulomb Interactions in a Degenerate Electron Gas," *Physical Review* **92** no. 3, (Nov, 1953) 609–625. On page 99.

[87] M. Gell-Mann and K. A. Brueckner, "Correlation Energy of an Electron Gas at High Density," *Physical Review* **106** no. 2, (Apr, 1957) 364–368. On page 99.

[88] J. Hubbard, "The Description of Collective Motions in Terms of Many-Body Perturbation Theory," *Proceedings of the Royal Society A: Mathematical, Physical and Engineering Sciences* **240** no. 1223, (Jul, 1957) 539–560. On page 99.

[89] P. Czerski, W. H. Dickhoff, A. Faessler, and H. Müther, "Δ isobars in finite nuclei and nuclear matter," *Physical Review C* **33** no. 5, (May, 1986) 1753–1761. On page 99.

[90] P. Arthuis, T. Duguet, A. Tichai, R. D. Lasseri, and J. P. Ebran, "ADG: Automated generation and evaluation of many-body diagrams I. Bogoliubov many-body perturbation theory," `arXiv:1809.01187 [nucl-th]`. On page 105.

[91] A. Carbone, A. Cipollone, C. Barbieri, A. Rios, and A. Polls, "Self-consistent Green's functions formalism with three-body interactions," *Physical Review C* **88** no. 5, (Nov, 2013) 054326. On page 112.

université PARIS-SACLAY | ÉCOLE DOCTORALE PHENIICS

Titre : Indépendance de la renormalisation d'observables à N corps dans $\not\pi$EFT

Mots-clés : Théorie quantique à N corps, Théorie des champs effectifs, Renormalisation, Matière nucléaire, Structure nucléaire

Résumé : Actuellement l'intéraction nucléaire est décrite par une théorie effective des champs chirale (χEFT). De cette façon, les contributions aux observables sont organisées en suite d'importance décroissante. Le calcul de la contribution principal nécessite de résoudre exactement l'équation de Schrödinger pour un certain Hamiltonien. Une description alternative, considérant uniquement des nucléons ($\not\pi$EFT) comme degrés de liberté, mène à la même nécessité d'une résolution exacte. En pratique, de tels calculs sont irréalistes, même numériquement, pour des observables à N corps avec $N \gg 10$. Par conséquence, des approximations supplémentaires doivent être développées. Dans cette thèse, des approximations non-perturbatives basées sur des fonctions de Green auto-cohérentes (SCGF) ainsi que des approximations basé sur des théories des perturbations à N corps (MBPT) sont considérées au sein de $\not\pi$EFT. Le but de cette thèse est d'étudier l'invariance par le groupe de renormalisation d'observables à N corps dans de tels cas où $N \gg 10$ avec l'espoir que les conclusions tirées puissent être étendu à χEFT. Dans le cas de SCGF, l'analyse des résultats numériques produits avec un code à l'état de l'art révèle une instabilité critique amenant à des observables dépendant de la renormalisation. Un correctif est proposé et devra être implémenté avant tout futur calcul SCGF dans $\not\pi$EFT. Cette étude révèle l'importance critique des approximations numériques sur l'invariance par le groupe de renormalisation des observables. Dans le cas de MBPT, une étude formelle ouvre la voie pour formuler la renormalisation d'un large ensemble d'approximation à N corps dans le future.

Title: Renormalization invariance of many-body observables within $\not\pi$EFT

Keywords: Quantum many-body theory, Effective field theory, Renormalization, Nuclear matter, Nuclear structure

Abstract: The current paradigm to describe the nuclear interaction is within the frame of Chiral Effective Field Theory (χEFT) which organizes contributions to observables in a serie of decreasing importance. It happens that the leading contribution already requires to solve exactly the Schrödinger equation with a particular Hamiltonian. The same requirement is at play in $\not\pi$EFT which considers only nucleonic degrees of freedom. Such calculations are numerically intractable for A-body observables with A $\gg$ 10. One must design an additional expansion and truncation for many-body observables. In this thesis, non-perturbative approximations on the basis self-consistent Green's function (SCGF) and on many-body perturbation theory (MBPT) are considered together with a $\not\pi$EFT. The goal of the present thesis is to investigate, in such framework, the renormalization invariance of many-body observables computed in A-body sectors with A $\gg$ 10. Hopefully the lessons learnt can be extended to χEFT. Analysis of numerical calculations realized with a state-of-the-art SCGF code reveals a critical numerical approximation leading to renormalization dependent observables. A necessary fix is proposed and must be implemented before any calculations based on SCGF and EFT in the future. This emphasises the criticality of numerical approximations for any calculation within a $\not\pi$EFT. At the same time, renormalization invariance of observables computed within MBPT is studied formally, opening the path to formulate the renormalization of a wide range of many-body truncation schemes in the future.

Université Paris-Saclay
Espace Technologique / Immeuble Discovery
Route de l'Orme aux Merisiers RD 128 / 91190 Saint-Aubin, France